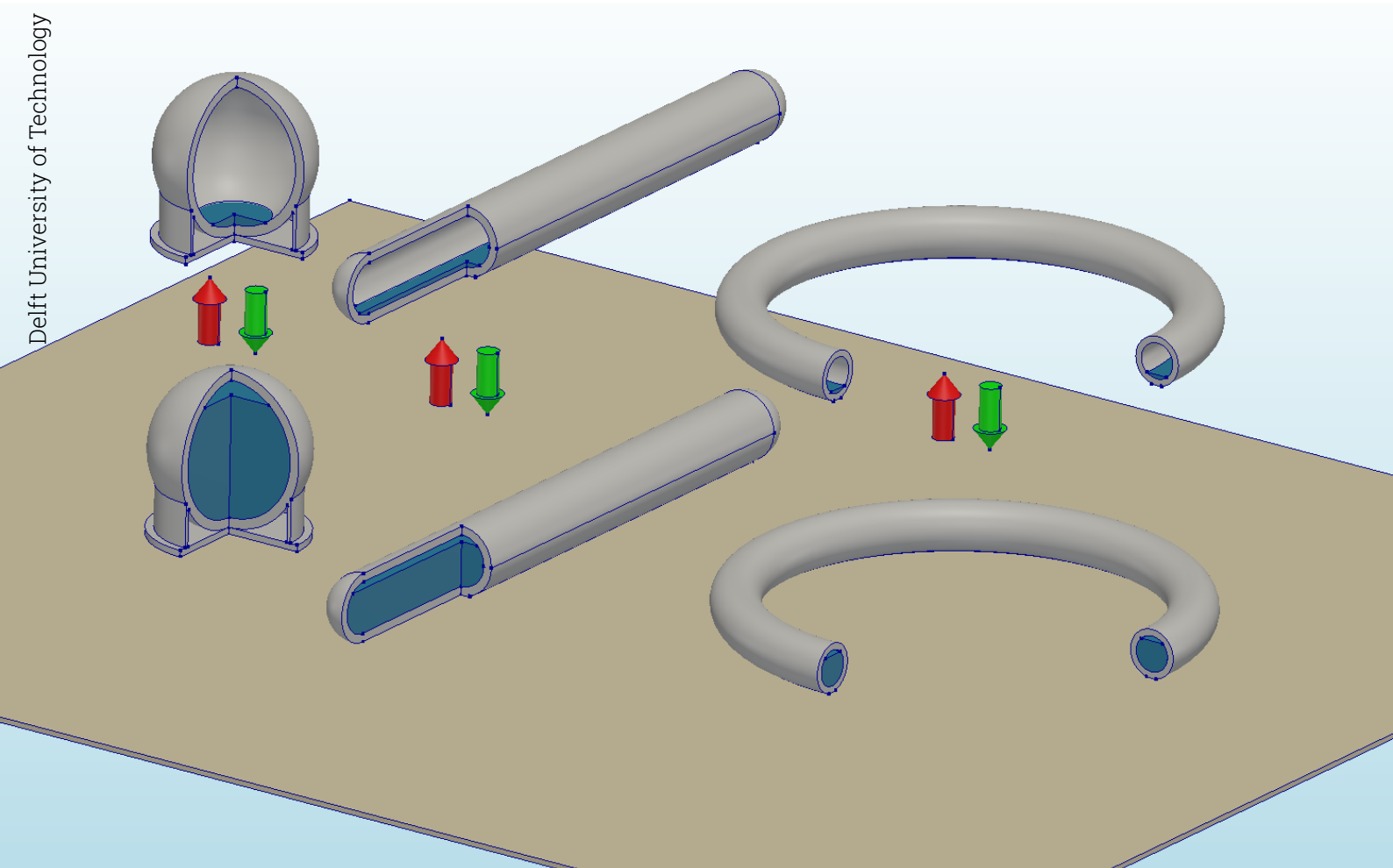


Marine Pumped Hydro Energy Storage

Shape design of the reservoir

Lucas Wesseling



Marine Pumped Hydro Energy Storage

Shape design of the reservoir

by

Lucas Wesseling

to obtain the degree of Master of Science

at the Delft University of Technology,

to be defended publicly on Friday March 22, 2024 at 10:00 AM.

Student number:	4600819	
Project duration:	July, 2023 – March, 2024	
Thesis committee:	Prof. dr. ir. M. A. N. Hendriks,	TU Delft, Chair
	Dr. ir. P. C. J. Hoogenboom,	TU Delft
	Ir. H. de Waardt,	Witteveen+Bos
	Ir. A. van Dalzen,	Witteveen+Bos

An electronic version of this thesis is available at <http://repository.tudelft.nl/>.

Preface

This thesis is the fruit of my labor over the preceding nine months. Embarking on this journey as a student of structural engineering, I have continuously appreciated the chance this topic has given me to play a part in the energy transition. The project has ignited a genuine fascination within me for offshore constructions. In many ways, this project signifies the beginning of a new phase in my academic and professional pursuits.

In the context of this project, I am thankful for the opportunity provided by Huig de Waardt to complete my graduation at Witteveen+Bos. His boundless enthusiasm for civil engineering, coupled with his extensive knowledge and keen interest in structural design, have made this project an enjoyable endeavor. Additionally, exchanging thoughts with and drawing inspiration from the incredibly relevant experiences of Arjen van Dalzen has been very helpful.

On the TU Delft side, I want to express my appreciation for Pierre Hoogenboom, for helping me on my way and his consistent availability for meaningful discussions. I will always remember his response when, after dedicating two hours to solving a challenging differential equation together, I offered to send him a paper I was certain he would find interesting. With a gracious smile, he replied: 'I would love to read it, but unfortunately I do need to be a bit efficient with my time.'. That very night I received an email with the answer to the very equation.

Lastly, I want to thank the chair of my committee, Max Hendriks, for his involvement. It has been impressive to observe his ability to comprehend and process matter in a vast pace. Furthermore, his kindness has always made me feel very welcome.

As this project symbolizes the conclusion of my study phase, it all commenced with the inspiration I found in one person: my dad. He has profoundly influenced my choice of study and remains a constant example whom I have always admired. Amidst his challenges over the past decade, appreciating all his professional endeavors may be difficult, yet his unwavering persistence and admirable qualities shine through to me. These insights have been enriched through numerous heartfelt conversations with my mother, who has had a tremendous influence on my perspectives and personality. Growing up in a dynamic household, I have had the opportunity to interact with a diverse array of people, thanks in part to my sister Laura. In combination with the warm thoughtfulness and continuous faith my girlfriend Margot has provided me with, I am truly grateful for the people that surround me.

*Lucas Wesseling
Rotterdam, March 2024*

Abstract

The offshore renewable energy market is rapidly growing, particularly in wind and solar sectors. The intermittent nature of these energy sources underscores the necessity for offshore energy storage solutions. Among the techniques being explored, Marine Pumped Hydro-Energy Storage (MPHES) emerges as a promising option. This innovative concept operates similarly to artificial lakes, where water is stored and released to generate electricity. In the MPHES system, a seabed-based reservoir is established, in which water flows, driving turbines to generate electricity. During periods of energy surplus, the system is charged by pumping water out of the reservoir.

The available energy storage capacity increases with both depth and volume. Current designs proposed in the literature discuss installation depths ranging from 600 to 1000 meters, while achieving internal volumes of 9.000 to 12.000 cubic meters. These system adopt a spherical shape of the reservoir, with external diameters ranging from 30 to 34 meters. The material of choice for these structures is concrete.

Through extensive interviews and a review of relevant literature, two significant challenges have been identified in these designs. The spherical shape and large dimensions of the reservoir make construction highly complex. The most promising construction approach outlined in the literature, involves a hybrid method of 3D Concrete Printing (3DCP) and conventional casting, where the formwork is constructed using 3DCP followed by concrete pouring. However, this method relies on unproven techniques that have never been implemented on this scale. Additionally, the draught of the structure is at least 26 meters. Despite using pontoons to provide extra buoyancy, this considerable draught seems too challenging for construction even in some of the world's largest dry docks.

The aforementioned challenges have prompted questions regarding the suitability of a spherical reservoir. Initially chosen for its effectiveness in distributing hydrostatic forces associated with significant depths, the spherical shape is now being reassessed. Investigations were undertaken to explore the most optimal shape for an MPHES system, considering the viability of a cylinder or torus. These shapes, identified through a literature review, maintain rounded features for efficient distribution of hydrostatic load, while potentially being constructible with existing techniques and offering a lower draught. However, it is anticipated that the cylinder and torus may require more material. The key question here is whether the ability to adopt simpler construction methods and achieve a lower draught outweighs the increased material usage, while also factoring in considerations of transportation and installation.

To assess the efficiency of a shape, a novel parameter, the CIV-ratio $\left(\frac{V_{\text{concrete}}}{V_{\text{internal}}}\right)$ is introduced. This quantifies the correlation between costs, indicated by the volume of material used, and benefits, expressed in internal volume. Through analytical methods and verified numerical simulations, the spherical reservoir has emerged as the most advantageous shape in terms of the CIV-ratio. With an internal volume of 10.000 m³ and a depth of 1000 meters, the sphere demonstrates a CIV-ratio of 0,78, whereas the cylinder exhibits a CIV-ratio of 1,09. At this volume, the cylinder and torus have a slenderness value of 12. While the method to achieve these results has not been applied to the torus, it showed results very similar to those obtained for the cylinder in other analyses. A neutral buoyant CIV-ratio is 0,75. Ultimately, the sphere exhibits a CIV-ratio that is 23% to 29% lower than that of the cylinder.

The slenderness values for the cylinder are defined as the ratio between its length and its internal radius, while for the torus, it is the ratio between its major radius and its minor radius. An analytical examination revealed that for both the cylinder and torus, a higher slenderness results in a lower CIV-ratio. However, higher slenderness values lead to significantly larger external dimensions of the reservoir, presenting challenges in terms of constructability and transportability. Drawing insights from reference projects involving dry docks and immersed tunnel construction, a favorable slenderness range of 10 to 20 was identified for the cylinder. A slenderness value of 12 in combination with an internal volume of 9.000 m³ yields an external diameter of 12,92 meters and a length of 129,0 meters. However, applying a

similar methodology, no such favorable range was found for the torus. Its external dimensions become impractically large, with a major diameter of approximately 100 meters for an internal volume of 9,000 m³ and acceptable slenderness values. These substantial dimensions impose constraints on feasible construction sites for the torus, contradicting the initial goal of avoiding such limitations. Consequently, further consideration of the torus was discontinued.

After conducting a literature review of reference projects and examining general concrete construction methods, five approaches for constructing a cylinder were identified and assessed. Through deductive analysis, reasoned evaluation, and expert interviews, the horizontal jump-forming technique emerged as the most practical method. This approach entails a semi-continuous process wherein the cylinder is constructed gradually using ring elements. The production cycle of each ring element begins with extending a launching girder, onto which inner formwork is affixed. Subsequently, the outer formwork is positioned to facilitate the pouring of concrete.

In contrast to the construction method for the sphere, literature demonstrates that the horizontal jump-forming technique has proven successful in tunnel construction, underscoring its reliability. Notably, while the preferred construction method for the cylinder is not suitable for the sphere, the reverse is not true. This observation suggests that constructing a cylinder is comparatively less complex than constructing a sphere.

During transport, the cylinder would be submerged and suspended from two or more catamaran-like pontoons, with tug boats facilitating the transportation process. This method, as evidenced in literature and verified analytically, seems to pose no more pronounced complications than transporting a sphere, which would also rely on tug boats for transportation and installation.

Furthermore, a review was conducted to assess the favorability of adopting a hemispherical cap design for the cylinder compared to a flat one. Through analytical calculations, it was found that opting for a hemispherical cap design can result in a significant reduction in material usage. Additionally, the hemispherical design proves to distribute hydrostatic pressure more effectively than its flat counterpart, with no significant additional stresses observed, as confirmed through finite element analysis.

A comparative analysis suggests that the cylindrical design presents a feasible option, especially for larger internal volumes. Here, the additional costs associated with increased material usage may be offset by the enhanced constructability of the cylindrical design, making it more desirable than the spherical option. Potential investors should therefore carefully consider the trade-off between higher material consumption and a simpler construction process. Nonetheless, for lower internal volumes, it is evident that the sphere still stands out as the optimal choice.

Contents

Preface	1
Abstract	2
Nomenclature	12
1 Introduction	1
1.1 Problem definition	2
1.2 Shape proposal	2
1.3 Research question	4
1.4 Project approach	4
1.5 Report structure	5
2 State of the art	6
2.1 Depth, volume and energy storage potential	6
2.2 Required storage capacity	7
2.3 Reservoir size	8
2.4 Competitiveness of MPHES to existing storage techniques	9
2.5 Requirements for potential MPHES installation locations	12
2.6 Experiments	13
2.7 Construction methods spherical design	15
2.7.1 Hemisphere concept by MIT	16
2.7.2 Hybrid 3D concrete printing and casting method by RCAM	16
2.7.3 Air pressured formwork by HTS	17
2.7.4 Other construction techniques	18
2.8 Implementation aspects spherical design	18
2.8.1 Construction location	18
2.8.2 Transport	19
2.8.3 Installation	19
2.8.4 Watertightness	19
2.9 Feasibility considerations	19
2.9.1 Market feasibility	19
2.9.2 Financial feasibility	20
2.9.3 Construction feasibility of spherical design	20
2.10 Cost analysis	21
2.11 Conclusions from literature	22
3 Starting points for initial structural design	23
3.1 Starting points	23
3.2 Shape geometries	24
3.2.1 Sphere	24
3.2.2 Cylinder	25
3.2.3 Torus	26
3.2.4 Slenderness	27
3.3 Definitions of membrane forces and internal stresses	29
3.4 Pump/turbine system placement	32
3.5 Loading conditions	33
4 Initial structural design	36
4.1 Initial reservoir design	36
4.1.1 Initial thickness estimation	37

4.1.2	Iterative adjustment of thickness	38
4.1.3	Internal Radius - Wall Thickness Relation	40
4.1.4	Optimization of cylinder- and torus-configuration	40
4.1.5	Sensitivity study concrete strength	41
4.2	Initial foundation design	42
4.2.1	Foundation design spherical reservoir	42
4.2.2	Foundation design cylindrical and toroidal reservoir	44
4.2.3	CIV-ratio comparison in foundation design	47
4.3	Reservoir and foundation design combination	47
5	Construction and implementation of cylindrical design	49
5.1	Dimensions of cylindrical and toroidal designs	50
5.1.1	Cylinder dimensions	50
5.1.2	Torus dimensions	51
5.1.3	Evaluation of dimensional suitability for construction locations	51
5.2	Exploration construction methods cylindrical design	52
5.2.1	Cast-in-place	52
5.2.2	Precast elements	52
5.2.3	Horizontal jump-forming	53
5.2.4	Vertical slip-forming	53
5.2.5	Hybrid 3DCP + cast-in-place	54
5.2.6	Trade-off	54
5.3	In-depth analysis construction methods cylindrical design	54
5.3.1	Precast elements	55
5.3.2	Horizontal jump-forming	56
5.3.3	Watertightness	56
5.3.4	Evaluation	59
5.4	Implementation aspects cylindrical design	59
5.4.1	Transport	59
5.4.2	Immersion	62
5.4.3	Stability	63
6	Optimization	64
6.1	Cap refinement cylindrical design	64
6.1.1	Reduction of the edge disturbance	65
6.1.2	Hemispherical cap design	66
6.1.3	Numerical verification of edge disturbance reduction	67
6.1.4	Redistribution of stress concentrations at cylinder-hemisphere transition	75
6.1.5	Contribution of hemispherical cap to CIV-ratio	82
6.2	Verification of uniform compression assumption	83
6.2.1	Analytical verification of uniform stress assumption for sphere	83
6.2.2	Analytical verification of uniform stress assumption for cylinder	84
6.2.3	Numerical model of sphere and cylinder	85
6.2.4	Evaluation of uniform stress assumption	86
6.3	Revised CIV-ratios	87
6.3.1	Increased wall thickness by satisfying found pressure distribution	87
6.3.2	Introduction of uncertainty in CIV-ratios	89
7	Synthesis, Implications, and Future Directions	91
7.1	Summary of results	91
7.2	Discussion	95
7.3	Conclusion	97
7.4	Recommendations	97
	References	99
A	Draughts	105
A.1	Draught of sphere in state-of-the-art	105
A.2	Draught of sphere in summary of results	107

A.3 Draught of cylinder in summary of results	108
B Hochtief construction technique	110
C Membrane forces	114
C.1 Spherical and cylindrical membrane forces	114
C.2 Toroidal membrane forces	115
D Calculation of concrete volumes	118
D.1 Determination of reservoir dimensions	118
D.1.1 Initial thickness estimation of spherical design	119
D.1.2 Initial thickness estimation of cylindrical design	119
D.1.3 Initial thickness estimation of toroidal design	120
D.1.4 Iterative thickness determination	121
D.1.5 Calculation of volumes of concrete	123
D.1.6 Iterations of calculations for graph production	124
D.2 Determination of foundation dimensions	124
D.2.1 Sphere	124
D.2.2 Cylinder foundation width	130
D.2.3 Torus foundation width	132
D.2.4 Iterative foundation width determination for cylinder and torus	135
D.3 CIV-ratio for cylinder with hemisphere cap	137
D.4 Python code	138
E Interview Bernhard Ernst, Deputy Head of Energy Storage at Fraunhofer IEE	154
F General concrete construction techniques	156
F.1 Conventional casting using formwork	156
F.2 Slip-forming	157
F.3 Jump-forming	159
F.4 Shotcrete	160
F.5 3D Concrete Printing	161
G Relevant construction locations	162
G.1 Land-based factory	162
G.2 Dry dock	162
G.3 Fjord	163
G.4 Open sea	164
H Concrete connection methods	165
I Diana models	168
I.1 Verification of uniform stress assumption	168
I.1.1 Sphere model	168
I.1.2 Cylinder model	172
I.2 Reduced models of cylindrical design	175
I.2.1 Validation of reduction of cylinder tube length	175
I.2.2 Validation of axisymmetrical reduction	180
I.3 Edge disturbance models	185
I.3.1 Validation of edge disturbance with thin shell	185
I.3.2 Models with various hemisphere thicknesses	189
I.3.3 Models for redistribution of stress concentration at cylinder-hemisphere transition	195

List of Figures

1.1	Concept overview of MPHES	1
1.2	Design for spherical, cylindrical and toroidal reservoir	3
2.1	Installed offshore wind capacity in 2019 [14]	8
2.2	Power and energy densities of different energy storage techniques [18]	9
2.3	Comparison of specific investment per installed capacity and storage capacity of MPHES, PHES and CAES [9]	10
2.4	Comparison of power generation costs of MPHES, PHES and CAES [9]	11
2.5	Price arbitrage in correlation with yearly storage operation hours for net zero annuity for a farm with 80 units [9]	11
2.6	Potential installation locations in Mediterranean sea [8]	13
2.7	The MIT experimental configuration: (a) SolidWorks model of the test setup, (b) the physical representation of the built system, and (c) the comprehensive test assembly, including the high reservoir. [5]	14
2.8	The Fraunhofer experimental configuration: (a) lift operation, (b) tugging operation to the final location in the lower left, and (c) the comprehensive test assembly on the right. [7]	15
2.9	Hemisphere concept by MIT [5]	16
2.10	Hybrid 3DCP + in situ casting construction method [29]	17
2.11	Formwork system for full-scale construction patented by HTS [7]	17
2.12	Potential design of MPHES-system, including pedestal and foundation[10]	18
2.13	Pie-chart of annual costs of implementation of MPHES-system[9]	22
3.1	Schematic cross-section of sphere	24
3.2	Schematics of cylinder	25
3.3	Schematics of torus	27
3.4	Sphere membrane forces and stress definitions at cross-section	30
3.5	Cylinder membrane forces and stress definitions at cross-section	31
3.6	Torus membrane forces and stress definitions at cross-section	32
3.7	Potential incorporated pump/turbine designs	33
3.8	Load situations for empty and full reservoir	35
4.1	Workflow for determining required volume of concrete	36
4.2	Concrete and internal volume relation for a sphere and various cylinder and torus configurations with initial thickness estimation; at $d = 1000$ m and $f_{cd} = 40$ MPa	38
4.3	Algorithm for determining shell thickness for sphere, cylinder and torus	39
4.4	Concrete and internal volume relation for a sphere and various cylinder and torus configurations with iterative thickness estimation; at $d = 1000$ m and $f_{cd} = 40$ MPa	39
4.5	Relationship between internal radius and wall thickness for the sphere, cylinder, and torus with different slenderness values; at $d = 1000$ m and $f_{cd} = 40$ MPa	40
4.6	Optimized concrete to internal volume ratios for cylinder and torus configurations with iterative approach; at $d = 1000$ m and $f_{cd} = 40$ MPa	41
4.7	Sensitivity analysis of concrete strength	42
4.8	Sphere foundation design with pedestal and shallow foundation [10]	43
4.9	CIV-ratio for concrete volume of spherical foundation design vs. Internal volume; at $d = 1000$ m and $f_{cd} = 40$ MPa	43
4.10	Algorithm for determining foundation width for cylinder and torus	44

4.11 Foundation design: CIV-ratio vs. Internal volume for different cylinder and torus slenderness values; with corresponding base widths; at $d = 1000$ m and $f_{cd} = 40$ MPa	45
4.12 Cylinder and torus cross-section visualisations	46
4.13 CIV-ratios of reservoir and foundation design combined; at $d = 1000$ m and $f_{cd} = 40$ MPa	48
5.1 External cylinder dimensions for various internal volumes and slenderness values; at $d = 1000$ m and $f_{cd} = 40$ MPa	50
5.2 External torus dimensions for various internal volumes and slenderness values; at $d = 1000$ m and $f_{cd} = 40$ MPa	51
5.3 Precast element method	55
5.4 Construction cycle of horizontal jump-forming method	57
5.5 Cylinder possible axial stresses at connections	58
5.6 Launch and transport of cylinder	60
5.7 Mechanic scheme of cylinder hanging from floater	61
6.1 Radial stiffness, k_{rad} [$N\ m^{-1}$]	64
6.2 Alternative cap designs for cylinder can reduce or eliminate edge disturbances	65
6.3 Bending moment and transition of tangential membrane force at cylinder-hemisphere connection [62]	65
6.4 Hemisphere cap details	67
6.5 Diana slice model for determining influence of hemisphere thickness on moment induced by edge disturbance	68
6.6 Moments due to edge disturbance for $t_h = t_c$	69
6.7 Moments due to edge disturbance for $t_h = 0, 6t_c$	70
6.8 Moments due to edge disturbance for $t_h = 0, 5t_c$	71
6.9 Moments due to edge disturbance for $t_h = 0, 4t_c$	72
6.10 Fitted polynomials for moments in edge disturbance hemisphere and cylinder interface; at $d = 1000$ m and $f_{cd} = 40$ MPa; Extracted from Figures 6.6b, 6.7b, 6.8b and 6.9b	73
6.11 Mechanical scheme of explanation for jump in moment line at cylinder edge	74
6.12 Shear forces caused by edge disturbance in hemisphere and cylinder interface; at $d = 1000$ m and $f_{cd} = 40$ MPa; Derivatives of fitted polynomials from Figure 6.10	75
6.13 Abrupt hemisphere-cylinder connection; model	76
6.14 Abrupt hemisphere-cylinder connection; principal stresses in XZ-plane	76
6.15 Abrupt hemisphere-cylinder connection; principal stresses in hemisphere	77
6.16 Abrupt hemisphere-cylinder connection; principal stresses in cylinder	77
6.17 Triangular hemisphere-cylinder connection; model	78
6.18 Triangular hemisphere-cylinder connection; principal stresses in XZ-plane	78
6.19 Triangular hemisphere-cylinder connection; principal stresses in hemisphere	79
6.20 Triangular hemisphere-cylinder connection; principal stresses in cylinder	79
6.21 Circular hemisphere-cylinder connection; model	80
6.22 Circular hemisphere-cylinder connection; principal stresses in XZ-plane	80
6.23 Circular hemisphere-cylinder connection; principal stresses in hemisphere	81
6.24 Circular hemisphere-cylinder connection; principal stresses in cylinder	81
6.25 CIV-ratio of reservoir and foundation for hemispherical cap design; at $d = 1000$ m and $f_{cd} = 40$ MPa	82
6.26 Thick-walled sphere with internal and external load	84
6.27 Thick-walled tube with internal and external load, representing the cylinder cross-section	85
6.28 Numerical verification of uniform compression assumption with Diana FEA	85
6.29 Uniform stress over wall thickness verification; at $d = 1000$ m and $f_{cd} = 40$ MPa	87
6.30 Revised workflow for determining wall thickness	88
6.31 CIV-ratios for sphere and cylinder for uniform and non-uniform pressure distribution at $d = 1000$ m and $f_{cd} = 40$ MPa; $V_{internal,cylinder} = 9.000\ m^3$	88

6.32 CIV-ratios for sphere and cylinder with hemispherical cap after introducing wall thickness uncertainty; at $d = 1000$ m and $f_{cd} = 40$ MPa; $V_{\text{internal,cylinder}} = 9.000$ m ³	90
A.1 Spherical cap volume [66]	106
B.1 HTS construction method: Phase 1, front view [30]	111
B.2 HTS construction method: Phase 1, top view [30]	112
B.3 HTS construction method: Phase 2, front view [30]	112
B.4 HTS construction method: Phase 3, front view [30]	112
B.5 HTS construction method: Phase 4, 3D view [30]	113
C.1 Derivation of Barlow's formula [36]	115
C.2 The geometry of a torus [36]	115
C.3 Membrane forces in a torus under hydro static pressure p	117
C.4 Maximum value for membrane force n_{yy} in a torus under hydro static pressure p	117
D.1 Number of iterations required to determine thickness, for $V = 10.000$ m ³ , $depth = 1000$ m	123
D.2 Sphere foundation design in [10]	125
D.3 Negative bending moment in circular foundation plate	126
D.4 Schematization of negative bending moment in circular foundation plate	126
D.5 Cross-section of sphere	128
D.6 Cylinder foundation side view	130
D.7 Torus foundation side view, cross-section AA of Figure D.8	132
D.8 Torus foundation top view; Quadrant plot	134
D.9 Algorithm for determining foundation width for cylinder and torus	136
D.10 Number of iterations in cylinder and torus foundation design	137
F.1 Schematic diagram of a typical slip-form system [70]	158
F.2 Novel horizontal slip-form technique for regenerating existing tunnel [48]	158
F.3 Construction of Steinhaus tunnel [47]	159
F.4 Shotcrete application in the repair of a concrete face [75]	160
F.5 Maximum overhang angle (β) [79]	161
G.1 Map of fjords [94]	163
G.2 Towing of Troll A platform to its final location [93]	164
H.1 Compression seal [55]	165
H.2 Wet joint [95]	166
H.3 Reinforcement continuities for cold joints [98]	166
H.4 Water leakage prevention measures	167
I.1 Octant sphere 3D model	169
I.2 Octant sphere mesh	169
I.3 Octant sphere global deformation	170
I.4 Octant sphere principal stresses	170
I.5 Octant sphere principal stresses; range -38 to -48 MPa	171
I.6 Octant sphere principal stresses; zoomed in	171
I.7 Quarter cylinder 2D model	172
I.8 Quarter cylinder mesh	172
I.9 Quarter cylinder global deformation	173
I.10 Quarter cylinder principal stresses	173
I.11 Quarter cylinder principal stresses; range -30 to -50 MPa	174
I.12 Quarter cylinder principal stresses; zoomed in	174
I.13 Length-reduced flat cap models for analyzing influence length	177
I.14 Length-reduced hemisphere cap models for analyzing influence length	177
I.15 Meshes of length-reduced flat cap models with nodes used for data collection highlighted	178

I.16	Meshes of length-reduced hemisphere cap models with nodes used for data collection highlighted	178
I.17	Stresses in the cross-section of length-reduced flat and hemispherical cap models . . .	179
I.18	Incompatible support conditions in edge of sliced model	181
I.19	$\frac{1}{64}$ th slice of hemisphere model with $L_{tube} = L_{influence}$	181
I.20	$\frac{1}{64}$ th slice of hemisphere model with $L_{tube} = 2L_{influence}$	182
I.21	Slice model mesh	182
I.22	Stresses in the cross-section of slice models	183
I.23	Principal stresses at the singularity of the slice	184
I.24	Schematic representation of cross-section used for edge-disturbance	185
I.25	Thin shell model for validation	187
I.26	Mesh of thin shell model for validation	188
I.27	Output of thin shell model for validation	188
I.28	Output of thin shell model for validation, adjusted for slice width	189
I.29	Hemisphere thickness model; $t_h = t_c$	191
I.30	Hemisphere thickness model; $t_h = 0, 6t_c$	192
I.31	Hemisphere thickness model; $t_h = 0, 5t_c$	193
I.32	Hemisphere thickness model; $t_h = 0, 4t_c$	194
I.33	Abrupt transition model; $t_h = 0, 5t_c$	196
I.34	Triangular transition model; $t_h = 0, 5t_c$	197
I.35	Circular transition model; $t_h = 0, 5t_c$	198

List of Tables

1.1	Membrane forces across sphere, cylinder and torus under distributed normal load p . . .	3
2.1	Illustrative parameters for MPHES-sphere	7
2.2	Potential locations for MPHES [8]	13
3.1	Frequently recurring parameters	24
3.2	Sphere dimensional parameters	25
3.3	Cylinder dimensional parameters	26
3.4	Torus dimensional parameters	26
3.5	Illustrative configurations for cylinder and torus	28
4.1	Membrane forces and volumes for sphere, cylinder, and torus	37
5.1	Trade-off exploration cylinder construction methods	54
5.2	Dimensions of illustrative cylinder	55
5.3	Concrete connection types of cylinder	59
5.4	Summary features precast element method and horizontal jump-forming method	59
6.1	Modelled hemisphere thicknesses	68
6.2	Maximum absolute moments for various hemisphere thicknesses	74
6.3	Span-thickness ratios of sphere and cylinder	83
6.4	Diana FEA model parameters for verification of uniform stress assumption	86
6.5	Comparison of established spherical design dimensions with literature	89
7.1	Summary of results	94
A.1	Parameters of sphere as described in Section 7.1	107
A.2	Parameters of cylinder as described in Section 7.1	108
B.1	Components in HTS construction technique	110
C.1	Membrane forces overview for several thin-walled shapes	114
C.2	Geometrical torus parameters [36]	115
D.1	Relevant parameters for soil stress assessment in cylinder and torus foundation	135
F.1	Comparison of various formwork systems [67]	157
G.1	List of the worlds largest land-based dry docks	163
I.1	Diana FEA model parameters for verification of uniform stress assumption	168
I.2	Cylinder flat cap and hemisphere model parameters	176
I.3	Cylinder hemisphere cap $\frac{1}{64}th$ slice model parameters	180
I.4	Thin shell model parameters	187
I.5	Moments caused by edge disturbance model parameters	190
I.6	Cylinder-hemisphere transition model parameters	195

Nomenclature

Abbreviations

Abbreviation	Definition
3DCP	3D concrete printing
CAES	Compressed Air Energy Storage
CIV-ratio	Concrete to Internal Volume ratio
CS	Cross-section
GIS	Geographical Information System
HTS	Hochtief Solutions AG
kWh	kilowatt-hour
MIT	Massachusetts Institute of Technology
MW	Megawatt
MWh	Megawatt-hour
MPHES	Marine Pumped Hydro Energy Storage
PHES	Pumped Hydro Energy Storage
RCAM	Reinforced Concrete Additive Manufacturing
SSV	Semi-Submersible Vessel
SW	Seawater

Symbols

Symbol	Definition	Unit
a	Internal radius	[m]
b	Major radius torus	[m]
C	Electrical storage capacity	[MWh]
d	Depth	[m]
d_{pump}	Pump diameter	[m]
F	Force	[N]
h_{pump}	Pump height	[m]
k_{rad}	Radial stiffness	[N m ⁻¹]
L	Length	[m]
n	Membrane force	[N m ⁻¹]
p	Hydrostatic pressure	[N m ⁻²]
P	Electrical capacity	[MW]
q	Distributed load	[N m ⁻¹]
t	Thickness	[m]
t_c	Thickness cylinder	[m]
t_h	Thickness hemisphere	[m]
V	Volume	[m ³]
W	Width	[m]
γ	Factor of safety	[-]
ϵ	Strain	[-]
η	Efficiency	[-]
ρ	Density	[kg m ⁻³]
σ	Stress	[MPa]

1

Introduction

The world is at a critical juncture when it comes to meeting its energy needs. With growing concerns over CO₂ emissions and the limited availability of fossil fuels, the global focus on renewable energy has intensified. Notably, wind and solar energy have emerged as promising contenders, contributing approximately 6,6% and 3,5% of the world's electricity production in 2021, with their proportion continuing to increase [1, 2]. However, their intermittent nature poses a significant distribution challenge. In this context, energy storage emerges as a critical solution to address this issue.

At present, approximately 90% of the world's energy storage capacity relies on pumped hydro-energy storage (PHES) systems, colloquially referred to as artificial lakes or reservoirs [3]. These innovative setups harness the height difference between two reservoirs, allowing water to be pumped to the upper reservoir during periods of energy surplus. When energy demand rises, the water is released to the lower reservoir, generating electricity through turbines. These systems naturally operate on land, requiring a specific geographical layout for the construction of the upper and lower reservoirs.

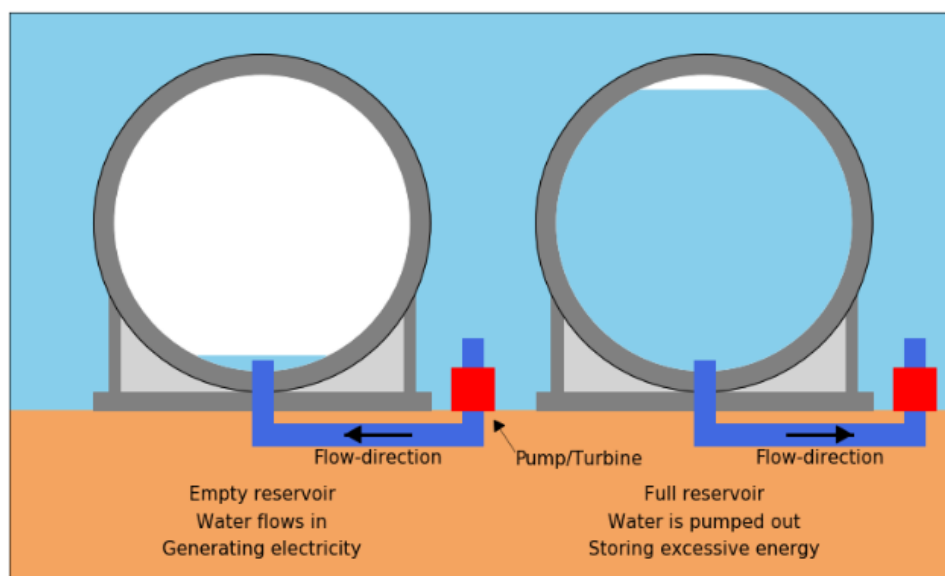


Figure 1.1: Concept overview of MPHES

In 2011 a novel deep-sea PHES system was presented by German physicists Professor Horst Schmidt-Böcking and Dr. Gerhard Luther [4]. It involves a lower reservoir in the form of a concrete sphere situated on the seabed [5]. During periods of energy surplus, the sphere is charged by pumping water out of it. When energy demand increases, the ocean water is released, flowing back into the sphere, and

generating electricity through turbines. This innovative idea explores the potential of utilizing the ocean floor for energy storage, offering a promising alternative to traditional land-based PHES systems.

This concept, illustrated in Figure 1.1, is referred to as marine pumped hydro-energy storage (MPHES). While the system has not been implemented yet, current designs envision a sphere-shaped reservoir with a diameter of up to 30 meters. The construction and scalability of such structures pose significant challenges and raise questions about the suitability of a sphere as the shape for the reservoir.

This thesis undertakes an in-depth exploration and assessment of cylindrical and toroidal-shaped reservoir designs for the MPHES system. The core question driving this research is: What is the optimal shape for a Marine Pumped Hydro Energy Storage system, taking into account factors such as material usage, construction feasibility, and installation requirements? By addressing this question, this study aims to move the concept of deep-sea energy storage one step closer to practical realization and implementation. This exploration will contribute to our understanding of how to enhance the viability of deep-sea energy storage as a sustainable and efficient solution.

1.1. Problem definition

The concept of MPHES was introduced in 2011 [4]. However, despite initial promising experiments and investigations into its technological feasibility, full-scale tests and actual implementation of the system are yet to be achieved. To propel the technological progress of MPHES and attract potential investors, further research is imperative. The conducted experiments have successfully demonstrated the proof of concept for MPHES as a viable energy storage solution. Additionally, extensive investigations have been carried out to assess the technological feasibility of the system. The results indicate that, under suitable conditions, MPHES holds promising potential and can attract investor interest. However, at present, the construction phase poses a significant bottleneck in the overall development process.

As described in Section 2.7 the proposed spherical shape of the MPHES system presents notable challenges in the construction phase. A monolith is favorable because of its watertightness, but reuse of the formwork is complex. A component-method on the other hand offers reusability of the mold, but the watertightness and the weight of the components become a challenge. Currently, the most promising construction method involves 3D Concrete Printing. However, its effectiveness on the intended scale remains uncertain.

Furthermore, the ambitious scale of the project results in significant draughts of the structure, which traditional dry docks cannot accommodate.

The complexities associated with the spherical design prompt a critical examination of the system's shape. A sphere is theoretically the optimal shape for distributing internal pressure under hydrostatic conditions. However, practical constructability poses substantial complications, necessitating the consideration of alternative shapes as potential solutions. Exploring different shapes can lead to a more feasible and efficient construction process for the MPHES system, ensuring its successful implementation and functionality as an effective energy storage solution. Important aspects in the consideration are concrete to internal volume ratio, watertightness of the design, constructability, transportability and the foundation design.

1.2. Shape proposal

The assumption of a spherical design as the starting point for all publications on MPHES necessitates a critical reassessment of its suitability. A literature gap exists regarding the study of alternative shapes for these systems. Although the spherical shape offers unmatched internal pressure distribution, exploring other shapes becomes essential to optimize the construction process and overall efficiency. Two particularly promising shapes to consider are the cylinder and the torus.

Both of these shapes still have a circular cross-section, an advantageous property for the installation of a structure at substantial depths. A form-finding analysis into the optimal cross-sectional shape of an immersed tunnel showed that at greater depths, the optimal shape of the cross-section for distributing pressure quickly converges to a circle [6]. Therefore, only circular shapes are considered.

The cylindrical configuration can be likened to a tube with enclosed ends. Although the cylindrical shape is inherently suitable for withstanding high external pressures, concerns arise regarding the end caps. At the transition from the cylindrical midsection to the end caps, an edge disturbance may arise, due to a change in curvature, potentially increasing internal stresses in this area. Reinforcement or additional concrete might be necessary to address this concern. Nonetheless, the cylinder's construction is envisioned to be less complicated, its utilization possibly allowing for reusable formwork, making it a strong contender.

On the other hand, the torus represents a long cylinder with its end connecting back to the start. This unique property eliminates edge disturbances that may occur with the cylinder design. The torus may lend itself well to construction with multiple prefabricated components, such as eight sections.

Both the cylinder and torus experience a maximum membrane force approximately twice as high as that of a sphere when subjected to the same hydrostatic pressure, as quantified in Table 1.1. To gain a comprehensive understanding of the internal pressure distribution in the three shapes (sphere, cylinder, and torus), detailed information is available in Appendix C.

Shape	Max. membrane force [N/m]
Sphere	$\frac{pa}{2}$
Cylinder	$-pa$
Torus	$< -pa$

Table 1.1: Membrane forces across sphere, cylinder and torus under distributed normal load p

Due to these higher membrane forces, a cylinder and torus require a thicker concrete wall than a sphere to resist the same hydrostatic pressure. Consequently, it is hypothesized that a higher volume of concrete is required for these shapes to achieve the same internal volume. This thesis revolves around the question of whether the higher material usage of the cylinder or torus, compared to the sphere, can be justified by simpler construction methods.

Further research and analysis are necessary to determine the most appropriate shape for MPHES. An illustrative design for each shape is presented in Figure 1.2, adhering to a constant internal volume across all shapes.

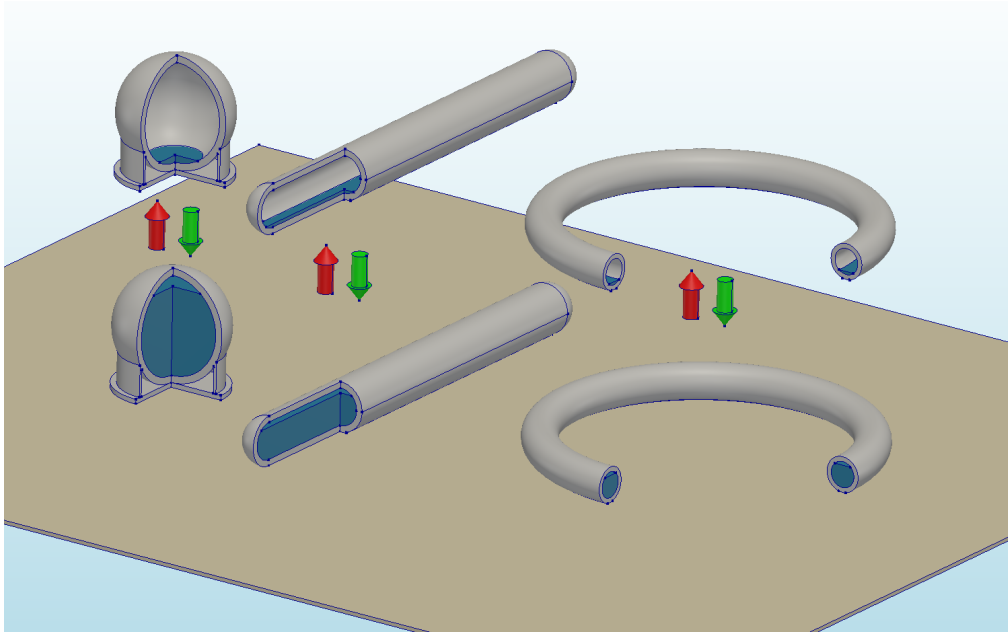


Figure 1.2: Design for spherical, cylindrical and toroidal reservoir

1.3. Research question

The analysis of construction feasibility, coupled with the unexplored potential of the torus and cylinder shapes, gives rise to the following research question:

What is the optimal shape for a Marine Pumped Hydro Energy Storage system, taking into account material usage, construction feasibility and other implementation aspects?

For this study, three shapes will be considered: the sphere, cylinder, and torus. The research question will be addressed by investigating the following sub-questions, which will be explored for all three shapes.

- *What key design parameters must be considered initially for each shape?*
- *What is the total material usage for each shape, taking into account both the reservoir and foundation components?*
- *What are the dimensions of each shape, and which construction methods are most appropriate for those dimensions?*
- *What factors need to be taken into account regarding transportation, installation, and ensuring watertightness for each shape?*

1.4. Project approach

The research methodology adopted in this thesis is structured to systematically address the research inquiries and achieve the set objectives. The sequence of the research will align with the identified questions, guiding the formulation of an optimal design for the MPHES system. Given the iterative nature of the design process, it is expected that adjustments will be made following the exploration of sub-questions, with opportunities for significant optimization emerging as the design progresses. Additionally, potential areas for optimization may become apparent as the design process unfolds, allowing for further refinement towards the conclusion of the thesis. The approach to the design process is delineated as follows:

1. *Identification of Design Parameters:*

- Conduct a comprehensive literature review to identify relevant design parameters for the MPHES system.
- Perform basic hand calculations to determine essential parameters such as installation depth, storage volume, and pressure distribution.

2. *Initial Design:*

- Utilize the identified design parameters as input to generate initial designs for the sphere, cylinder, and torus.
- Conduct analytical calculations to establish the initial dimensions of each shape, considering factors such as internal volume, slenderness, and concrete class.
- Apply established relationships to assess the impact of various design aspects on the dimensions and performance of each shape.
- Evaluate the material utilization-to-internal volume ratio for each design to determine performance and economic viability of the proposed designs.

3. *Construction Method Development:*

- Review existing construction methods for the sphere.
- Engage in interviews with experts and conduct literature research to establish construction methods tailored to the cylinder and torus.
- Evaluate the feasibility and effectiveness of each construction method for the MPHES system.

4. *Implementation aspects:*

- Identify appropriate transport and installation methods for the MPHES system, considering structural requirements and logistical constraints.
- Estimate watertightness by studying similar projects and consulting with experts to ensure the integrity of the system during operation.

5. *Evaluation of assumptions and optimization:*

- Evaluate the impact of key assumptions on the accuracy of design results.
- Identify areas for potential optimization in the design process, considering factors such as material usage, structural efficiency, and operational performance.
- Recognize the iterative nature of the design process and be prepared to revisit and adjust assumptions as necessary.

6. *Synthesis:*

- Summarize the findings and conclusions drawn from the research and design process.
- Draw conclusions regarding the optimal shape for the MPHES system based on performance, feasibility, and economic considerations.

Considering the established designs for spherical reservoirs, one might contend that reassessing wall thicknesses and concrete volumes for this geometry is redundant. However, the methodologies employed to derive these parameters in extant literature lack transparency. Consequently, adapting such methodologies to cylinder and torus configurations becomes intricate. Thus, there arises a compelling need to devise a novel approach for establishing an initial design and estimating wall thicknesses and concrete volumes. This effort is essential for ensuring a fair comparison among spherical, cylindrical, and toroidal geometries, thereby maintaining methodological rigor throughout the assessment process.

Throughout the project, an iterative design process will be applied, allowing for adjustments and improvements as new insights are gained. The combination of literature research, expert interviews, analytical calculations, and finite element simulations will contribute to a comprehensive study that guides the design and implementation of an efficient and effective MPHES system. It remains possible that certain shapes may be eliminated from consideration if they prove impractical or uncompetitive relative to others during the process.

1.5. Report structure

This report systematically investigates the optimal shape for an MPHES system. Initially, a comprehensive literature review is conducted to identify the current state-of-the-art, focusing on construction feasibility and implementation aspects of the sphere, detailed in Chapter 2. Following this, starting parameters for the initial design are outlined in Chapter 3. Subsequently, an initial structural design for the reservoir and foundation is developed for three shapes: sphere, cylinder, and torus, as discussed in Chapter 4, with a focus on estimating material usage for each shape.

Next, a construction method for the cylinder is elaborated upon in Chapter 5, along with other implementation considerations. Chapter 6 involves verification and optimization processes. Firstly, the accuracy of material usage determination assumptions is verified, followed by an optimization of the cylinder cap design.

In summary, Chapters 3 and 4 examine all three shapes, while Chapters 5 and 6 focus on a specific investigation into the cylinder.

Finally, the results and findings are synthesized, leading to conclusions drawn in Chapter 7.

2

State of the art

Energy storage plays a crucial role in addressing the imbalance between energy production and demand, particularly in the context of renewable energy sources characterized by intermittent production. The concept of MPHES is specifically tailored to function as an energy storage facility for floating wind farms or solar panel farms, aligning its storage capacity with the specific needs and demands of these renewable energy installations. Since the storage capacity of a single unit has limitations in scalability, the number of units must be carefully determined to ensure the overall storage capacity requirement for an energy farm is fully met. By strategically managing the number of units, the MPHES system can effectively accommodate the energy needs of the renewable energy farm it serves.

The energy storage capacity of a single MPHES system relies predominantly on two key parameters: the height difference between the upper and lower reservoirs and the volume of water they can hold. A greater hydraulic head translates to increased turbine drive, while larger reservoir volumes offer more water to power the turbines. However, these factors pose limitations on the structural design of MPHES. Higher hydraulic heads are achieved at deeper depths, resulting in greater hydrostatic forces exerted on the structure. Larger storage volumes necessitate larger sphere diameters, leading to higher internal stresses within the structure. Both these factors demand a thicker sphere or higher concrete class to withstand these forces, inevitably leading to increased construction costs. The tradeoff between energy storage capacity and the volume of concrete used is a critical factor in the design and will significantly influence the overall performance of MPHES systems.

2.1. Depth, volume and energy storage potential

The feasibility of MPHES is contingent on a substantial water depth. During the early stages of its development, minimal construction depths of 200 meters were considered achievable [5]. Currently, the Fraunhofer Institute, the leading developer of this concept, is targeting an installation depth ranging from 600 to 800 meters [7, 8, 9]. It was found that a minimum depth of 600 meters is required for techno-economically sufficient storage capacity. A different case study off the coast of Scotland aimed for a greater depth of 1000 meters [10]. For comparison, traditional PHES systems typically operate with a hydraulic head ranging from below 100 to more than 1000 meters [11]. Among the five largest pumped hydro-energy storage (PHES) systems, their hydraulic heads range from 350 to 550 meters [12].

Where intended installation depths may differ in various studies, the targeted internal volume of the MPHES construction remains relatively consistent, ranging from 9.000 to 12.000 m³ [5, 8, 9, 10]. Correspondingly, for a sphere, this would result in an inner diameter ranging between 25,8 and 28,5 meters.

Ultimately, the performance of the concept is dependent on the storage capacity. The relation between that, the internal volume and depth can be expressed by Equation 2.1 [5]:

$$C = \rho_{sw} \cdot g \cdot d \cdot V_{internal} \cdot \eta_{turbine} \quad (2.1)$$

Where:

- C is the storage capacity
- ρ_{sw} is the density of seawater
- g is the gravitational constant
- d is the operational depth
- $V_{internal}$ is the internal volume of the reservoir
- $\eta_{turbine}$ is the efficiency of the turbine

It is important to note that the efficiency of the entire system is not solely reliant on the efficiency of the turbine, but also dependent on the efficiency of the pumps. Key parameters, derived from [5, 8], are outlined in Table 2.1. Utilizing these parameters, a storage capacity of 22,9 MWh is calculated, employing a conversion factor of 3,6E9 to transform units from Joules to MWh.

$$C = \frac{1025 \cdot 9,81 \cdot 1000 \cdot 10.000 \cdot 0,82}{3,6E9} = 22,9 \text{ MWh}$$

Considering these illustrative parameters, one can anticipate a roundtrip efficiency of approximately 73% for the MPHES system. However, it is worth noting that experiments conducted to date have not yet achieved this level of efficiency, primarily because the focus has been on establishing a proof of concept rather than optimizing pump efficiency [13].

Parameter	Symbol	Value	Unit
Density seawater	ρ_{sw}	1025	kg m ⁻³
Gravitational constant	g	9,81	m s ⁻²
Construction depth	d	1000	m
Internal radius of sphere	a	13,37	m
Internal volume of sphere	$V_{internal}$	10.000	m ³
Wall thickness	t	2,72	m
Electrical storage capacity	C	22,9	MWh
Installed electrical capacity	P	5	MW
Efficiency of turbine	$\eta_{turbine}$	0,82	-
Efficiency of pumps	η_{pump}	0,89	-

Table 2.1: Illustrative parameters for MPHES-sphere

2.2. Required storage capacity

The necessary storage capacity of an energy storage system is closely tied to the power output of the energy farm it supports. Within the framework of MPHES, offshore wind and solar energy emerge as the primary and compelling candidates for energy storage. Offshore wind farms are experiencing a notable surge, both in their increasing numbers and a discernible trend toward higher capacities [14, 15]. Conversely, offshore solar farms, while not yet widespread, exhibit clear potential for growth. A noteworthy projection from TNO suggests the installation of 45 GW of offshore solar power in the Netherlands by 2050 [16]. This trajectory underscores the dynamic evolution of renewable energy landscapes, underscoring the need for adaptive energy storage solutions like MPHES.

As depicted in Figure 2.1, over 50% of offshore wind farms in 2019 had a power capacity of 100 MW or higher, with 20% exceeding 300 MW [14]. Considering an MPHES system designed to provide energy for approximately 4 hours in the absence of wind [7, 8, 9], a storage capacity of 400 MWh is required for more than 50% of existing offshore wind farms and is at the lower limit of meeting energy demands.

Using Equation 2.1 and the data provided in Table 2.1, 400 MWh of storage capacity translates to a total internal volume of 175.000 m³. Represented differently, this internal volume could be achieved with 18 spheres of 10.000 m³ at a depth of 1000 meters. Alternatively, considering the same parameters, it involves the need for 290.000 m³ of storage at a depth of 600 meters.

$$\begin{aligned}
 V_{\text{internal}} &= \frac{C}{\rho_{\text{sw}} \cdot g \cdot d \cdot \eta_{\text{turbine}}} \\
 &= \frac{400 \cdot 3,6E9}{1025 \cdot 9,81 \cdot 1000 \cdot 0,82} \\
 &= 174.645 \text{ m}^3
 \end{aligned}$$

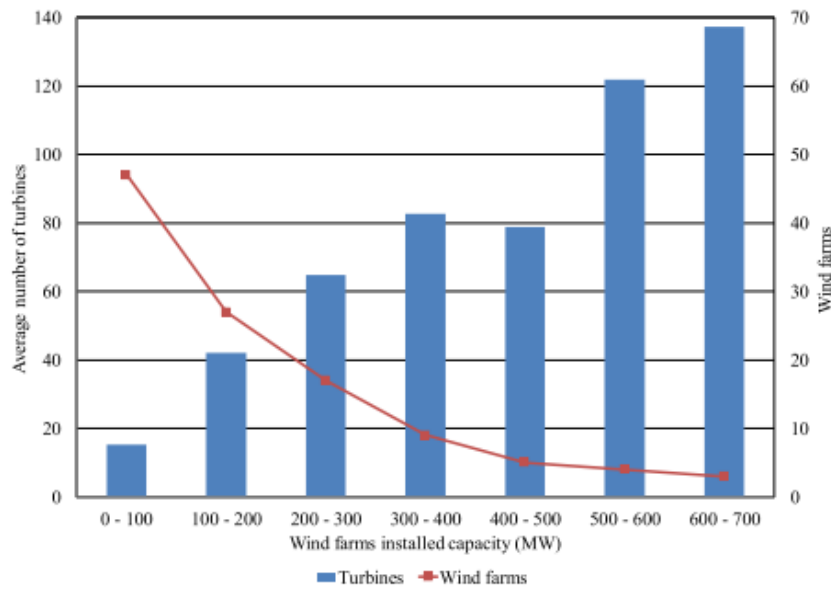


Figure 2.1: Installed offshore wind capacity in 2019 [14]

While this simplified model lacks precision for actual storage capacity demands, it provides valuable insight into the envisioned scale of the MPHES system. In essence, storage farms demand significant total internal volumes to meet the energy storage requirements of offshore wind farms, and as the power capacity of these wind farms continues to increase, so does the scale of the necessary storage.

2.3. Reservoir size

As discussed in section 2.2, the need for significant amounts of storage capacity for offshore wind farms results in a substantial required total internal volume of the reservoirs in the MPHES system. This prompts the exploration of the optimal reservoir size. The central inquiry revolves around whether constructing multiple smaller reservoirs or a single larger reservoir is more advantageous.

Commencing with the recognition of a conceivable upper limit to the internal volume for a single unit—albeit undefined at this stage—practical constraints, such as construction and transportation feasibility, imply its existence.

A pivotal factor in this decision-making process involves the pump/turbine system. The escalation in the number of pump/turbine combinations within an MPHES system corresponds to an increased potential for asset breakdowns, thereby elevating operational risks and costs. Given that pumps represent the most maintenance-intensive aspect, expanding their quantity results in heightened operational expenditures. The impact on capital expenditures between multiple smaller pump/turbine combinations and a single, larger pump/turbine combination remains uncertain.

The efficiency of hydro power turbines tends to ascend with greater capacity. Larger turbines provide an expanded flow area, leading to diminished friction losses. Moreover, large-scale hydro power systems are typically designed with precision, contributing to heightened efficiency [17].

While a single pump/turbine system could potentially serve multiple reservoirs, this necessitates central placement among the reservoirs, interconnected by pipes. However, engineering challenges arise, including the need for these conduits to withstand considerable hydrostatic pressure at significant depths [13]. Settlement variations in the reservoirs further pose challenges, potentially exerting significant loads on the connecting pipes. Consequently, each reservoir should ideally possess its own pump/turbine system.

Given that larger pump/turbine systems offer superior efficiency, lower operational expenditures, and reduced risks, coupled with the necessity for each reservoir to have its own pump/turbine system, the conclusion emerges that each reservoir should be designed to maximize its internal volume for optimal energy generation. The determination of the largest feasible internal volume and the consideration of its effect on the usage of material are crucial aspects explored in Chapter 4.

2.4. Competitiveness of MPHES to existing storage techniques

Energy storage techniques play a crucial role in addressing the intermittent nature of renewable energy sources like wind and solar. One of the key factors influencing the profitability of energy storage systems is the price arbitrage, which refers to the difference in energy prices between periods of low demand and peak demand. Price arbitrage is typically expressed in €cents per kWh. A higher price arbitrage signifies a larger disparity between low and peak energy prices, creating a more favorable and financially viable environment for energy storage systems. As the world transitions from fossil fuels to renewable energy sources, the intermittency of energy production tends to increase. This shift can lead to a rise in the price arbitrage, as the variation in energy supply becomes more pronounced with the integration of renewable energy technologies.

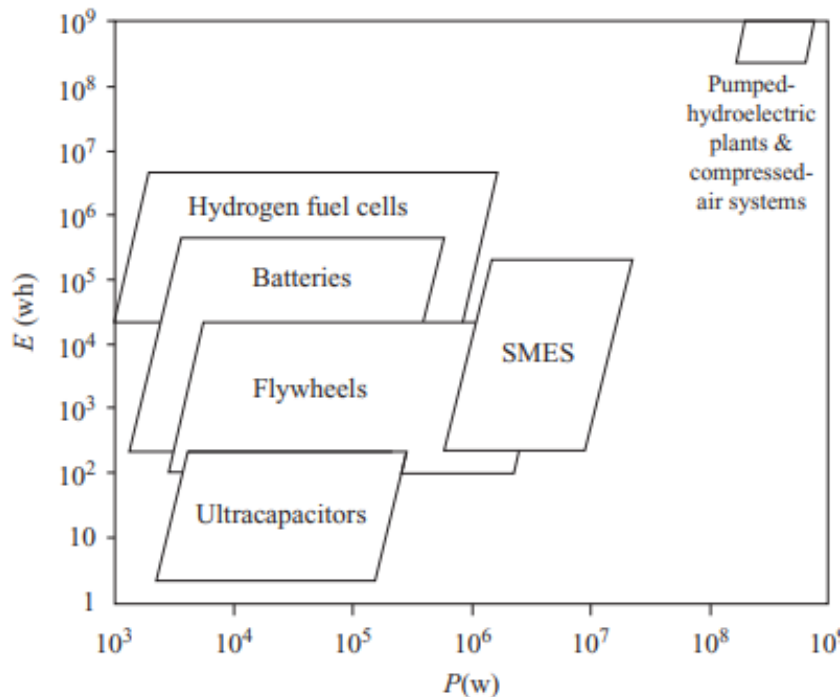


Figure 2.2: Power and energy densities of different energy storage techniques [18]

Today, a variety of energy storage systems serve diverse purposes and harness different forms of energy. These include Pumped Hydroelectric Energy Storage (PHES), Compressed Air Energy Storage (CAES), hydrogen fuel cells, Superconducting Magnetic Energy Storage (SMES), flywheels, batteries, and ultracapacitors, the latter commonly employed for regenerative braking in automobiles [19]. These

systems vary in storage capacity, power capabilities, and duration of load and release cycles, as depicted in Figure 2.2. The x-axis of the graph represents power output in Watts, while the y-axis indicates typical total energy storage in Watt-hours associated with each energy storage technique. The lower left quadrant of the Figure corresponds to short load and release cycles, generally with lower energy storage capacities, whereas the upper right quadrant represents longer-term load and release cycles with higher energy storage capacities.

Recalling the electrical storage capacity of a single sphere from Table 2.1, which is approximately 20 MWh, and the installed electrical capacity of 5 MW, the combined operation of multiple spheres as a storage system positions MPHES in the top right of Figure 2.2. This indicates that MPHES operates on a comparable scale in terms of power and energy densities, positioning it as a competitor to PHES and CAES. Hence, a techno-economic assessment comparing MPHES to these two storage systems is pertinent. Such an assessment has been conducted in [9].

PHES plants are known for their long asset life, reaching up to 100 years, relatively long discharge times (≥ 4 hours), high capital costs but low operation and maintenance costs, and a roundtrip efficiency of 75% to 80% [9, 20, 21].

With several plants in operation and numerous ongoing projects, CAES is a commercially proven large-scale technique. CAES facilities typically utilize large underground storage caverns to accommodate high capacity systems, necessitating specific geographical conditions. Energy is stored by compressing air in these spaces, and later released to drive a turbine and generate electricity [22]. CAES plants typically exhibit discharge times of 4 or more hours in underground installations and 2-4 hours in over-ground installations, achieving a roundtrip efficiency of approximately 70% [23].

In [9] it was estimated that the investment costs for a single MPHES unit varies from €7,8 to €9,9 million, depending on the farm size, with 120 and 5 units considered. With a power capacity of 5 MW, this translates to specific investment costs of approximately €1560 to €1980 per kW of installed capacity. Considering the storage capacity of each unit, which is 18,3 MWh, the specific costs become approximately €426 to €541 per kWh of storage capacity.

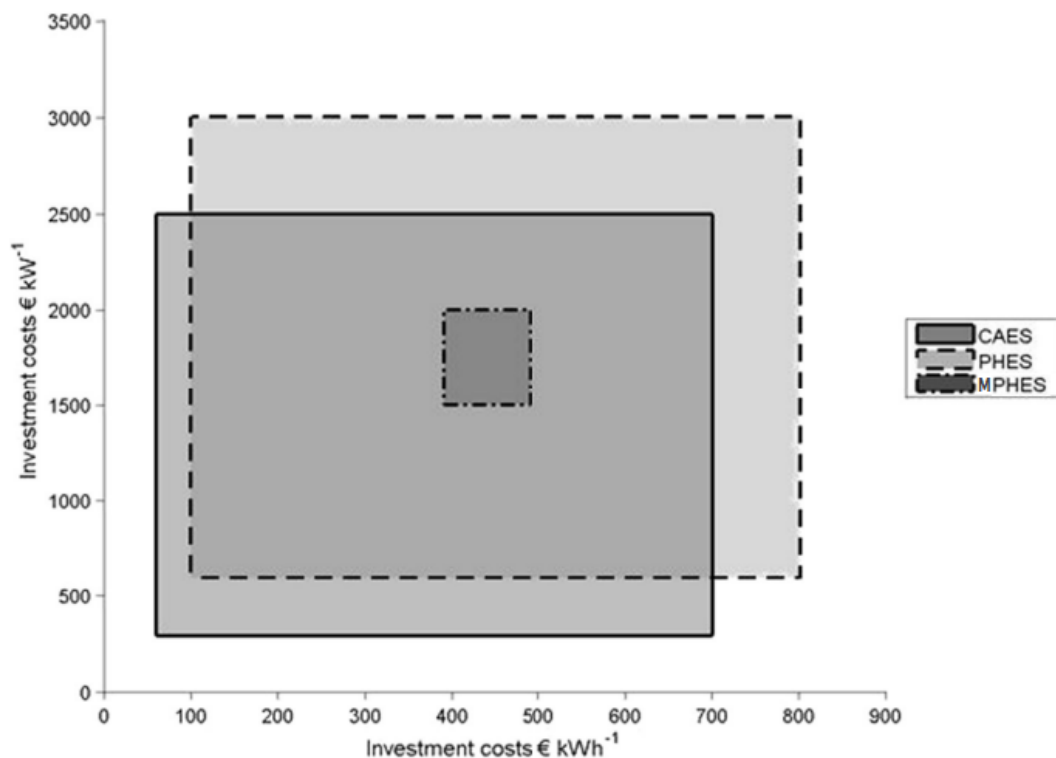


Figure 2.3: Comparison of specific investment per installed capacity and storage capacity of MPHES, PHES and CAES [9]

According to [9], the annual costs for a farm amount to €1,3 million to €1,6 million per unit, including

the capital investment, over an expected service life of 20 years. With an assumption of 1000 cycles per year, the specific power generation costs for MPHES are estimated to be in the range of 7,2 €cents to 8,9 €cents per kWh.

In Figure 2.3, the investment costs of MPHES are compared with those of PHES and CAES. The x-axis denotes the total investment costs per installed kilowatt of power capacity, while the y-axis represents the total investment costs per kilowatt-hour of energy storage capacity. A lower position on the graph indicates a more favorable ratio of investment per storage and power capacity.

The strikingly wider range of investment costs associated with both CAES and PHES, as compared to MPHES, is notable. For PHES, this variation can be attributed to geographical and topological factors, as well as capacity considerations. Investment costs are significantly influenced by the availability of naturally occurring elevation differences in the terrain and proximity to the electrical grid. Similarly, for CAES, the wider range is influenced by comparable factors. The presence of an underground storage cavern has a significant impact on investment costs. Overground CAES typically incurs higher investment costs due to the necessity of constructing containment facilities for air compression, whereas underground storage utilizes the existing landscape as a readily available compression chamber.

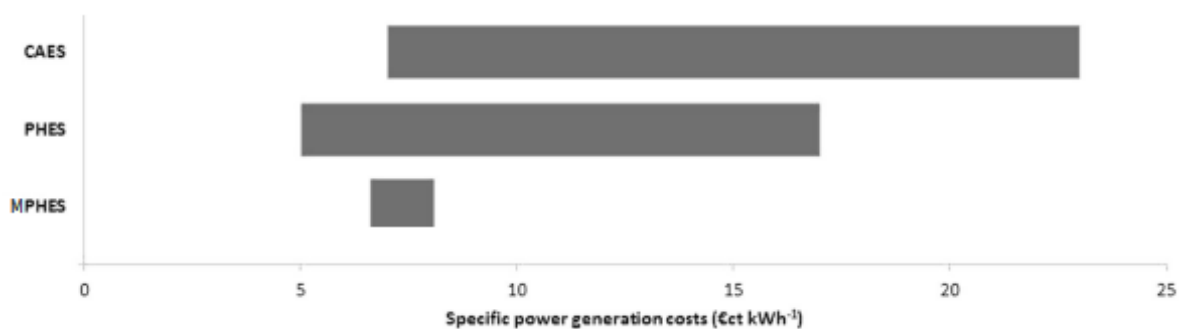


Figure 2.4: Comparison of power generation costs of MPHES, PHES and CAES [9]

In Figure 2.4, the comparison focuses on power generation costs rather than investment costs, as seen in Figure 2.3. The wider range observed for PHES and CAES, as opposed to MPHES, in Figure 2.4 can be attributed to the methodology used to obtain the data. The figures for PHES and CAES were derived from literature studies, whereas the numbers for MPHES were estimated through calculations as outlined in [9].

Analysis of Figures 2.3 and 2.4 suggests that MPHES can be cost-competitive with both PHES and CAES.

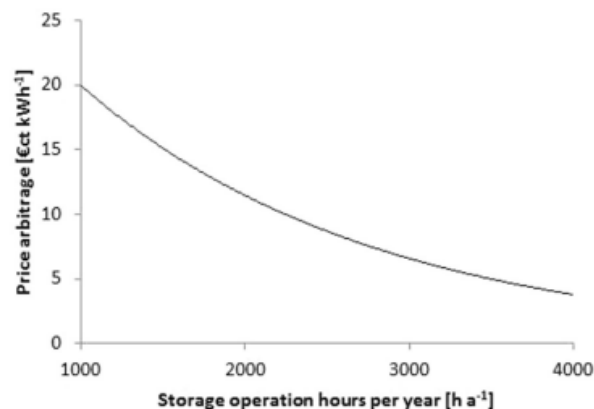


Figure 2.5: Price arbitrage in correlation with yearly storage operation hours for net zero annuity for a farm with 80 units [9]

The annual costs and revenues in [9] were calculated using the annuity method, which is a financial tool used to determine the equal periodic payments required to repay a loan or investment over a

specified period. This method allows for the transformation of the initial investment, as well as any non-recurring and regular payments, into a constant business ratio that occurs periodically throughout the investment's assessment period [24]. In this context, a positive annuity represents an annual net profit.

For MPHES, the estimated annuity for a single unit varies from €231.770 to €544.090, contingent upon the farm size (120 or 5 units, respectively). As previously noted, the profitability of MPHES is significantly influenced by price arbitrage and operational hours. A correlation between these factors has been established and is depicted in Figure 2.5. In this graph, the threshold of net zero annuity is represented by the line. Operations above this line are deemed cost-effective, while those below it are not. To achieve a net zero annuity within a range of 1000 to 4000 operational hours, a price arbitrage of 20 €cents to 4 €cents per kWh, respectively, is necessary.

2.5. Requirements for potential MPHES installation locations

In the context of PHES systems, traditional implementations typically necessitate large head differences between reservoirs, making countries with lowland topography unsuitable [25]. However, the novel concept of MPHES introduces its own unique topographic requirements. The energy-generating potential of a location is of utmost importance; without significant wind or solar energy generation, there would be no energy to store. Additionally, water depth plays a crucial role in determining the performance of the MPHES system, while considering other geomorphological, geotechnical, and social properties [5, 8].

For the successful installation of the MPHES system, a flat seabed is essential. A sloped or hilly seabed cannot support a stable foundation, leading to uneven distribution of stresses in the structure. Therefore, geomorphologies such as trenches, spreading ridges, rift valleys, canyons, seamounts, escarpments, and fans are considered unsuitable [8]. While a foundation on piles might be conceivable, it was not discussed in the literature, and introducing piles at the intended depths could pose unnecessary challenges. Moreover, the bearing capacity of the soil at these depths, primarily composed of muddy sand [10], is limited. Although identifying site-specific soil conditions may be complex, some frameworks are available for this purpose [26].

The suitability of a location for MPHES implementation is not solely determined by the presence or absence of wind- or solar farms, as MPHES systems can be seamlessly integrated into an existing energy infrastructure, where wind or solar farms have yet to be constructed. However, the presence of such farms in a region indicates a demand for energy procurement, which is a crucial requirement. In the absence of electricity demand, energy storage becomes redundant. Hence, proximity to the electrical grid is a significant factor in identifying suitable locations, necessitating close vicinity to cities or industrial centers. Moreover, the distance from the shore should be reasonable and should not conflict with other marine activities, such as fishing or military operations [5]. Furthermore, the identified area should not fall within a marine protected area.

To identify potential installation sites, a Geographical Information System (GIS) analysis was performed. The analysis allocated potential locations to the Exclusive Economic Zones of various countries, using the following hard parameters [8]:

- Water depth: 600-800 m
- Bedslope: $\leq 1^\circ$
- Unsuitable geomorphology as mentioned earlier
- Distance to electrical grid: ≤ 100 km
- Distance to maintenance bases: ≤ 100 km
- Distance to installation bases: ≤ 500 km

Figure 2.6 illustrates the results of the conducted GIS analysis, focusing on potential installation locations around the Mediterranean Sea. However, the complete study revealed other suitable locations worldwide, with the United States emerging as the most promising candidate, as shown in Table 2.2. The identification of suitable areas was done by the GIS-analysis and the capacity was determined based on the assumption of a 20x20 grid of spheres per km², providing 50x50 meters of available

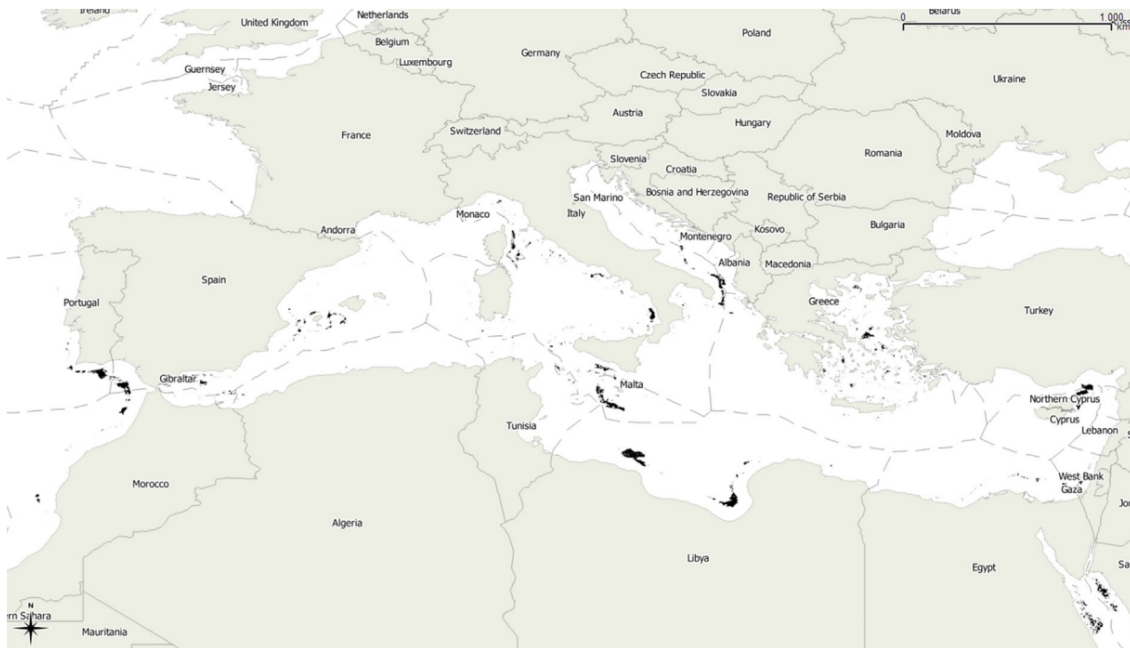


Figure 2.6: Potential installation locations in Mediterranean sea [8]

Country	Area [km ²]	Share of total area	Capacity [GWh]
Total area	111.659	100%	817.344
TOP 10	64.965	58%	475.544
United States	10.226	9%	74.854
Japan	9511	9%	69.621
Saudi Arabia	8535	8%	62.476
Indonesia	8002	7%	58.575
Bahamas	6201	6%	45.391
Libya	5836	5%	42.720
Italy	5572	5%	40.787
Spain	4299	4%	31.469
Greece	3476	3%	25.444
Kenya	3307	3%	24.207

Table 2.2: Potential locations for MPHES [8]

space per sphere. It was further assumed that each sphere provides 18,3 MWh of storage capacity. Similar site-location analyses were also conducted in [5].

2.6. Experiments

This Section describes two distinct experiments and the plans for a third one. The first one, carried out by the Massachusetts Institute of Technology (MIT) and presented in [5] during 2013, primarily aimed to validate the concept of MPHES. The second experiment, executed by the Fraunhofer Institute and published in 2017, involved a 1:10 scale test conducted in Lake Constance [7].

MIT Experiment

In the MIT experiment, a concrete sphere with an inner diameter of 75 centimeters was utilized, constructed by joining two hemispheres together. To simulate depth, a water reservoir was placed 10 meters above ground level. For an overview of the test setup, refer to Figure 2.7. Given the limited scale of this setup, a separate pump and turbine were employed, though the full-scale system is envisioned to feature a single pump-turbine system. The necessity of a ventilation line to maintain atmospheric pressure inside the sphere was point of discussion. It was hypothesized that the inflow of water might

compress the remaining air, potentially leading to a decrease in generated power.

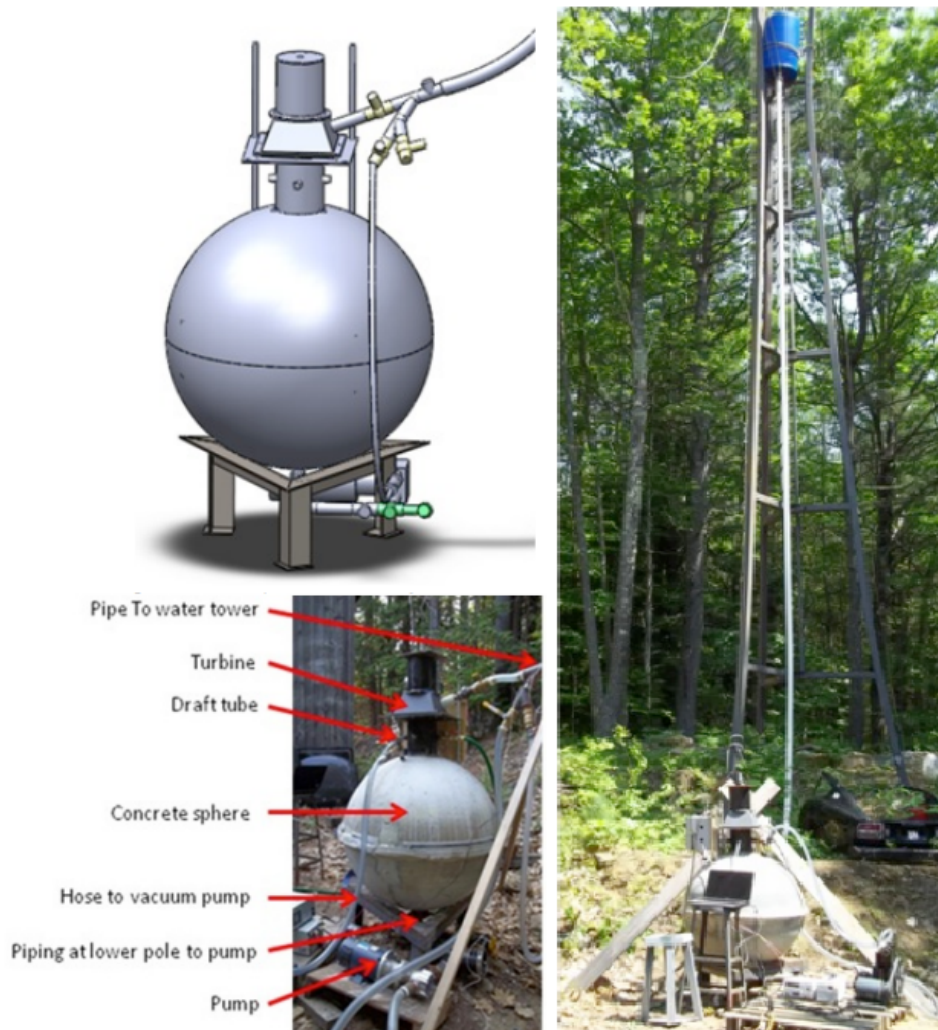


Figure 2.7: The MIT experimental configuration: (a) SolidWorks model of the test setup, (b) the physical representation of the built system, and (c) the comprehensive test assembly, including the high reservoir. [5]

During testing, the researchers found that the absence of a ventilation line could actually be used as an advantage, by reducing the pressure inside the sphere when it was empty. This increased the roundtrip efficiency without ventilation line from 11% to 12%. This effect is considered to be less significant in deeper water. Although the experiments yielded relatively low efficiencies, it is important to note that these were attributed to the generally low pressures during the tests and do not raise concerns about the efficiency of a full-scale system.

Fraunhofer Experiment

The Fraunhofer experiment was conducted offshore in lake Constance at a depth of 100 meter. The 1:10 scaled prototype measured an outer diameter of 3 meter, inner volume of 8 m³ and weighed 21 tons. It was built by Hochtief Solutions (HTS). As opposed to the MIT-setup, which mainly aimed to validate the concept, all tasks in this experiment were completed with regard to the application of the full-scale system [7]. The setup was transported over the road to the test site and lifted in the water with a crane. The complete installation was heavier than the weight of the displaced water, so lift bags were used to tug it to the final installation site, where it was submersed by means of a winch. An overview of the test-setup is displayed in Figure 2.8. The prototype's final shape deviated slightly from a perfect sphere, incorporating cylindrical extensions at the top and bottom to accommodate the pump and form a foundation, while the full-scale system is intended to be more spherical in shape.

In total a series of 12 full cycles with open ventilation and 10 cycles with closed ventilation were performed. It was found that closed ventilation did not lead to significant efficiency decreases, although charging the system did require more time and energy. This discovery indicated that ventilation is not a strict requirement for operating the system. This is a great advantage, as ventilation lines to the water surface impose complicated challenges at the projected installation depth. Roundtrip efficiencies of 39% were described in the experiment. The main identified complications in the implementation of the full-scale system are the construction and assembly of the full-scale sphere, offshore logistics operations, the electro-mechanical equipment and the grid integration of the system [7].

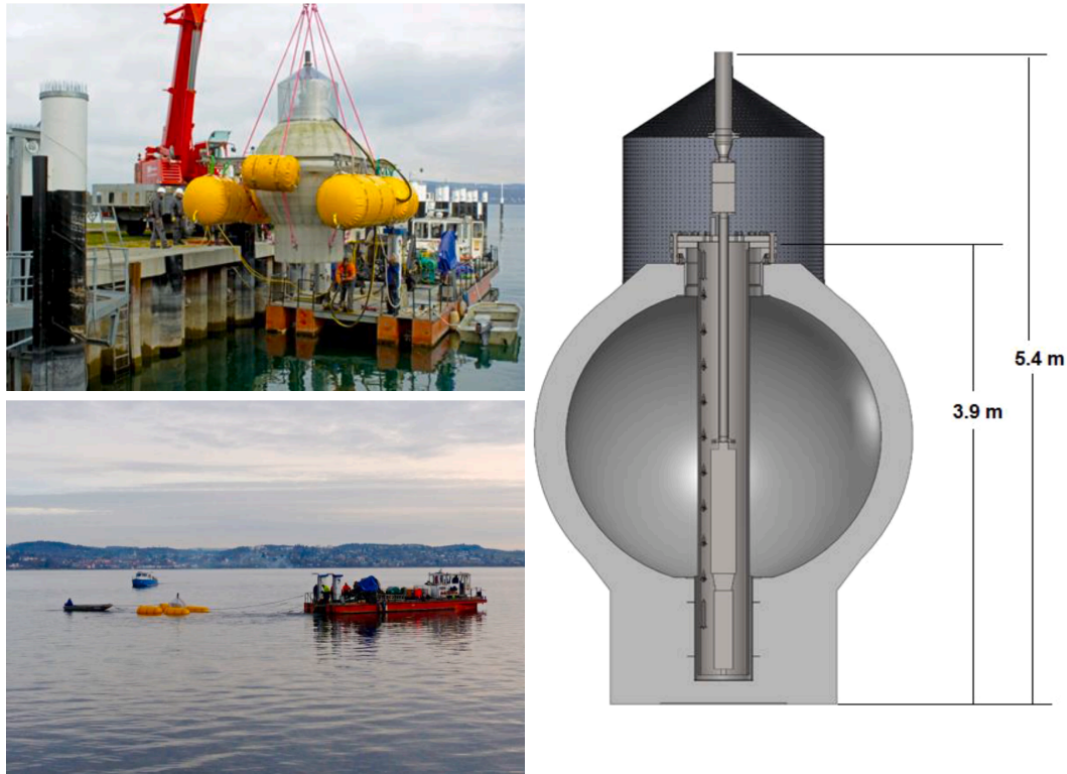


Figure 2.8: The Fraunhofer experimental configuration: (a) lift operation, (b) tugging operation to the final location in the lower left, and (c) the comprehensive test assembly on the right. [7]

Future planned experiment

Another experiment is envisioned to take place in 2025 off the coast of California. This experiment is set to be conducted at a reduced scale of 1:3, featuring a sphere with an approximate diameter of 10 meters. The targeted depth for this experiment is 500 meters. As of now, the logistics regarding whether the system will remain afloat during the experiment after its descent from a barge or be placed on the seabed are yet to be determined.

This experiment is the result of a collaborative effort between several key players, including the Fraunhofer Institute, Hochtief Solutions, and RCAM Technologies. In this venture, RCAM Technologies will be responsible for constructing the sphere, employing 3DCP. Hochtief Solutions will plan the logistics and assess the loads on the structure throughout the construction and transportation phases.

The primary objective of this experiment is to enhance understanding of the intricacies involved in constructing, transporting, and installing the MPHES system, thereby shedding light on the practical challenges and opportunities in this pioneering field [13, 27, 28].

2.7. Construction methods spherical design

The realization of energy storage at the seabed holds immense promise, yet constructing the required spherical storage tanks poses a significant challenge. This Section delves into various proposed construction techniques to address this challenge, all of which begin with a spherical design for the seabed

reservoir. Specific focus is placed on construction methodologies employing concrete, a material characterized by its wide availability and cost-effectiveness — qualities particularly advantageous given the anticipated volumetric requirements. Moreover, concrete possesses well-established properties, excelling in its ability to endure compressive forces. Given the substantial intended operational depth, the suitability of concrete as the material of choice becomes apparent.

2.7.1. Hemisphere concept by MIT

In [5] a preliminary construction method was presented consisting of two identical hemispheres with a grout line at the circumferential interface. These hemispheres can be cast using a simple two-piece mold. Subsequently, the hemispheres are sealed together by pumping epoxy grout in the grout line. The bottom of each hemisphere can be a steel plate or a pre-cast post-tensioned concrete plate, which serves as part of the mold during concrete casting and provides extra weight to counter buoyancy.

This design takes into account the potential dual-functionality of the system to serve as an anchor for a floating wind turbine (FWT). In this configuration, the FWT would be connected to the anchor with a mooring line. The estimated time required for casting two hemispheres is 42 hours [5]. No estimations were provided for the required time to complete the rest of the construction or the installation process. The construction method is illustrated in figure 2.9.

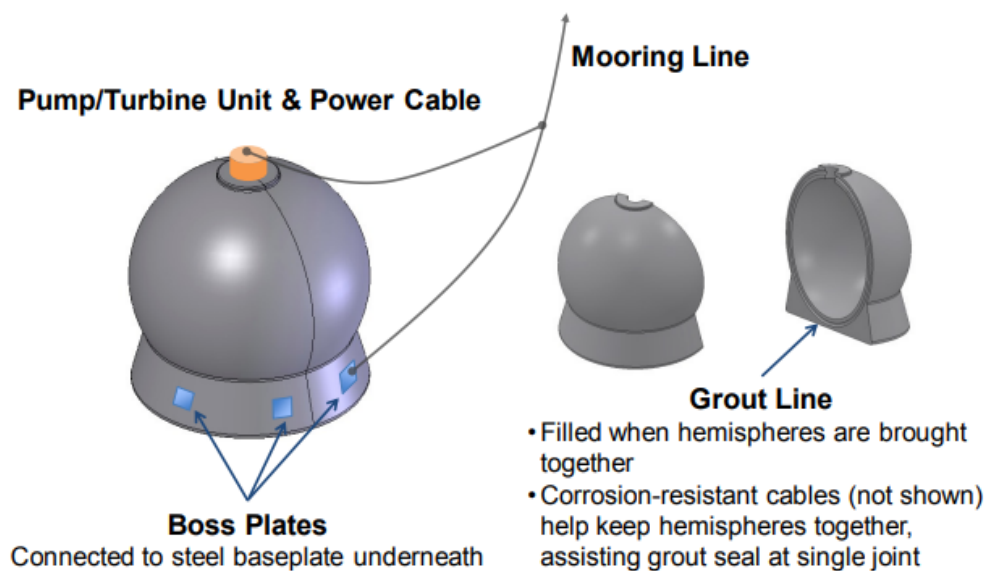


Figure 2.9: Hemisphere concept by MIT [5]

2.7.2. Hybrid 3D concrete printing and casting method by RCAM

As concrete design subcontractor on the STORE Consortium, Witteveen+Bos supervised a TU-Delft graduation project on a novel MPHES construction-method [29]. This master's thesis examined a hybrid technique involving casting and 3D concrete printing (3DCP), as illustrated in Figure 2.10. A prefab element is utilized for the bottom of the sphere, and a formwork is constructed using 3DCP. Inner and outer shells are 3D printed, and concrete is poured between them. A minimum free height of the formwork is dictated by the hardening time of 3D printed concrete. Conversely, the maximum free height of the formwork relies on its resistance against buckling. As 3DCP can not be applied at an inclination of more than 45°, the top of the sphere is constructed using a prefab element. The minimum total construction time for this method is reported to be 24 days. This method will be referred to as the RCAM-method. RCAM Technologies, member of the STORE Consortium is a tech company dedicated to achieving 3D Concrete Printed Renewable Energy and Energy Storage. RCAM is an abbreviation of Reinforced Concrete Additive Manufacturing.

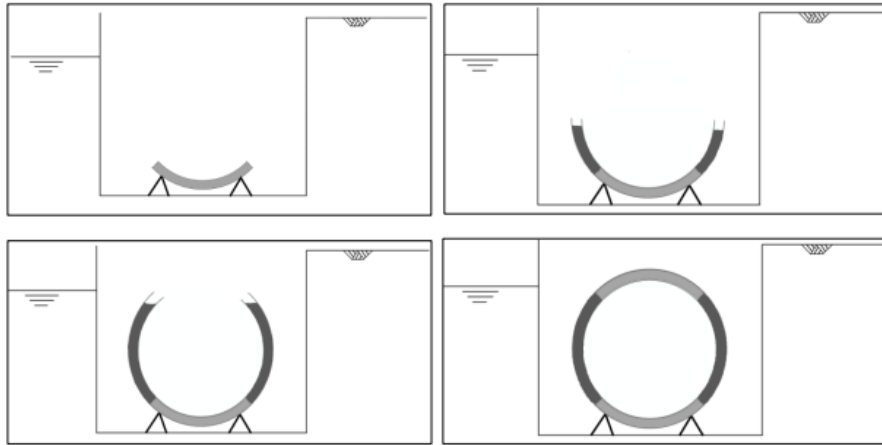


Figure 2.10: Hybrid 3DCP + in situ casting construction method [29]

2.7.3. Air pressured formwork by HTS

An innovative construction technique patented by HTS (EP2700594A1) and approved in 2014, involves pouring concrete as a monolith within a specially designed spherical formwork on pontoons [30]. The formwork comprises stacked toroidal rings, reinforced by air pressure, and a membrane as depicted in Figure 2.11). To facilitate the process, the concrete is poured from a curved truss structure that can rotate. The construction occurs in several phases, allowing the concrete to gain stiffness before each subsequent pour. Gradual stacking of the toroidal rings takes place between pours, with gluing and hook-and-loop fasteners serving as the primary connection methods. An essential feature of this technique is the creation of a circular opening approximately 3 meters in diameter at the upper area of the construction. This is achieved by anchoring a steel ring to the concrete shell. Subsequently, the inner formwork and auxiliary scaffolding tower can be removed through this opening and reused for further construction purposes. The production of one sphere will approximately take eight days and the installation will require eight additional days [7]. For a more detailed explanation of this construction technique, please refer to appendix B. In light of HTS's decision not to assume responsibility for sphere production in the future, it has led to the discontinuation of the development of this particular construction method [28].

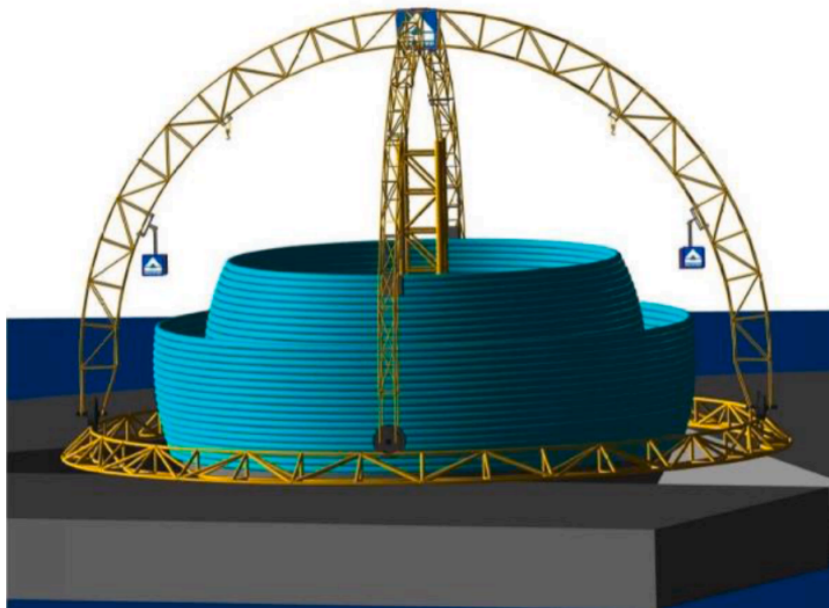


Figure 2.11: Formwork system for full-scale construction patented by HTS [7]

2.7.4. Other construction techniques

Several other construction techniques have been found in literature, although they have not been extensively developed, likely due to early-stage recognition of potential challenges or perceived limited feasibility. Here, a brief overview of these techniques is provided:

- Bringing six equal sections (i.e. staves) together and banding them with steel cables, similar to the construction of a barrel [5]. A similar concept, using prefab elements, was presented in [29] and rejected due to its limited scalability and concerns regarding watertightness.
- Using 3DCP to print the entire sphere [29], a method that is reported to be time-consuming.
- Slip/jump forming the sphere, wherein the formwork is moving and the construction is carried out piecewise [29]. This method may also be time-consuming, and multiple formwork segments are required due to variations in the diameter of the rings forming the sphere at different heights.

2.8. Implementation aspects spherical design

In this Section, the discussion revolves around the construction location, transport and installation, followed by an analysis of the watertightness of the design. The complete module, comprising the sphere, pedestal, and foundation, is considered, as illustrated in Figure 2.12.

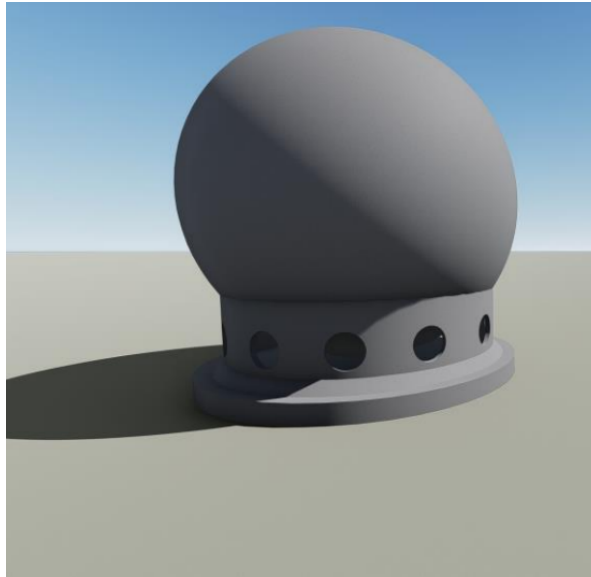


Figure 2.12: Potential design of MPHES-system, including pedestal and foundation[10]

2.8.1. Construction location

The initial consideration in the logistical process is the construction location of the sphere. During construction, it is planned to cover the holes in the pedestal to entrap air between the sphere, pedestal, and foundation. This ensures that the module's weight is approximately equivalent to the displaced water [10].

As discussed in Appendix A, the proposed spheres have a draught of over 25 meters without providing additional buoyancy. Standard dry docks are not equipped to handle such a draught, presenting significant challenges in selecting suitable construction locations for the spheres. Consequently, it becomes essential to use pontoons with substantial air volumes to provide buoyancy.

In a technical report, it was mentioned that pontoons with a total volume of 8.500 m³ were required to provide sufficient buoyancy for the structure to be floated out of a dry dock at a draught of 11,7 meters. It was proposed to use two pontoons with dimensions of 50 meters by 30 meters by 2,84 meters [10]. However, it should be noted that most dry docks cannot accommodate pontoons of such large dimensions. A list of the world's largest dry docks is available in Appendix G.2.

Alternatively, building the sphere in a fjord presents a more viable option. The serene weather conditions and ample depths facilitate smooth construction operations. However, constructing in a fjord introduces complexities, as the construction site is now situated on water. Moreover, the availability of suitable fjords worldwide is limited. For more information on suitable construction locations, refer to Appendix G.

2.8.2. Transport

Once the structure is liberated from its construction location, it can be towed to the final installation site. The design, as outlined in [10], is essentially weightless in water, facilitating its transportation to the installation location. This implies that minimal or no additional buoyancy is required in open sea. Tugboats can handle the transportation process.

As an alternative proposal, there is a suggestion to pack the spheres together in units of 3, 4, or 6, resembling an egg carton [31]. These grouped spheres would then be placed on a semi-submersible vessel (SSV). Upon arrival at the installation location, the spheres are unloaded from the SSV. However, this configuration appears to be most advantageous when using smaller units, which can be easily loaded from the construction location onto the SSV. Unfortunately, an illustration cannot be provided as the report containing this information is confidential.

2.8.3. Installation

Upon reaching the installation location, the holes in the pedestal are exposed, allowing water to fill the free area between the sphere, pedestal, and foundation. The weight of the water results in the module acquiring negative buoyancy. At this point, the module can be lowered to the seabed.

Prior to any installation activities, a survey campaign will take place to ensure seabed is suitably clear, level and conditioned for installation of spheres. A special boulder grab tool is employed to clear any boulders [31].

2.8.4. Watertightness

The RCAM method stands out as the most promising construction approach, a decision that is detailed further in Section 2.9.3. In this approach, the prefab bottom is attached to the mid-section of the spheres through a cold joint. Subsequently, the prefab top is placed atop the mid-section and connected, presumably using a wet joint. In both types of joints, ensuring watertightness is crucial.

To enhance watertightness in cold joints, waterstops can be employed, as discussed in Appendix H. Similarly, in wet joints, virtually the same techniques are applied, resulting in a cold joint on either side of the wet joint concerning watertightness.

Additionally, the presence of cracks in the concrete significantly influences the watertightness of the structure. Therefore, verifying the maximum crack width of the structures is crucial. However, this aspect is not further discussed in this report.

2.9. Feasibility considerations

This Section provides an assessment of the feasibility of MPHES and offers a reflective analysis of its standing in the current state of the art. First the market potential for energy storage is examined, followed by an evaluation of the financial aspects of MPHES. Finally, the feasibility of its construction is discussed. The topographical feasibility is not considered, as its requirements have been previously established in Section 2.5.

2.9.1. Market feasibility

The transition from fossil fuels to renewable energies is an inevitable and essential step in combating climate change and ensuring a sustainable energy future. As the share of wind and solar energy in the energy mix increases, the need for effective energy storage solutions becomes increasingly critical. The intermittent nature of renewable energy sources creates a market demand for energy storage technologies to balance energy supply and demand and enhance grid stability.

Research and development in the field of energy storage are rapidly growing worldwide, as scien-

tists and engineers seek innovative and efficient techniques to store renewable energy for later use. Large-scale energy storage solutions are becoming increasingly necessary to address the challenges of integrating variable renewable energy sources into the grid effectively.

MPHES, as a large-scale energy storage system, has shown great potential as a competitor to established energy storage technologies like PHES and CAES. As demonstrated in [9], MPHES operates on a comparable scale in terms of power and energy densities and can be cost-competitive with other large-scale storage systems.

2.9.2. Financial feasibility

While MPHES has demonstrated potential cost-competitiveness with other large-scale energy storage techniques, there are several considerations from a financial standpoint. Figure 2.3 indicates that MPHES is not yet within the most favorable region of the graph, represented by the lower left. The wide investment cost ranges for both CAES and PHES, influenced by geographical properties, can be misleading. The overlapping region of MPHES with CAES and PHES does not inherently imply consistent cost-competitiveness. Instead, it suggests that MPHES could be more financially attractive in regions where geographical and topographical constraints make the implementation of CAES or PHES more expensive, such as areas near offshore wind farms.

For MPHES to garner investor interest, it must offer a net positive annuity. The study in [9] estimated that a single MPHES unit could yield a positive annuity of several hundred thousand euros. However, as depicted in Figure 2.5, achieving a net zero annuity for an MPHES farm with 80 units requires significant price arbitrage, necessitating at least 4 ¢cents per kWh at 4000 operation hours. This implies that the plant should ideally achieve 1000 full cycles in a year, or 2,7 full cycles per day. This operational requirement is substantial, and the expected price arbitrage poses a potential challenge. Research in [32] demonstrated that the daily price differentials in Europe ranged from 0.8 ¢cents per kWh in Norway to 5,5 ¢cents per kWh in Ireland. These figures indicate that the outlook presented in [9] might be overly optimistic.

Overall, while MPHES shows potential as a cost-competitive energy storage solution, careful consideration of multiple factors, including price arbitrage, operational hours, and geographical location, is crucial to determine its economic viability and attractiveness to investors in practical applications. Further research and real-world data will be essential to provide a more comprehensive assessment of MPHES's profitability in various scenarios.

2.9.3. Construction feasibility of spherical design

The construction feasibility of MPHES is an important aspect to consider when assessing the practicality of implementing such large-scale energy storage systems. As mentioned in the previous sections, several construction techniques have been proposed for MPHES, each with its advantages and challenges. However, it is important to note that the construction of a full-scale MPHES system has not been realized yet. The largest sphere built was only a 1:10 scale model, which was constructed as a monolith with conventional casting. Reflecting upon the aforementioned construction approaches:

- Hemisphere concept by MIT
- Air pressured formwork concept by HTS
- Hybrid method of 3DCP and concrete casting by RCAM

The hemisphere concept by MIT was proposed in [5], which was published in 2013. The technique has shown difficulties in achieving a proper seal at the circumferential interface of the two hemispheres during the 1:35 scale experiment. This raises concerns about the feasibility of scaling up this construction method to full-size spheres. Additionally, the weight of a single hemisphere with a diameter of 30 meters would be 10.000 tonnes of concrete. Once the hemispheres are sealed together, the pump/turbine installation should be installed and the construction is loaded onto a barge. At this point, the construction is heavier than the highest weight a crane has ever lifted, which is 20.000 tonnes [33]. The lack of further publications on this specific construction technique may suggest considerable difficulties in overcoming the identified challenges or a potential abandonment of the project.

The air pressured formwork concept by HTS, while avoiding the lift problem by constructing in a dry

dock or water, presents other challenges. Many dry docks may not be able to accommodate the draught of the MPHES structure [34]. Furthermore, execution of the air pressured formwork seems like a challenge. Pneumatic formwork is generally suitable for thin curved shells [35]. With a radius of 15 meter and thickness of 2,5 meter, the MPHES sphere will be a typical thick shell [36]. Hence, the lateral pressure of the wet concrete on the air pressured toroidal rings might become problematic. Moreover, the proposed connection methods between the rings with hook-and-loop fasteners or glue may not be sufficient for the intended scale. As previously mentioned, this project was abandoned by HTS.

The hybrid method of RCAM has its own flaws. While the application of 3DCP offers the advantage of casting the structure as a monolith, the use of a prefab element as the base of the sphere deviates from this approach and may potentially impact the watertightness of the structure. The same concern applies to the top of the structure, where it will be completed with another prefab element. Additionally, the use of 3DCP is time-consuming, which becomes a disadvantage when multiple spheres need to be constructed.

The primary objective of the examined construction techniques is to tackle the intricacies associated with spherical formwork. Considering that a fully operational MPHES system comprises multiple units, the reusability of formwork becomes instrumental in reducing construction time and costs. However, achieving formwork reusability while adhering to the specific spherical configuration required for MPHES units presents a notable challenge.

The hemisphere concept by MIT poses scalability challenges, while the air pressured formwork by HTS appears somewhat makeshift. Among the proposed construction methods in literature, the RCAM method stands out as the most promising. This is supported by the development of various construction methods for the MPHES sphere in [29], where the RCAM method was assessed as the most promising. Additionally, the Fraunhofer Institute, a leading developer of this concept, plans to collaborate with RCAM and use the RCAM method for constructing the spheres.

In addition to the challenges associated with the construction techniques discussed earlier, the choice of construction location for MPHES spheres introduces its own set of difficulties. Most dry docks are not equipped to handle the draught of the sphere, and fjords, which can accommodate substantial draughts, are not widely distributed globally. Consequently, the feasibility of implementing MPHES systems with a spherical design appears to be constrained to installation locations near some of the world's largest dry docks or fjords. This limitation further underscores the intricate nature of addressing both the construction method and the suitable installation sites for these innovative energy storage systems.

2.10. Cost analysis

As highlighted in Section 2.4, a techno-economic analysis has demonstrated that MPHES can achieve cost competitiveness compared to existing energy storage techniques. Beyond this assessment, it is insightful to examine the detailed breakdown of the overall costs associated with the implementation and operation of the MPHES system. According to [9], a significant proportion. Specifically, 73,7% of the annual costs is allocated to servicing capital investments. In Figure 2.13, an expanded view of the capital-related costs provides a closer look at how these costs are distributed among various expenditure categories.

The intriguing revelation from the analysis is that the pump turbine claims the most significant share of the investment, closely trailed by the expenses associated with the construction and installation of the concrete sphere. It is essential to recognize that these figures are estimations, given that the system has not been physically implemented, and hence specific data on the costs is unavailable. Nonetheless, despite being projections, this assessment proves instrumental in pinpointing critical factors influencing the economic viability of the MPHES system.

The costs linked to construction and installation constitute 2,8% of the total annual costs of the system, making up 30,9% of the 73,7% capital-related costs. While the calculations in [9] lack full transparency, it is assumed that factors such as material costs, construction labor costs, rental costs of the construction location (dry dock or factory hall), rental costs of construction material (crane, concrete pumps, etc.), and rental costs of towing boats and immersion ships have been considered.

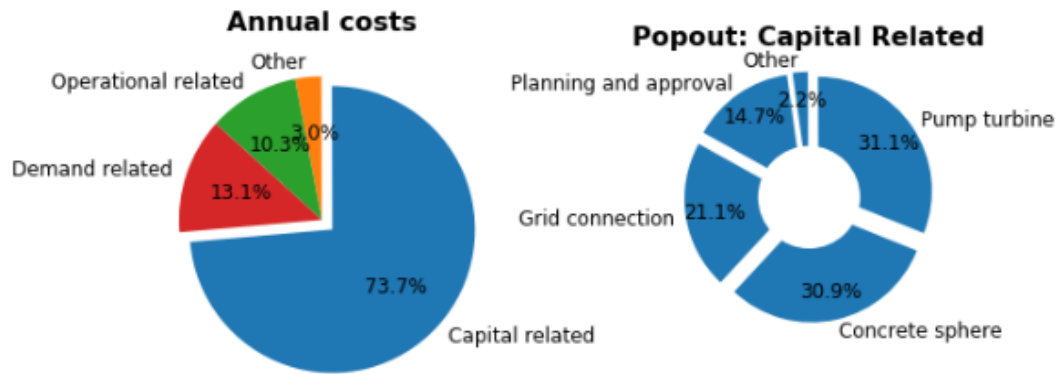


Figure 2.13: Pie-chart of annual costs of implementation of MPHES-system[9]

Recognizing that the list provided is not exhaustive, and acknowledging the inherent complexity of estimating the actual construction costs of the system, it is crucial to note that only 22,8% of the total annual costs are estimated to be allocated to construction and installation. From this, one can infer that material costs exert a modest influence on the overall project costs. Therefore, the anticipated additional material associated with the construction of the cylinder and torus might be deemed acceptable. These increased material costs might even be offset by the cylinder and torus outperforming in other expenditure categories.

2.11. Conclusions from literature

The review of literature has provided valuable insights applicable to the design considerations. Firstly, the energy storage capacity of an MPHES system must align with the specific requirements of the supported energy farm, with a typical demand exceeding 400 MWh for offshore wind farms, as discussed in Section 2.2.

The potential energy storage capacity increases with greater depth and internal volume. However, limitations on installation depth, considering topography, hydrostatic pressure, and accessibility, necessitate a focus on augmenting storage capacities by increasing the total internal volume of the system.

As outlined in Section 2.3, achieving a higher total internal volume for a storage farm is more favorable by enhancing the internal volume of individual units rather than increasing the number of units. This preference is shaped by considerations related to system efficiency, vulnerability, and capital expenditures, particularly those associated with the pump/turbine system. Additionally, it is advisable for each reservoir to have its own pump. The impact of increasing the internal volume on the material usage of the reservoir is a critical consideration, explored extensively in Chapter 4.

While GIS analyses have indicated suitable locations for installing the MPHES system, some analyses are limited to specific regions, such as the Mediterranean Sea, and may require updates. Moreover, a technoeconomic assessment has highlighted the clear potential for economic profitability of the MPHES system. However, the current construction feasibility of the system appears to be a significant bottleneck that warrants further exploration.

From the proposed construction techniques found in literature, the RCAM-method, which uses a combination of 3DCP and conventional casting, emerges as the most promising construction method for the sphere.

Due to the required dimensions, constructing the sphere is highly complex. Current proposed construction methods rely on unproven techniques. Additionally, the high draught of the structure during construction limits potential construction locations. Therefore, the construction process should prioritize the feasibility of the construction method over optimizing construction costs.

3

Starting points for initial structural design

In this Chapter, the foundation for the design process is laid through the establishment of key starting points, analysis of initial parameters, and consideration of structural loads. It serves as the basis for the subsequent calculations that determine the material usage for each shape in Chapter 4.

To evaluate the effectiveness of a shape, a new parameter, the CIV ratio $\left(\frac{V_{\text{concrete}}}{V_{\text{internal}}}\right)$, is introduced. This metric quantifies the relationship between costs, represented by the volume of material used, and benefits, expressed in internal volume.

The chapter begins by establishing the intended installation depth, guiding the selection of materials for the project. Following this, key definitions at the cross-section of each shape are documented, providing clarity and context. A detailed layout of the design is then presented. Finally, the chapter delves into discussions surrounding structural loading conditions.

3.1. Starting points

This Section outlines the initial parameters for the design phase. The selected water depth for these structures is initially fixed at 1000 meters. As discussed in Section 2.1, this depth represents the most ambitious depth in existing literature. While shallower installation sites are feasible, the choice of this depth is normative. A design suitable for 1000 meters can also be adapted for shallower depths. It is important to note that shallower depths offer advantages like thinner walls and reduced concrete usage, but come with the trade-off of smaller storage capacities.

Consistent with earlier designs documented in the literature (refer to Section 2.7), concrete emerges as the material of choice for this project. The selection is underpinned by its widespread availability and cost-effectiveness, both of which are pivotal factors due to the substantial volume of concrete required for construction. Moreover, concrete is renowned for its capacity to withstand significant compressive forces, a quality of paramount importance given the intended operational depth.

In the analyses in this Chapter, the concrete grade C60/75 is employed. Taking into account a material safety factor of $\gamma_c = 1,5$, the design compressive strength (f_{cd}), is established at 40 N/mm².

In this specific phase of the design process, the consideration of reinforcement is deliberately omitted. The focus of this chapter is to estimate the requisite concrete volumes for each structural configuration. It is not intended to preclude the possibility of reinforcement being required in the reservoir, foundation, or structural detailing. Given the considerable length of cylinders and tori, it is anticipated that some reinforcement will be essential for resistance against bending. However, at this stage, such considerations are intentionally set aside.

The design of the reservoir assumes a level seabed, facilitating the adoption of a shallow foundation

design. While the possibility of employing a foundation supported by piles exists, it is important to note that this aspect is beyond the current scope of the report. The emphasis remains on the feasibility and practicality of a shallow foundation design.

Throughout this report, several parameters frequently recur, ensuring consistency and clarity in the calculations. They are listed in Table 3.1.

Parameter	Symbol	Value	Unit
Concrete compressive design strength	f_{cd}	40	N mm^{-2}
Density concrete	ρ_{concrete}	2400	kg m^{-3}
Density seawater	ρ_{sw}	1025	kg m^{-3}
Depth	d	1000	m
Gravitational constant	g	9,81	m s^{-2}
Hydrostatic pressure	p		N mm^{-2}
Membrane force	n		N m^{-1}
Maximum effective compressive stress	σ_{max}		N mm^{-2}

Table 3.1: Frequently recurring parameters

3.2. Shape geometries

In this Section, the parameters that shape the geometry of each form are detailed. Referring to this Section helps in remembering the definitions of the parameters within their context and facilitates visualization.

3.2.1. Sphere

In Figure 3.1 a visualization of the cross-section of the sphere design is presented. The parameters are also listed in Table 3.2. The parameter a refers to the inner radius of the sphere.

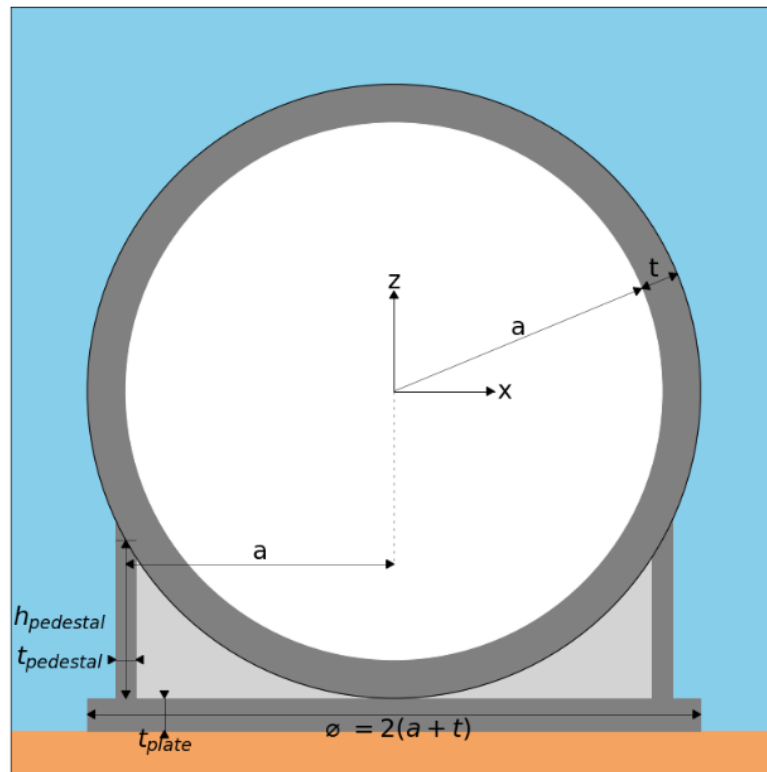


Figure 3.1: Schematic cross-section of sphere

Parameter	Symbol	Unit	Formula
Internal radius	a	m	
Shell thickness	t	m	
Pedestal height	h_{pedestal}	m	
Pedestal thickness	t_{pedestal}	m	
Foundation plate thickness	t_{plate}	m	
Foundation plate diameter	\varnothing	m	$2(a + t)$
Internal volume	V_{internal}	m	$\frac{4}{3}\pi a^3$

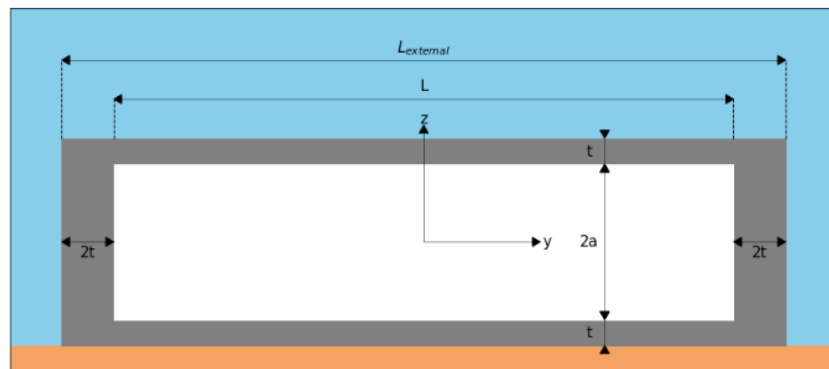
Table 3.2: Sphere dimensional parameters

3.2.2. Cylinder

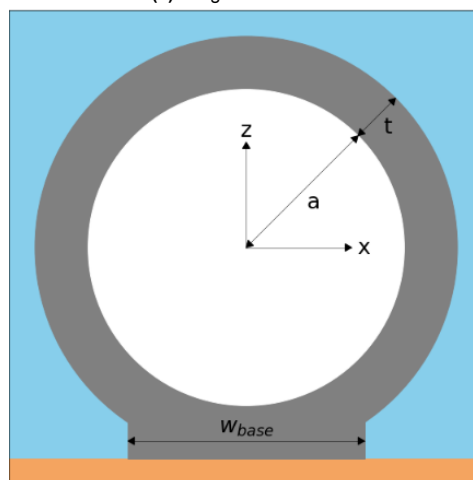
The cylindrical reservoir adopts a tube design with flat, circular plates serving as caps. While this design may not be the most optimal for withstanding hydrostatic pressure, transmitting internal stresses arising from edge disturbances, or conserving concrete usage, its simplicity facilitates a preliminary estimation that yields useful results at this stage in the design process.

The shell of the reservoir mainly transfers the hydrostatic loads into membrane forces. However, it is expected that a bending moment will arise in the center of the cap. To resist this bending moment, it is assumed that the caps require twice the thickness of the shell. This is not further elaborated on.

A visualization of the cylindrical design is presented in Figure 3.2, while Table 3.3 explains the parameters. Both a and L refer to the internal surface of the reservoir.



(a) Longitudinal section



(b) Cross-section

Figure 3.2: Schematics of cylinder

Parameter	Symbol	Unit	Formula
Internal radius	a	m	
Shell thickness	t	m	
Internal length	L	m	
External length	L_{external}	m	
Width of foundation base	W_{base}	m	
Slenderness	-	-	$\frac{L}{2a}$
Internal volume	V_{internal}	m	$\pi a^2 L$

Table 3.3: Cylinder dimensional parameters

3.2.3. Torus

The torus closely resembles the cylinder, essentially a curved tube with connected ends, eliminating the need for a cap design. However, as discussed in detail in Appendix C, the membrane force is not uniform across the entire circumference of the cross-section.

The maximum membrane force is slightly higher than that of the cylinder, while the minimum membrane force is marginally lower. Refer to Appendix C for a detailed derivation of these findings. The positions of these membrane forces are indicated in Figure 3.3b. The membrane force acts in a tangential direction, as discussed in Section 3.3.

The cross-sectional thickness, determined by the capacity to withstand the maximum membrane force, remains constant around its circumference. This may potentially lead to overdimensioning, as the design thickness is based on the normative membrane force. Optimizing the location of the tunnel through the torus shell by placing it more outward can result in a more efficient distribution of the load, thereby leading to material savings [37].

A visualization of the torus is provided in Figure 3.3, and detailed parameters are explained in Table 3.4. Similar to the sphere and cylinder, a refers to the internal surface of the torus. The major radius b remains unaffected by the shell thickness, eliminating any distinction between internal and external major radii.

Parameter	Symbol	Unit	Formula
Minor radius internal	a	m	
Major radius	b	m	
Shell thickness	t	m	
Width of foundation base	W_{base}	m	
Slenderness	-	-	$\frac{b}{a}$
Internal volume	V_{internal}	m	$2\pi^2 a^2 b$
Maximum membrane force	n_{max}	N m ⁻¹	$-pa \frac{-\frac{1}{2} + \frac{b}{a}}{-1 + \frac{b}{a}}$
Minimum membrane force	n_{min}	N m ⁻¹	$-pa \frac{\frac{1}{2} + \frac{b}{a}}{1 + \frac{b}{a}}$

Table 3.4: Torus dimensional parameters

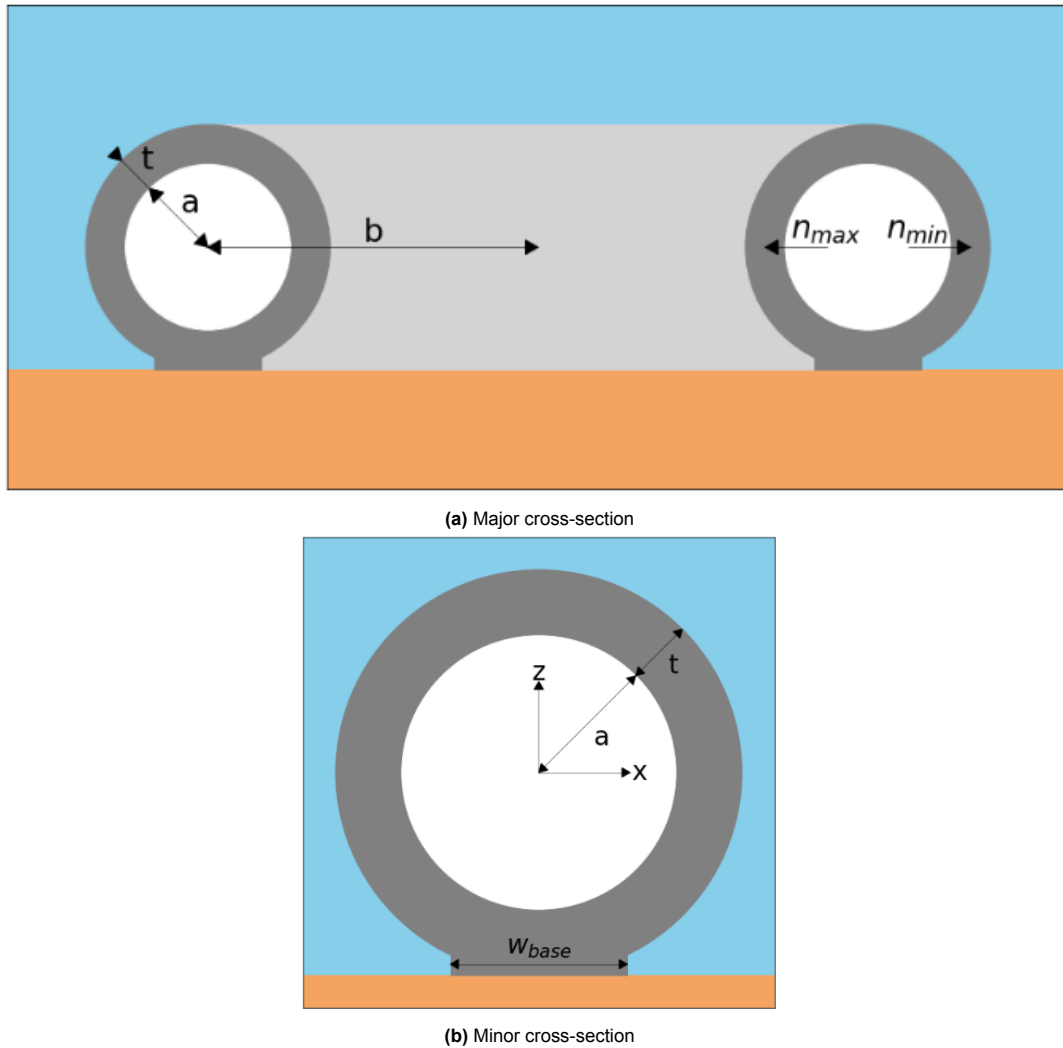


Figure 3.3: Schematics of torus

3.2.4. Slenderness

When designing a structure with a specified volume, the choice of shape and its dimensions becomes crucial. For a sphere, the volume solely depends on the radius a , simplifying the design process. Conversely, for a cylinder, the shape is dictated by the ratio of its radius a to its length L . Similarly, for a torus, the shape is determined by the ratio between its minor radius a and major radius b . Utilizing these dimensions, one can compute the membrane forces within these structures, which in turn are instrumental in estimating the required thickness of the structural material.

For cylinders and tori, the ratios between length and width are referred to as slenderness. They are defined as, $\frac{L}{2a}$ for cylinders and $\frac{b}{a}$ for tori, where a higher value represents a more slender shape.

Table 3.5 demonstrates various configurations of cylinders and tori, highlighting the impact of increasing these parameter ratios. These configurations illustrate how higher ratios can lead to structures that are significantly slender, potentially compromising their robustness. It is important to note that the wall thickness in Table 3.5 does not necessarily reflect the actual required thickness to withstand hydrostatic pressure at a depth of 1000 meters. The primary focus here is to showcase different slenderness values for cylinders and tori.

A significant portion of the figures in this chapter contains plots for different slenderness values for the cylinder and torus. To ensure consistency, plots with selected slenderness values of 4, 8, and 12 have been chosen. Three different values are sufficient to demonstrate that slenderness has an influence

on the calculated results, and it allows for the observation of observable trends. Including more than three values could make most plots unclear.

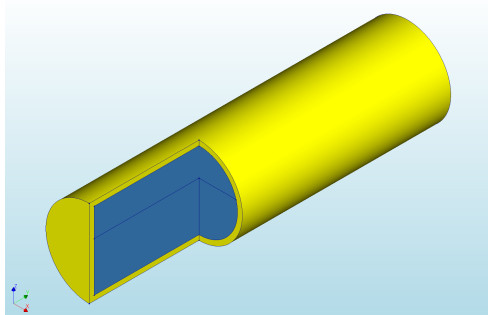
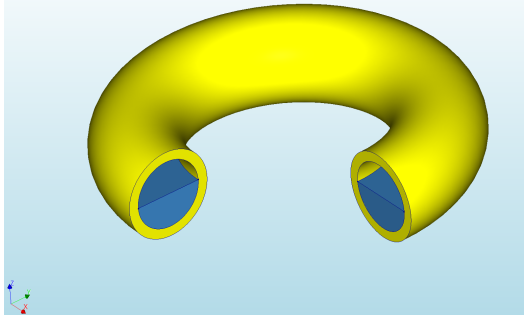
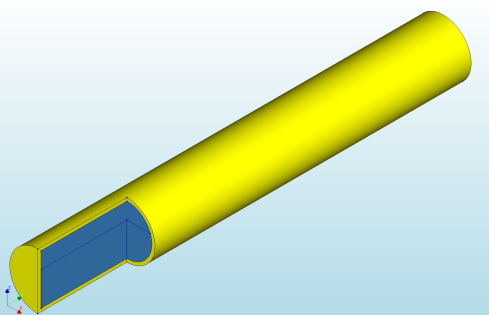
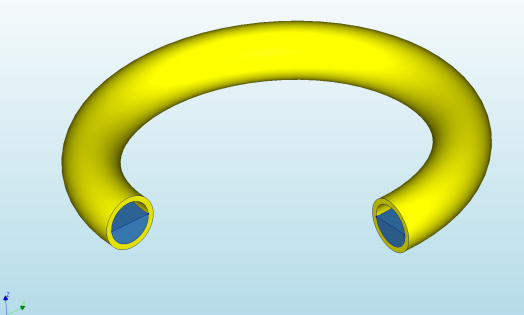
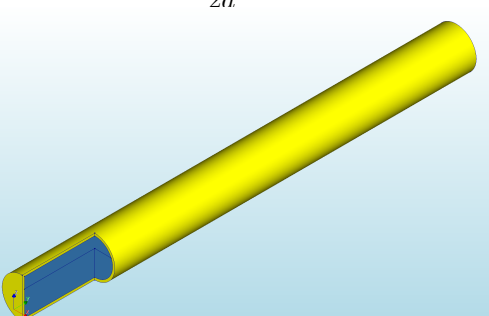
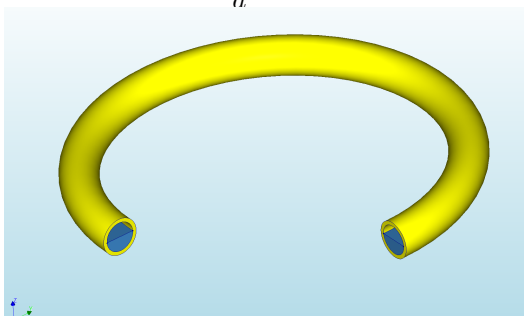
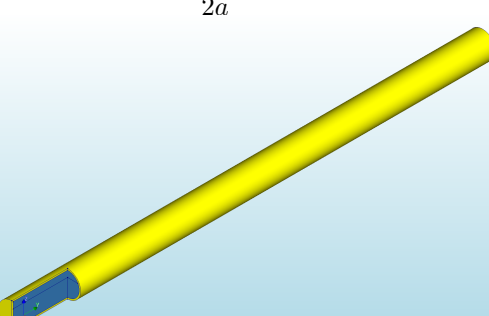
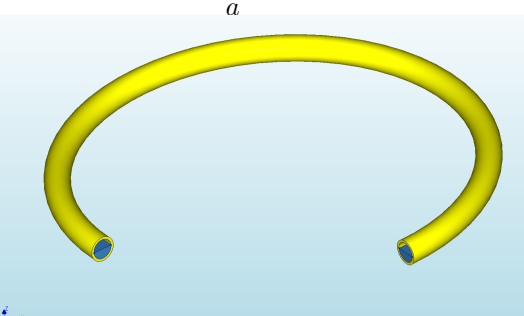
<i>Cylinder</i>	<i>Torus</i>
 $\frac{L}{2a} = 4$	 $\frac{b}{a} = 4$
 $\frac{L}{2a} = 8$	 $\frac{b}{a} = 8$
 $\frac{L}{2a} = 12$	 $\frac{b}{a} = 12$
 $\frac{L}{2a} = 20$	 $\frac{b}{a} = 20$

Table 3.5: Illustrative configurations for cylinder and torus

3.3. Definitions of membrane forces and internal stresses

In Chapter 4, the determination of wall thickness is based on the maximum membrane force. The sphere, due to its geometry, experiences membrane forces solely in the tangential direction, as illustrated in Figure 3.4. Conversely, the cylinder and torus encounter membrane forces in both longitudinal and tangential directions, depicted in Figures 3.5 and 3.6 respectively.

To establish the wall thickness, considering the maximum membrane force, it is crucial to identify whether the longitudinal or tangential membrane force prevails. For thin-walled cylinders, the following relationships apply [38]:

$$n_{LL,cylinder} = -\frac{pa}{2}$$

$$n_{\theta\theta,cylinder} = -pa$$

Regarding a torus, longitudinal and maximal tangential membrane forces have been derived in Appendix C:

$$n_{LL,torus} = -\frac{pa}{2}$$

$$n_{\theta\theta,torus} = -pa \frac{-\frac{1}{2} + \frac{b}{a}}{-1 + \frac{b}{a}}$$

Given that for a torus $\frac{b}{a} > 1$, the maximal tangential membrane force consistently exceeds the longitudinal membrane force. In fact, the minimum tangential membrane force for a torus is $-\frac{3pa}{4}$, a derivation detailed in Appendix C. Refer to Section 3.2 for definitions of a and b .

In Chapter 4, the assumption is made that the normal tangential stress in the shell wall $\sigma_{\theta\theta}$ is constant across the wall thickness. This assumption generally holds for membranes with a $\frac{a}{t}$ ratio exceeding 4000. For thin shells (with $4000 > \frac{a}{t} > 30$), the normal stress in the shell wall linearly varies over the shell thickness [36].

Earlier designs of the spherical reservoir indicate a thickness-span ratio of $\frac{a}{t} = 5.26$ [8] and $\frac{a}{t} = 5.38$ [10]. Classified as a thick shell, these typically exhibit a non-linear stress distribution over the shell thickness [36]. Consequently, it is expected that in reality, $\sigma_{\theta\theta}$ varies non-linearly across the shell thickness.

Despite this expectation, calculations based on the assumption are still deemed valuable. The verification of this assumption is undertaken in Section 6.2.

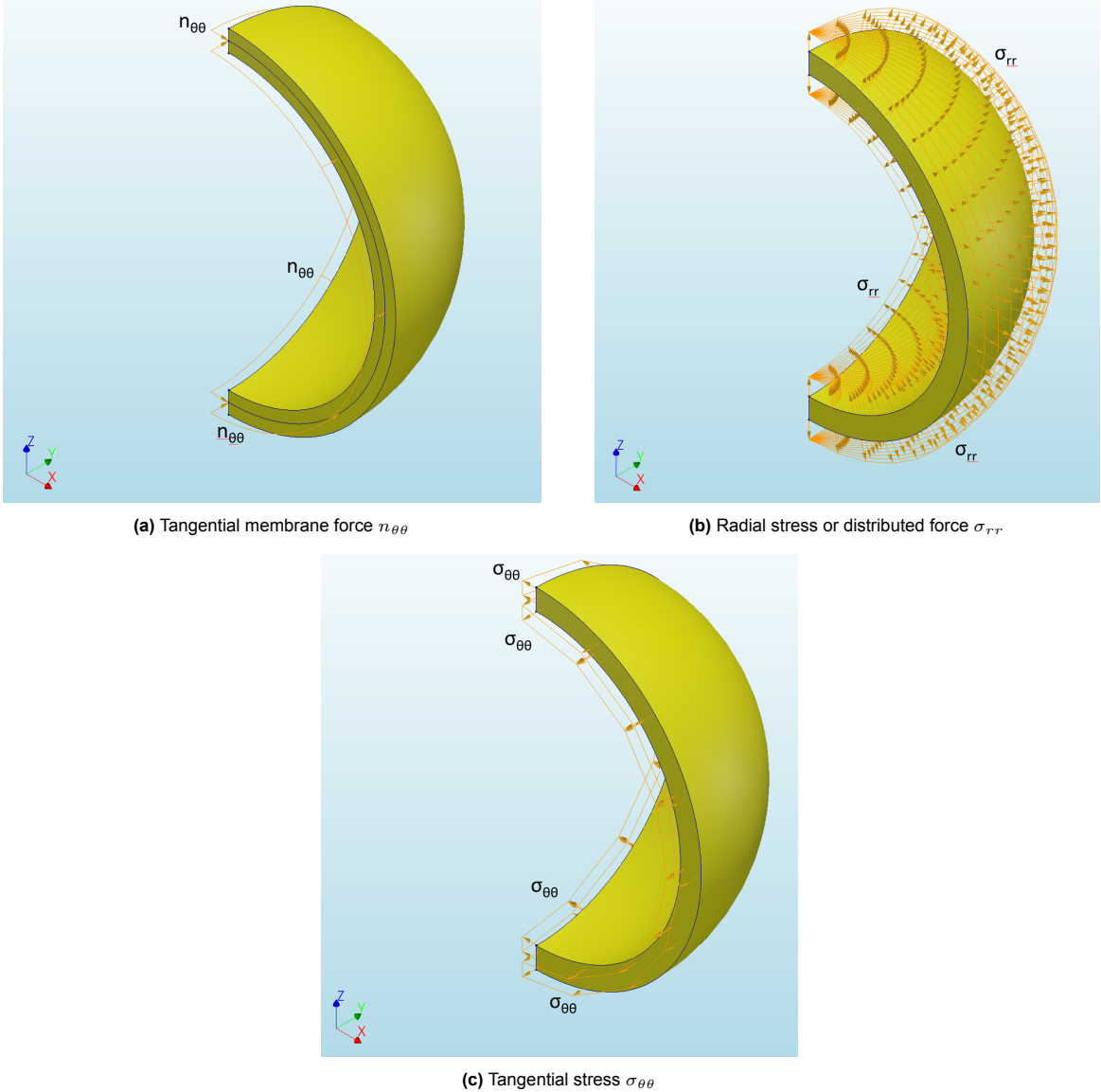


Figure 3.4: Sphere membrane forces and stress definitions at cross-section

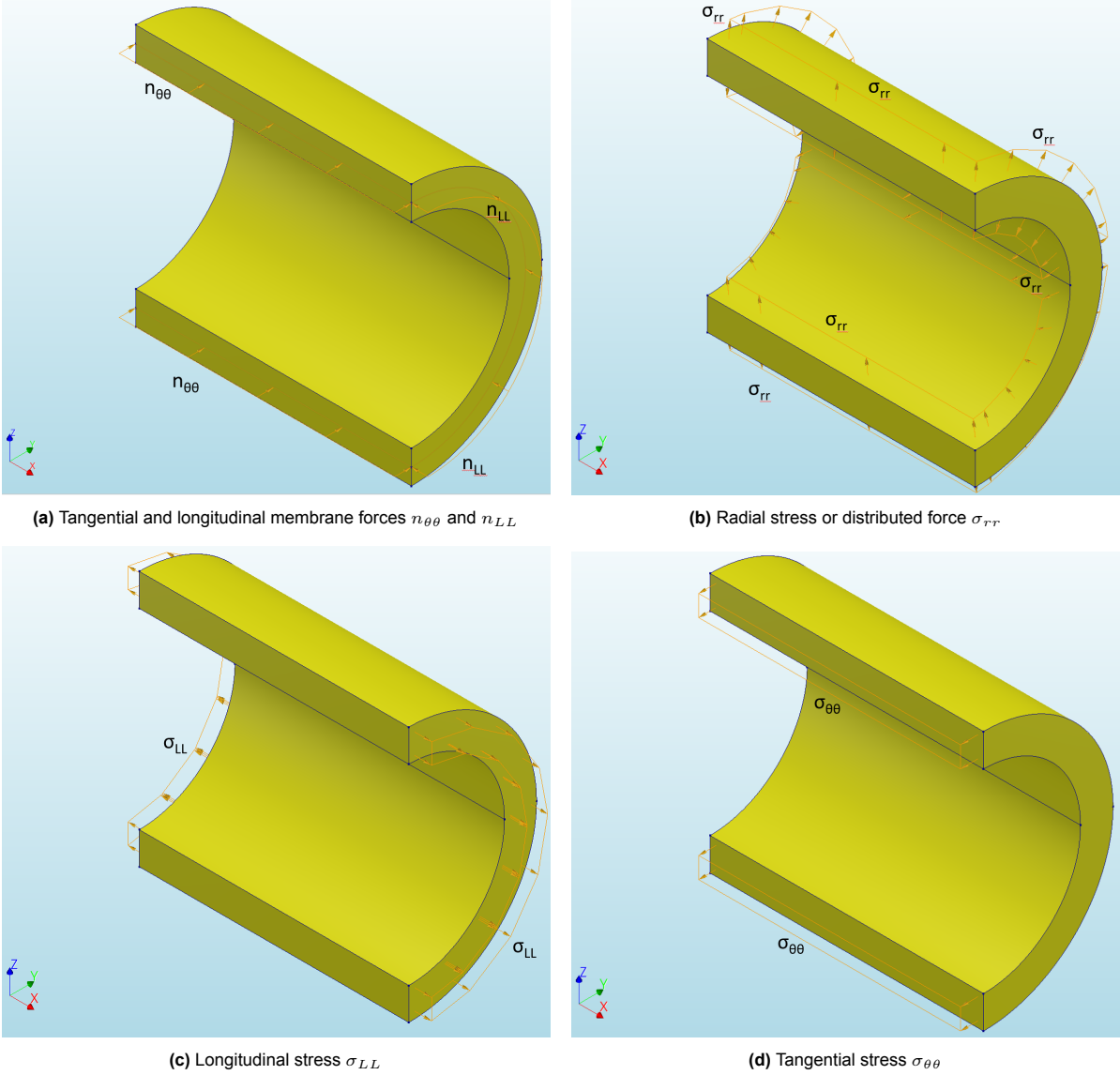


Figure 3.5: Cylinder membrane forces and stress definitions at cross-section

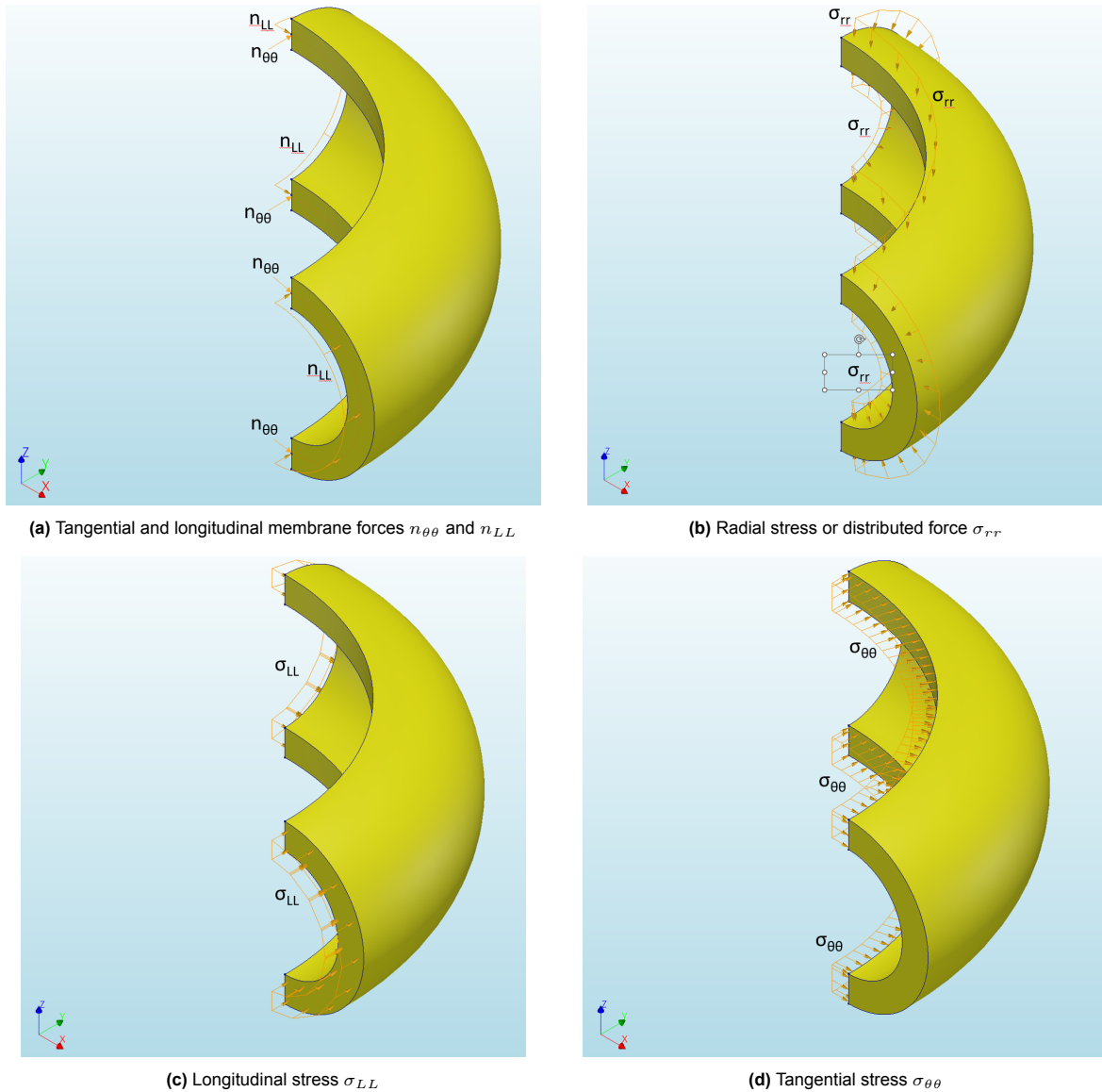


Figure 3.6: Torus membrane forces and stress definitions at cross-section

3.4. Pump/turbine system placement

The designs discussed in Section 3.2 do not address the placement of the pump/turbine system. Given that the primary emphasis of this thesis is on constructing the reservoir, the placement of the pump/turbine system is considered more suitable for later design stages. This Section outlines potential locations for the placement of the pump and provides a qualitative assessment. However, it is important to note that this aspect is not further explored in this thesis.

Several key considerations come into play when determining the placement of the pump/turbine, including the lowest point of the reservoir, accessibility, and the impact on the structural integrity of the reservoir.

To ensure effective pumping of all water out of the reservoir, the pump's inlet should be positioned at the lowest point in the reservoir. Failure to do so could result in water being trapped, reducing the available internal volume and diminishing the overall system efficiency.

Given that the pump/turbine is a critical component requiring frequent monitoring and maintenance, it is crucial to ensure easy access to the pump [13]. Accessibility is vital for inspections and potential removal of the pump to the surface. Consequently, burying the pump in the seabed or placing it under

the reservoir is not advisable.

Moreover, the placement of the pump/turbine should not compromise the structural integrity of the reservoir. Openings in the shell of the reservoir, whether accommodating the pump/turbine or auxiliary tubes, should be minimized. Larger openings could potentially lead to increased stresses around the opening.

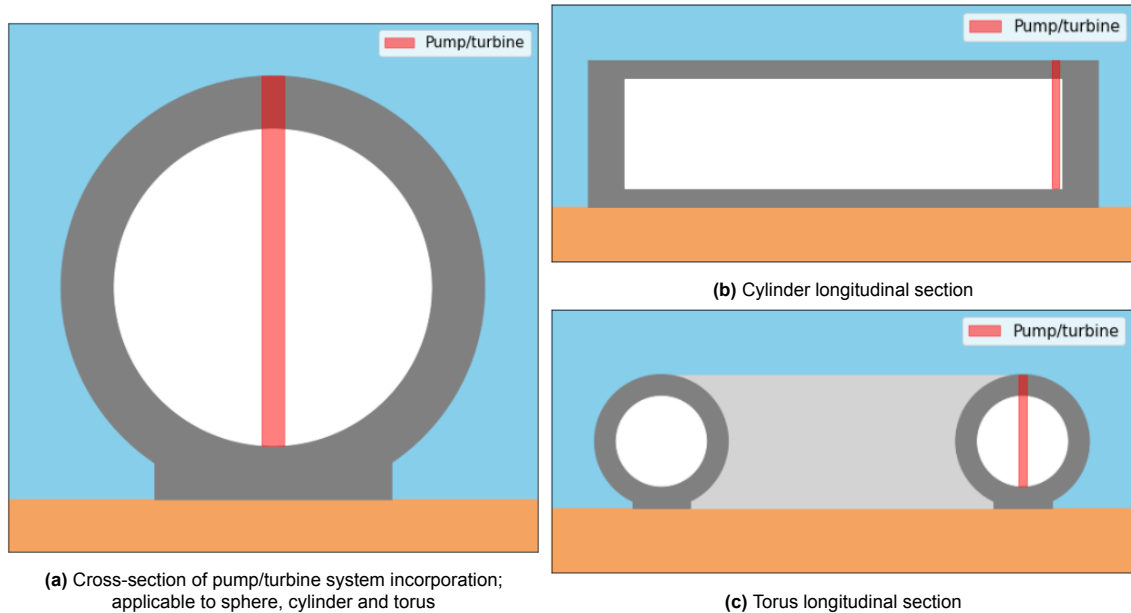


Figure 3.7: Potential incorporated pump/turbine designs

Taking these considerations into account, the placement of the pump/turbine can be either on the exterior of the reservoir or incorporated within it, as depicted in Figure 3.7. When placed on the exterior, the pump/turbine needs to be connected to the reservoir's lowest point using tubes capable of resisting hydrostatic pressure. However, there is a potential risk of damage due to differential settlements between the pump/turbine and the reservoir. On the other hand, incorporating the pump/turbine within the reservoir eliminates the concerns related to differential settlement and minimally impacts the available internal volume. As mentioned in [13], the required pump/turbine, with a diameter of 0,5 meters and a length equal to the internal diameter of the sphere, would occupy less than 0,05% of the available internal volume when used in a reservoir with an internal diameter of 28,8 meters, providing a storage capacity of 12.500 m³.

$$\begin{aligned} \frac{V_{\text{pump}}}{V_{\text{internal}}} &= \frac{\frac{1}{4}\pi d_{\text{pump}}^2 h_{\text{pump}}}{V_{\text{internal}}} \\ &= \frac{\frac{1}{4}\pi \cdot 0,5^2 \cdot 28,8}{12.500} \\ &= 0,0452\% \end{aligned}$$

3.5. Loading conditions

The applied loading conditions in the calculations represent a simplification of the actual loads, which include hydrostatic pressure, gravity, horizontal water flow, transport loads, and accidental loads. Among these, hydrostatic pressure is the most significant factor. At a depth of 1000 meters, the hydrostatic pressure amounts to 10,06 MPa.

$$\begin{aligned}
 p_{\text{hydrostatic}} &= \rho_{\text{sw}} g h \\
 &= 1025 \cdot 9,81 \cdot 1000 \\
 &= 10.055.250 \text{ N/m}^2
 \end{aligned}$$

In reality, there exists a gradient in the hydrostatic pressure value. However, considering that the structure's height will be a maximum of approximately 30 meters and the depth is 1000 meters, the pressure variation is less than 3% from the bottom to the top of the structure. Since this gradient introduces only a minor discrepancy in load between the top and bottom of the structure, it is neglected in the calculations. Therefore, all computations consider a constant distributed normal force of 10,06 MPa.

Two different loading conditions are distinguished, considering the filling level of the reservoir, as depicted in Figure 3.8. When the reservoir is full, the hydrostatic pressure inside the reservoir pushes against the wall of the reservoir. In addition to the constant hydrostatic pressure on the exterior of the reservoir, this results in a compression-compression situation inside the concrete wall, which is favorable for the material. Therefore, the situation where the reservoir is empty, and no hydrostatic pressure is present in the interior of the reservoir, is considered normative.

It is essential to clarify that the exterior hydrostatic pressure, denoted as p_{out} , does not exert the same force on the interior of the reservoir under normal operational conditions. This scenario only occurs when the pump/turbine opening is uncovered, and a static situation prevails with no water flow. However, the system is not designed to operate in this manner. The intentional filling of the last available volume in the reservoir would lead to a shock wave due to the water hammer phenomenon. To avert this, it is necessary to gradually close the pump/turbine opening during the reservoir filling process. Consequently, in the context of hydrostatic pressure, if the structure is used as intended, only the loading conditions depicted in Figure 3.8 are relevant during the use phase. In the case of a calamity, the structure should be able to resist the water hammer-induced shock wave. However, this aspect is not further elaborated in this report.

Conflicting statements regarding the available internal volume for filling were found in the literature. According to the STORE Consortium, an available filling level of 90% was reported, leaving the remaining volume for air. It was mentioned that this air was necessary to initiate the pumps [10]. In a full-reservoir situation, the compressed air would then exert pressure on the interior wall of the reservoir. In contrast, the Fraunhofer Institute assumes a 100% available internal volume, achieved by creating a vacuum in the empty reservoir before installation [13]. This report opts to work with a 100% available internal volume, acknowledging that the last bit of volume cannot be practically filled due to the water hammer phenomenon, as described earlier.

Gravitational load of the structures own weight is considered negligible. The weight of concrete in water is $\rho_{\text{concrete}} - \rho_{\text{sw}} = 1375 \text{ kg / m}^3$. A concrete column of 30 meters thick would then exert a pressure on the structure that is equal to a mere 4% of the hydrostatic pressure.

$$\begin{aligned}
 p_{\text{concrete column}} &= (\rho_{\text{concrete}} - \rho_{\text{sw}}) g h_{\text{structure}} \\
 &= (2400 - 1025) \cdot 9,81 \cdot 30 \\
 &= 404.663 \text{ N/m}^2
 \end{aligned}$$

There is little temperature change in the deep ocean, as it is far removed from significant heat sources, making it one of the most thermally stable regions on earth. Temperature may fluctuate by less than half a degree per year in the deep ocean [39]. Given the intended installation depth in the deep ocean, temperature loads—resulting in structural expansion and contraction—are not considered relevant for this analysis.

Moreover, flow velocity loads are disregarded. At the intended installation depth, flow velocities are typically low [40]. Consequently, loads induced by flow are omitted, although they might influence the

stability of the structures. However, such considerations are beyond the scope of this report. Additionally, accidental loads and transport loads are not addressed here.

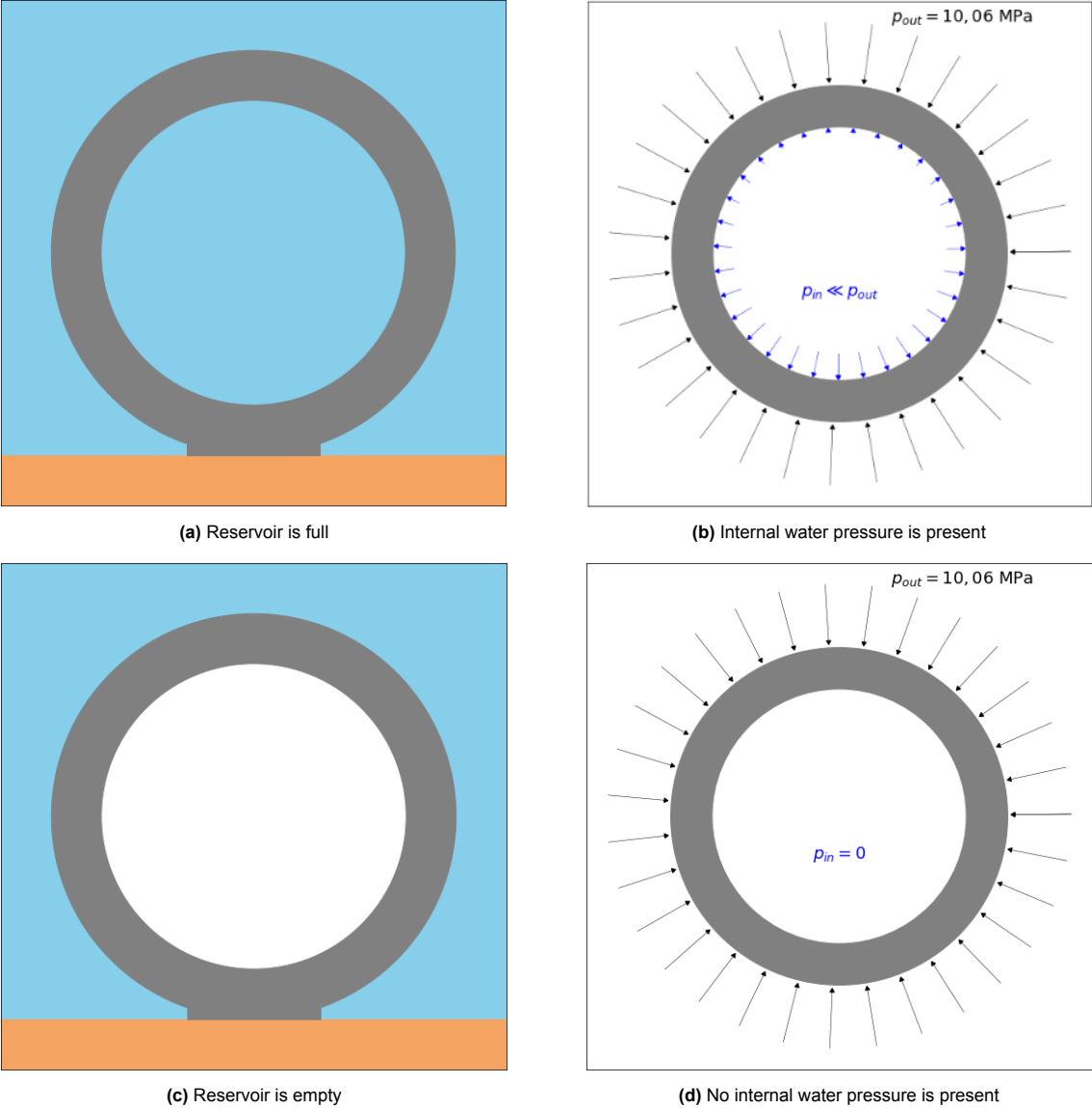


Figure 3.8: Load situations for empty and full reservoir

4

Initial structural design

In this Chapter, the CIV-ratios for the reservoirs and foundations are analyzed. Each of the proposed shapes — sphere, cylinder, and torus — undergoes a comprehensive assessment based on preliminary calculations. These initial analyses serve as the basis for subsequent design choices.

It is crucial to emphasize that, in the interest of clarity and scientific rigor, the spherical design is anticipated to yield a lower and thus more favorable CIV-ratio. However, the advantages of the cylindrical and toroidal designs may stem from different aspects, such as constructability and transportability. Therefore, the cylinder and torus are not immediately dismissed even in the presence of an unfavorable CIV-ratio.

In this Chapter, a description of the principles that guide the calculations is provided where necessary. To ensure transparency, the calculations leading to the findings presented herein are available in Appendix D.

4.1. Initial reservoir design

In this section, an estimation is performed for the necessary concrete volume required to construct spherical, cylindrical and toroidal reservoirs. Subsequently, these results are employed to determine the CIV-ratio specific to each shape. The procedural steps for these calculations are outlined in Figure 4.1.

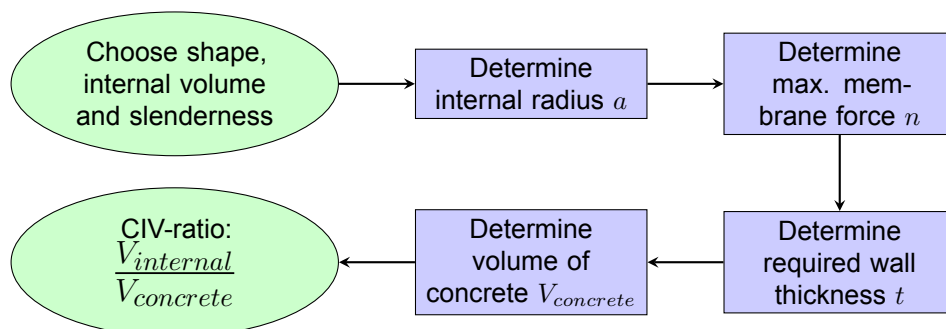


Figure 4.1: Workflow for determining required volume of concrete

In the initial design phase the membrane forces n are utilized as a starting point. These forces operate within the plane of the shell. In the context of this Chapter, they represent the force experienced within an infinitesimally thin structural wall and are quantified in units of Newtons per meter. Table 4.1 provides a comprehensive overview of the maximum membrane forces and volumes for spheres, cylinders, and tori. The parameters involved include the hydrostatic pressure denoted by p and the respective internal radii for each shape (a for spheres and cylinders, and both a and b for tori). Refer to Section 3.2 for their definitions. The derivation of the values in Table 4.1 is outlined in Appendix C.

Given that required internal radii are established according to a specified internal volume and, if applicable, slenderness, the equations for volume presented in the first column of Table 4.1 have been reformulated to express the internal radius as a function of volume and slenderness. These revised equations are depicted in the third column.

Shape	Volume (V) [m^3]	Slenderness [-]	Internal radius (a) [m]	Max. membrane force (n) [N/m]
Sphere	$\frac{4}{3}\pi a^3$	-	$\sqrt[3]{\frac{3V}{4\pi}}$	$-\frac{pa}{2}$
Cylinder	$\pi a^2 L$	$\frac{L}{2a}$	$\sqrt[3]{\frac{V}{2\pi\frac{L}{2a}}}$	$-pa$
Torus	$2\pi^2 a^2 b$	$\frac{b}{a}$	$\sqrt[3]{\frac{V}{2\pi^2\frac{b}{a}}}$	$-pa\frac{-\frac{1}{2} + \frac{b}{a}}{-1 + \frac{b}{a}}$

Table 4.1: Membrane forces and volumes for sphere, cylinder, and torus

4.1.1. Initial thickness estimation

The relation between the membrane force n [N/m] and the compressive design strength of the concrete f_{cd} [N mm⁻²] is articulated through Equation 4.1:

$$t = \frac{n}{f_{cd}} \quad (4.1)$$

In this context, t [m] represents the required thickness of the concrete, assuming an idealized scenario of uniform stress distribution across the cross-section, as discussed in Section 3.3. It is important to acknowledge that in reality, stress distribution is non-uniform across the cross-section, necessitating a greater thickness. However, for the purposes of this Chapter, this simplified approach yields practical results. It is worth noting that this thickness is applied exclusively to the external surface of the structure, ensuring that no internal volume is sacrificed in the design process. This methodology allows for a preliminary assessment of the concrete volume needed for constructing the reservoir across different shapes.

The results of this parameter identification and thickness estimation process are depicted in Figure 4.2, illustrating the CIV-ratio for spheres and various configurations of cylinders and tori. Interestingly, the relationship between the volume of concrete and the internal volume exhibits a linear correlation for each shape, although the slopes vary with shape and slenderness.

The neutral buoyancy is also depicted in the plot. This line represents the volume of concrete necessary to counteract buoyant forces. Any design situated below this line will inherently display buoyancy and remain afloat. With the exception of non-slender cylinders, all reservoirs have positive buoyancy. Nevertheless, it is important to acknowledge that some additional concrete is anticipated to be incorporated in the foundation design, which would contribute to stabilizing the structure.

These initial findings confirm the expected result that, for the same internal volume, a sphere requires a smaller volume of concrete compared to a cylinder or torus. In other words, the sphere demonstrates a more favorable CIV-ratio than the cylinder and torus. The influence of different slenderness values on cylinders and tori has been explored. Strikingly, slenderness values significantly affect the required volume of concrete. The slope of the lines in the plot indicates that higher slenderness values result in a lower CIV-ratio for cylinders and tori.

In the case of the cylinder, the caps are configured as circular plates with double the thickness of the shell. Notably, when the caps are completely excluded from the design, effectively transforming the cylinder into a tube, the slenderness no longer influences the required volume of concrete. In this case, all various configurations of the cylinder converge onto the same line in Figure 4.2. To maintain clarity,

this line is omitted from the graph. This observation underscores that the non-linear behavior in the cylinder's CIV-ratio is solely attributable to the design of the caps.

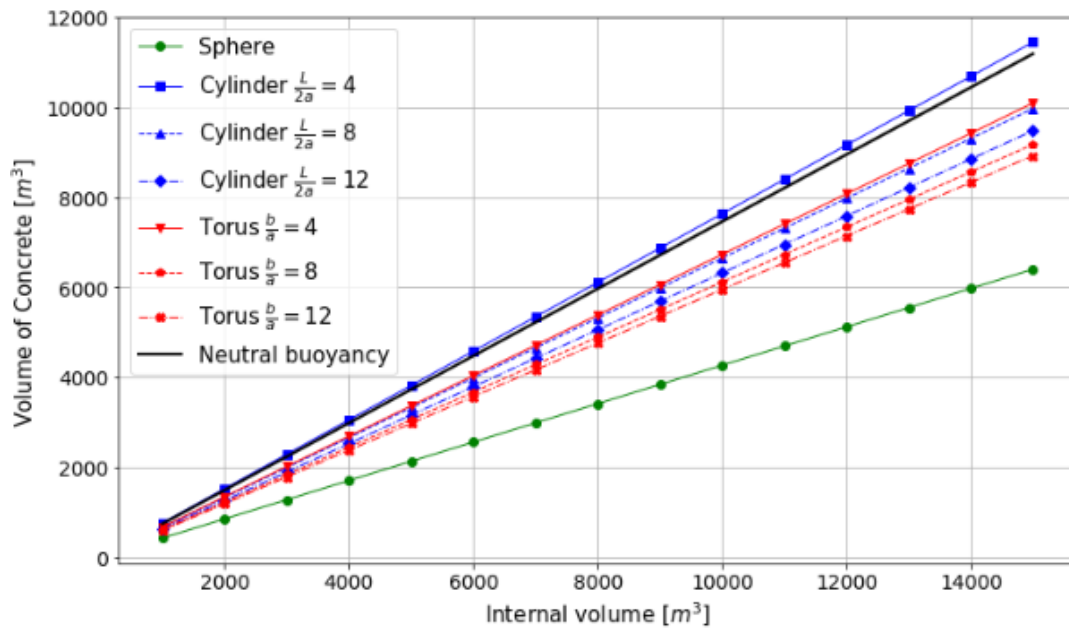


Figure 4.2: Concrete and internal volume relation for a sphere and various cylinder and torus configurations with initial thickness estimation; at $d = 1000$ m and $f_{cd} = 40$ MPa

4.1.2. Iterative adjustment of thickness

The previously described approach, where an infinitesimally thin wall was employed, not only simplifies the analysis but also overlooks the impact of altering dimensions due to changes in thickness. Specifically, as the thickness of the structure is adjusted, the radius of the cross-sectional shape undergoes corresponding changes, resulting in variations in the membrane forces as dictated by the equations in Table 4.1.

It is essential to emphasize that the determination of the required thickness was initially based on achieving the maximum allowable compressive stress within the cross-section, as defined by Equation 4.1. Any increase in the membrane forces automatically results in exceeding the maximum allowable compressive stress, necessitating an increase in the shell's thickness.

To address this iterative requirement, an algorithm outlined in Figure 4.3 was utilized. A tolerance of 0,001 MPa was selected, allowing for smooth results.

Comparing the results of this iterative approach with the initial thickness estimation, the differences are evident in Figure 4.4. Clearly, employing the iterative approach to determine the shell thickness results in a higher CIV-ratio for each shape. These effects are more pronounced for shapes that initially had an unfavorable CIV-ratio. The iterative process significantly enhances the performance of the spherical design compared to the cylindrical and toroidal designs in terms of the CIV-ratio. This outcome aligns with the fact that shapes with unfavorable CIV-ratios initially have thicker shell requirements, resulting in a higher increase in membrane force and necessitating a greater increment in thickness.

For instance, with the iterative approach in place, the increase in concrete volume is more significant for the torus (78%) than for the cylinder (42%) when $\frac{b}{a} = \frac{L}{2a} = 4$. However, this discrepancy diminishes for higher configurations and stabilizes at 39%, whereas the sphere exhibits a concrete volume increase of 16%. It is noteworthy that the percentage increase in the volume of concrete remains consistent relative to the internal volume, explaining the linear data observed in both Figure 4.2 and Figure 4.4.

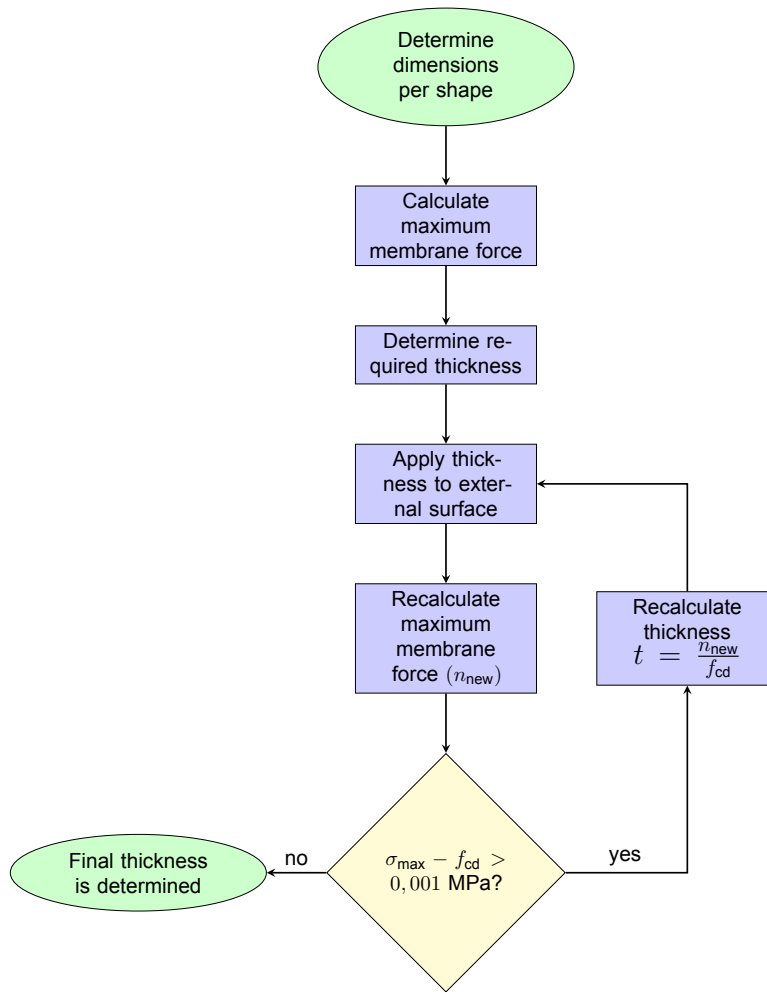


Figure 4.3: Algorithm for determining shell thickness for sphere, cylinder and torus

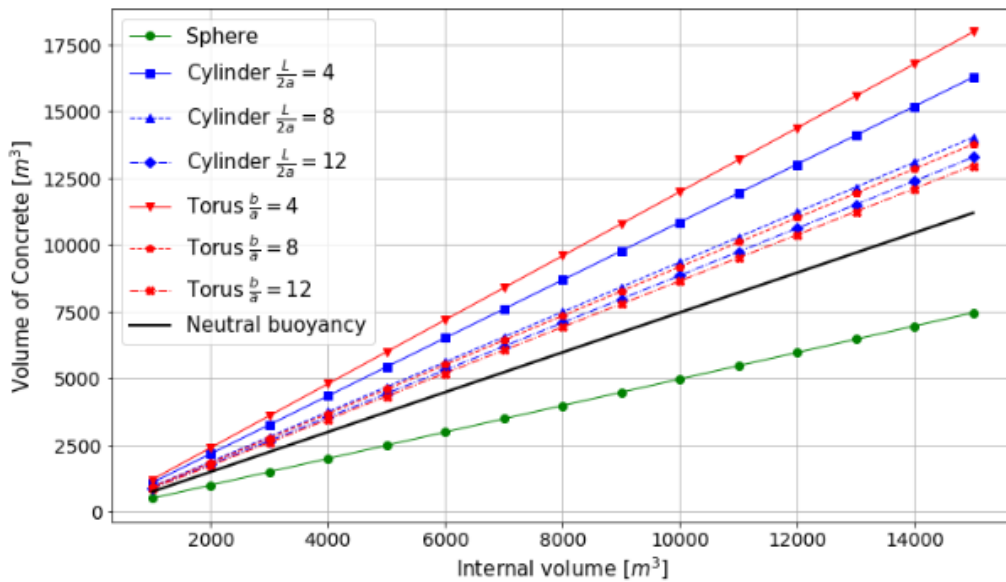


Figure 4.4: Concrete and internal volume relation for a sphere and various cylinder and torus configurations with iterative thickness estimation; at $d = 1000$ m and $f_{cd} = 40$ MPa

4.1.3. Internal Radius - Wall Thickness Relation

The iterative approach previously described yields the necessary wall thickness, determined by the shape and internal radius, and in the case of the cylinder and torus, the slenderness as well. In Figure 4.5, the required wall thickness for a specific internal radius is graphed for various internal volumes and different slenderness values.

When the sphere is chosen as the shape for a given internal volume, the algorithm produces a singular wall thickness. In contrast, for the cylinder and torus, the wall thickness for a given internal volume is also contingent on the slenderness. In Figure 4.5, the wall thickness for the cylinder and torus is determined using $4 \leq \frac{b}{a} = \frac{L}{2a} \leq 20$. This results in a single data point per internal volume per slenderness value, representing the sphere as dots and the cylinder and torus as lines.

The relationship between internal radius and wall thickness is linear for the sphere and cylinder. This aligns with the observation made in subsection 4.1.1, where it was noted that the non-linear behavior in the cylinder's CIV-ratio is solely attributable to the design of the caps. Conversely, the wall thickness of the torus increases exponentially for larger internal radius. This effect can be attributed to the non-linear relation between the membrane force and the internal radius of the torus.

It is noteworthy that for both the cylinder and the torus, the lower ends of the data ranges represent higher slenderness values. For the cylinder, the wall thickness is inversely proportional to the slenderness. In the case of the torus, there exists an inverse exponential relationship between the wall thickness and the slenderness.

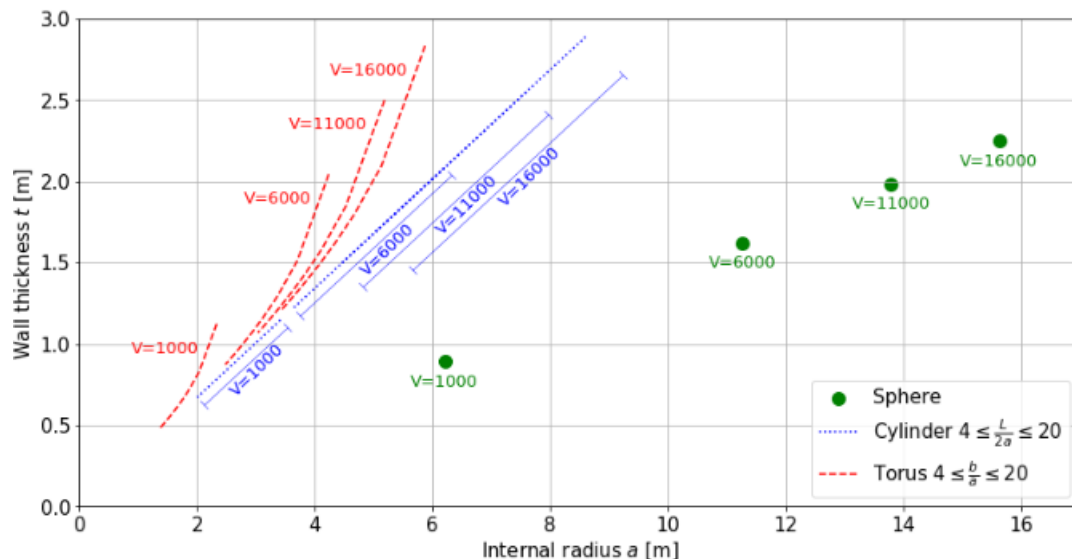


Figure 4.5: Relationship between internal radius and wall thickness for the sphere, cylinder, and torus with different slenderness values; at $d = 1000$ m and $f_{cd} = 40$ MPa

4.1.4. Optimization of cylinder- and torus-configuration

Further investigation of the slopes of the lines in Figure 4.4 reveals that the correlation between volume of concrete and internal volume can be optimized by adjusting the ratio between the dimensions of cylinders and tori. Figure 4.6 showcases the optimized CIV-ratio for various cylinder and torus configurations under the same depth and concrete strength conditions.

This optimization process suggests that, at the specified depth and concrete compressive strength, an optimal configuration exists for cylinder and torus shapes in terms of material usage, characterized by $\frac{L}{2a} = \frac{b}{a} \approx 40$. Notably, the most significant improvements occur at lower ratios, after which the curves approach a plateau.

However, as greater slenderness is inherently associated with increased external dimensions, particularly the length of the cylinder and the major diameter of the torus, it appears that a favorable range for the slenderness of the cylinder and torus lies between 10 and 20. The benefits in terms of the CIV ratio

diminish beyond a slenderness value of 20.

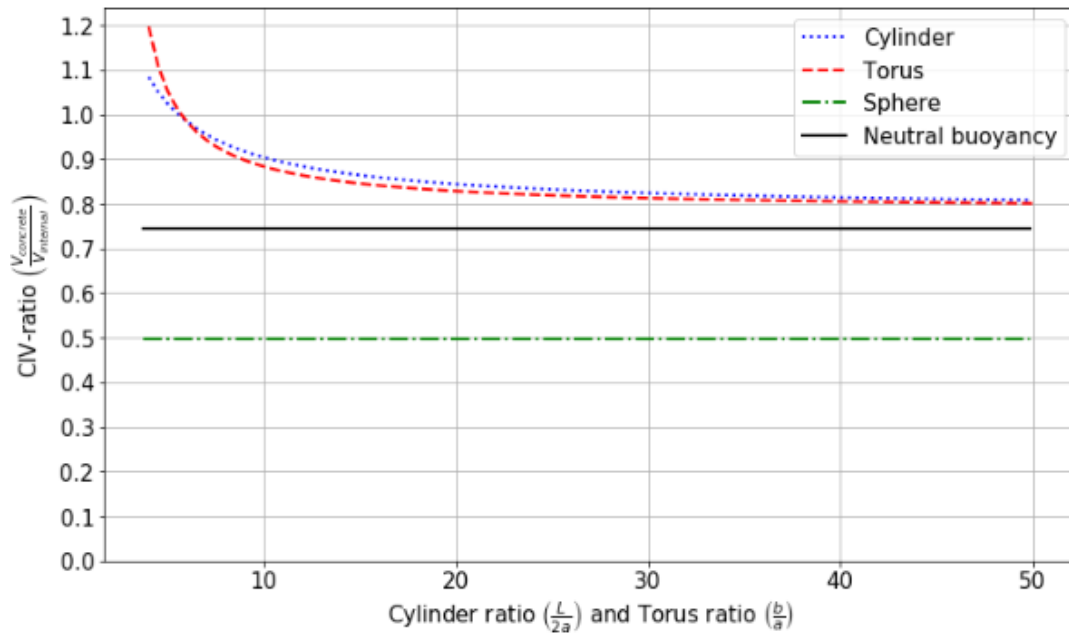


Figure 4.6: Optimized concrete to internal volume ratios for cylinder and torus configurations with iterative approach; at $d = 1000$ m and $f_{cd} = 40$ MPa

Moreover, the sphere consistently maintains a more favorable concrete-to-internal volume ratio, utilizing 37% less material than the cylinder and torus for high values of slenderness. The sphere's advantage over the cylinder and torus fluctuates with varying concrete strengths. For further insights into the influence of concrete strength, please refer to the results of the sensitivity analysis in Section 4.1.5.

While Figure 4.6 provides valuable insights into favorable configurations for the cylinder and torus, it is crucial to remain aware of the limitations of the model. It is essential to emphasize that the thickness estimation, which directly influences the required concrete volume, is merely indicative. This approach does not account for all internal forces within the structures, as moments are expected to be present in addition to the membrane forces.

4.1.5. Sensitivity study concrete strength

As previously mentioned, the strength of concrete exerts a significant influence on the CIV-ratio. In the initial approach, the effect of the adjusted cross-sectional shape radius due to the estimated thickness was not considered, resulting in a linear relationship between the CIV-ratio and the concrete strength class. However, a shift in this relationship occurred upon the adoption of the iterative approach, as elaborated in Section 4.1.2.

Referring to the flowchart presented in Figure 4.3, which outlines the thickness iteration process, it is evident that the recalculated maximum membrane force necessitates an increase in thickness. This augmented thickness, in turn, results in a heightened maximum membrane force, necessitating an increment in the volume of concrete. After numerous iterations, a state of equilibrium is achieved between these two consequences.

When dealing with concrete possessing lower strength properties, a more significant increase in thickness is essential, resulting in higher membrane forces and the need for an even thicker shell. This phenomenon becomes less pronounced when using concrete of higher strength, as a slight augmentation in thickness adequately addresses the escalating maximum membrane force. Consequently, a nonlinear correlation between the concrete-to-internal-volume ratio and the concrete strength is established.

This relationship is visually demonstrated in Figure 4.7. Notably, the influence of varying concrete

strength is most pronounced for shapes already exhibiting an unfavorable CIV-ratio. This is particularly evident in the case of the torus with a slenderness value of 4. However, the non-linear association between CIV-ratio and concrete strength is unmistakable. Across all shapes, the advantages of higher concrete strength are evident, as they result in substantial material savings.

When examining Figure 4.7, it is essential to recognize that the changes in concrete volume shown on the y-axis are specific to the given shape and its configuration. It is important not to misinterpret the greater percentage of material savings observed for the torus, with a configuration of $\frac{b}{a} = 4$, at higher concrete strength as indicating a more advantageous CIV-ratio compared to the sphere.

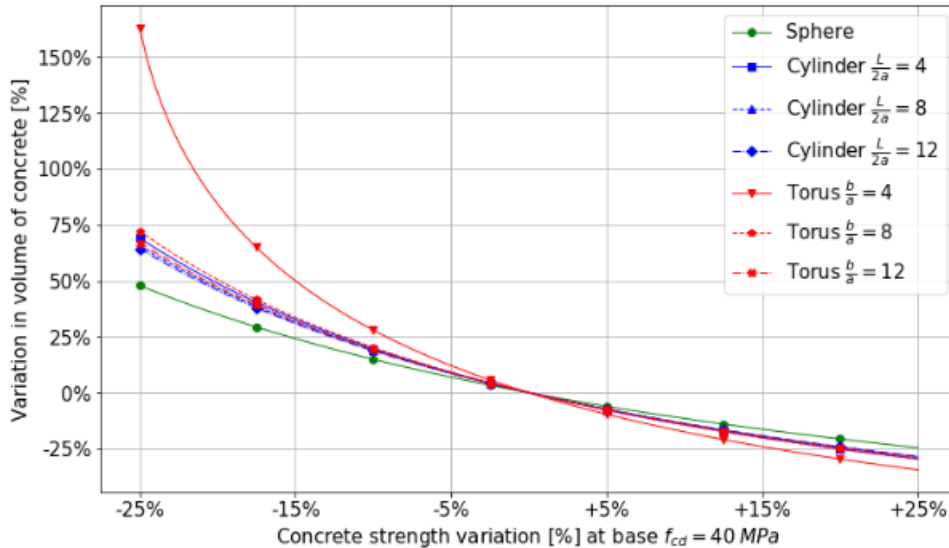


Figure 4.7: Sensitivity analysis of concrete strength

4.2. Initial foundation design

This Section outlines the foundation design process for sphere, cylinder and torus. The discussion commences with the design of the sphere, followed by the cylinder and torus. The foundation design for the cylinder and torus exhibits significant similarities, and as such, their designs are presented together. In conclusion, the designs of these three foundations are compared, focusing on their CIV-ratios.

4.2.1. Foundation design spherical reservoir

The concept for the spherical foundation draws inspiration from the configuration presented in [10]. The layout incorporates a ring-shaped pedestal to provide support for the sphere. The pedestal, in turn, is supported by a shallow circular foundation slab. In this specific design, the internal volume of the sphere is 9.000 m^3 , with the pedestal having a thickness of 1 meter. The circular foundation slab boasts a diameter of 30 meters and a thickness of 1,6 meters. A visual representation of this structural configuration is illustrated in Figure 4.8.

To reduce weight and optimize buoyancy control, circular holes are strategically extruded from the pedestal wall. During transport, these holes are covered to increase buoyancy, making it easier to move the structure. Once the structure reaches its intended location, the holes are uncovered, allowing for a gradual descent to the seabed.

In the described design, the concrete sphere exerts a compressive force on the pedestal due to its weight. The pedestal, which has a thickness of 1 meter, is responsible for supporting this load. As a result, the vertical compressive stress at the base of the pedestal can be calculated, yielding a value of $1,15 \text{ N/mm}^2$ in [10].

In this stage of the design, the thickness of the ring-shaped pedestal is determined based on the computed vertical compressive stress. To accommodate various internal volumes, the algorithm presented in Section 4.1.2 is employed to calculate the required thickness of the sphere shell. Subsequently, the

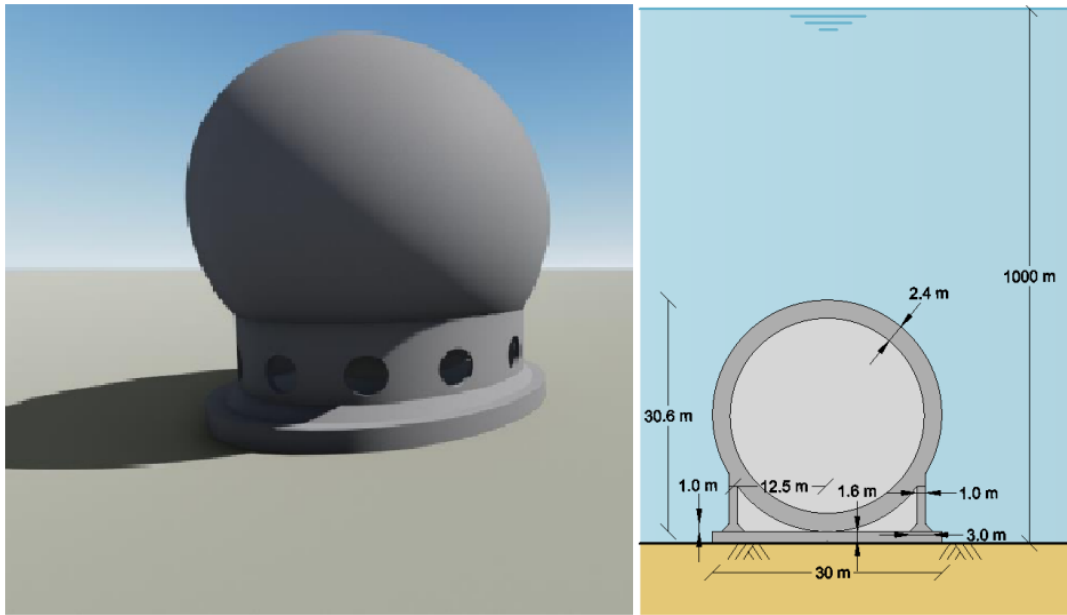


Figure 4.8: Sphere foundation design with pedestal and shallow foundation [10]

required thickness of the ring-shaped pedestal is calculated, ensuring that it maintains the same level of compressive stress in the bottom of the pedestal.

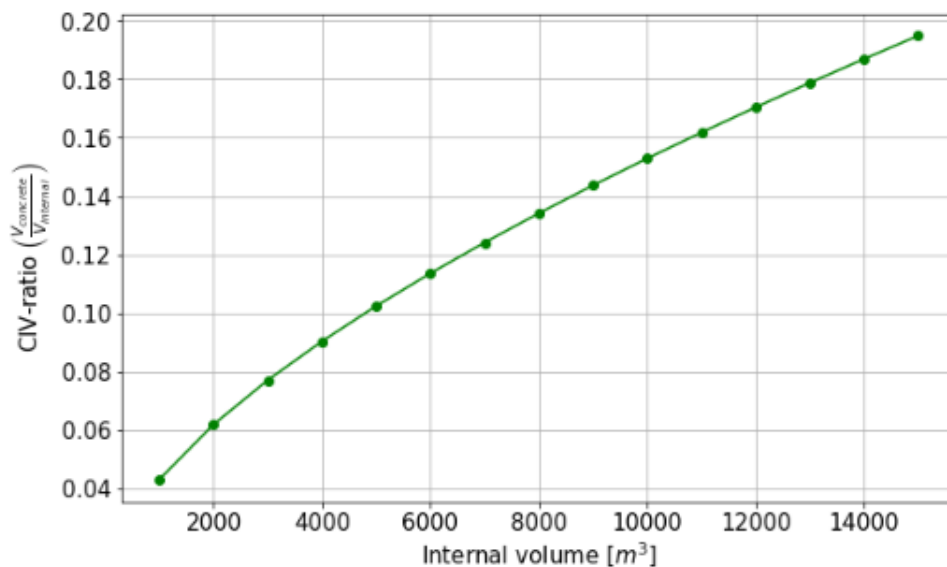


Figure 4.9: CIV-ratio for concrete volume of spherical foundation design vs. Internal volume; at $d = 1000$ m and $f_{cd} = 40$ MPa

Within the foundation structure, the vertical compressive load is supported by the perimeter of the circular slab. The soil exerts a reaction force on the slab, generating a negative bending moment at the center of the slab. Consequently, the foundation slab must possess the capacity to withstand this bending moment. In the design discussed in [10], the thickness of the foundation primarily hinges on its ability to resist this bending moment.

During this particular design phase, a simplified approach is employed to calculate the magnitude of the bending moment in the center of the slab. The bending moment in [10] is noted to be 5,76 MNm, necessitating a plate thickness of 1,6 meters. A bending moment resistance of $5,76/1,6 = 3,60$ MNm per meter of plate thickness is used to determine the required thickness for the scaled foundation

design.

While it is acknowledged that this approach might lack precision and does not encompass all load combinations within the structure, it effectively serves the purpose of providing initial estimates for the required concrete volume. The outcomes derived from this methodology are valuable at this stage of the design process.

The findings from this approach are visually presented in Figure 4.9, depicting the relationship between the CIV-ratio and the internal volume for the spherical foundation design. Notably, the CIV-ratio tends to rise as the internal volume increases.

4.2.2. Foundation design cylindrical and toroidal reservoir

During this design phase, the foundation for both the cylinder and torus adopts a straightforward approach. It involves the creation of a solid base designed to establish a level and stable surface on the ground. The width of this base is determined based on the maximum allowable foundation pressure.

Given the absence of a specific installation location, it is assumed that the soil consists of muddy sand, similar to the assumptions made in [10]. As precise soil parameters for muddy sand are unavailable, they are derived from those of clean compact sand. According to the Dutch National Annex (NEN-EN 1997-1/NB) to Eurocode 7 (EN 1997-1) the bearing capacity for clean compact sand is 1000 kPa. To account for the influence of cohesion and the assumption that the soil is essentially muddy sand, a safety factor of 5 is applied. This results in a maximum allowable bearing capacity of $\sigma_{f,d} = 200$ kPa.

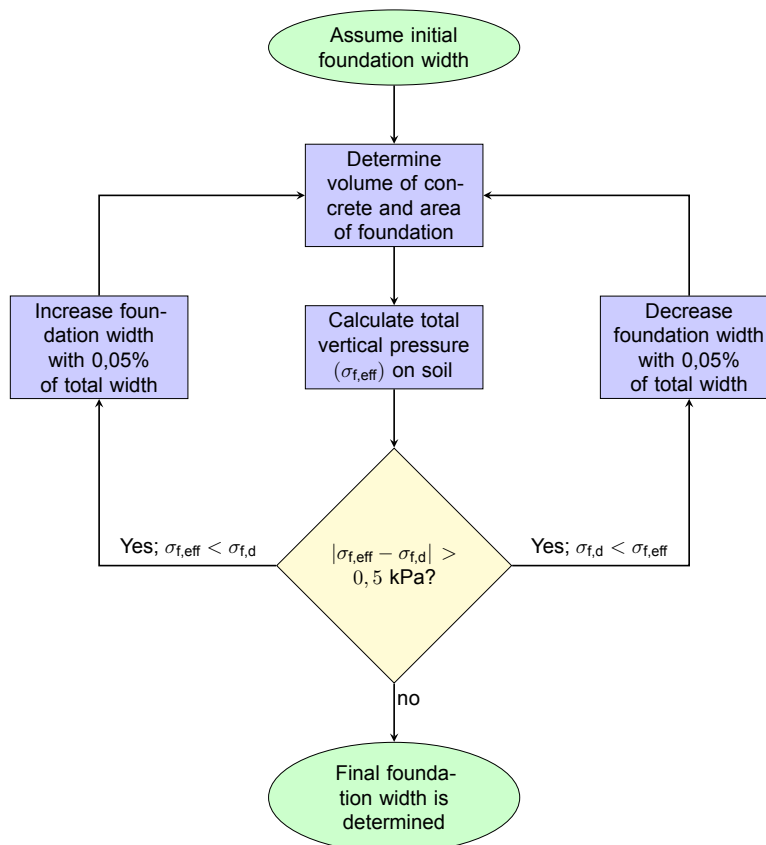


Figure 4.10: Algorithm for determining foundation width for cylinder and torus

The design of the foundation depends on the dimensions of the cross-section of the reservoir. For both the cylinder and the torus, these dimensions are intricately linked to the specified internal volume and the slenderness, as described in section 4.1 To determine the required width of the foundation

that would yield the specified foundation pressure, an initial estimate is made, expressed as a percentage of the total width of the cross-section. Subsequently, the volume of concrete within the foundation is computed and the total weight of the structure is calculated. Following this, the pressure that this foundation exerts on the soil is calculated. If the calculated pressure exceeds the maximum bearing capacity of the soil, the foundation should be wider. Conversely, if the pressure falls below the soil's maximum bearing capacity, the width of the foundation can be reduced to economize on material usage. This iterative process is visually represented in Figure 4.10. The tolerance of 0,5 kPa and the increase/decrease factors of 0,05% provide smooth results.

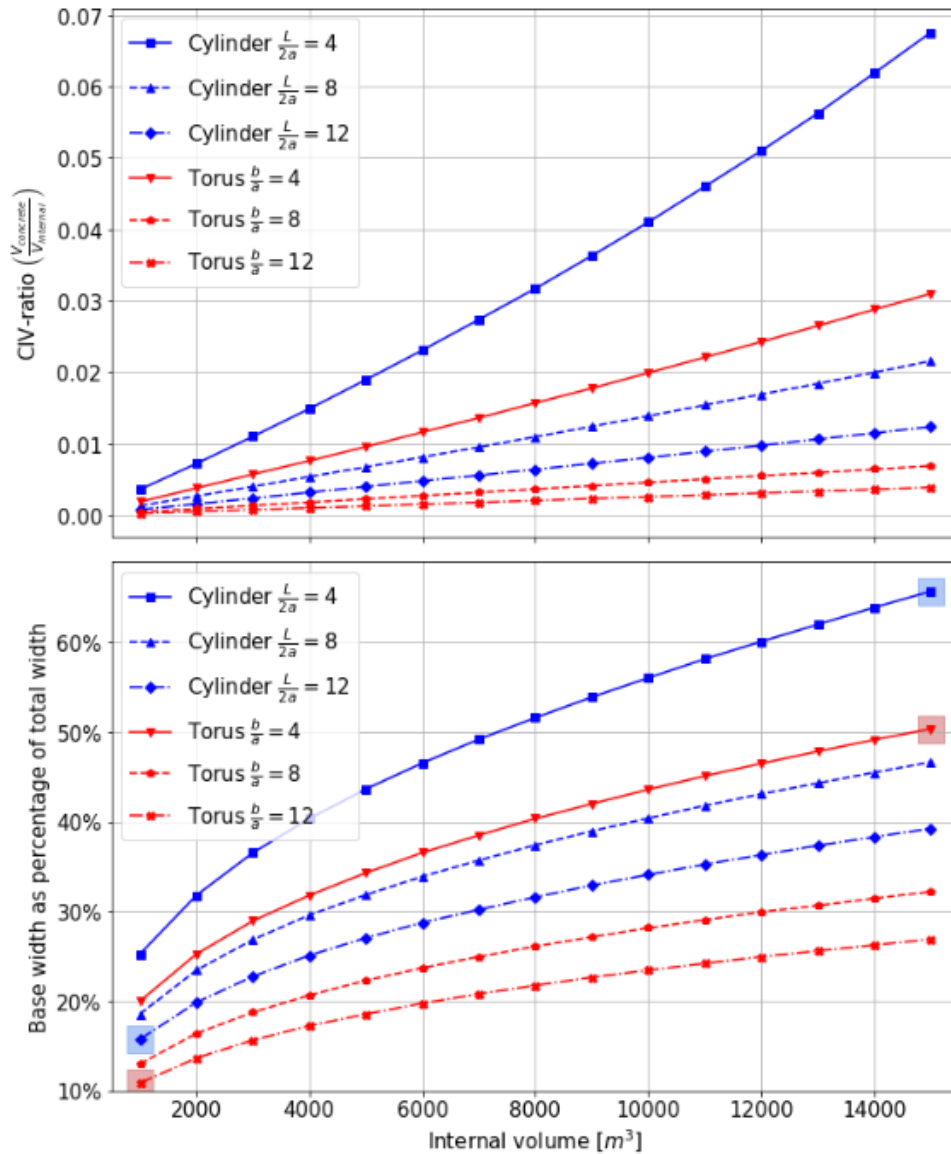


Figure 4.11: Foundation design: CIV-ratio vs. Internal volume for different cylinder and torus slenderness values; with corresponding base widths; at $d = 1000$ m and $f_{cd} = 40$ MPa

The determination of concrete volume in the cylinder foundation relies on trigonometric principles. Essentially, the foundation is conceptualized as a solid block, and the intersecting circular cross-section of the cylinder is subtracted from it. The width of the cylinder's foundation plays a crucial role, significantly influencing the overall structural stability.

In contrast, the concrete volume in the torus foundation is calculated using numerical methods. The base is divided into a set of n cylinder-shaped rings, each with a thickness equal to $\frac{\text{base width}}{n}$. The

height of each cylinder corresponds to the point where the base intersects with the torus ring. The volume of each cylinder is computed, and their summation yields the volume of the torus foundation. This approach proves to be both precise and reliable when $n \geq 100$.

The process described in Figure 4.10 was implemented to determine the dimensions of the foundation. The results are portrayed in Figure 4.11. The CIV-ratio reveals an observable trend: it increases with higher internal volumes and lower values of slenderness. Additionally, the torus consistently exhibits a lower CIV-ratio than the cylinder when their slenderness values are identical.

Notably, the contribution of the foundation to the CIV-ratio is minimal, with the highest value observed in this graph being an order of magnitude smaller than the values obtained in the reservoir design (as seen in Figure 4.4).

To visually convey the foundation widths corresponding to the CIV-ratio results, Figure 4.12 is presented. This figure illustrates the extreme widths, both high and low, for the cylinder and torus. These values are derived from Figure 4.11, where they are marked with a transparent square.

The wall thicknesses displayed in this figure were determined through the earlier established procedure. It is worth noting that the wall thickness for the torus with $\frac{b}{a} = 4$ (Figure 4.12c) is noticeably higher than that of the other configurations.

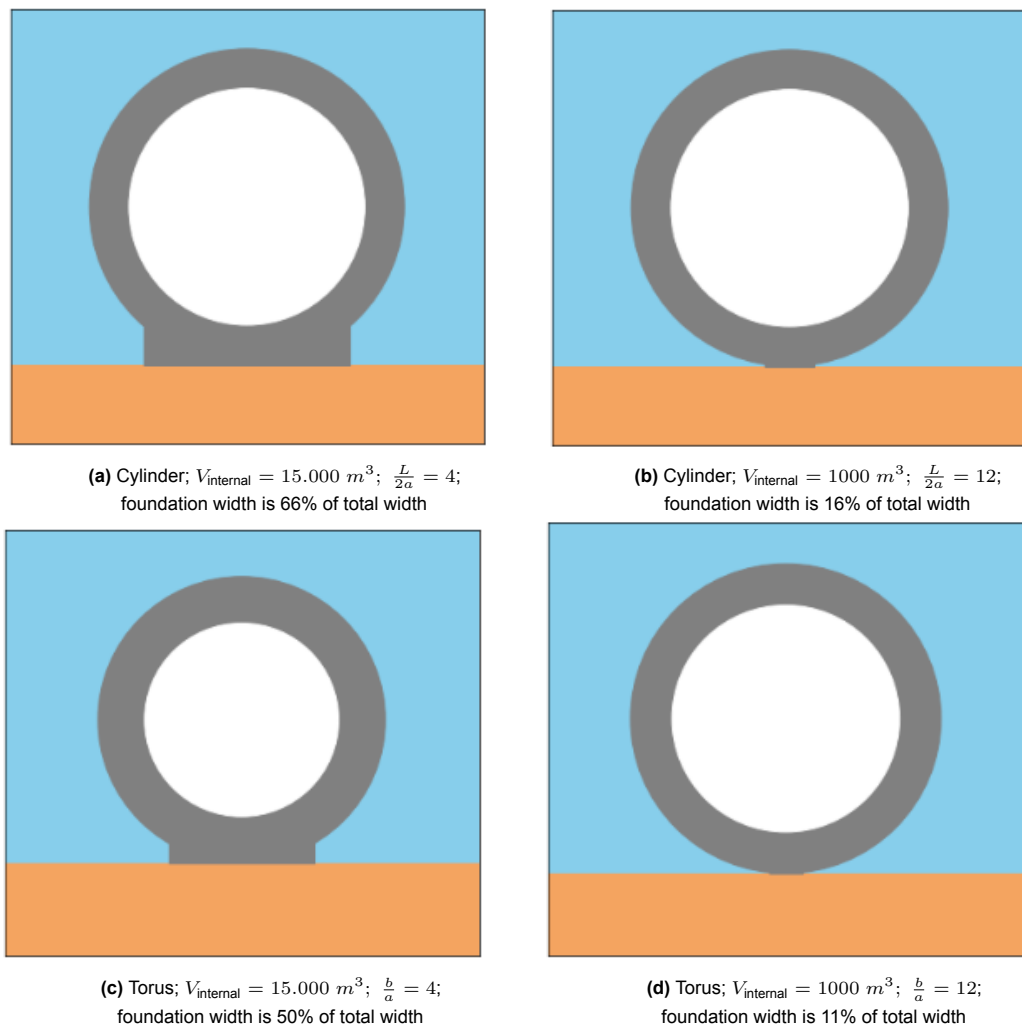


Figure 4.12: Cylinder and torus cross-section visualisations

Furthermore, the low foundations widths observed in Figure 4.12b and Figure 4.12d suggest that the design could potentially eliminate the need for a foundation. In such cases, the structure could be

placed directly on the seabed. However, for the cylinder, this raises concerns about its stability. In the absence of a level surface on the ground, the structure might be susceptible to rolling over.

4.2.3. CIV-ratio comparison in foundation design

The methodologies outlined in Sections 4.2.1 and 4.2.2 were employed to determine the concrete volumes necessary for the construction of foundations for both spherical, cylindrical and toroidal structures. These volumes were subsequently divided by the internal volume of the respective structures, resulting in the CIV-ratio.

A comparison of the results presented in Figure 4.9 and Figure 4.11 reveals a noteworthy discrepancy between the CIV-ratios in the foundation design for the spherical structure and those for the cylindrical and toroidal structures. Specifically, the CIV-ratio for the sphere is approximately an order of magnitude larger than that for the cylindrical and torus foundations. This observation is important, as it influences the evaluation of the sphere's suitability when compared to the cylindrical and toroidal alternatives.

It is worth noting that the CIV-ratios display substantial variation across different internal volumes in all three cases. This variation can be attributed to the increasing dimensions of the structures as the internal volume increases. A larger internal volume necessitates a greater width and height for each shape. As these structures become wider and taller, the dimensions of the foundation also grow in size.

In the case of the spherical structure, the increase in reservoir dimensions leads to a higher overall weight and subsequently results in a greater line-load under the pedestal. This, in turn, induces an increase in the negative bending moment experienced by the foundation plate, necessitating a corresponding increase in thickness.

Similarly, for the cylindrical and torus-shaped structures, increased dimensions result in a heavier structure, thereby elevating the load exerted on the soil. To maintain a constant stress level on the soil, a wider foundation is required. Consequently, the augmentation in the volume of concrete necessary for the foundation design is primarily attributed to the expansion in the foundation's width.

These findings underscore the complex interplay between internal volume, structural dimensions, and foundation design parameters, further emphasizing the importance of evaluating these factors when making design choices.

4.3. Reservoir and foundation design combination

The figures showcased in Sections 4.1 and 4.2 present results pertaining to the CIV-ratios for the construction of both the reservoir and foundation, encompassing all three geometric shapes. These findings have been consolidated to generate Figure 4.13. In this graph, the data for the spherical configuration is depicted on the lower x-axis, and it varies in response to changes in internal volume, exclusively influenced by the scaled foundation design of the sphere.

On the upper x-axis, one can observe the data for both the cylinder and torus configurations, displaying variations in response to changes in slenderness. It is worth noting that the CIV-ratio for the cylinder and torus shows marginal fluctuations as internal volume varies, though these differences are of minor significance. This observation is further supported when closely examining Figure 4.11. However, this is not entirely the case for cylinders with a slenderness value of approximately 4. Nonetheless, as discussed in Section 4.1.4, such low slenderness values are not considered relevant. Therefore, the slight discrepancy in the contribution of the foundation to the total CIV ratio for these lower slenderness values is deemed insignificant. Consequently, for both cylinders and tori, the internal volume was maintained constant at 10.000 m³.

It becomes apparent that, when considering the foundation design, the CIV-ratio of the sphere tends to converge with that of the cylinder and torus. Nevertheless, a noticeable gap remains, especially evident at lower internal volumes of the sphere, where the foundation's contribution to the CIV-ratio remains minimal.

In summary, the following conclusions can be drawn from the analyses in this Chapter:

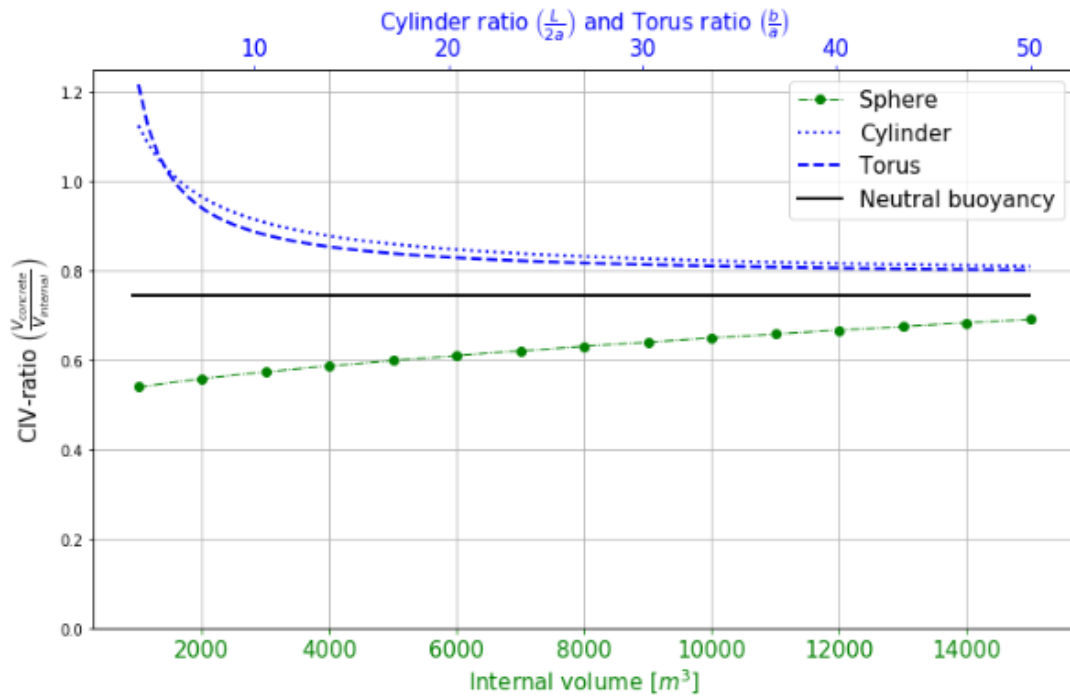


Figure 4.13: CIV-ratios of reservoir and foundation design combined; at $d = 1000$ m and $f_{cd} = 40$ MPa

- The CIV-ratio for both the cylinder and torus decreases with an increase in slenderness.
- The CIV-ratio of the sphere's reservoir is 37% lower than that of slender cylinders and tori.
- The CIV-ratio of the sphere's foundation is a factor 10 higher than than of the cylinder and torus
- The CIV-ratio of the sphere exhibits variations with changing internal volume, while for the cylinder and torus, this influence is negligible.

5

Construction and implementation of cylindrical design

This chapter is dedicated to formulating construction methods and considering implementation aspects for the cylindrical designs. While construction methodologies have been established for the spherical design, the techniques for the cylindrical configurations remain undetermined. The level of detail attained in the construction methods for the spherical reservoir is not expected to be exceeded in the development of construction methods for the cylindrical design. Consequently, the construction techniques for the spherical design are not covered in this Chapter. It is essential to note, however, that the existing plans for constructing the spherical design may not be fully matured. Nevertheless, the level of detail currently achieved in those plans will not be achieved for the cylinder in this Thesis work.

It became apparent that the toroidal design is not suitable as a reservoir shape, as its dimensions become too large to facilitate a smooth construction process. Further elaboration on this can be found in Section 5.1.

The construction methods discussed in this Chapter have been devised with a focus on internal volume, repetitiveness and complexity.

Internal volume

As detailed in Section 2.3, each reservoir should possess significant internal volume. Opting for a single large reservoir with the same internal volume is preferred over multiple smaller reservoirs. However, the construction process serves as a limiting factor in maximizing internal volume.

Repetitiveness

The second criterion involves the repetitiveness of the construction methodology. As discussed in Section 2.2, achieving the required total internal volume involves the construction of multiple units. Therefore, an efficient construction process is essential to reduce time and costs. Thus, construction methods should prioritize construction time and material reusability.

Complexity

As discussed in Section 1.1 and Section 2.9.3, the intricate challenges faced in constructing the spherical reservoir led to the motivation for this thesis project. The existing plans for the spherical reservoir are complex, involving partially or entirely new methods, significant time consumption, and heavy lifting. Noteworthy construction methods discussed in this context include:

- Constructing and connecting two hemispheres (MIT method)
- 3D-printing formwork and casting (RCAM method)
- Air pressured formwork by HTS

Considering that the elevated CIV-ratios of the cylinder and torus are accepted based on the assumption that the construction method is significantly simpler, it is imperative to avoid unnecessary complexities in the construction process development.

Chapter outline

To gain an understanding of the relevant dimensions for the cylinder and torus designs, an overview is provided in Section 5.1. It concludes that, for the torus, maximizing internal volume conflicts with construction location flexibility, ruling it out as an option. For the cylinder, a two-step method is devised to select the most suitable construction approach.

5.1. Dimensions of cylindrical and toroidal designs

This section aims to provide insights into the dimensions of the proposed structures, considering various slenderness values. As discussed in Section 4.2, the slenderness of the reservoirs plays a crucial role in the CIV-ratio, with higher slenderness values showing more favorable outcomes.

The dimensions in this Section are presented for slenderness values of 12, 16, and 20, deviating from those in most plots in Chapter 4, where values of 4, 8, and 12 were utilized. While no final decision on the ultimately used slenderness value has been made yet, it was shown in Section 4.2 that more slender reservoirs have a lower CIV-ratio. Hence, higher slenderness values become more relevant in this Section.

5.1.1. Cylinder dimensions

The dimensions of the cylinder are intricately linked to its internal volume and slenderness. Following the methodology outlined in Chapter 4, the required wall thickness (t) is calculated. The caps of the cylinder are designed as flat circular slabs with a thickness twice that of the shell. The overall length of the cylinder is determined by the length of the tube, augmented by four times the shell thickness. For a cross-sectional sketch, refer to Section 3.2.2.

Figure 5.1 showcases the external dimensions of the cylinder for various internal volumes and slenderness values. Notably, as internal volumes increase, the dimensions become substantial, resulting in elongated structures for higher slenderness values and relatively taller and wider structures for lower slenderness values.

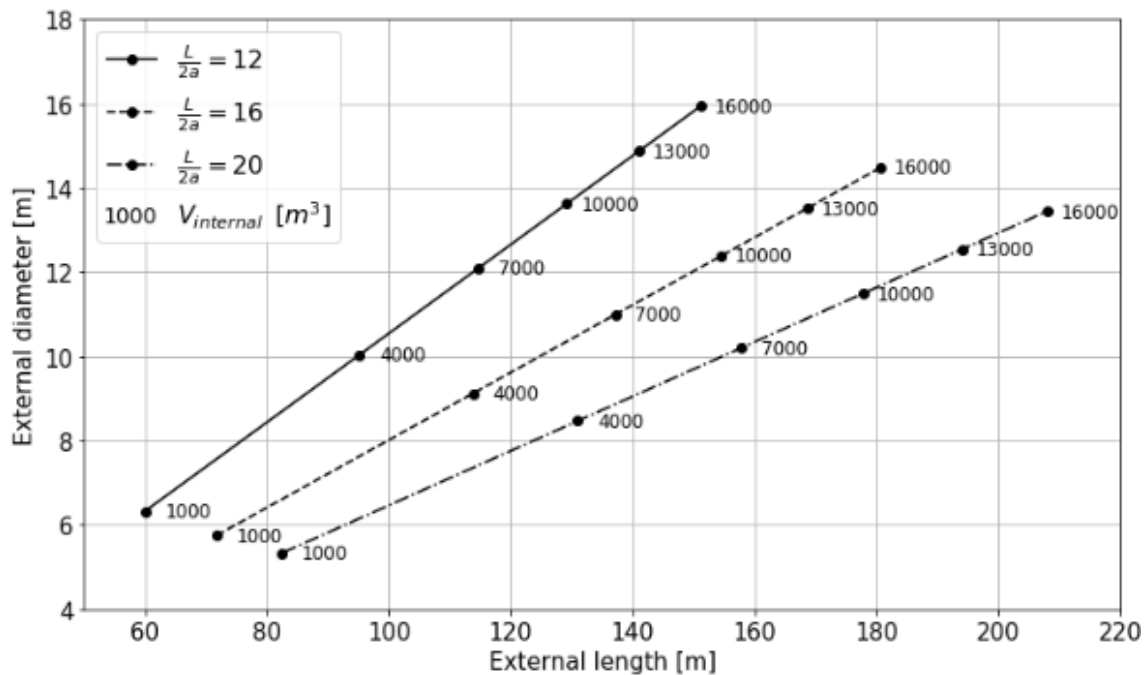


Figure 5.1: External cylinder dimensions for various internal volumes and slenderness values; at $d = 1000$ m and $f_{cd} = 40$ MPa

5.1.2. Torus dimensions

In the case of the torus, relevant parameters include the internal minor radius (a) and major radius (b). The wall thickness is determined using the algorithm outlined in Section 4.2. Refer to Section 3.2.3 for a cross-sectional sketch.

Figure 5.2 provides insights into torus dimensions for different internal volumes and slenderness values. Even at low internal volumes, the dimensions are substantial, considering the major radius of the torus present in 360° . The structure appears both long and wide.

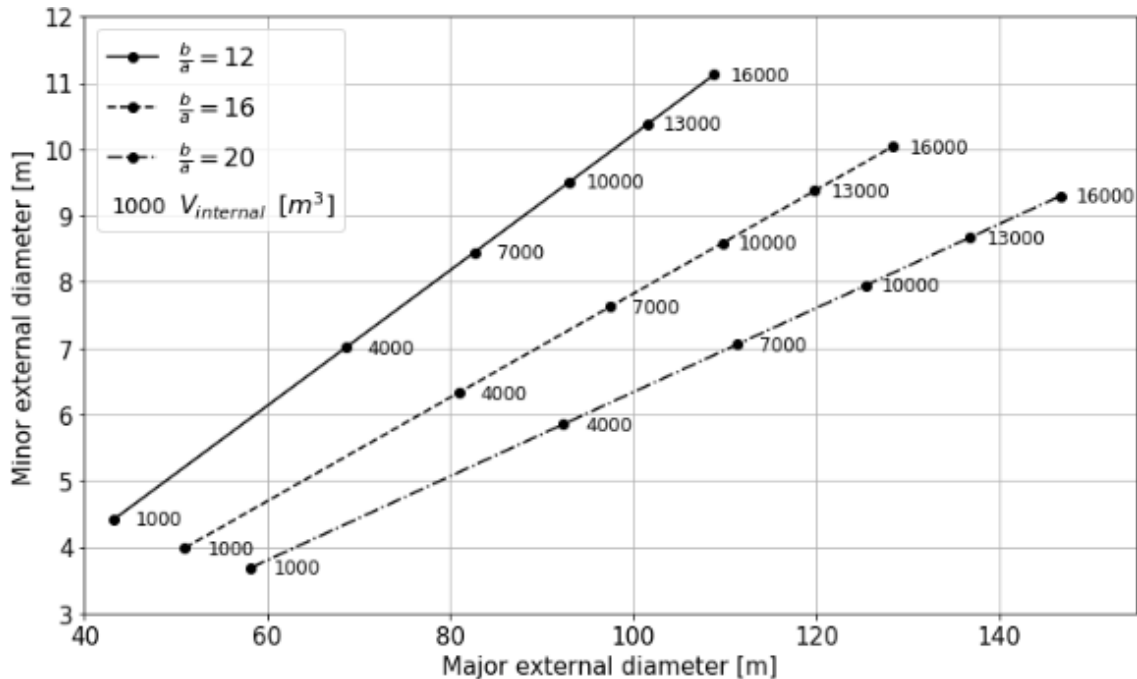


Figure 5.2: External torus dimensions for various internal volumes and slenderness values; at $d = 1000$ m and $f_{cd} = 40$ MPa

5.1.3. Evaluation of dimensional suitability for construction locations

As detailed in Appendix G, potential construction locations for large concrete projects are classified into on-land factories, dry docks, fjords, and open sea. For the MPHES system, both constructing the entire structure and assembling parts at open sea are deemed impractical due to the complexities of stabilization operations and the high costs associated with offshore construction vessels. Without specifying a construction method, it is inferred that the structure should be transported to the final installation location as a whole. Consequently, construction of the reservoir is narrowed down to options on land, in a dry dock, or in a fjord.

Analysis of Figures 5.1 and 5.2 reveals that, for the same internal volume, the dimensions of the cylinder are mainly substantial in length, whereas the torus's dimensions are significant in both length and width. With a slenderness value of 16 and an internal volume of $10,000$ m^3 , a cylinder has a length of approximately 155 meters and a diameter of about 12 meters. In comparison, a torus with the same internal volume and slenderness has a major diameter of roughly 110 meters and a diameter of about 8,5 meters, with dimensions increasing for larger internal volumes. As discussed in Section 2.3, maximizing internal volume is crucial, with the construction process being the limiting factor.

The cylinder, resembling a large ship due to its long and narrow shape, can be constructed on land and launched similarly to a ship, or it can be built in a dry dock. Larger dry docks can accommodate its construction, with the allowed draught being an essential consideration.

Conversely, the torus, with its non-ship-like shape and dimensions, cannot be launched like a ship. Additionally, its size prohibits construction in a standard dry dock, as most docks cannot accommodate both the length and width of the structure. Consequently, the torus should be constructed in multiple

elements that can be assembled in a fjord. However, as outlined in Appendix G.3, fjords are limited to polar regions, making locations like the Mediterranean Sea impractical.

As the system aims to be adaptable and not case-specific, with minimal limitations on its implementation, the torus will not be further investigated due to the challenges associated with constructing a reservoir of high internal volume combined with the need for flexibility in location selection. While it is not excluded that the torus might be a viable option at installation locations near a fjord, it is ruled out for the rest of this research.

5.2. Exploration construction methods cylindrical design

In this section, five construction methods for the cylinder are presented and evaluated. Each method's execution and features are explained, and their suitability is assessed using a trade-off matrix. The focus is on selecting the two most promising methods for further exploration.

As highlighted in Section 3.1, the need for reinforcement is yet to be addressed. With the cylinder's substantial length, bending moments are anticipated along its structure, especially during transport or immersion, where it is hung on cables, or at the seabed with potential uneven surfaces. These moments result in tensile stresses, necessitating the incorporation of longitudinal reinforcement. Hence, the evaluation of proposed construction methods includes an assessment of their suitability for implementing reinforcement.

In Section 5.1.3, it was established that the cylinder can be constructed on land or in a dry dock. Post-construction, the structure must be transferred to water for shipping and towing to its final location. Launch, in this context, denotes the transfer of the structure from the construction location into water, involving either a process akin to ship launch or the flooding of a dry dock.

5.2.1. Cast-in-place

In the traditional cast-in-place method, a monolithic cylinder is formed by continuously pouring concrete between inner and outer formwork. To accommodate the weight of the structure, construction either begins on a launching system or in a dry dock. The process involves:

1. Placement of formwork outer shell
2. Placement of reinforcement
3. Placement of formwork inner shell
4. Casting of concrete
5. Removal of formwork
6. Launch of structure

The suitability of cast-in-place for a structure of this magnitude is validated by notable examples such as the Shanghai Tower, where 60,000 m³ of concrete was continuously poured, without any post-cooling measures [41]. While facilitating the incorporation of reinforcement and ensuring a seamless structure, challenges arise from the substantial use of formwork, possibly contributing to over 50% of total construction costs [42]. Retrieving inner formwork poses difficulties, requiring careful consideration of leaving it behind or removing it through a hole in the cylinder, subsequently demanding concrete coverage. Alternatively, inflatable formwork allows for simpler retrieval. However, at the intended scale, it has not yet been applied [43].

5.2.2. Precast elements

The precast elements approach involves constructing the cylinder using multiple precast ring-shaped elements produced in a controlled factory environment. Assembly can take place in the same factory on a launching system or in an adjacent dry dock. The production process includes:

1. Production of reinforced concrete elements in factory
2. Lifting elements to assembly location
3. Connection of elements

4. Launch of structure

Prefabrication ensures high concrete quality and facilitates the integration of reinforcement. This method requires two distinct molds: a standard mold for constructing the mid-section rings and a custom mold for the caps. The length of the elements is yet to be determined. Some of the world's largest precast elements are currently under construction at the Fehmarnbelt tunnel project, where tunnel elements of over 200 meters in length and 40 meters in width are built [44].

Similar to the first phase of concrete silo construction, production of the elements can be performed upright, ensuring a flat bottom that can rest on the ground without requiring auxiliary scaffolding [45]. Alternatively, construction of the ring-shaped elements can be done horizontally.

Closing the seams is a critical aspect, as the structure must be watertight [31].

5.2.3. Horizontal jump-forming

Horizontal jump-forming is a process where a moving formwork constructs the tubular mid-section of the cylinder horizontally [46]. The process ensures monolithic construction of the mid-section, while the caps are installed separately. The production process involves:

1. Placement of formwork outer shell
2. Placement of reinforcement
3. Placement of formwork inner shell
4. Casting of concrete
5. Continue launching girder and repeat steps 1 to 4
6. Prefab production and connection of cap elements
7. Launch of structure

This challenging technique, detailed in Appendix F.3, has been successfully executed, resulting in a substantial, monolithic mid-section [47]. To facilitate the launch of the structure, construction should take place on a launching system or in a dry dock.

Special attention is needed for the connection between the mid-section and the caps.

5.2.4. Vertical slip-forming

Applied in high-rise core construction, vertical slip-forming involves continuous vertical concrete pouring as the formwork moves. The process includes:

1. Placement of formwork outer shell
2. Placement of reinforcement
3. Placement of formwork inner shell
4. Casting of concrete
5. Jack up formwork and repeat steps 1 to 4
6. Rotation of upright mid-section to flat position
7. Prefab production and connection of cap elements
8. Launch of structure

Unlike horizontal slip-forming, this configuration does not require immediate stiffness of the concrete, as there is no span [48].

Rotating the monolithic mid-section from upright to flat presents challenges, such as toe-crushing, stabilization issues and bending [49, 50]. This rotational movement restricts the maximum length of the mid-section. An alternative approach would involve constructing and rotating the structure in water. However, since the draught of the cylinder is directly related to its length, this method necessitates a considerable water depth, often reaching many tens of meters. As previously discussed, the requirement for such depths significantly restricts potential construction locations worldwide.

Special attention is needed for the connection between the mid-section and the caps.

5.2.5. Hybrid 3DCP + cast-in-place

This innovative technique involves 3D concrete printing of formwork and casting concrete horizontally, with construction in a dry dock or on a launching system [29]. The steps are:

1. Production and placement of prefab bottom element
2. Placement of reinforcement
3. 3D printing of outer formwork
4. 3D printing of inner formwork
5. Pouring of concrete
6. Repeat steps 3 to 5 until required height of cross-section is met
7. Production and connection of prefab top element
8. Launch of structure

By integrating 3DCP formwork into the final structure, the need for separate formwork is eliminated. However, as outlined in Appendix F.5, the 45° maximum overhang angle of the printed material poses challenges [51]. Consequently, the bottom and top of the structure must be prefab elements, with their dimensions limiting the scalability of this method. Additionally, attention is required for the seam between the prefab element and the 3DCP body.

5.2.6. Trade-off

To evaluate the described construction methods, a trade-off matrix is utilized, assigning scores as follows:

- ++ Very good
- + Sufficient
- Poor
- Bad

The methods undergo assessment based on a comprehensive evaluation, considering the critical factors of complexity, construction time, and scalability in order to identify the most promising construction methods for the next phase of exploration. Complexity is crucial, as the construction method should be simpler than those used for the sphere. Decreasing construction time not only reduces costs but also enhances the feasibility of the project. Given the goal of maximizing reservoir size, scalability of the construction method is equally significant.

	Cast-in-place	Precast elements	Horizontal Jump-forming	Vertical slip-forming	Hybrid 3DCP + cast-in-place
Complexity	++	+	+	+	-
Construction time	+	++	+	+	+
Scalability	-	++	++	--	--

Table 5.1: Trade-off exploration cylinder construction methods

The trade-off matrix in Table 5.1 guides the selection of the precast elements approach and the horizontal jump-forming method for further in-depth analysis. The remaining methods will not be considered further.

5.3. In-depth analysis construction methods cylindrical design

This section provides a more detailed analysis of the two selected construction methods for the cylinder: precast elements and horizontal jump-forming. Each method's construction process is visually depicted, thoroughly discussed, and associated risks are identified.

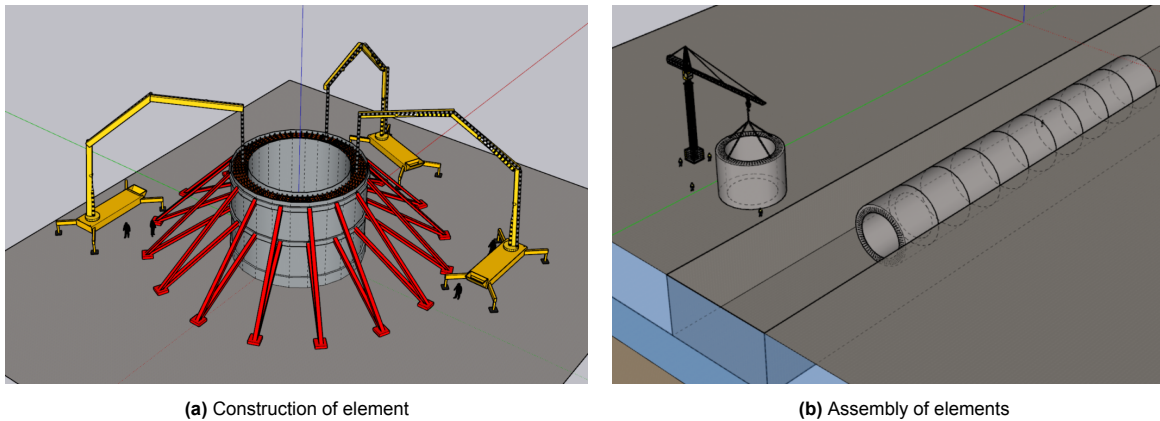
To illustrate the analysis, a cylinder is considered with an internal volume of 10.000 m^3 and a slenderness ratio of $\frac{L}{2a} = 12$. The properties of this illustrative cylinder are presented in Table 5.2.

Parameter	Value	Unit
Internal volume	9.000	m^3
Volume of concrete	7.958	m^3
Slenderness	12	[-]
Internal radius	4,92	m
Wall thickness	1,65	m
External length	124,8	m
Cross-sectional weight	$153,04 \cdot 10^3$	kg m^{-1}

Table 5.2: Dimensions of illustrative cylinder

5.3.1. Precast elements

This method involves precasting concrete-reinforced elements in a controlled factory environment. The method is graphically displayed in Figure 5.3. Notably, the base is seamlessly integrated into the elements, allowing for the simultaneous casting of the foundation and reservoir. However, this integration is not illustrated in Figure 5.3.



(a) Construction of element

(b) Assembly of elements

Figure 5.3: Precast element method

Element size

Determining the appropriate element size in this method is a multifaceted aspect of the design process. The mid-section comprises multiple standard elements, with two special elements needed for constructing the caps. Given that a single standard element represents the entire cross-section of the cylinder, its length becomes the variable factor.

As elements become longer, their weight increases. As indicated in Table 5.2, the weight of each element is 153 tonnes per meter. Although these weights can be lifted, the associated crane rental costs escalate significantly with increasing length.

During the assembly process, ensuring watertight joints is critical. Joints represent the most vulnerable part of the entire structure, emphasizing the need to minimize their number. One strategy to achieve this is by increasing the length of the elements.

Element connection

As highlighted previously, ensuring a secure element connection is a critical aspect of the construction method. Achieving watertightness is paramount, adding complexity to the connection process. Rubber joints, commonly employed in immersed tunnels, have demonstrated efficacy at depths below 50 meters [52]. However, the suitability of rubber joints in the context of extreme depths, as in this proposed

structure, remains debatable. It is worth noting that rubber joints often introduce ductility and accommodate significant displacements, which may not be essential for the intended characteristics of the cylinder.

Considering this, an alternative approach involves the use of wet joints. However, the primary challenge lies in preserving watertightness. The probability of watertightness failure is directly tied to the number of joints, highlighting the imperative need to minimize their occurrence in the structure.

5.3.2. Horizontal jump-forming

This semi-continuous construction method involves the use of a launching girder, supporting the inner formwork. The process is graphically displayed in Figure 5.4. Notably, the foundation is directly integrated into the formwork.

Launching girder

The girder is supported by already hardened concrete on one side and by the ground on the other side. The length of the girder dictates the length of each segment, a critical aspect determining the number of cold joints and construction time.

Concrete shrinkage is a crucial consideration, with thermal shrinkage being particularly relevant due to the substantial thickness of the elements. The exothermic reaction during the concrete hardening process causes expansion, followed by shrinkage upon cooling. This can lead to high internal stresses, posing a risk of cracking [53]. This is especially relevant at the interface between fresh and existing concrete. Reinforcement helps resist the internal stresses caused by shrinkage. At the free end, deformation is not restrained, so shrinkage is less of an issue.

As the length of the segment increases, it not only leads to a rise in the amount of costly formwork but also extends the span and increases the weight that the launching girder must support. The substantial weight of the cylinder's thick wall places a considerable load on the launching girder, suggesting potential limitations on its maximum length.

Cap connection

The construction of the cylinder's ends deviates from the semi-continuous process used for the mid-section. Consequently, a dedicated connection method needs to be developed. Potential options include the use of rubber seals or wet joints. Notably, the caps of the cylinder experience compression in the longitudinal direction, enhancing the feasibility of achieving a watertight connection.

The connection of the caps and the construction of the last element are critical stages in the construction process. The envisioned approach begins with precasting the caps of the cylinder, initiating the construction process. Subsequently, production cycles start by connecting the caps to the first element. Progress then occurs from both ends, with the production cycles moving towards the center of the cylinder. As the two emerging tubes converge in the middle, the final ring element is constructed. This methodology effectively separates the complex task of connecting the cap to the cylinder from the intricate process of pouring the last element, thereby streamlining the overall construction process. However, a drawback of this method is the requirement for two launching girders, one of which needs to be removed from inside the cylinder upon completion of construction.

5.3.3. Watertightness

Both of the remaining construction methods, precast elements, and horizontal jump-forming, require connections in the design since both methods do not allow for a fully monolithic structure. Two types of connections are involved in these designs. One pertains to connecting an existing concrete member with a freshly poured element, commonly known as a cold joint. The other involves connecting two precast concrete elements, termed the 'precast connection.' More background information on joint types is available in Appendix H.

Cold joints are a key point of attention regarding watertightness. Enhancing the casting surface's roughness can improve the concrete-concrete bond, and the continuation of longitudinal reinforcement can be achieved using reinforcement couplers. Additional measures, such as waterstops, can also be implemented. However, products like waterstops have not been used at these depths, and the watertightness of a cold joint remains uncertain [54].

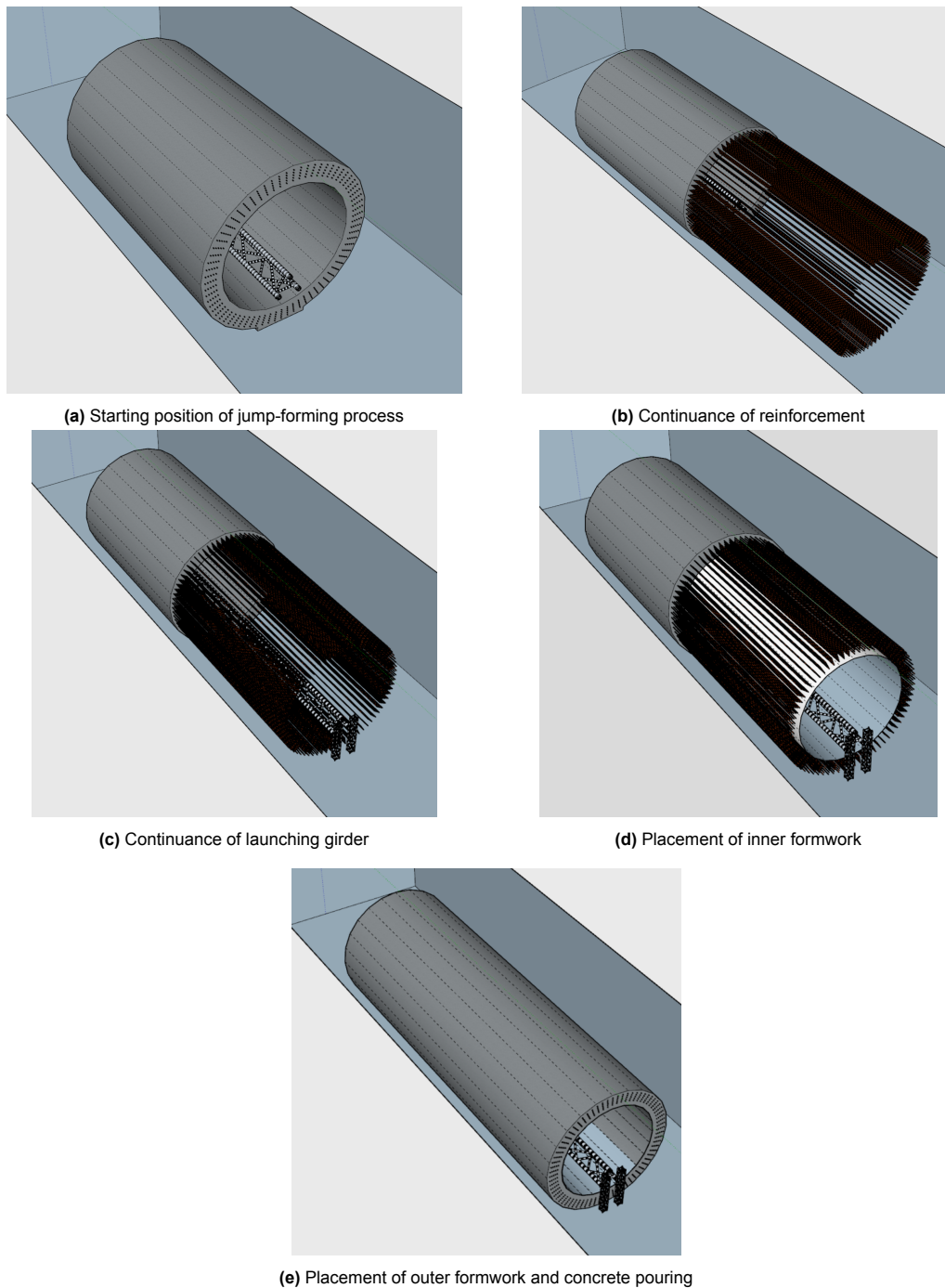


Figure 5.4: Construction cycle of horizontal jump-forming method

Precast connections can be implemented using either rubber joints or wet joints. The only rubber joint capable of resisting the hydraulic pressure at the intended installation depth is a compression seal. Ensuring watertightness with such a seal requires a contact pressure equivalent to 2.5 times the hydraulic pressure, maintained consistently around the connection's circumference [55]. When a wet joint is used, any longitudinal reinforcement should extend through the joint. Additionally, the freshly poured concrete should bond to the precast elements, essentially creating a cold joint on either side of the freshly poured concrete.

The proposed connections are all fixed. Generally, opting for a more flexible connection, such as a

Gina gasket or other rubber profile, typically results in reduced watertightness [56]. As elaborated in section 3.5, no expansions or contractions of the structure due to changes in temperature should be anticipated, given the intended installation depth. Consequently, flexibility might only be deemed necessary to accommodate unequal settlements [56].

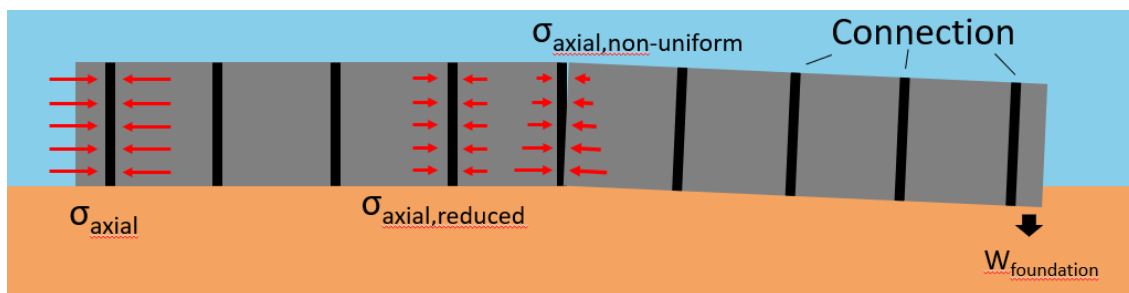


Figure 5.5: Cylinder possible axial stresses at connections

In Figure 5.5, three distinct axial stress situations in the cylinder are illustrated. From left to right, the first scenario shows axial stress induced by the hydraulic pressure. In the second scenario, there is a potentially reduced axial stress near the middle of the cylinder, as some of the axial stress might be transferred to the foundation. Lastly, the third scenario depicts a potential foundation settlement, resulting in a bending moment that causes non-uniform axial stress in the cylinder.

Both the potentially reduced axial stress and the non-uniform axial stress situation are unfavorable for the functioning of a rubber seal. The required contact pressure might not be guaranteed, making rubber seals unfeasible as connecting elements in the middle of the cylinder. However, rubber seals might be feasible at the ends of the cylinder to create the connection between the cylinder and the cap.

These challenges become less prominent when employing a wet joint for connecting precast elements, as its performance is not directly dependent on contact pressure. In fact, there is no contact pressure involved, as the wet joint seamlessly integrates both concrete elements together. However, the ability of a wet joint to retain water is highly influenced by the concrete-concrete bonding, present on both sides of the joint. A wet joint has two concrete-concrete bonds, whereas a cold joint only has one. Therefore, the wet joint is considered a higher risk for compromising the watertightness requirement. To avoid the use of wet joints or rubber seals, the horizontal jump-forming method can be applied.

Apart from connections in the structure, watertightness can be influenced by cracks in the concrete. The maximum crack width and its path along the thickness of the wall are crucial. These effects can be reduced by applying enough reinforcement. While this issue may arise at wet joints or cold joints too, it is not further elaborated.

Certainly, the watertightness of the structure is directly affected by the number of connections present within it. A lower quantity of connections enhances watertightness. In the precast element method, the number of connections is tied to the length of the elements, constrained by the maximum lifting capacity of the crane. With a weight of 154 tonnes per meter, as indicated in Table 5.2, the elements quickly become exceedingly heavy. On the other hand, in the horizontal jump-forming method, the length of the elements is restricted by the maximum extension length of the launching girder. As this girder must support the weight of the wet concrete, it bears a substantial load. While a larger crane can be rented, and a more robust truss structure for the launching girder can be implemented, the limiting factors in both options appear to be more financial than structural in nature. It is assumed, without further elaboration, that increasing the dimensions of the launching girder is comparatively inexpensive in contrast to the heightened rental expenses associated with higher lifting capacities. No additional attention is spent on this aspect.

A summary of the described connection elements and their applicability to the precast element method and the horizontal jump-forming method is presented in Table 5.3. Cold joints are deemed more watertight than wet joints. As a result, the precast element method is concluded to have a lower level of watertightness compared to the horizontal jump-forming method.

	Precast elements	Horizontal jump-forming
Precast connections	At mid-section and caps	-
Potential type of mid-connections	Wet joints	Cold joints
Number of mid-connections	Dependent on max. lifting capacity of crane	Dependent on max. length of launching girder
Potential type of cap connections	Rubber seals or wet joints	Rubber seals or wet joints
Water tightness	Complex	Feasible

Table 5.3: Concrete connection types of cylinder

5.3.4. Evaluation

The summarized features of both construction methods are presented in Table 5.4. The conclusion drawn is that the horizontal jump-forming method holds an advantage over precast elements, particularly in terms of achievable watertightness. This aspect takes precedence as it significantly impacts the overall performance of the system.

	Precast elements	Horizontal jump-forming
Construction location	Factory and dry dock	Dry dock
Operations	Lifting elements in dry dock	Continuance of launching girder
Water tightness	Complex	Feasible

Table 5.4: Summary features precast element method and horizontal jump-forming method

5.4. Implementation aspects cylindrical design

This section addresses the transportation and installation methods for the cylinder. A specific method is formulated, and the principal loads acting on the structure during transport and immersion are identified and quantified.

5.4.1. Transport

Due to its oblong shape, the launching methods for the cylindrical reservoir are akin to those used for ships. Common ship launching techniques include longitudinal or side-way slide launching and floating-out launching. In slide launching, the ship is slid down a slope, utilizing gravity to initiate motion. However, during the initial contact with the water, the ship encounters resistance, leading to deceleration. This approach may be deemed unfavorable for the cylinder, as the dynamic impact of the water could impose a significant load on the structure [57].

Conversely, floating-out launching is a more gradual and controlled process. In this method, the dry dock where the ship (or, in this case, the cylinder structure) is constructed is flooded, causing the structure to become immersed. Due to the gravitational load on the cylinder exceeding its buoyant force, the cylinder will remain immersed throughout the process.

Consequently, the cylinder must be lifted by pontoons and then towed to its final location, a method commonly utilized in the construction of submerged floating tunnels [58, 59]. A graphical representation of this process is provided in Figure 5.6. The catamaran-like pontoons bear the cylinder, and towing boats facilitate its transportation. The base of the cylinder contributes to stabilizing it during transport. In this scenario, the cylinder is supported by two pontoons, a number that can be increased if necessary to reduce the load per cable and the bending moment.

Alternatively, employing a gradual skidding technique imposes minimal stresses on the structure. This method involves the structure being incrementally moved from land into water utilizing reinforced rubber or steel cylinders as skidding beams, facilitated by the controlled lowering from cables [60]. Such an approach is well-established in the transportation of large objects, exemplified by the launching of the Pavilion Bridge in Zaragoza, Spain, where a 140-meter-long steel bridge was smoothly maneuvered into its installation position [61]. This skidding process necessitates the placement of the structure on designated skidding beams and still entails the utilization of pontoons for subsequent transport.

Although not further detailed herein, this method remains a viable alternative.

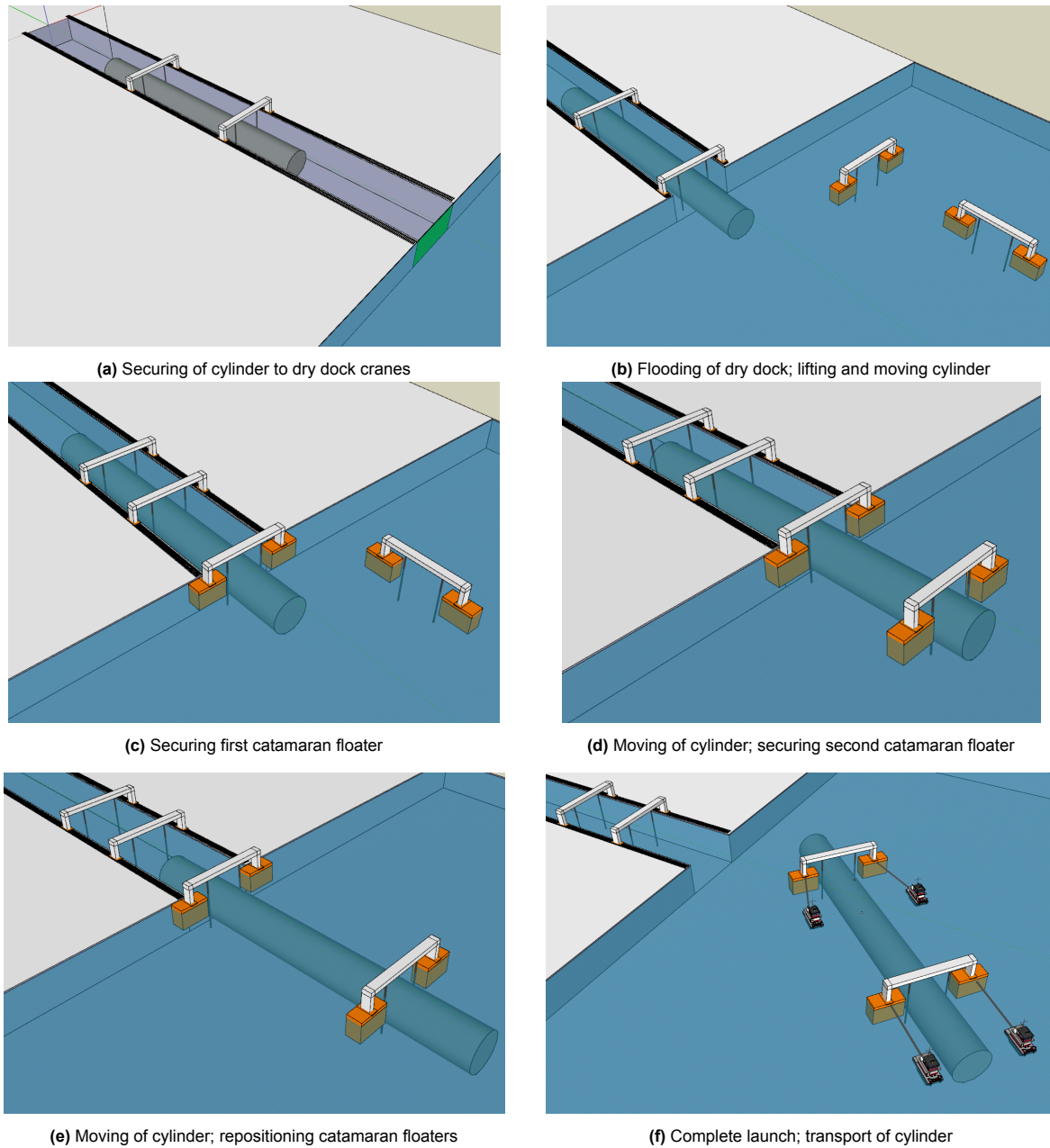


Figure 5.6: Launch and transport of cylinder

When lifting the cylinder, a bending moment is induced. The cylinder, supported by catamaran floaters, can be conceptualized as a 1D beam with two hinged supports. The distributed load q [kN/m] on this beam is equivalent to the cylinder's own weight in water. To minimize the bending moment, the supports are strategically placed at $\frac{L}{4}$ and $\frac{3L}{4}$, where L is the external length of the cylinder. Utilizing parameters from Table 5.2, the following simplification is made in the schematization.

$$\begin{aligned}
 q_d &= \gamma_d q_{\text{own weight in water}} \\
 &= \gamma_d \frac{(V_{\text{concrete}} (\rho_{\text{concrete}} - \rho_{\text{sw}}) - V_{\text{internal}} \rho_{\text{sw}}) g}{L_{\text{external}}} \\
 &= 3 \frac{(7.958 (2400 - 1025) - 9.000 \cdot 1025) 9,81}{124,8} \\
 &= 404.91 \text{ kN/m}
 \end{aligned}$$

It is important to note that this representation does not account for the flat caps, which are better modeled as point loads. This simplification is adopted with the understanding that in a subsequent design phase, as outlined in Section 6.1, the caps will be modeled as hemispheres. These hemispheres are significantly less massive and closely resemble the situation outlined below.

To account for dynamic loads induced by waves, a safety factor of $\gamma_d = 3$ is considered.

The distributed load is then translated into the mechanical scheme presented in Figure 5.7.

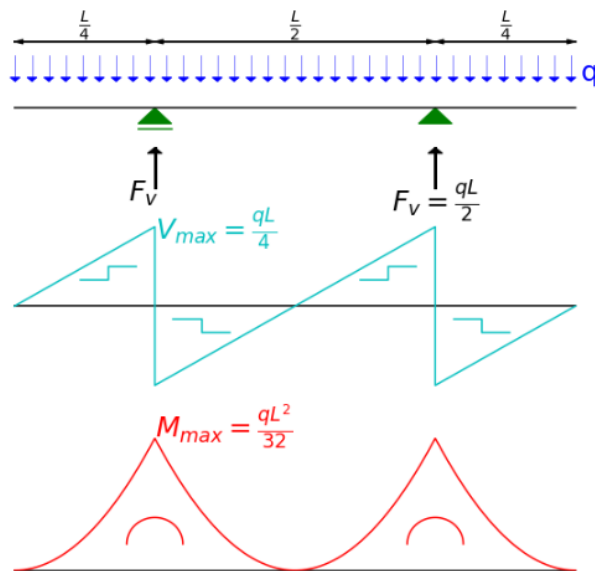


Figure 5.7: Mechanic scheme of cylinder hanging from floater

The maximum shear force and moment are:

$$V_{\max} = \frac{qL}{4} = \frac{404,91 \cdot 128,4}{4} = 12,63 \text{ MN}$$

$$M_{\max} = \frac{qL^2}{32} = \frac{404,91 \cdot 128,4^2}{32} = 196,08 \text{ MNm}$$

Assuming a 50% activity of the cross-section, the maximum shear stress is 0,43 MPa.

$$\begin{aligned}
 \sigma_{\text{shear}} &= \frac{V_{\max}}{\frac{1}{2} A_{\text{cross-section}}} \\
 &= \frac{12,63}{\frac{1}{2} \cdot \left((4,92 + 1,65)^2 - 4,92^2 \right)} \\
 &= 0,43 \text{ MPa}
 \end{aligned}$$

The section modulus W of the cylinder, neglecting the contribution of the base, is calculated as follows:

$$\begin{aligned} W &= \frac{\pi \left((a+t)^4 - a^4 \right)}{4(a+t)} \\ &= \frac{\pi \left((4,92 + 1,65)^4 - 4,92^4 \right)}{4(4,92 + 1,65)} \\ &= 152,69 \text{ m}^3 \end{aligned}$$

Consequently, the stress in the outermost fiber, induced by the bending moment, is equal to $\pm 1,29$ MPa. The concrete should be able to withstand this load, even under tension.

$$\pm \sigma_{\text{outermost fibre}} = \pm \frac{M}{w} = \pm \frac{197,08}{152,69} = \pm 1,29 \text{ MPa}$$

5.4.2. Immersion

Once the structure has been towed to its installation location, the next step is to lower it down to the seabed. Given the substantial depth of 1000 meters, the own weight of the cables will become a significant factor.

Assuming that the cylinder is lowered using four cables, each cable must bear $\frac{qL}{4} = 12.63$ MN of the cylinder's own weight. To meet this requirement, a cable with a design yield strength of $f_y = 1500$ MPa, a density of $\rho_{\text{steel}} = 8,000$ kg/m³, and a diameter of 15 cm is sufficient. This calculation is made with a material safety factor of $\gamma_c = 1.15$ and a static load factor of $\gamma = 1.2$ applied to account for the self-weight of the cable.

$$\begin{aligned} F_{\text{ed,cable}} &= \frac{qL}{4} + \gamma \rho_{\text{steel}} g A_{\text{cable}} \text{depth} \\ &= \frac{404,91 \cdot 128,4}{4} \cdot 10^{-3} + 1,2 \cdot 8000 \cdot 9,81 \cdot \pi \cdot 0,075^2 \cdot 1000 \cdot 10^{-6} \\ &= 14,30 \text{ MN} \end{aligned}$$

$$\begin{aligned} F_{\text{R,cable}} &= \frac{f_{yd} A_{\text{cable}}}{\gamma_c} \\ &= \frac{1500 \cdot \pi \cdot 0,075^2}{1,15} \\ &= 23,05 \text{ MN} \end{aligned}$$

$$U.C. = \frac{F_{\text{ed,cable}}}{F_{\text{R,cable}}} = \frac{14,30}{23,05} = 0,62$$

The influence of potential horizontal forces generated by the current is not taken into account in this analysis. However, it may be necessary to deploy a remote-operated vehicle to manage the cylinder and ensure a controlled installation [31].

5.4.3. Stability

As detailed in Section 4.2.2, the foundations do not necessitate significant widths to distribute the weight of the structure sufficiently to the soil. In some instances, it was suggested that the foundation width might be minimal or even eliminated. However, this consideration does not account for horizontal loads at the seabed.

Although the current at the seabed is low, it imposes a horizontal load on the structure. The impact of this load on the stability of the structure has not been verified. However, it may be necessary to implement additional measures, such as a wider base or a different base design, to ensure sufficient stability.

6

Optimization

The content of this Chapter is twofold. First, an attempt is made to improve the design of the cap of the cylinder. Secondly, it is verified to what extent the most important assumption of this thesis, uniform compressive stress in the wall of the reservoir, deviates from reality. These findings are then used to reestablish material usage.

6.1. Cap refinement cylindrical design

The flat cap design of the cylinder, as introduced in Section 3.2.2, is reevaluated in this section. Initially presented as a simplified version for early CIV-ratio determinations in Chapter 4, it deviates from an optimized design, potentially resulting in high concentrated stresses. Apart from significant bending moments at the plate's center, the abrupt disruption of curvature at the cylinder ends is expected to induce concentrated local stresses. To mitigate these effects, a smoother transition from the cylinder tube to its cap is considered.

In addition to the differences in curvature, stress concentrations in the connection between the cylinder tube and cap are expected as a result of an edge disturbance. In this context, the edge disturbance is a consequence of the difference in radial stiffness, k_{rad} , defined as the resistance of the member against radial deformation of the cross-section Δ_a , as illustrated in Figure 6.1.

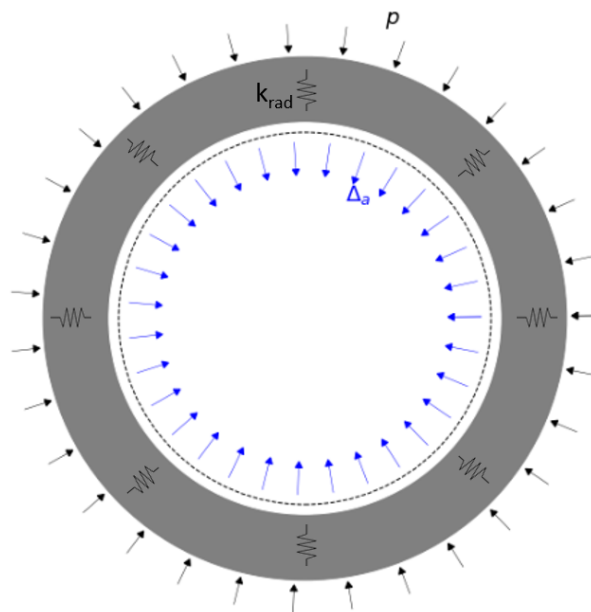


Figure 6.1: Radial stiffness, k_{rad} [N m^{-1}]

6.1.1. Reduction of the edge disturbance

As a thought experiment, the connection between a cylindrical tube section (on the left) and three different shapes (on the right) is considered, as illustrated in Figure 6.2. The tube-tube connection in Figure 6.2a is present in each cross-sectional cut of the monolithic cylinder tube. It is obvious that such a 'connection' does not result in an edge disturbance. Conversely, it is conceivable that the radial stiffness of the tube in Figure 6.2b is substantially lower than that of the flat plate it is connected with, causing an edge disturbance. This disturbance can lead to high bending moments and concentrated stresses at the connection.

It is hypothesized that there is a hemisphere-like cap design that allows for the minimization of edge disturbances at the connection interface between the cylinder tube and cap. Such a design, as presented in Figure 6.2c, has a radial stiffness that is approximately equal to that of the cylinder tube.

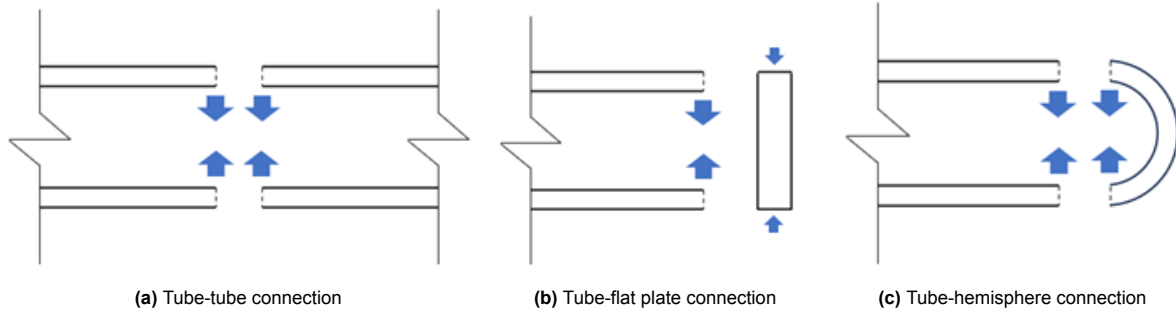


Figure 6.2: Alternative cap designs for cylinder can reduce or eliminate edge disturbances

Edge disturbance in boiler drums

In a cylindrical pressure vat with a hemispherical cap, an edge disturbance arises due to a discrepancy in radial stiffness. Consequently, a bending moment occurs, as illustrated in Figure 6.3. The magnitude of the bending moment and the tangential membrane force are determined by Equations 6.1 - 6.4 [62]. It is essential to note that these equations are applicable only to thin shells, where the thickness of the cylindrical shell is equal to the thickness of the hemispherical shell.

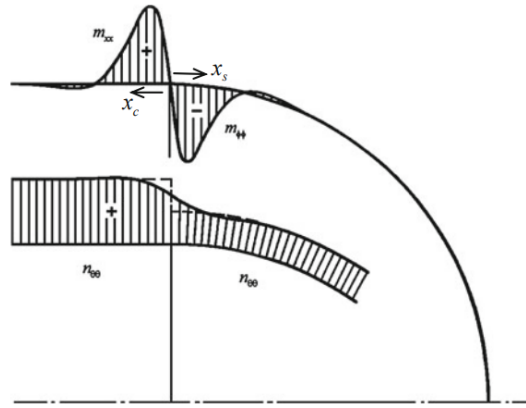


Figure 6.3: Bending moment and transition of tangential membrane force at cylinder-hemisphere connection [62]

$$m_{xx} = \frac{pl_i^2}{8\pi^2} \sin \frac{\pi x_c}{l_i} \exp \frac{-\pi x_c}{l_i} \quad (6.1)$$

$$m_{\phi\phi} = \frac{pl_i^2}{8\pi^2} \sin \frac{\pi x_s}{l_i} \exp \frac{-\pi x_s}{l_i} \quad (6.2)$$

$$n_{\theta\theta, \text{cylinder}} = pa \left(1 - \frac{1}{4} \exp \frac{-\pi x_c}{l_i} \cos \frac{\pi x_c}{l_i} \right) \quad (6.3)$$

$$n_{\theta\theta,\text{sphere}} = pa \left(\frac{1}{2} + \frac{1}{4} \exp \frac{-\pi x_s}{l_i} \cos \frac{\pi x_s}{l_i} \right) \quad (6.4)$$

6.1.2. Hemispherical cap design

A thin walled sphere and cylinder under constant pressure p are considered. The tangential strains of these shapes are calculated as follows:

$$\begin{aligned} \epsilon_{\text{sphere}} &= \frac{\sigma_{\text{sphere}}}{E_{\text{concrete}}} \\ &= \frac{n_{\text{sphere}}}{t_{\text{sphere}} E_{\text{concrete}}} \\ &= \frac{pa}{2t_{\text{sphere}} E_{\text{concrete}}} \end{aligned}$$

$$\begin{aligned} \epsilon_{\text{cylinder}} &= \frac{\sigma_{\text{cylinder}}}{E_{\text{concrete}}} \\ &= \frac{n_{\text{cylinder}}}{t_{\text{cylinder}} E_{\text{concrete}}} \\ &= \frac{pa}{t_{\text{cylinder}} E_{\text{concrete}}} \end{aligned}$$

Imposing $\epsilon_{\text{sphere}} = \epsilon_{\text{cylinder}}$ results in:

$$t_{\text{sphere}} = \frac{t_{\text{cylinder}}}{2} \quad (6.5)$$

This analogy is useful for making an initial estimation of the required wall thickness of the hemispherical cap. When the tangential strains of a thin-walled sphere and cylinder are equal, their radial strains will also be equal. Therefore, Equation 6.5 is used as a starting point in the hemispherical cap design.

For thin-walled structures, it can be assumed that the deformation is concentrated in the centre line of the wall. Therefore, in an initial design, the hemispherical cap is connected to the cylinder tube in such a way, that the center lines are continuous, as illustrated in Figure 6.4a. As explained in section 3.3, the cylinder and hemisphere are not truly thin-walled, rendering the mentioned relations as approximations.

Under the assumption of uniform stress throughout the wall thickness, the suggested relationship between the thicknesses of the cylinder and hemisphere, with $t_h = 0,5t_c$, leads to equal tangential stresses in both the cylinder and hemisphere walls. However, the resulting longitudinal stress in the cylinder wall is half the magnitude of the corresponding tangential stress in the hemisphere wall.

$$\begin{aligned} \sigma_{\theta\theta,\text{hemisphere}} &= \frac{n_{\theta\theta,\text{sphere}}}{t_{\text{hemisphere}}} = \frac{pa}{2t_{\text{hemisphere}}} = \frac{pa}{t_{\text{cylinder}}} \\ \sigma_{\theta\theta,\text{cylinder}} &= \frac{n_{\theta\theta,\text{cylinder}}}{t_{\text{cylinder}}} = \frac{pa}{t_{\text{cylinder}}} \\ \sigma_{LL,\text{cylinder}} &= \frac{n_{LL,\text{cylinder}}}{t_{\text{cylinder}}} = \frac{pa}{2t_{\text{cylinder}}} \end{aligned}$$

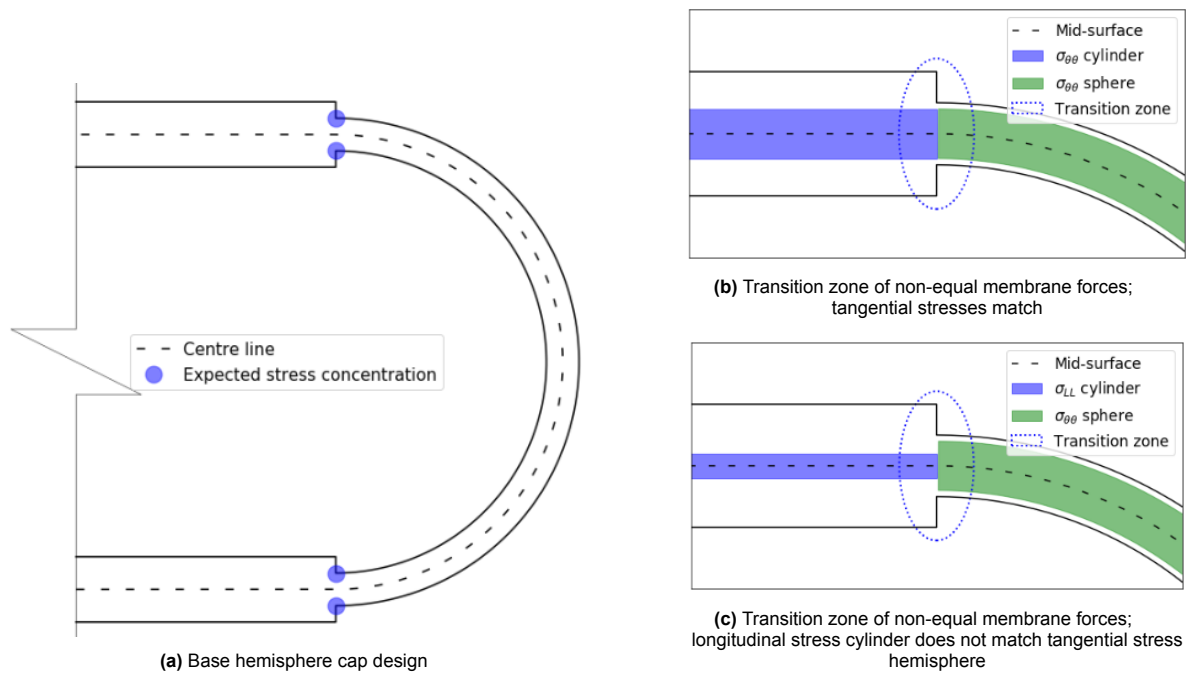


Figure 6.4: Hemisphere cap details

These Equations are graphically displayed in Figures 6.4b and 6.4c. It is important to note that the abrupt change from lower longitudinal stress in the cylinder to higher tangential stress in the hemisphere cannot occur instantaneously. Instead, there will be a transitional zone, as illustrated in Figure 6.4. The stress distribution in this region is uncertain for varying thicknesses of the hemisphere.

For thin shells where the cylinder and hemisphere share the same thickness, the stress distribution in the transition zone is well-defined, as shown in Figure 6.3 and described by Equations 6.3 and 6.4. In contrast to the earlier case, the discrepancy in stresses here arises from a mismatch in tangential membrane forces.

To address potential stress concentration zones, various semi-hemispherical cap designs are proposed. Subsequently, these designs are modeled in Diana FEA and subjected to comprehensive analysis in Section 6.1.4. Prior to the detailed analysis, various thicknesses are tested to evaluate the impact of the hemisphere's thickness on the magnitude of the bending moment.

6.1.3. Numerical verification of edge disturbance reduction

To verify the hypothesis that the edge disturbance can be minimized by varying the thickness of the hemispherical cap, a Diana FEA model is employed. Using the axisymmetry of the cylinder and hemisphere, the structure is modelled by a slice, representing the full structure. Since it is only interesting to verify the bending moment near the cylinder edge, a reduced length of the cylinder is used. It is validated whether this model still accurately represents the full structure in Appendix I.2.

As previously mentioned, the bending moment resulting from the edge disturbance can be analytically determined using Equations 6.1 and 6.2. However, it is essential to recognize that these equations are tailored for thin shells. Given that the cylinder and hemispherical cap under consideration here are classified as thick to very thick shells, the outcomes derived from numerical analysis regarding edge disturbance lack validation against an analytical solution. Additionally, in cases where the hemisphere wall thickness differs from that of the cylinder, there exists no analytical solution, even for thin shells.

A validation of the model's ability to capture the actual moments induced by an edge disturbance is conducted. This validation can be found in Appendix I.3. It involves a thin shell to allow comparison with an analytical solution.

While the moment in the thick shell is not expected to precisely match the analytical solution, it is still valuable to compare the numerical results with the analytical solution. Such a comparison helps verify whether the shape and order of magnitude of the solutions correspond. However, this comparison is only relevant for the case where the hemisphere thickness is equal to the cylinder tube thickness.

The illustration in Figure 6.5 provides an overview of the utilized model, featuring a hemisphere thickness of $0.5t$. Although various hemisphere thicknesses are examined, the models remain identical in all other aspects. This 3D solid model employs a composed line to extract moments around the Y-axis, corresponding to m_{xx} as depicted in Figure 6.3. For further elaboration on the models, refer to Appendix I.3.

The numerical output of the composed line is given in MNm. At each node along the composed line, it accumulates the contributions from all nodes within a plane perpendicular to the composed line. To convert the composed line output to MNm/m, each data point of the composed line needs to be divided by the width of the mid-section of the slice model at that specific location. While the width remains constant in the cylinder tube, it decreases with decreasing Z-coordinate in the hemisphere. The Diana models' outputs have not been adjusted for this slice width. Corrections for the slice width are applied in the plots.

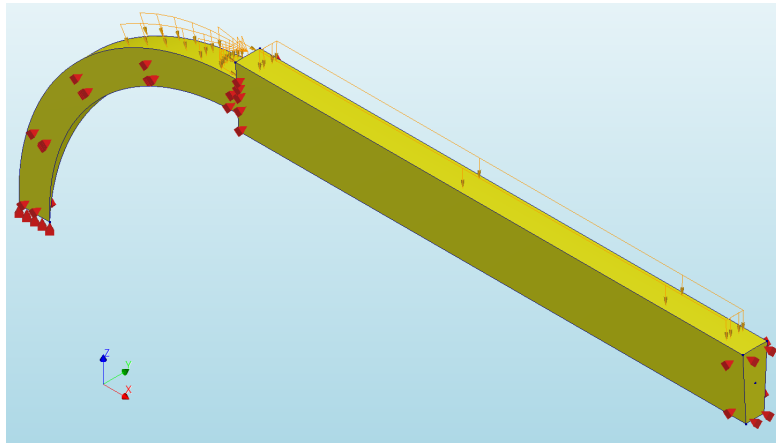


Figure 6.5: Diana slice model for determining influence of hemisphere thickness on moment induced by edge disturbance

The following paragraphs present and discuss the results, organized by hemispherical thickness. In each instance, a polynomial curve is fitted through the data points for both the hemisphere and the cylinder tube results. These fitted polynomials serve as a basis for comparing the results across different thicknesses.

Interpreting the results proves challenging due to the necessity to correct for slice width, rendering the outputs complex. Moreover, inconsistencies and inaccuracies are observed in the hemisphere results across all thicknesses, making it challenging to draw meaningful conclusions from the analyses. However, in the cylinder tube, the results exhibit consistency. As the distance from the cylinder edge increases, the moments appear to approach zero. This observation aligns with theoretical expectations, as the influence of the edge disturbance diminishes further away from the cylinder edge.

The modeled hemisphere thicknesses correspond to a cylinder with $V_{\text{internal}} = 9000 \text{ m}^3$ and $\frac{L}{2a} = 12$ at $d = 1000$ meters, leading to an internal radius of $a = 4,84$ meters and a wall thickness of $t_{\text{cylinder}} = 1,62$ meters. The parameters of the hemisphere thicknesses are listed in Table 6.1.

Thickness fraction	1	0,6	0,5	0,4
Thickness [m]	1,62	0,972	0,81	0,648
Inner radius hemisphere [m]	4,84	5,164	5,245	5,326
Outer radius hemisphere [m]	6,46	6,136	6,055	5,974

Table 6.1: Modelled hemisphere thicknesses

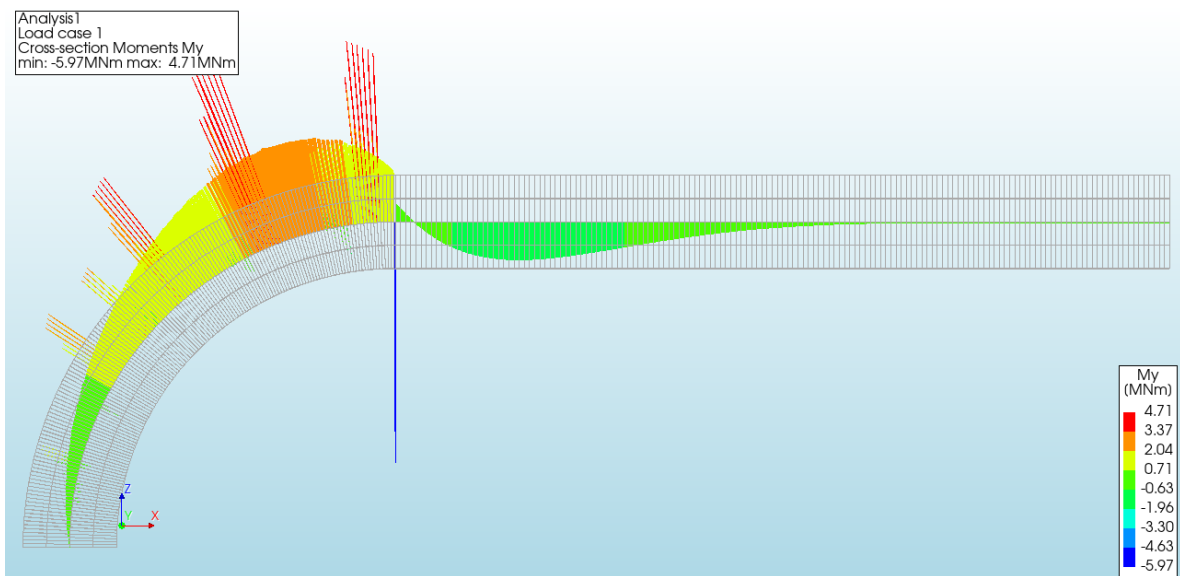
For detailed information on the Diana FEA models utilized in this section, refer to Appendix I.3.2.

Hemisphere thickness: $t_h = t_c$

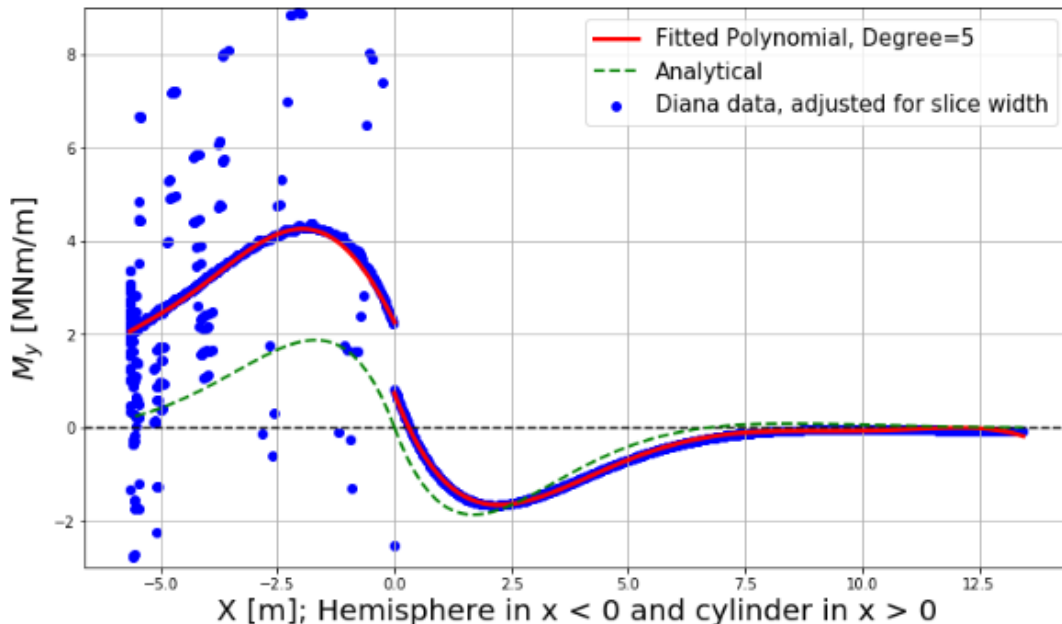
The moment observed in the cylinder tube closely aligns with the analytical solution. However, an unexpected jump in the moment occurs at the transition from cylinder to hemisphere, contrary to the anticipated zero moment. This discrepancy is puzzling and suggests unreliable results, given the absence of any additional load that could generate such a moment at the transition zone.

In the hemisphere, the fitted polynomial appears to be shifted upward compared to the analytical solution, which consistently remains lower. This discrepancy further indicates potential unreliability in the hemisphere results.

The numerous outliers observed in Figure 6.6b (at $x < 0$) are attributed to spikes in the Diana results within the hemisphere, as observed in Figure 6.6a.



(a) Diana output



(b) Diana output post-processed in python, adjusted for slice width

Figure 6.6: Moments due to edge disturbance for $t_h = t_c$

Hemisphere thickness: $t_h = 0,6t_c$

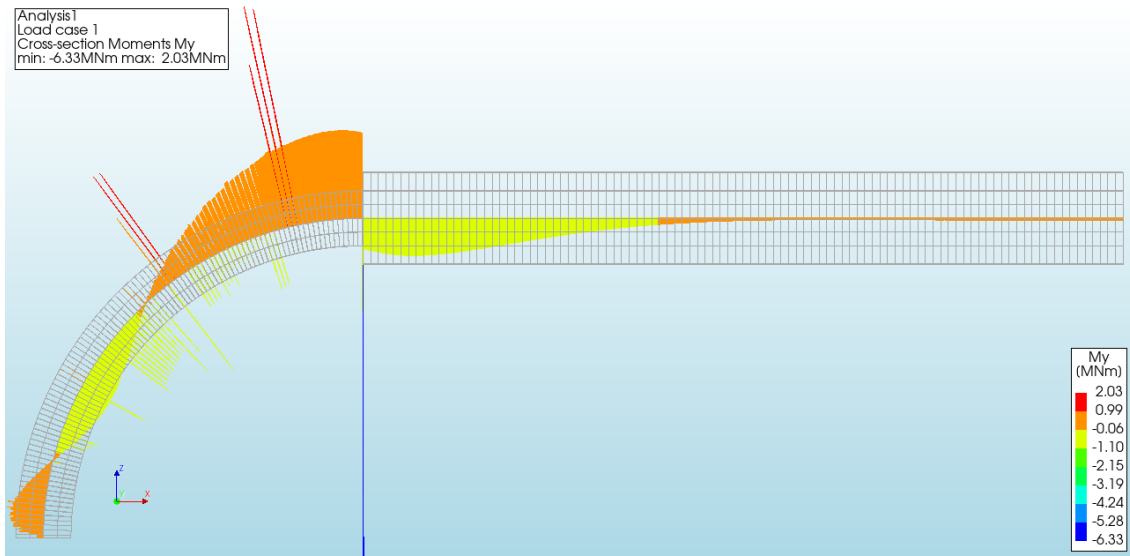
The Diana output, as depicted in Figure 6.7a, shows oscillations around the mid-surface in the hemisphere, which gradually diminish further from the edge disturbance. However, when considering slice width adjustments, substantial oscillations become apparent in the hemispherical region.

At the interface between the hemisphere and the cylinder tube, a noticeable jump in the moment-line occurs. This jump can be attributed to the distributed normal force present in the uncovered portion of the cylinder wall thickness, where the thinner hemisphere is no longer connected to the cylinder.

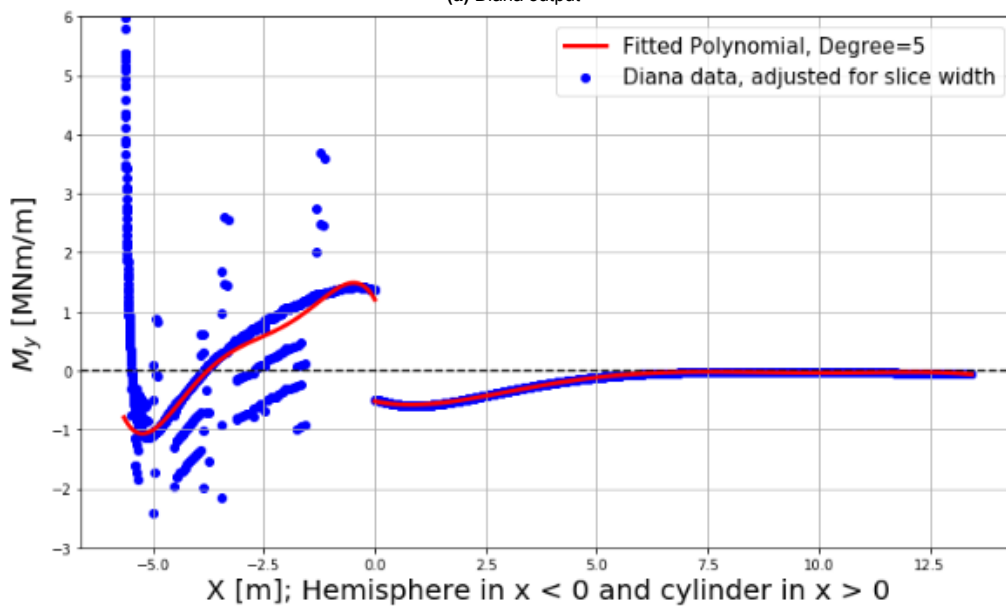
The results in the cylinder tube demonstrate consistency, gradually decaying away from the edge disturbance, consistent with theoretical expectations.

The maximum moment in the cylinder tube is located approximately 1 meter from the cylinder edge.

Once more, numerous spikes are evident in the hemisphere region in Figure 6.7a, resulting in outliers in Figure 6.7b. These outliers lead to inconsistency between the polynomial curve fit and the data in the hemisphere region. Consequently, the results in this area are deemed unreliable.



(a) Diana output



(b) Diana output post-processed in python, adjusted for slice width

Figure 6.7: Moments due to edge disturbance for $t_h = 0,6t_c$

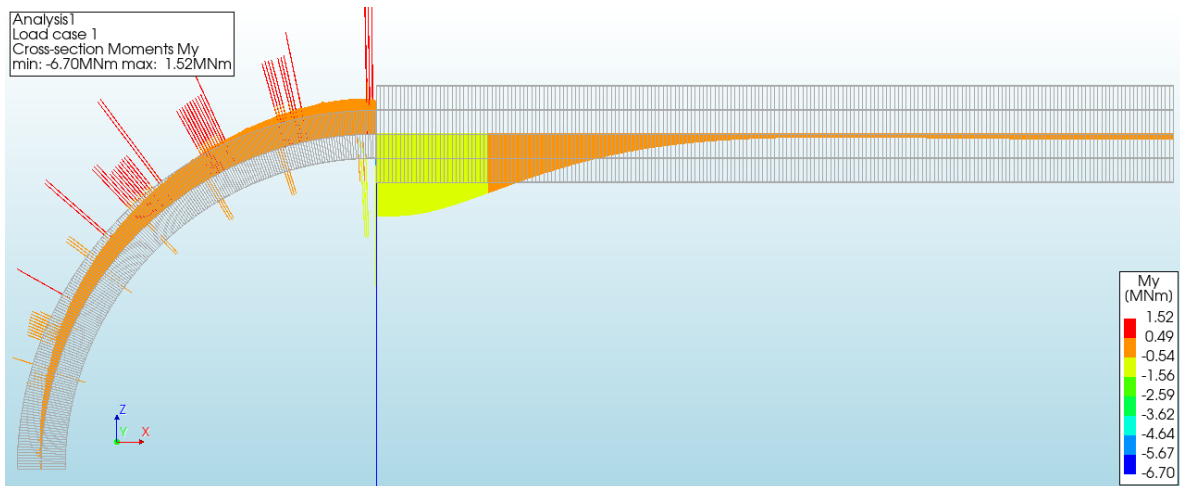
Hemisphere thickness: $t_h = 0,5t_c$

The Diana output, as illustrated in Figure 6.8a, exhibits extremes at the interface between the hemisphere and cylinder tube. Subsequently, it gradually decreases to zero further away from the edge disturbance, consistent with theoretical expectations.

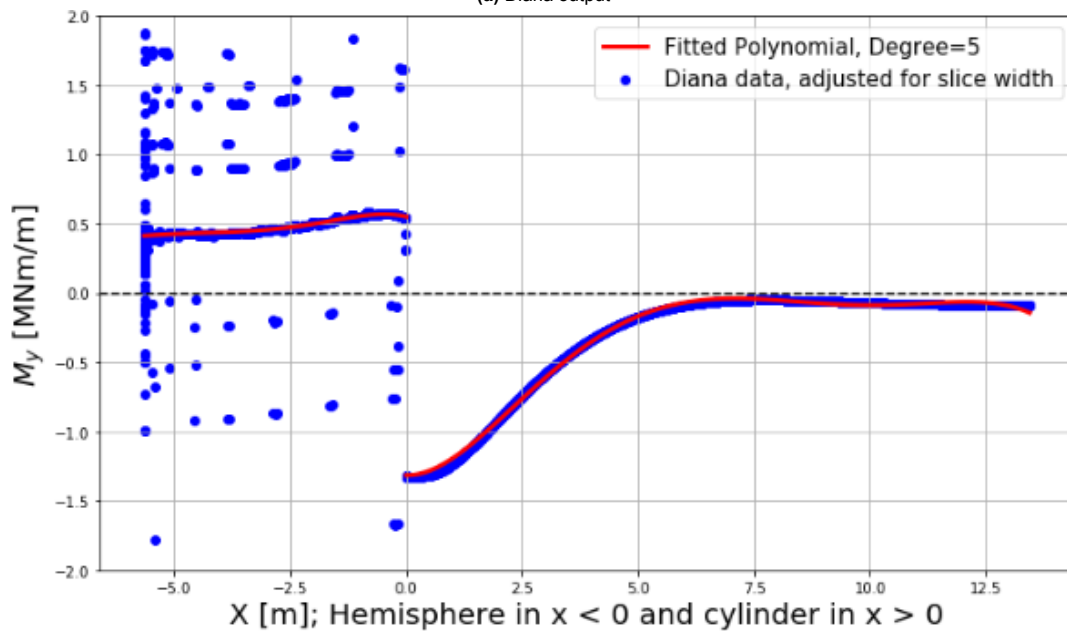
However, upon applying a correction for the slice width, the moment in the hemisphere does not seem to decrease away from the transition zone, which is unexpected.

A jump in the moment-line occurs at the location of the edge disturbance. As previously mentioned, this can be attributed to the presence of the distributed normal force perpendicular to the cross-section of the cylinder tube, where the hemisphere and cylinder no longer connect.

Once again, the spikes in the hemispherical region in Figure 6.8a result in outliers in the data points in Figure 6.8b, making the results in the hemispherical region unreliable and complex to interpret.



(a) Diana output



(b) Diana output post-processed in python, adjusted for slice width

Figure 6.8: Moments due to edge disturbance for $t_h = 0,5t_c$

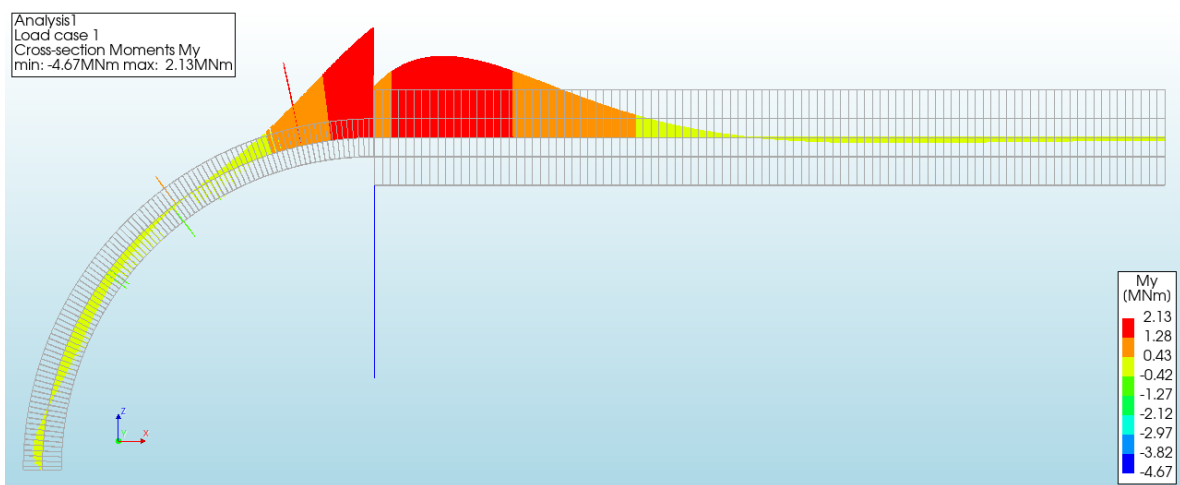
Hemisphere thickness: $t_h = 0,4t_c$

The output of the Diana model reveals bending moments at the cylinder edge where the edge disturbance is present, as depicted in Figure 6.9a. These bending moments gradually decay away from the edge disturbance, with oscillations observed in the hemispherical part.

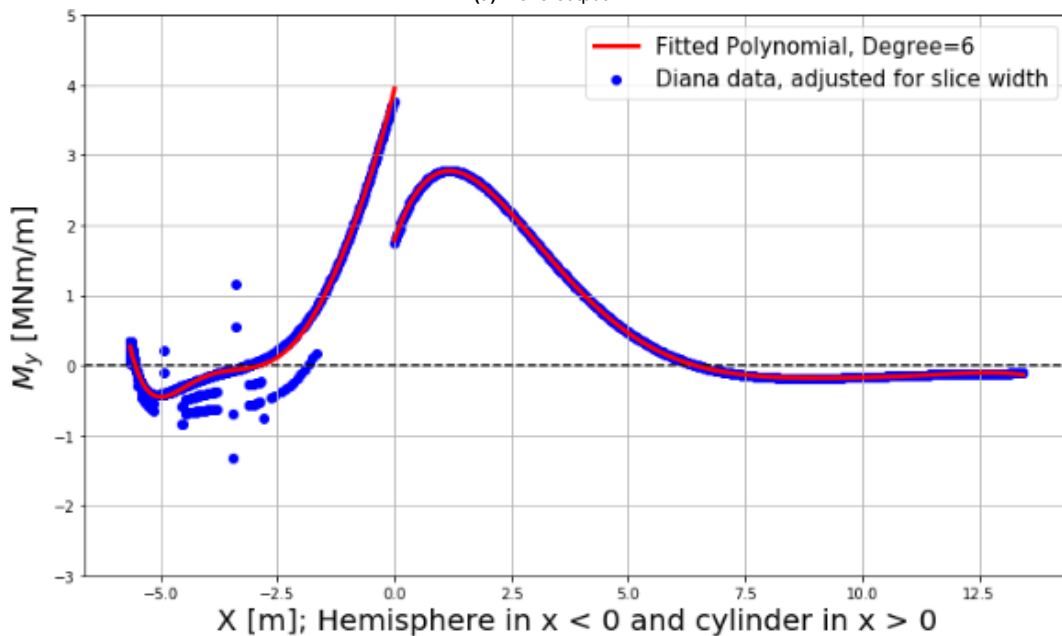
A jump in the moment line is observed at the transition, attributed to the presence of the distributed normal force acting perpendicular to the cross-section of the cylinder tube, where the hemisphere and cylinder no longer connect. Unlike in other models, this jump in the moment line does not cause the moment to change from positive to negative.

The moment near the transition zone consistently exhibits a positive value, deviating from the patterns observed in the other models. This suggests a threshold for the hemisphere thickness, falling within the range of $0,4t_c < t_h < 0,5t_c$, where the radial stiffness of the cylinder surpasses that of the hemisphere.

Once again, the spikes in the hemispherical region in Figure 6.9a result in outliers in the data points in Figure 6.9b, making the results in the hemispherical region unreliable and complex to interpret.



(a) Diana output



(b) Diana output post-processed in python, adjusted for slice width

Figure 6.9: Moments due to edge disturbance for $t_h = 0,4t_c$

Combination of results

While acknowledging the inaccuracies and inconsistencies observed in the fitted polynomials within the hemispherical region of the results, some tentative observations can still be made, albeit with caution.

The moment present in the cylinder tube can be influenced by adjusting the thickness of the hemisphere. Careful consideration is required as the chosen thickness can either increase or decrease the moment. It seems that the moment cannot be reduced to zero under the conditions of constant distributed normal force on a thick shell.

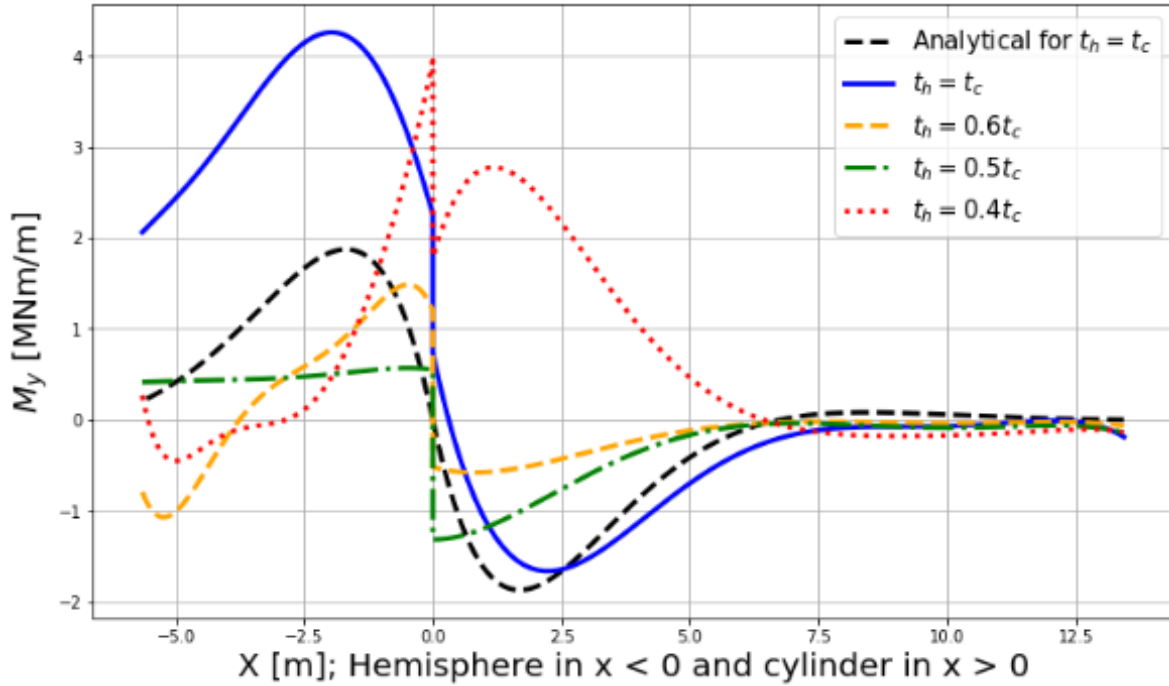


Figure 6.10: Fitted polynomials for moments in edge disturbance hemisphere and cylinder interface; at $d = 1000$ m and $f_{cd} = 40$ MPa; Extracted from Figures 6.6b, 6.7b, 6.8b and 6.9b

The magnitude of the moments falls within the range of ± 5 MNm/m. Considering this moment acts around the circumference of the mid-surface, its total value acting on the entire cross-section can be calculated by multiplying it by the length of the circumference. Subsequently, the additional stresses arising from this moment can be determined by dividing by the section modulus W of a circular hollow section.

For the given cylinder with an inner radius of $a = 4,84$ meters and a wall thickness of $t_{\text{cylinder}} = 1,62$ meters, the radius of the mid-surface is thus $a + \frac{t_{\text{cylinder}}}{2} = 5,65$ meters. The normative hemisphere for this bending moment is the thinnest one, where $t_h = 0,4t_c$.

$$W = \frac{\pi (r_2^4 - r_1^4)}{4r_2} = \frac{\pi (5,974^4 - 5,326^4)}{4 \cdot 5,974} = 61,66 \text{ m}^3$$

$$\sigma_{\max} = \pm \frac{M_y}{W} = \pm \frac{M_{xx} \cdot 2\pi r_{\text{midsurface}}}{W} = \frac{5 \cdot 2\pi \times 5,65}{61,66} = \pm 2,88 \text{ MPa}$$

The resulting normative additional stress caused by the bending moment is $\pm 2,88$ MPa, specifically in the hemisphere with thickness $t_t = 0,4t_c$. Comparing this to the anticipated effective design stresses of 40 MPa, the contribution of the edge disturbance appears marginal.

Moreover, the abrupt transition from cylinder to hemisphere, where the hemisphere is thinner than the cylinder, leads to a jump in the moment line. This is due to the distributed normal force acting on the

cylinder cross-section. Smoothing the transition from cylinder to hemisphere by adding some material may result in a reduction of the jump.

The expected value of the jump can be calculated and compared to the observed value of the jump. It is equal to the free height above the hemisphere, multiplied by the distributed normal force p , and the distance of the center of the resultant force to the mid-surface. This is illustrated in Figure 6.11. The expected value of the jump in the moment line for the hemisphere with thickness $t_h = 0,4t_c$ is equal to 2,77 MNm/m.

$$\begin{aligned} M_{\text{jump}} &= p \frac{t_c - t_h}{2} \left(\frac{t_c - t_h}{4} + \frac{t_h}{2} \right) \\ &= 10,06 \cdot \frac{1,62 - 0,648}{2} \left(\frac{1,62 - 0,648}{4} + \frac{0,648}{2} \right) \\ &= 2,77 \text{ MNm/m} \end{aligned}$$

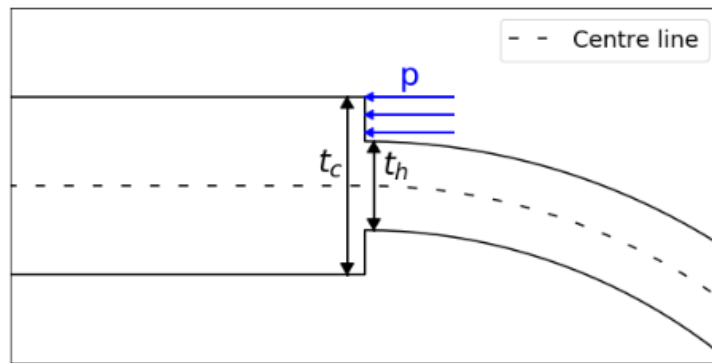


Figure 6.11: Mechanical scheme of explanation for jump in moment line at cylinder edge

All expected values of the height of the jump in the moment line are higher than the values observed in the data, except for the hemisphere equal in thickness to the cylinder edge. In that case, a jump in the moment line is observed where no jump is expected.

Thickness fraction	1	0,6	0,5	0,4
Thickness [m]	1,62	0,972	0,81	0,648
Section modulus [m ³]	145,0	90,42	76,19	61,66
$M_{y,\text{cylinder,max,Diana}}$ [MNm]	-0,94	-0,34	-0,75	1,57
$M_{xx,\text{cylinder,max}}$ [MNm/m]	-1,66	-0,58	-1,32	2,77
$M_{y,\text{hemisphere,max,Diana}}$ [MNm]	2,34	0,80	0,32	2,13
$M_{xx,\text{hemisphere,max}}$ [MNm/m]	4,26	1,49	0,57	3,95
Expected value jump in moment line [MNm/m]	0	2,11	2,47	2,77
Observed value jump in moment line [MNm/m]	1,52	1,72	1,87	2,16

Table 6.2: Maximum absolute moments for various hemisphere thicknesses

The presence of moments in both the hemisphere and cylinder tube implies the existence of shear forces as well. The derivatives of the fitted polynomials from Figure 6.10, representing the shear forces in the cross-section, have been plotted and are depicted in Figure 6.12.

In all cases, except for $t_h = 0,5t_c$, there appears to be a jump in the shear line. However, this jump is more likely a consequence of inaccurate polynomial fitting rather than an actual discontinuity. In reality, such a jump cannot exist, as there is no support or concentrated load present at the transition from the hemisphere to the cylinder.

As mentioned, the polynomial fits in the hemisphere are inaccurate, leading to inaccuracies in their derivatives as well. Therefore, it is challenging to draw meaningful conclusions about that part of the graph. In the cylinder tube, the shear forces appear to be lowest for the hemisphere thicknesses of $0,5t_c$ and $0,6t_c$.

Near the truncation of the cylinder tube, the polynomial fits show some inaccuracies, as evident in Figures 6.6b, 6.7b, 6.8b, and 6.9b. Despite the expectation of zero moment in that region, the shear forces do not appear to be zero in Figure 6.12.

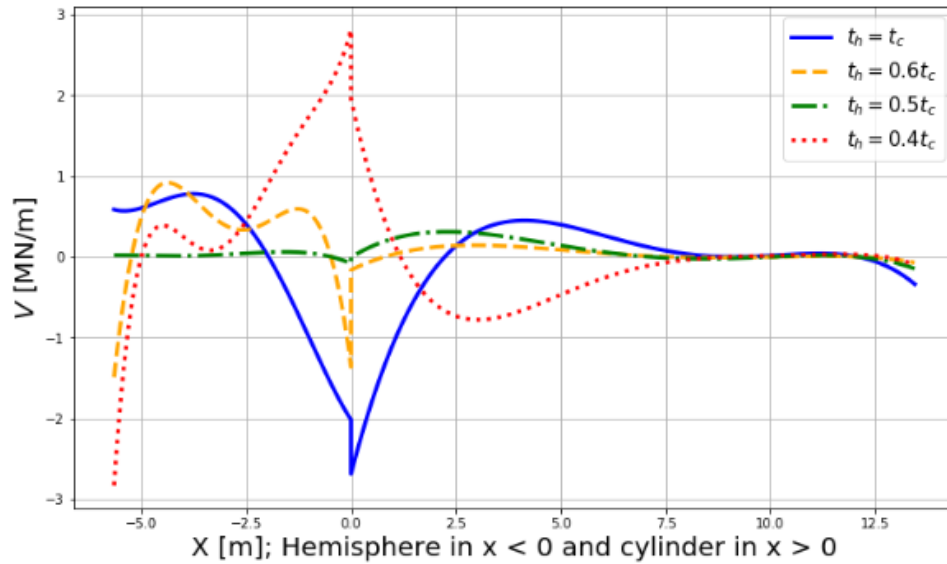


Figure 6.12: Shear forces caused by edge disturbance in hemisphere and cylinder interface; at $d = 1000$ m and $f_{cd} = 40$ MPa; Derivatives of fitted polynomials from Figure 6.10

6.1.4. Redistribution of stress concentrations at cylinder-hemisphere transition

As anticipated in Figure 6.4, stress concentration zones are indeed evident at the internal angle where the hemisphere intersects with the cylinder.

A hemispherical structure with a thickness equivalent to half of the cylinder's thickness, represented by $t_h = 0,5t_c$, is being analyzed through computational simulations using Diana FEA software. The simulation involves exploring three variations in the transition from the cylinder to the hemisphere.

Firstly, an investigation into an abrupt transition is conducted, wherein no additional material is introduced to facilitate a smoother connection between the two geometries. This configuration is referred to as an abrupt transition.

Secondly, a triangular transition is explored, characterized by a gradual reduction in the cylinder's thickness at a 45-degree angle until it integrates with the hemisphere. This configuration, due to its triangular shape, is termed a triangular transition.

Lastly, a smoother connection approach is scrutinized, involving a gradual reduction in the cylinder's thickness along the tangent of a circle until it smoothly merges with the hemisphere. This configuration is referred to as a circular transition.

In all three designs, material is only added at the hemisphere without shaving off any material from the cylinder wall. The thickness of the cylinder wall was determined based on its capacity to withstand the distributed normal force, thus no material can be removed from there.

These three variations are selected to illustrate potential strategies for reducing stress concentrations. It is important to note that while these configurations may mitigate stress concentrations to some extent, achieving an optimal connection devoid of elevated stresses may require further refinement.

As detailed in Section 6.2.4, the maximum tangential stress observed in the cylinder wall is $-45,8$ MPa. Given that this value represents the design stress norm, it is imperative that the transition from the cylinder to the hemisphere does not exacerbate the maximum tangential stress within the cylinder wall. For definitions of radial, tangential and longitudinal stress, refer to Section 3.3.

Detailed information on the models that were used in this Section is found in Appendix I.3.3.

Abrupt transition

As anticipated, the abrupt transition leads to a stress concentration at the internal angle where the cylinder and hemisphere intersect. In the cylinder, the longitudinal stress is approximately half of the tangential stress observed in the hemisphere, as depicted in Figure 6.14. Transitioning from the cylinder to the hemisphere confines the stress into a narrower path, evident from the trajectory of the principal stress lines in this figure.

A significant tangential stress concentration of $-79,34$ MPa is detected within the hemisphere, as depicted in Figure 6.15. Additionally, both tangential and radial stress concentrations in the cylinder marginally surpass the normative design stress, as illustrated in Figure 6.16.

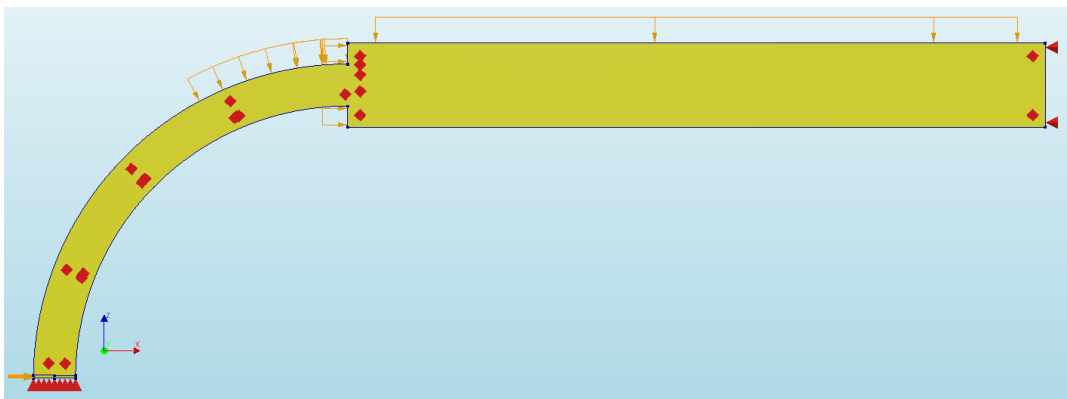


Figure 6.13: Abrupt hemisphere-cylinder connection; model

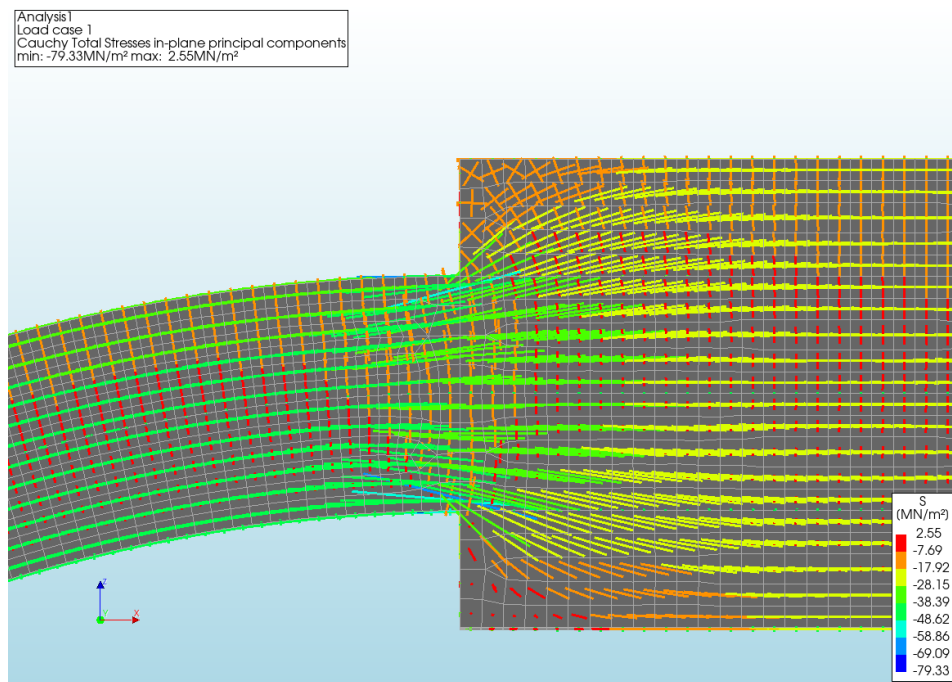


Figure 6.14: Abrupt hemisphere-cylinder connection; principal stresses in XZ-plane

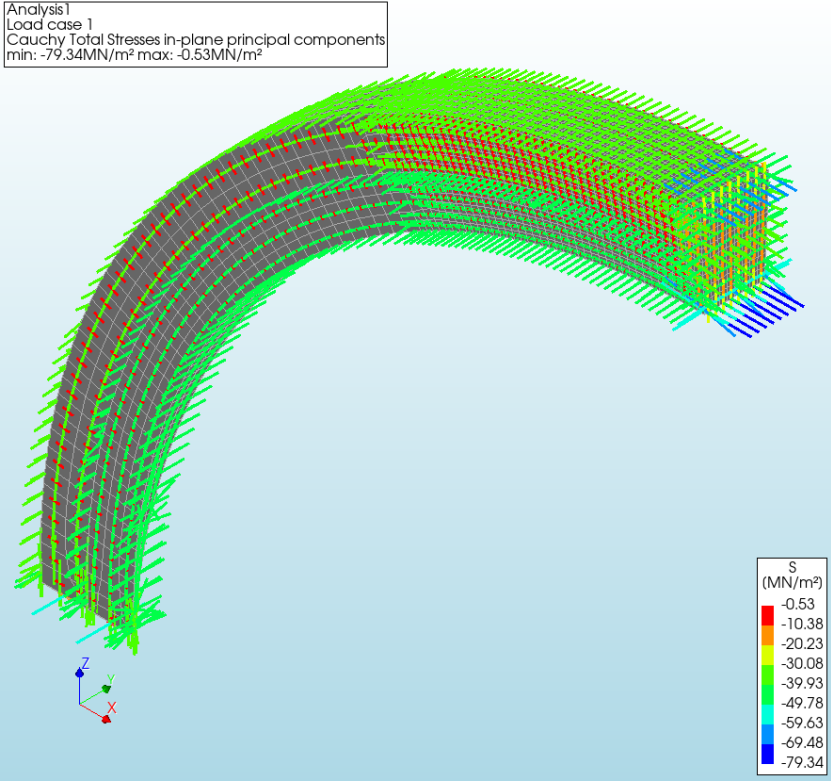


Figure 6.15: Abrupt hemisphere-cylinder connection; principal stresses in hemisphere

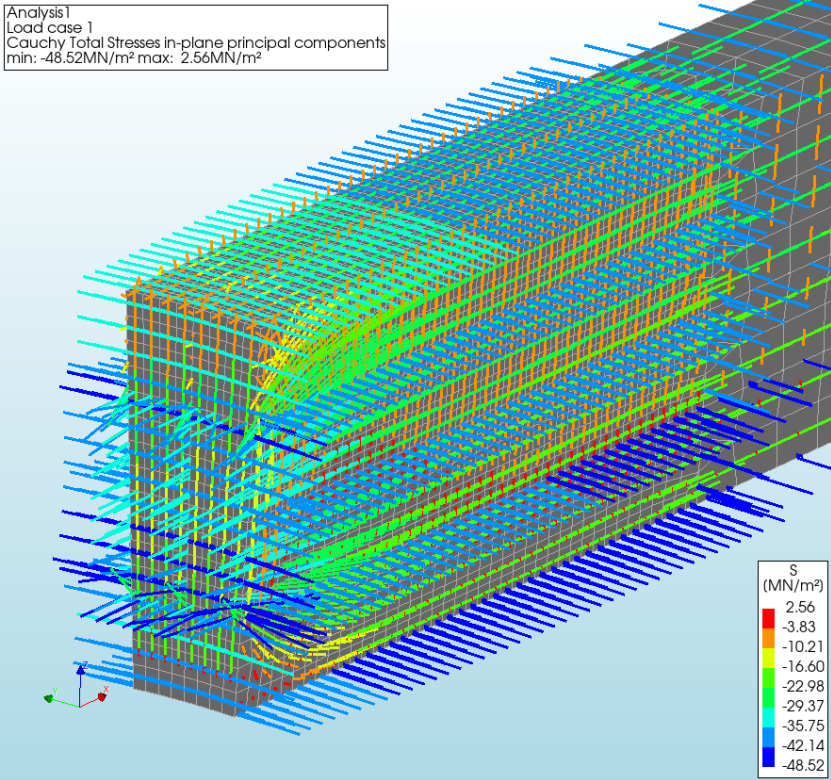


Figure 6.16: Abrupt hemisphere-cylinder connection; principal stresses in cylinder

Triangular transition

Like the abrupt transition, the triangular transition from the cylinder to the hemisphere also channels the stress into a narrower path, as evidenced by the trajectory of the principal stress lines in Figure 6.18. There seems to be insufficient additional material to facilitate a smooth transition of the stresses.

Furthermore, a very high stress concentration is observed at the internal angle of the lower triangle where it meets the hemisphere, as illustrated in Figure 6.19. This suggests that the sharp angle between the triangle and the hemisphere still results in a singularity.

However, apart from this singularity, there are no extreme values of principal stress observed. The normative design stress is not exceeded.

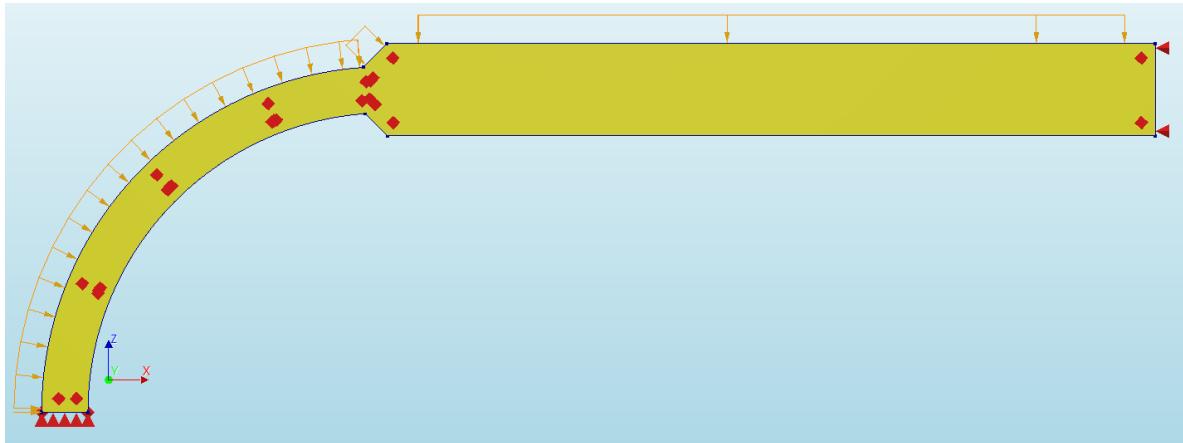


Figure 6.17: Triangular hemisphere-cylinder connection; model

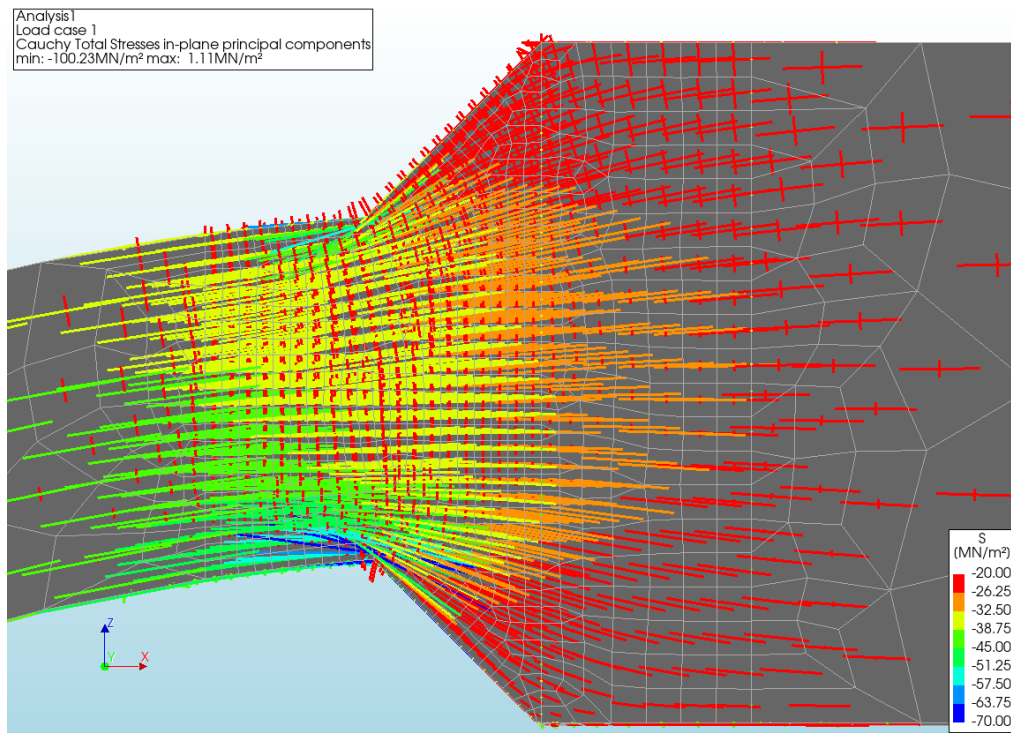


Figure 6.18: Triangular hemisphere-cylinder connection; principal stresses in XZ-plane

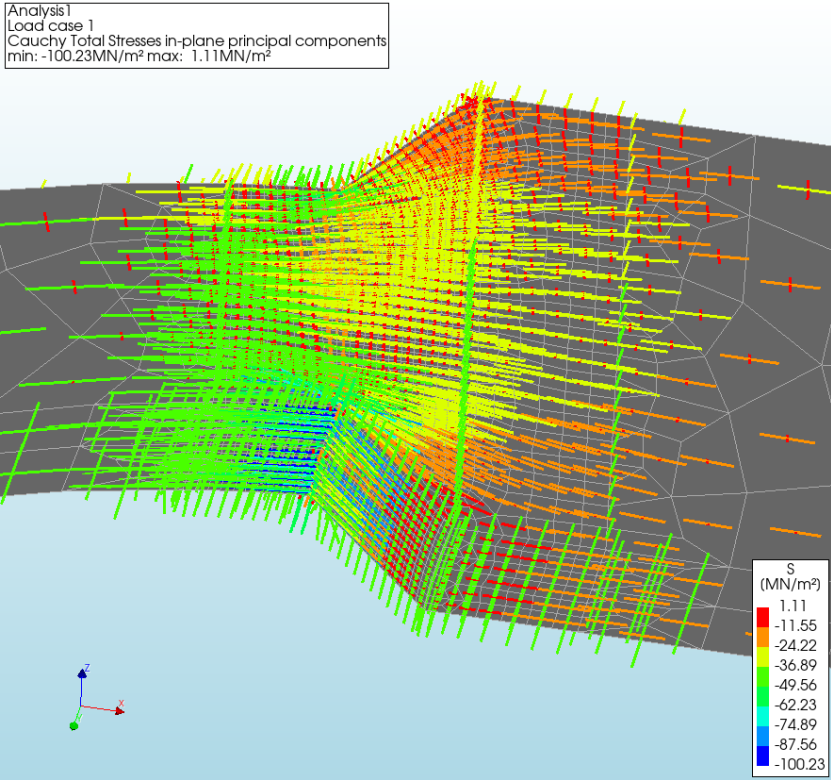


Figure 6.19: Triangular hemisphere-cylinder connection; principal stresses in hemisphere

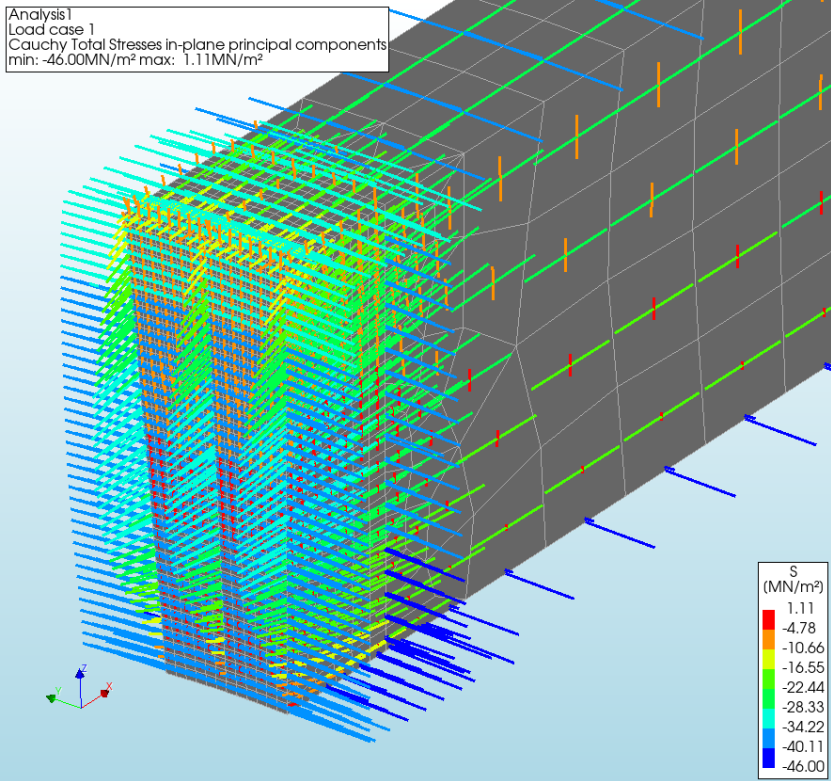


Figure 6.20: Triangular hemisphere-cylinder connection; principal stresses in cylinder

Circular transition

The circular transition notably facilitates a smooth transition of the longitudinal stress in the cylinder wall to the heightened radial stress in the hemisphere. This can be observed in the direction of the principal stresses, as depicted in Figure 6.22, closely aligning with the shape of the cross-section. It indicates effective transfer of loads to normal stresses.

A slight increase in the principal stress level is observed at the point where the curvature of the internal surface of the hemisphere undergoes a change. This alteration in curvature is most clearly visible in Figure 6.21, while the elevated stress is best observed in Figure 6.23.

Furthermore, no other increases in stress levels are observed in the circular transition.

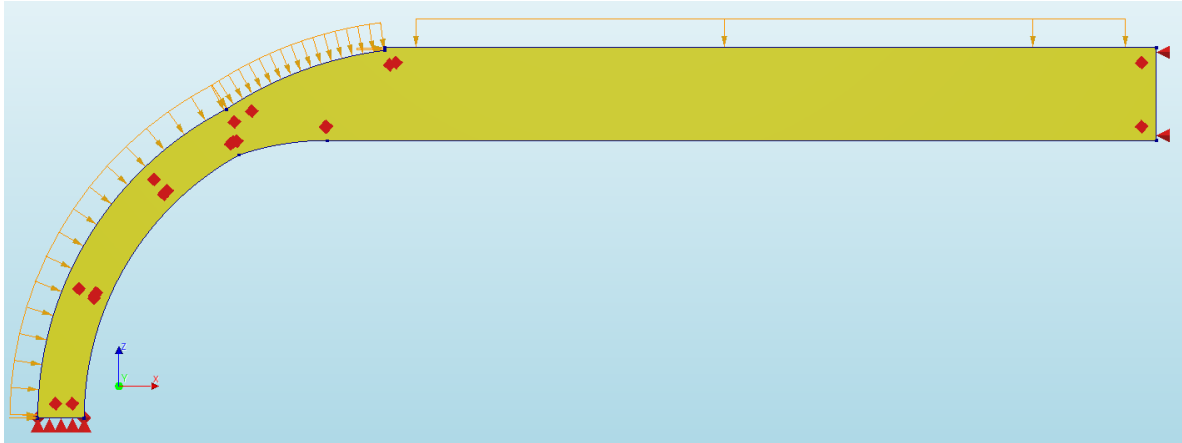


Figure 6.21: Circular hemisphere-cylinder connection; model

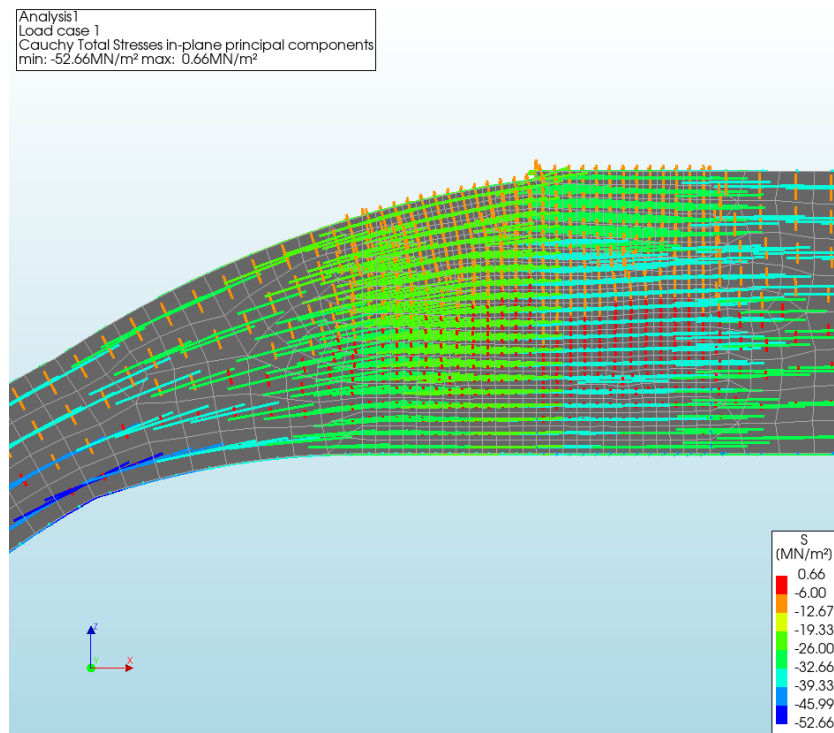


Figure 6.22: Circular hemisphere-cylinder connection; principal stresses in XZ-plane

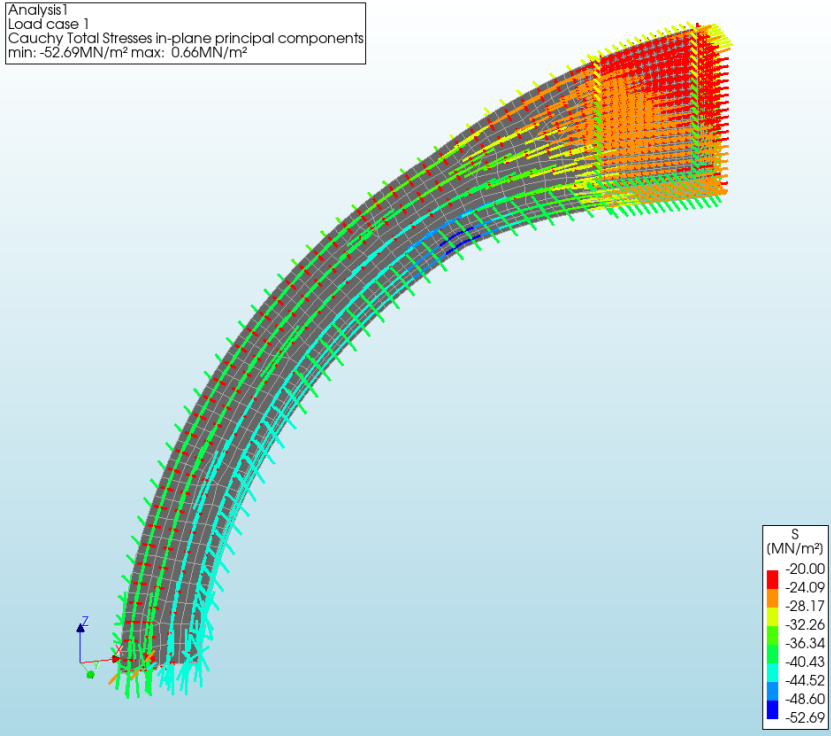


Figure 6.23: Circular hemisphere-cylinder connection; principal stresses in hemisphere

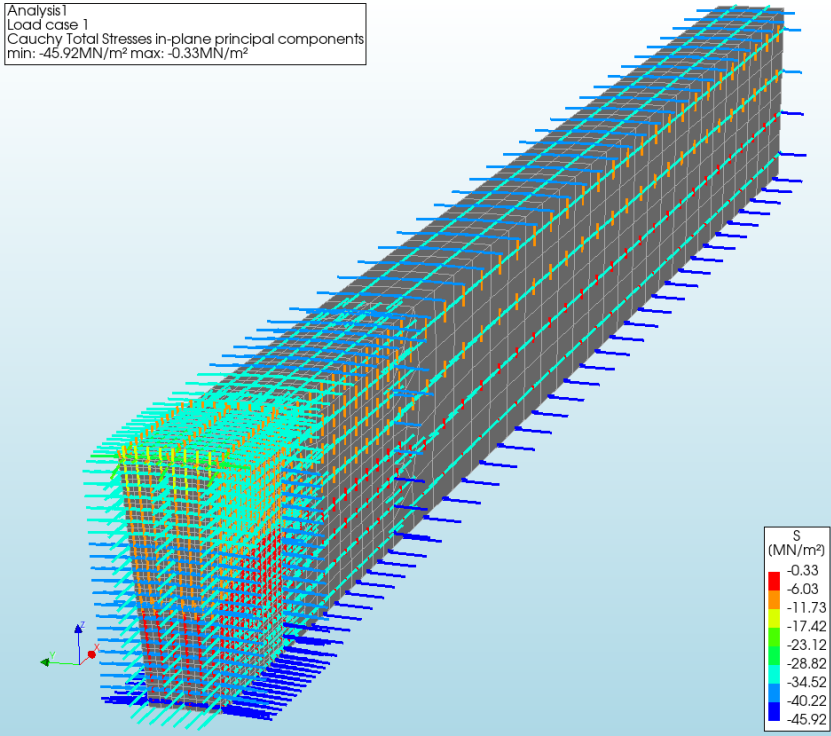


Figure 6.24: Circular hemisphere-cylinder connection; principal stresses in cylinder

Conclusion on stress concentration reduction

A detailed examination of the three transition variations reveals that a smoother transition has the potential to diminish or entirely eliminate stress concentrations at the junction between the cylinder and hemisphere. Additionally, even minor fluctuations in surface curvature can lead to stress concentrations.

However, achieving such a smooth connection in practice may present challenges. The quality of the final product is inherently tied to the capability to create smooth formwork. Nonetheless, the analysis above demonstrates that significant reductions in high stress concentrations are feasible.

6.1.5. Contribution of hemispherical cap to CIV-ratio

In addition to examining the distribution of internal forces, the analysis of the hemispherical cap design extends to its impact on the CIV-ratio of the cylinder. Multiple proposed designs are evaluated, and for the calculations, a baseline design with the same thickness as the cylinder is employed. As discussed in Section 6.1.2, it is acknowledged that the wall thickness of the hemisphere is expected to be approximately half of the wall thickness of the cylinder. Consequently, these calculations lead to a slight overestimation of the CIV-ratio.

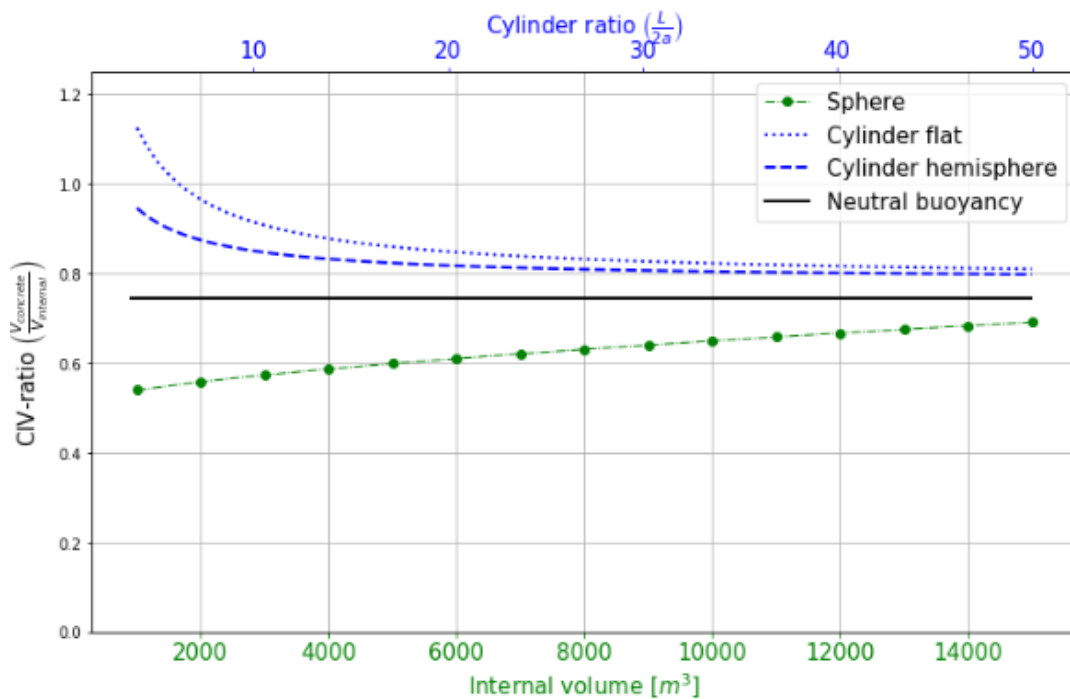


Figure 6.25: CIV-ratio of reservoir and foundation for hemispherical cap design; at $d = 1000$ m and $f_{cd} = 40$ MPa

Figure 6.25 presents the CIV-ratios of the sphere and the cylinder with both flat and hemispherical cap designs, including considerations for the foundations. The CIV-ratio for the sphere varies over the internal volume, while the cylinder's CIV-ratio varies over its slenderness. Detailed calculations supporting the results presented in Figure 6.25 can be found in Appendix D.3.

The hemispherical cap design demonstrates improved material usage compared to the flat cap design. As slenderness increases, this advantage diminishes. However, slenderness values exceeding 30 are highly unrealistic due to the impractical length of the cylinder for construction. Consequently, there is a tangible improvement in the CIV-ratio of the hemispherical cap design compared to its flat counterpart. Nevertheless, the sphere still exhibits a lower CIV-ratio, making it more favorable in terms of material usage.

6.2. Verification of uniform compression assumption

The analyses in Chapter 4 rest on the assumption of uniform compressive stress in the reservoir wall, as detailed in Section 3.3. This simplification is typically justified for very thin shells where the ratio between span and thickness ($\frac{a}{t}$) exceeds 4000 [36]. Interestingly, for both the sphere and the cylinder, this $\frac{a}{t}$ ratio is lower. The internal volume and slenderness do not seem to play a role in determining this ratio, as illustrated in Figure 4.5. Factors influencing this ratio are the installation depth and the concrete compressive design strength.

Parameter	Symbol	Value	Unit
Installation depth	d	1000	[m]
Concrete compressive design strength	f_{cd}	40	[N mm ⁻²]
Hydrostatic pressure	p	-10,06	MPa
Spherical span-thickness ratio	$\frac{a}{t}$	6,96	[-]
Cylindrical span-thickness ratio	$\frac{a}{t}$	2,98	[-]

Table 6.3: Span-thickness ratios of sphere and cylinder

As indicated in Table 6.3, the $\frac{a}{t}$ ratio for the sphere is 6,96, classifying it as a thick shell. Conversely, for the cylinder, the ratio is 2,98, suggesting that it structurally behaves differently from a shell [36].

6.2.1. Analytical verification of uniform stress assumption for sphere

To assess the uniform stress assumption, Equations 6.6 and 6.7 are applied for thick-walled spheres [63, 64].

$$\sigma_{rr,\text{sphere}} = C_1 - \frac{C_2}{r^3} \quad (6.6)$$

$$\sigma_{\theta\theta,\text{sphere}} = C_1 + \frac{C_2}{2r^3} \quad (6.7)$$

Here, the constants C_1 and C_2 are determined by applying boundary conditions for $\sigma_{rr,\text{sphere}}$ at $r = a$ and $r = a + t$, which originate from the pressure loads on the sphere.

$$\begin{aligned} r = a &\quad \rightarrow \quad \sigma_{rr} = p_{\text{in}} = 0 \\ r = a + t &\quad \rightarrow \quad \sigma_{rr} = p_{\text{out}} = -p \end{aligned}$$

These boundary conditions lead to the solved expressions for tangential and radial stress for the thick-walled sphere under hydrostatic pressure, as formulated in equations 6.8 and 6.9. Relevant parameters for this context are illustrated in Figure 6.26a.

$$\sigma_{rr,\text{sphere}} = \frac{p(a+t)^3(r^3 - a^3)}{\left((a+t)^3 - a^3\right)r^3} \quad (6.8)$$

$$\sigma_{\theta\theta,\text{sphere}} = \frac{p(a+t)^3(2r^3 + a^3)}{2\left((a+t)^3 - a^3\right)r^3} \quad (6.9)$$

Following the methodology outlined in Chapter 4, a spherical reservoir with an internal volume of $V_{\text{internal}} = 9000 \text{ m}^3$ has an internal radius of $a = 12,90$ meters and a wall thickness of $t = 1,86$ meters. Utilizing these parameters in Equations 6.8 and 6.9 yields the radial and tangential stresses, as depicted in Figure 6.26b. It is important to note that the wall thickness was determined based on a maximum allowable tangential stress of 40 MPa.

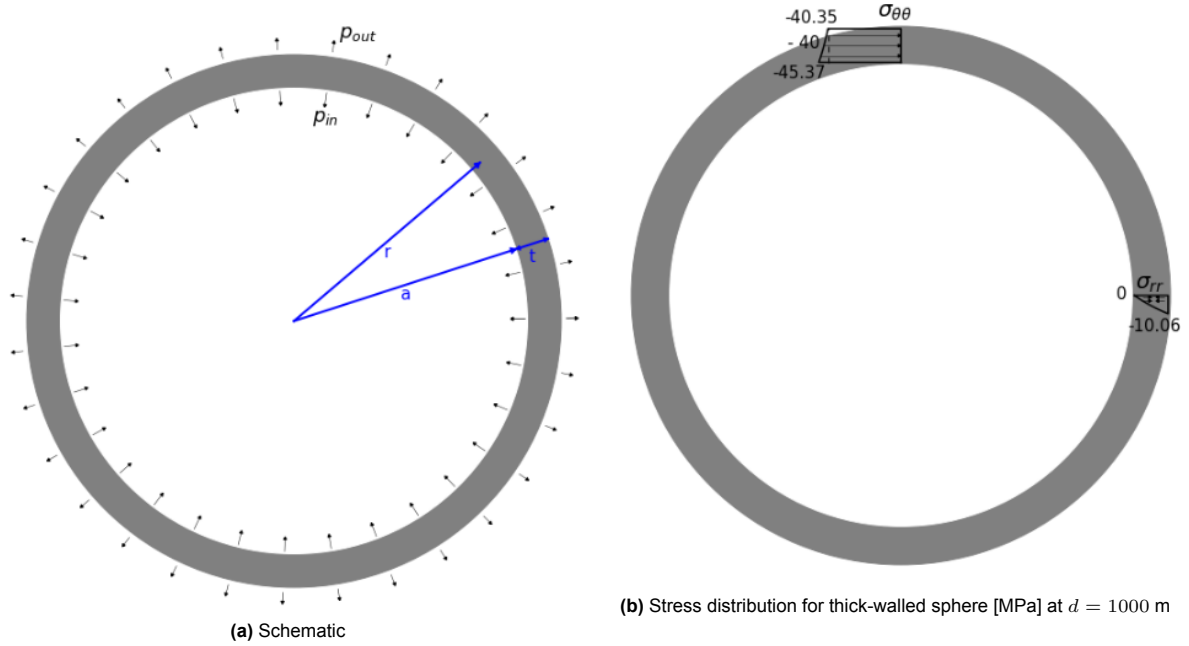


Figure 6.26: Thick-walled sphere with internal and external load

6.2.2. Analytical verification of uniform stress assumption for cylinder

To validate the assumption of uniform stress over the wall thickness, equations 6.10 and 6.11 for circular discs and plates are employed [65]. These equations are applicable to the cylindrical reservoir, while for the spherical reservoir, they do not hold.

$$\sigma_{rr,cylinder} = \frac{a^2 (a+t)^2 (q_{in} - q_{out}) + r^2 \left((a+t)^2 q_{out} - a^2 q_{in} \right)}{r^2 \left((a+t)^2 - a^2 \right)} \quad (6.10)$$

And:

$$\sigma_{\theta\theta,cylinder} = \frac{-a^2 (a+t)^2 (q_{in} - q_{out}) + r^2 \left((a+t)^2 q_{out} - a^2 q_{in} \right)}{r^2 \left((a+t)^2 - a^2 \right)} \quad (6.11)$$

The parameters employed in Equations 6.10 and 6.11 are depicted in Figure 6.27a. Using $\frac{a}{t} = 2,98$ and $q_{in} = 0$, the equations can be further simplified as follows:

$$\sigma_{rr,cylinder} = 2,28q_{out} \left(1 - \frac{a^2}{r^2} \right)$$

$$\sigma_{\theta\theta,cylinder} = 2,28q_{out} \left(1 + \frac{a^2}{r^2} \right)$$

By substituting $a < r < a+t = 1,336a$, derived from the known $\frac{a}{t}$ ratio, an expression for the minimum and maximum radial and tangential stress in the wall is obtained, which is solely dependent on q_{out} :

$$0 \leq \frac{\sigma_{rr,cylinder}}{q_{out}} \leq 1$$

$$3,552 \leq \frac{\sigma_{\theta\theta, \text{cylinder}}}{q_{\text{out}}} \leq 4,552$$

Upon evaluating a unit strip of the cylinder, width = 1 meter, $q_{\text{out}} = p \cdot 1 = -10,06 \text{ N/m}$, the corresponding stress-values are obtained, as illustrated in Figure 6.27b. It is crucial to emphasize that the wall thickness was determined based on the maximum allowable tangential stress of 40 MPa.

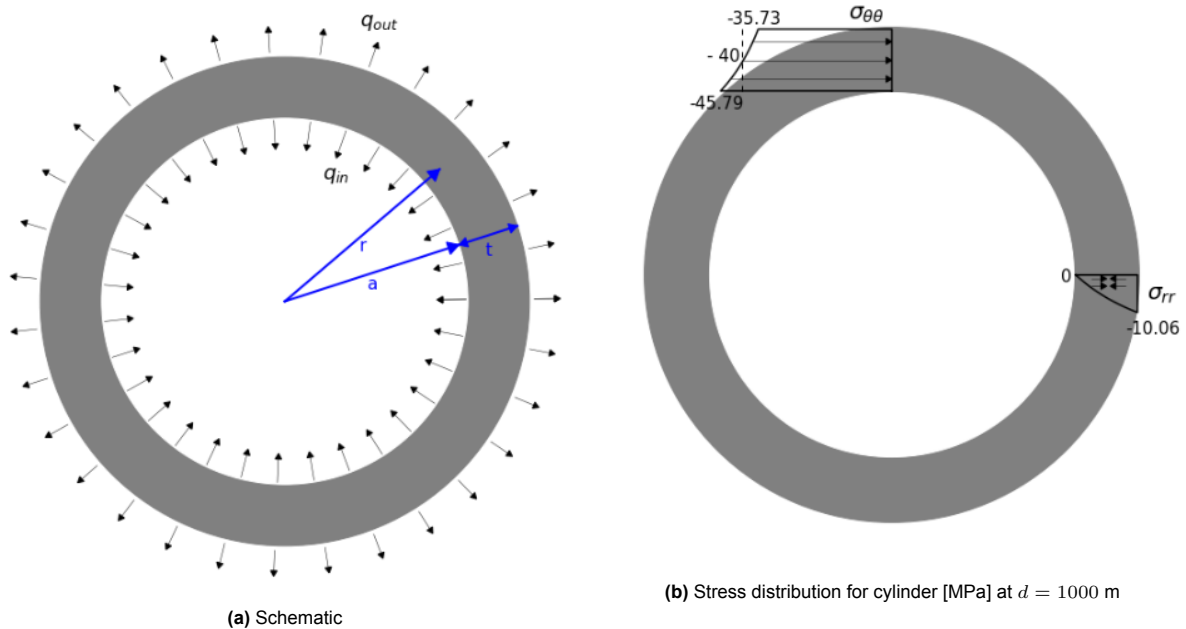


Figure 6.27: Thick-walled tube with internal and external load, representing the cylinder cross-section

6.2.3. Numerical model of sphere and cylinder

The analytical solutions presented in Subsections 6.2.1 and 6.2.2 undergo numerical verification using Diana FEA. Given the round shapes of both the sphere and cylinder, multiple symmetry axes are utilized to reduce the number of elements in the numerical analysis. This approach facilitates the avoidance of singularities, by eliminating the need for point supports. Additionally, a constant distributed force, normal to the external surface of both shapes, is applied as the load in the numerical models, mimicking the constant hydrostatic pressure assumed in the analytical calculations. Both models are illustrated in Figure 6.28. Detailed model outputs are presented in Appendix I.1.

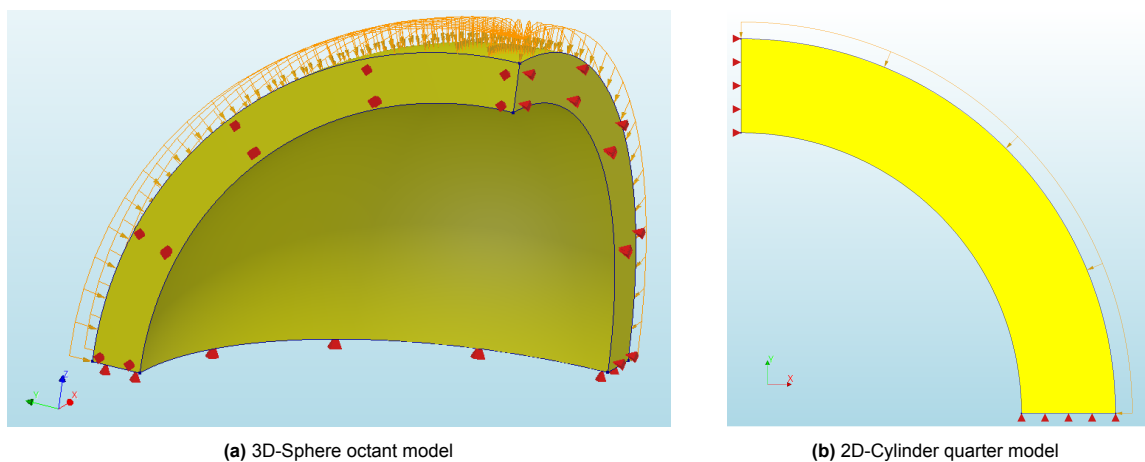


Figure 6.28: Numerical verification of uniform compression assumption with Diana FEA

The parameters used to create the models for the sphere and cylinder are detailed in Table 6.4. Given the axisymmetric nature of both models, any cut that traverses the entire wall thickness can be utilized to analyze the tangential stress in the wall.

Model parameter	Sphere	Cylinder
Internal volume V [m ³]	9000	9000
Internal radius a [m]	12,9	4,92
Wall thickness t [m]	1,86	1,65
Distributed normal force [MPa]	10,06	10,06
Young's Modulus [MPa]	39100	39100
Model dimension	3D	2D
Number of symmetry axes	3	2
Model fraction	$\frac{1}{8}$	$\frac{1}{4}$
Element type	Structural solids CHX60 & CPY39 CTE30 & CTP45	Plane stress CQ16M & CT12M CQ16M & CT12M
Element size [mm]	155	50
Number of elements	30.169	1.452
Number of nodes	108.358	4.547
Number of dofs	650.148	9.094
Number of elements over wall thickness	6	17
Element thickness [mm]	n.a.	1000
Type of analysis	Linear Elastic	Linear Elastic

Table 6.4: Diana FEA model parameters for verification of uniform stress assumption

6.2.4. Evaluation of uniform stress assumption

The analytically determined values of tangential stress across the wall thickness were calculated using Equations 6.9 and 6.11 and are presented in Figures 6.26b and 6.27b. The numerical values of the tangential stress were determined by Diana FEA, utilizing the models as described in Figure 6.28 and Table 6.4.

The results of these analyses are depicted in Figure 6.29. The analytically determined tangential stresses perfectly coincide with the numerical ones, confirming the accuracy of the analytical solutions. This result is expected, given that, under the imposed conditions, the resulting elastic stresses were previously proven [63, 64, 65].

Figure 6.29 illustrates that the assumption of uniform compressive stress over the wall thickness results in a slight underestimation of the maximum tangential stress. For both the sphere and cylinder, the maximum tangential stress occurs at the inner radius of the shape. Interestingly, the tangential stress in the sphere wall is consistently higher than the design compressive stress. In contrast, the tangential stress for the cylinder is higher than the design stress on the interior surface, reducing to a value lower than the design stress on the exterior surface of the cylinder.

The maximum compressive stresses for the sphere and cylinder are exceeded by 13,41% and 14,47% respectively.

$$\frac{\sigma_{\theta\theta, \text{sphere, max}} - f_{cd}}{f_{cd}} = \frac{-45,365 - (-40)}{-40} = 13,41\%$$

$$\frac{\sigma_{\theta\theta, \text{cylinder, max}} - f_{cd}}{f_{cd}} = \frac{-45,787 - (-40)}{-40} = 14,47\%$$

This observation suggests that the calculated CIV-ratios in Chapter 4 were overly optimistic. This aligns with findings in the literature, where proposed spheres exhibit substantially thicker walls considering

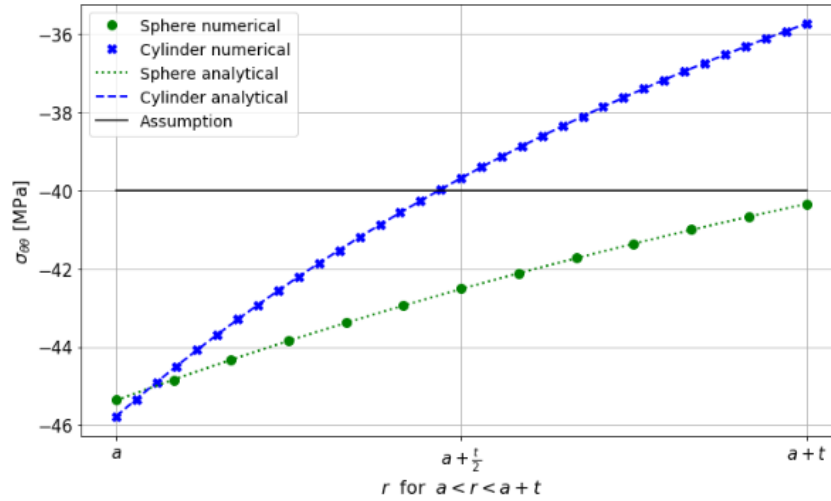


Figure 6.29: Uniform stress over wall thickness verification; at $d = 1000$ m and $f_{cd} = 40$ MPa

similar installation depths and concrete classes [5, 8, 10]. Nevertheless, despite this discrepancy, the calculated CIV-ratios retain their value for comparative purposes among spherical, cylindrical, and toroidal designs in assessing material usage.

6.3. Revised CIV-ratios

In Section 6.2, it was demonstrated that by applying the proposed wall thicknesses the maximum compressive design stress in the walls of both the sphere and cylinder is exceeded.

6.3.1. Increased wall thickness by satisfying found pressure distribution

Substituting $r = a$ and $q_{out} = p$ in Equations 6.9 and 6.11 an expression for the maximum stress in the sphere and cylinder walls is obtained.

$$\sigma_{\theta\theta, \text{sphere, max}} = \frac{3p(a+t)^3}{2((a+t)^3 - a^3)} \quad (6.12)$$

$$\sigma_{\theta\theta, \text{cylinder, max}} = \frac{2p(a+t)^2}{(a+t)^2 - a^2} \quad (6.13)$$

Through an iterative process of trial and error, the wall thicknesses were adjusted in the equations mentioned above until a thickness was reached that met the criteria of $\sigma_{\theta\theta, \text{sphere, max}} = 40$ MPa for the sphere and $\sigma_{\theta\theta, \text{cylinder, max}} = 40$ MPa for the cylinder. This process is outlined in Figure 6.30. The maximum stress $\sigma_{\theta\theta, \text{max}}$, which is present at the interior of the wall, is calculated following Equations 6.9 and 6.11.

Subsequently, the methodologies utilized earlier to estimate material usage for foundation construction, as detailed in Section 4.2, are implemented. The foundation's contribution is then incorporated into the total CIV-ratio for both the sphere and cylinder configurations.

The outcomes of this procedure are depicted in Figure 6.31. To facilitate comparison, the CIV-ratios obtained assuming a uniform pressure distribution in the walls are contrasted with the newly obtained CIV-ratios, which consider a non-uniform pressure distribution in the walls.

When examining Figure 6.31, two notable observations emerge. Firstly, the CIV-ratios obtained through a non-uniform pressure distribution consistently and significantly exceed those derived under the assumption of uniform pressure distribution. This suggests that for the sphere, larger internal volumes can lead to the weight of the design counteracting its buoyancy. Secondly, the increase in CIV-ratio

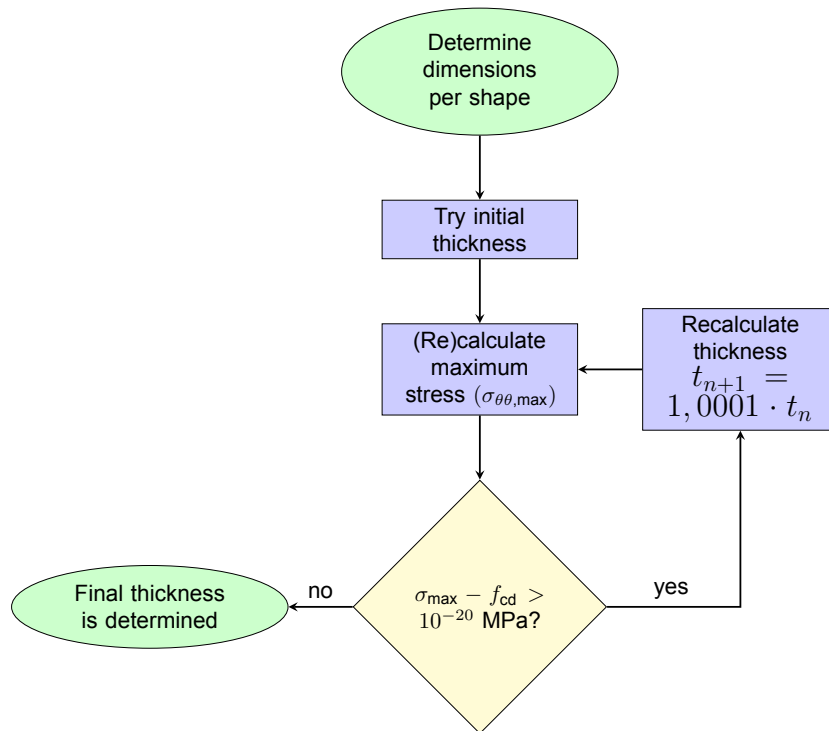


Figure 6.30: Revised workflow for determining wall thickness

for the sphere remains relatively constant, fluctuating between 21,69% and 21,81%. Conversely, the increment in CIV-ratio for the cylinder displays more variability, ranging between 10,31% and 27,06%, with higher increments corresponding to higher slenderness values.

The fluctuating increments result in a less noticeable effect of slenderness on the CIV-ratio of the cylinder. Interestingly, the CIV-ratios for non-slender cylinders obtained under the assumption of uniform pressure are closer to the results derived using the method of non-uniform pressure than the CIV-ratios found for slender cylinders.

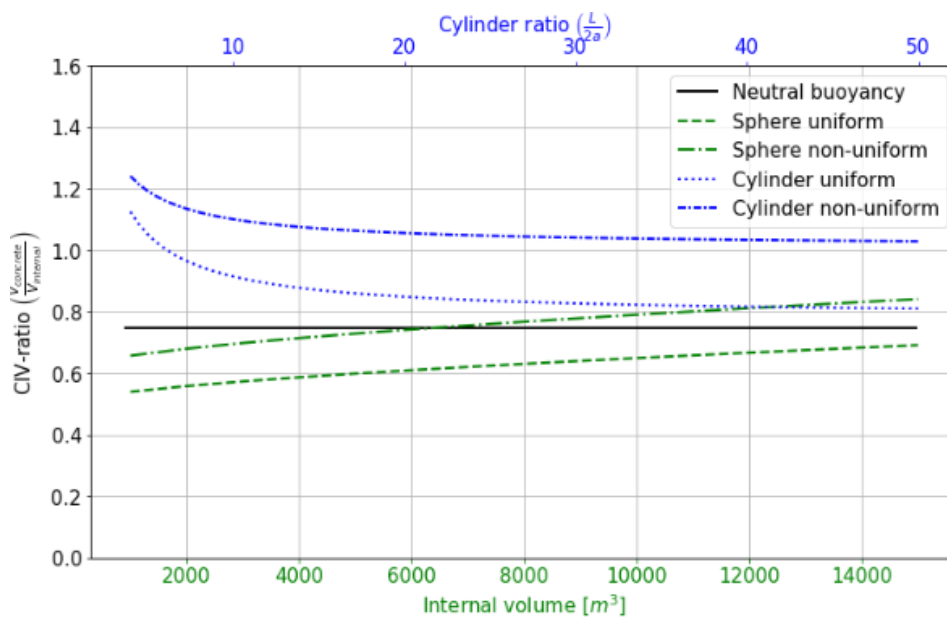


Figure 6.31: CIV-ratios for sphere and cylinder for uniform and non-uniform pressure distribution at $d = 1000$ m and $f_{cd} = 40$ MPa; $V_{\text{internal,cylinder}} = 9.000$ m³

As explained in Section 6.2.4, the surpassing of σ_{\max} is approximately equal for sphere and cylinder, given an internal volume of 9.000 m³ and a slenderness of $\frac{L}{2a} = 12$. These parameters result in an increase of CIV-ratio of 21,71% and 21,67% for sphere and cylinder, respectively.

6.3.2. Introduction of uncertainty in CIV-ratios

The newly established wall thicknesses and corresponding CIV-ratios are presented as the final values on material usage. It is interesting to compare these findings with known values in the literature. However, such a comparison is only feasible for the sphere, as there are no literature examples available for the cylinder. These values are summarized in Table 6.5.

Only one literature source, [10], provided sufficient data for comparison. Other papers, such as [9] and [5], lacked information on concrete compressive strength or foundation design, rendering any meaningful comparison unfeasible.

Origin of data	Symbol	Non-uniform method	Literature [10]	Unit
Installation depth	d	1.000	1.000	m
Concrete compressive design strength	f_{cd}	40	38	MPa
Internal volume	V_{internal}	9.000	8.992	m ³
Internal radius	a	12,904	12,900	m
Wall thickness	t	2,21	2,40	m
Pedestal thickness	t_{pedestal}	0,86	1,00	m
Foundation plate thickness	t_{plate}	1,47	1,6	m
Total volume of concrete	V_{concrete}	7.009	7.408	m ³
CIV-ratio	-	0,78	0,82	m

Table 6.5: Comparison of established spherical design dimensions with literature

The CIV-ratio obtained using the non-uniform method for a sphere is 5,5% lower than the value reported in literature [10], as evident from Table 6.5. This difference could be attributed to the lower concrete compressive design strength used in the literature. However, to address this inconsistency, an uncertainty bandwidth of 6% is added to the ultimate CIV-ratios of the sphere. The lower bounds of the bandwidth correspond to the values obtained with the non-uniform pressure method, while the upper bounds align with those reported in the literature.

For the cylinder, additional stresses in the cylinder wall are anticipated during both transport and installation, as detailed in Section 5.4. Suspending the cylinder from the water surface during these phases introduces a bending moment, resulting in a maximum additional stress of $\pm 1,29$ MPa in the outermost fiber of the cross-section of the cylinder. Additionally, as discussed in Section 6.1.3, a maximum additional stress of $\pm 2,88$ MPa is expected at the transition between the cylinder and hemisphere. These values are based on the wall thicknesses established using the uniform pressure method.

On the contrary, the necessary concrete volumes for the cylinder were calculated assuming a hemisphere thickness equal to that of the cylinder tube. However, as detailed in Section 6.1, a hemisphere with a thickness equal to half of the cylinder tube's thickness might suffice and even offer more advantages than maintaining equal thicknesses throughout. A cylinder with an internal volume of 9.000 m³ and a slenderness of $\frac{L}{2a} = 12$, a wall thickness of 2,01 meters is established using the non-uniform method. Utilizing a hemisphere with half the cylinder tube thickness, so that $t_h = 0,5t_c$, results in a 4,6% decrease of material usage compared to maintaining equal thicknesses.

To address the additional stresses in the cylinder, a 5% uncertainty bandwidth is added to the CIV-ratios obtained with the non-uniform method. Additionally, to account for the thinner hemispherical design, a

5% uncertainty bandwidth is subtracted from the CIV-ratios found with the non-uniform method.

The percentages have been integrated into the previously presented CIV ratios from Figure 6.31. A central line has been added across the bandwidths to enhance clarity. The revised results are illustrated in Figure 6.32. Specifically, for the cylinder, the design with a hemispherical cap is displayed in this graph.

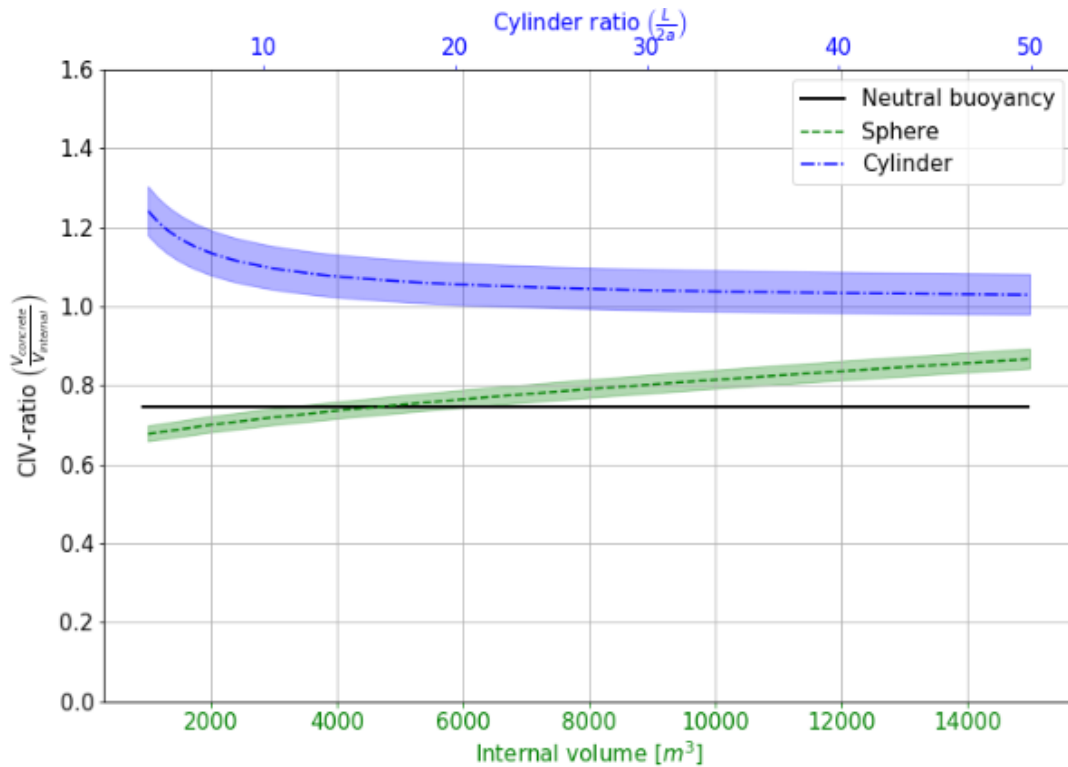


Figure 6.32: CIV-ratios for sphere and cylinder with hemispherical cap after introducing wall thickness uncertainty; at $d = 1000$ m and $f_{cd} = 40$ MPa; $V_{\text{internal,cylinder}} = 9.000$ m³

Introducing uncertainty bandwidths brings a fresh perspective to the CIV ratios of spheres and cylinders. The newfound uncertainty hints at the possibility of spheres relying solely on gravity, potentially removing the need for additional ballast. Despite this revelation, other findings remain consistent. It is still apparent that larger internal volumes tend to increase the CIV ratio for spheres, while the ratio for cylinders decreases with greater slenderness. Moreover, spheres consistently exhibit lower and more favorable CIV ratios compared to cylinders, on average.

A spherical design with an internal volume ranging from 9.000 to 12.000, necessitates 25,9% – 28,5% less material compared to a cylindrical design with a slenderness of $\frac{L}{2a} = 12$, and 23,5% – 26,4% less material than a cylindrical design with a slenderness of $\frac{L}{2a} = 20$.

7

Synthesis, Implications, and Future Directions

This Chapter synthesizes the extensive array of results presented and discussed throughout this report, aiming to offer readers a clear understanding and facilitate easy comparison through a concise summary presented in a tabular format. Following this summary, an in-depth discussion on the quality and implications of the results ensues, leading to a conclusive analysis. Furthermore, recommendations for future research directions are proposed to guide subsequent inquiries in the field.

7.1. Summary of results

In culmination, the findings presented in this thesis underscore the significance of considering the shape of reservoirs in relation to material usage. Moreover, they provide valuable insights into optimizing the construction process and enhancing cap design for cylindrical reservoirs.

As described extensively in Chapter 2, the potential for energy storage capacity grows with deeper depths and larger internal volumes. However, constraints on installation depth, taking into account factors such as topography, hydrostatic pressure, and accessibility, highlight the importance of enhancing storage capabilities by expanding the overall internal volume of the system.

Regarding the reservoirs

For all three shape variants—sphere, cylinder, and torus—the contribution of the reservoir to the total CIV-ratio remains constant across a broad spectrum of internal volumes, as illustrated in Figure 4.4.

Increasing the slenderness of the cylinder and torus results in a lower CIV-ratio for the reservoir, which is generally preferable. This reduction is most pronounced at lower slenderness levels, with the benefits diminishing around a value of $\frac{L}{2a} \approx 30$, as depicted in Figure 6.32. However, higher slenderness values lead to significantly larger external dimensions of the reservoir, presenting challenges in terms of constructability and transportability.

In terms of CIV-ratio, the spherical reservoir emerges as the most advantageous shape. Using the non-uniform method, the reservoir of the sphere attains a CIV-ratio that is 40% lower than that of the most slender variants of the cylinder. This discrepancy is particularly striking at lower slenderness values. For example, at a slenderness value of 4, the sphere's reservoir utilizes 50% less material compared to the reservoir of the cylinder. Similar results, albeit obtained with the less accurate uniform method, were observed for the torus.

The influence of slenderness on the CIV-ratio of the cylinder is solely attributable to the contribution of the caps. This influence becomes less pronounced when a hemispherical cap is used instead of a flat cap, as depicted in Figure 6.25. Conversely, for the torus, variations in slenderness affect the CIV-ratio predominantly due to the reduced membrane forces associated with lower slenderness values.

An optimal slenderness value falls within the range of 10 to 20 for the cylinder. Within this range, a satisfactory CIV-ratio is achieved while keeping external dimensions manageable. However, for the torus, such an ideal range was not pinpointed. Balancing acceptable CIV-ratios with realistic external dimensions remains challenging. The substantial dimensions present constraints on feasible construction sites for the torus, contradicting the initial goal of avoiding such limitations. Consequently, further consideration of the torus was discontinued.

When applying the uniform method, the spherical reservoir maintains buoyancy effortlessly throughout the entire spectrum of realistic internal volumes, suggesting the necessity of additional ballast. However, with the non-uniform method, the weight of the sphere surpasses its buoyancy from internal volumes of approximately 5.000 m³ and higher, as depicted in Figure 6.32. In contrast, the reservoirs of the cylinder and torus consistently outweigh the water they displace, even at the most extreme levels of slenderness, independent of the method used for wall thickness determination.

The CIV-ratios obtained with the non-uniform pressure method slightly fell below those reported in literature, prompting the introduction of an uncertainty bandwidth of 6%, as outlined in Section 6.3. Conversely, the additional stresses arising from transport and installation loads, as well as potential material savings in the hemispherical cap design, support an uncertainty bandwidth of 10% for the cylinder.

Regarding the foundations

In order to adequately support the spherical reservoir, the inclusion of a pedestal and foundation plate was considered. It became evident that this arrangement notably impacts the overall CIV-ratio of the sphere. The foundation's contribution to the CIV-ratio escalates with greater internal volumes, varying between 0,1 and 0,2 for internal volumes ranging from 4.000 to 15.000 m³.

For the cylindrical and toroidal reservoirs, a straightforward design approach is adopted to ensure a stable, flat surface on the ground. The required width of this base, determined by the maximum soil bearing pressure, shows minor fluctuations with changing internal volumes. However, the variations in its effect on the overall CIV-ratio for different internal volumes are insignificant. Its contribution to the CIV-ratio of the cylinder and torus ranges from 0,01 to 0,02.

Regarding construction

According to findings in the literature, a hybrid construction approach named the RCAM (Reinforced Concrete Additive Manufacturing) method, which combines 3D Concrete Printing (3DCP) with traditional casting, emerges as the most promising technique for building the sphere. The formwork is constructed using 3DCP, followed by the casting process. However, the feasibility of implementing 3DCP on this scale remains a topic of debate due to its novelty. Another challenge with this method is the constraint posed by the maximum inclination angle of the printer, set at 45 degrees, which requires the use of considerably large prefabricated elements for the bottom and top of the sphere.

As outlined in Section 5.3, the horizontal jump-forming method emerges as the most viable construction approach for the cylinder. This method entails a semi-continuous process, where the cylinder tube is built incrementally using ring elements. The production cycle of a single ring element begins with the extension of a launching girder, onto which inner formwork is affixed. Subsequently, the outer formwork is positioned, allowing for the pouring of concrete.

Unlike the RCAM method, the proposed horizontal jump-forming technique has been successfully utilized in tunnel construction, demonstrating its reliability. It is noteworthy that while the most suitable construction method for the cylinder is not feasible for the sphere, the reverse is not the case. This suggests that constructing the cylinder is less complex compared to the sphere.

Regarding cylinder cap design

As detailed in Section 6.1, a hemispherical cylinder cap offers several advantages over a flat one. By distributing loads in the normal direction, it optimally utilizes the high compressive resistance properties of concrete. Additionally, the hemispherical cap demonstrates superior material usage efficiency.

While it has not been demonstrated that additional stresses associated with bending moments introduced by an edge disturbance in the transition from cylinder to hemisphere can be entirely eliminated,

they can be mitigated or reduced. To achieve this, a hemisphere with a thickness between 40 – 60% of the cylinder thickness should be employed. This results in a maximum stress increase of approximately ± 3 MPa at a depth of 1000 meters.

To alleviate stress concentrations linked to the transition from cylinder to hemisphere, a smooth connection should be established. Sharp angles in the transition zone should be avoided, making a circular transition the most suitable option.

Regarding implementation aspects

Considering the internal volumes mentioned in the literature, the sphere boasts a draught exceeding 21 meters, while the cylinder maintains a draught of 13 meters or less, which decreases with increasing slenderness. Given the dimensions of some of the world's largest drydocks, it is apparent that floating the sphere out of a dock would require pontoons with substantial volumes to provide buoyancy. This poses a challenge due to the limited available space in the dry dock to accommodate such pontoons. Conversely, this issue is less problematic for the cylinder, given its lower height. Additionally, its slenderness can be adjusted to meet the required draught. Consequently, for a fixed internal volume over 9.000 m^3 , it is improbable that the sphere can be constructed in and floated out of a dry dock, whereas for a cylinder, it remains the preferred option.

With these considerations in mind, two options remain for the sphere. Firstly, aiming for a lower internal volume would decrease the draught of the structure. However, this approach demands a greater number of units to maintain the same level of energy storage, thereby posing risks of increased maintenance, decreased efficiency, and higher capital expenditures. Alternatively, shifting the construction location from a dry dock to a fjord eliminates constraints on the internal volume, allowing for greater flexibility in design and construction. Nevertheless, 3DCP construction on water introduces novel challenges. Additionally, the availability of fjords worldwide is limited, thereby restricting the number of topographically feasible installation locations.

While the sphere's draught poses challenges during load-out from a dry dock, its transport is relatively straightforward as it can be moved afloat using tug boats or a semi-submersible vessel. Conversely, transporting the cylinder necessitates the use of two or more catamaran-like pontoons, with the cylinder suspended from them. Throughout the transport, the cylinder remains submerged. The additional bending moment related to the suspension of the cylinder does not introduce high stresses in the cylinder.

The installation process for both the sphere and the cylinder entails similar aspects. In both cases, the seabed must be prepared by creating a level surface and removing large boulders. Subsequently, the sphere or cylinder will be lowered using steel cables and positioned onto the seabed.

The sphere requires two concrete connections, specifically between the body, its top, and its bottom. In contrast, the cylinder necessitates a multitude of connections, the precise number contingent on the length of the cylinder rings. Although it was only qualitatively examined, an increased number of connections negatively impacts the watertightness of the reservoir, consequently reducing the system's efficiency.

Comparison of spherical and cylindrical reservoirs

An overview of the key findings from this thesis research is presented in Table 7.1. Hyperlinks to relevant sections are provided where necessary. These sections explain in detail how these results were obtained.

The selected internal volume, which determines the other dimensional parameters for the sphere and cylinder as outlined in Table 7.1, is somewhat arbitrary. Currently, an internal volume of 9.000 m^3 has been utilized, as this value was sourced from literature [10].

As previously mentioned, the dimensions of the cylinder are also governed by its slenderness. In the summary provided in Table 7.1, slenderness values of $\frac{L}{2a} = 12$ and $\frac{L}{2a} = 20$ have been adopted. This choice strikes a balance, ensuring an acceptable CIV-ratio without overly elongating the structure. However, it is worth noting that alternative slenderness values can also be considered based on specific project requirements and constraints. Furthermore, a hemispherical cap is assumed.

The dimensional parameters presented in Table 7.1 are determined following the methodology outlined in Chapter 4, without accounting for uncertainty as introduced in Section 6.3.

Aspect	Sphere	Cylinder
Internal volume [m ³]	9.000	9.000
Slenderness [-]	n.a.	12 / 20
Internal radius [m]	12,9	4,84 / 4,11
Wall thickness [m]	2,21	2,06 / 1,74
External length [m]	n.a.	129,8 / 176,0
Volume of concrete in reservoir [m ³]	5.450	9.700 / 9.450
Volume of concrete in support structure [m ³]	1.550	100 / 50
Total volume of concrete [m ³] (4.3)	7.000	9.800 / 9.500
Draught of structure [m]	26,7 (A.2)	13,8 / 11,7 (A.3)
Additional buoyancy required for 10 meter draught [m ³]	10.600	8.500 / 5.450
In standard shipping containers [2,44×2,59×12,19] [m]	123	99 / 64
Components of reservoir	Prefab bottom and top of sphere, casted mid-section (2.7.2)	Cylinder ring segments, hemisphere caps
Components of support structure	Ring-shaped pedestal and circular foundation plate (2.8)	Base footing to provide flat contact surface with seabed (3.2.2)
Most feasible construction method	Hybrid 3DCP and casting (2.7.2)	Horizontal jump-forming (5.3.2)
Complex construction techniques involved	3D concrete printing	Horizontal jump-process with launching girder
Most feasible construction location	Fjord (2.8.1)	Dry dock (5.4.1)
Reference projects	Not executed on intended scale	Fehmarnbelt, Tunnel Steinhaus by Doka (F.3)
Transport method	Floating or on semi-submersible vessel (2.8.2)	Submerged (5.4.1)
Material for transport	Tug boats or semi-submersible vessel	Tug boats and catamaran-like pontoon
Requirements for installation	Seabed preparation and descend (2.8.3)	Idem dito
Points of attention		Additional stresses due to bending moment in cylinder (5.4.1)
Stability of structure	Verified in literature [10]	Not verified; additional measures might be necessary (5.4.3)
Vulnerable connections for watertightness	Prefab bottom/top - Casted mid-section (2.8.4)	Ring segment - Ring segment & Ring segment - Hemisphere cap (5.3.3)
Connection type (respectively)	Cold joint	Cold joint & Wet joint/compression seal

Table 7.1: Summary of results

7.2. Discussion

The results presented in this report encompass both quantitative and qualitative aspects. The quantitative findings stem from calculations, inherently carrying a level of uncertainty attributed to the assumptions made during their computation.

This Section aims to provide a critical analysis and interpretation of the findings presented in this thesis, elucidating their significance. It is divided into three parts: the starting points, the CIV-ratios, and the construction and implementation aspects.

After evaluating the dimensions of the structures, it became apparent that the torus would be unfeasible for implementation without restrictions on construction location. Consequently, it was ruled out as an option. However, it cannot be definitively stated that the torus is never a viable option.

Starting points

Three reservoir shapes underwent examination. It was argued that for a submerged structure, the most effective shape is round as it distributes compressive loads most efficiently. The rationale behind selecting these shapes was discussed in Section 1.2. However, other shapes were not taken into account. It is conceivable that there are shapes relying on different principles that could be suitable as reservoirs. One example is a modular honeycomb design, where hexagonal cells are utilized to distribute pressure. The cells would be cylindrical at the edges of the structure. Alternatively, a combination of shapes might be used to further optimize the balance between material usage and construction feasibility.

The design initially favored individual pump/turbine systems for each reservoir, highlighting advantages in system efficiency, resilience, and cost-effectiveness, as discussed in Section 2.3. The focus was on minimizing the number of pumps to mitigate maintenance needs, while also noting the typically higher efficiency of larger pump/turbines. Concerns were also raised about potential differential settlement issues between reservoirs, discouraging the connection of multiple reservoirs to a single pump. Consequently, it was concluded that each reservoir should have its own pump/turbine system. However, it is important to note that these assertions were qualitative, lacking quantification regarding maintenance requirements, the impact of pump/turbine size on efficiency, or the risk associated with differential settlements.

When evaluating the loads on the reservoirs, only a uniform distributed normal force of 10,06 MPa was accounted for, representing the hydrostatic pressure at a depth of 1000 meters. However, in reality, there exists a gradient in the hydrostatic load, decreasing linearly from the bottom to the top of the structure. Additionally, gravitational, horizontal or dynamic loads were not taken into consideration. These additional loads may impact the necessary wall thickness of the reservoirs. Their impact is believed to be limited.

When evaluating the structural loads, no safety factors have been factored in, while a material safety factor of 50% has been implemented. Incorporating appropriate load safety margins might present drawbacks in terms of material consumption. Conversely, reducing the material safety factor could lead to a favorable impact on material utilization.

Structural aspects

Upon assessing the required wall thickness for the reservoirs, an initial assumption was made that compressive stress across the wall is uniformly distributed, a presumption validated extensively in Section 6.3. Results indicated that the desired compressive stress levels were surpassed by 13,4% for the sphere and 14,5% for the cylinder. In light of these findings, the determined wall thicknesses outlined in Chapter 4 were deemed inadequate for the intended installation depth of 1000 meters, considering a design compressive strength of 40 MPa. Subsequently, a new calculation was performed based on non-uniform compressive stress in the walls for the sphere and cylinder. However, no such calculation was carried out for the torus, as it had already been disregarded as an option at this stage. Consequently, the CIV-ratios presented for the torus were ultimately too low. Nevertheless, this does not alter the conclusions reached.

In Section 5.4, additional loads due to transport and installation of the cylinder were determined. It was found that these loads, mainly bending moments implied due to the cylinder's own weight, do not result in significant additional stresses in the structure. These calculations were made based on the earlier

established wall thicknesses under the assumption of uniform compression. Since it was later found that the compression in the wall is actually non-uniform, leading to thicker required walls, transport and installation loads increase as well. However, due to the increased cross-section, the section modulus, and thus the resistance to bending moments increased too. The additional stresses due to transport and installation for the higher wall thicknesses, established with the non-uniform pressure method, have not been reconsidered. Nonetheless, it is expected that the new cross-section would actually decrease the additional stresses associated with bending moments from transport and installation. On the other hand, the necessary cable cross-section increases solely because of the additional weight of the structure. However, this is not deemed problematic since the number of cables can be readily augmented.

Similarly, the increased wall thicknesses lead to heightened deviation from thin shell behavior in the connection between the hemisphere and cylinder. It was demonstrated that adjusting the hemisphere thickness can align tangential stresses between the cylinder and hemisphere. It is not anticipated that an increase in wall thickness would diminish this possibility. Consequently, the anticipated additional stresses at the connection between the cylinder and hemisphere are not regarded as significant, even with thicker walls in place.

The foundation of the sphere was designed by adapting a foundation model presented in a technical report from literature [10] to match the desired reservoir size, as detailed in Section 4.2.1. It was assumed that the distributed load at the bottom of the pedestal, consisting of the weight of the reservoir and the pedestal itself, should remain constant. This assumption guided the determination of the required thickness of the pedestal. Additionally, it was presumed that the foundation plate's ability to withstand bending moments is solely dependent on its thickness. Consequently, the necessary bending moment resistance was calculated, and subsequently, the thickness of the foundation plate was determined. Particularly in determining the thickness of the foundation plate, this approach provides estimated values. Consequently, the scaling of the foundation design from [10] may have resulted in over- or underdimensioning. Nonetheless, it is improbable that this will significantly impact the final analysis.

The foundation design for the cylinder and torus is based on a different methodology. Through an iterative process, the investigation focused on determining the required foundation area to apply a pressure of 200 kPa on the soil. This approach often resulted in narrow foundations, particularly noticeable for structures with low slenderness values, raising questions about stability, especially in the case of the cylinder. Since stability considerations were not addressed, it is conceivable that additional material may be required, or the foundation design may need reassessment. However, it is not expected that this will introduce severe design challenges.

The varied approaches to foundation design for the reservoirs introduce complexities when comparing foundations across different shapes. While CIV-ratios can be compared, the disparate design methodologies raise questions about the accuracy of these values. That said, it is unlikely that these results will necessitate a reevaluation of the conclusions.

Construction and implementation aspects

When exploring suitable construction methods for the sphere and cylinder, two approaches were considered. For the sphere, a review of existing proposed construction techniques was undertaken, revealing the RCAM method as the most suitable. However, it is important to note that the literature reviewed for these construction methods already provided a preliminary design and dimensions. Since these parameters are not yet known in this report, alternative construction methods may also be viable.

Regarding the cylinder, five potential construction techniques were initially identified, as presented in Section 5.2. Each method underwent an evaluation based on complexity, construction time, and scalability, although these assessments were qualitative. Subsequently, in a second evaluation round, the two remaining construction methods were compared. Horizontal jump-forming was deemed preferable over precast elements due to lower risks of leakages, although this was only qualitatively argued. Hence, although horizontal jump-forming appears to be the most promising method, its suitability requires a more detailed examination.

Considering that the assessment of the watertightness of the sphere was qualitative as well, it is difficult

to reach a definitive conclusion regarding the ability of both the sphere and cylinder to prevent water infiltration.

As outlined in Section 3.4, it is recommended that the pump's inlet be positioned at the lowest point of the reservoir. Leaving water in the reservoir leads to unused internal volume, thereby reducing the system's efficiency. For the sphere, identifying the lowest point and installing the pump/turbine system there is relatively straightforward. However, for the cylinder, pinpointing the lowest point can be challenging. Slight tilting of the cylinder along its length may aid in this regard, but such considerations have not been factored in.

In the evaluation of load situations for transporting and installing the cylinder, as discussed in Section 5.4, only static scenarios were considered, overlooking the inherently dynamic nature of these operations. To address this, a load safety factor of 3 was applied. While this provides significant assistance, it may still not fully account for all dynamic loads, as further verification was not conducted.

7.3. Conclusion

In conclusion, this thesis emphasizes the suitability of a cylindrical reservoir for the MPHES system. The obstacles linked to the spherical shape, such as the untested nature of employing 3D Concrete Printing (3DCP) for construction on the intended scale and the substantial draught exceeding the capacity of some of the world's largest dry docks, can be effectively addressed by adopting a cylindrical design. The proposed construction method for the cylinder enhances the feasibility of the MPHES project. While the sphere exhibits a CIV-ratio that is 23% to 29% lower, the increased material usage associated with the cylindrical design is considered acceptable. Conversely, the toroidal reservoir is deemed unfavorable, as the heightened material usage does not translate to improved constructability.

In contrast to the spherical reservoir, constructing the cylindrical reservoir can leverage established methods proven successful in tunnel construction. Additionally, the structure's draught enables construction in dry docks, presenting significant advantages such as global availability and a streamlined dry construction process. Moreover, it has been demonstrated that the cylinder caps can be designed to induce acceptable additional stresses. Furthermore, transportation and installation methods pose no additional complications compared to those for the sphere.

As the required internal volume decreases, the advantages of the cylindrical design over the spherical reservoir diminish. There comes a turning point where constructing the sphere in a dry dock becomes feasible again, and the proposed construction method using 3D Concrete Printing becomes less complex. Additionally, the size of the prefabricated bottom and top of the sphere becomes manageable once again.

The examination indicates that the cylindrical design is a viable option, especially for larger internal volumes, where the additional costs associated with increased material usage may be offset by the enhanced constructability of the cylindrical design, making it more desirable than the spherical option. Investors should therefore carefully consider the trade-off between higher material consumption and a simpler construction process. Nonetheless, for lower internal volumes, it is evident that the sphere still stands out as the optimal choice.

7.4. Recommendations

Based on the findings elucidated in this study, several recommendations emerge to address the identified gaps and enhance future practice.

Considering that the stability of the cylinder has not been previously evaluated, it is essential to undertake such an assessment. The elongated shape and limited footing prompt concerns regarding the cylinder's ability to withstand horizontal forces caused by currents. Moreover, if an applicable case study is accessible, it is crucial to analyze the soil conditions at the site.

Additionally, it is important to note that the designs presented did not account for the use of reinforcement. While it is recognized that reinforcement may be required to ensure adequate resistance against tensional stresses during various stages such as construction, transport, or installation, specific calculations regarding reinforcement were not included. It is recommended that in subsequent design phases,

the incorporation of reinforcement into the design should be carefully considered and implemented as necessary to ensure the structural integrity and durability of the reservoir.

The current investigation into the optimal reservoir shape primarily focuses on material usage and construction feasibility. However, to attract investor interest, it is essential to examine the costs associated with constructing, transporting, and installing both spherical and cylindrical reservoirs. This analysis would facilitate a more informed comparison between the two shapes.

In addition to these smaller recommendations, several additional areas for future research have been identified.

Given the conclusion favoring cylinders over spheres for higher internal volumes, and vice versa for lower internal volumes, exploring the impact of smaller reservoirs on system performance becomes intriguing. While this report cautiously suggests that smaller reservoirs are more prone to pump failure, demand increased maintenance, and exhibit reduced efficiency, further research in this area is warranted to provide a deeper understanding of their effects.

Additionally, delving into the consequences of connecting multiple reservoirs to a single pump offers a compelling area for investigation. This approach brings forth fresh challenges, including the management of potential differential settlements and the selection of tubes capable of withstanding hydrostatic pressure. However, the advantages are notable: maintaining smaller, constructible individual reservoirs while enjoying the efficiency of a single pump setup, thereby mitigating maintenance demands and reducing the risk of pump failure.

In this report, an initial installation depth of 1000 meters served as the basis for the design. However, given the scarcity of topographical spots with such depth near offshore wind farms, it becomes intriguing to assess the viability of implementing the MPHES system at shallower depths. Shallower depths offer the benefit of reduced hydrostatic pressure but pose the challenge of diminished energy storage capacity per volume. Exploring the threshold depth value where shallower depths cease to be economically feasible is of interest.

Considering a broader perspective, it is imperative to review the costs related to implementing and maintaining the entire system, especially as the cylinder emerges as a feasible reservoir shape. To achieve practical realization, the MPHES system should be comparable to other offshore energy storage techniques.

References

- [1] IEA. *World Energy Balances: Overview*. Tech. rep. 2021. URL: <https://www.iea.org/reports/world-energy-balances-overview>.
- [2] Statista. *Electricity generation worldwide from 1990 to 2021*. 2021. URL: <https://www.statista.com/statistics/270281/electricity-generation-worldwide/#:~:text=Global%20electricity%20generation%20has%20increased,28%2C500%20terawatt%2Dhours%20in%202021..>
- [3] IEA. *Global grid-scale storage*. Tech. rep. 2022. URL: <https://www.iea.org/reports/grid-scale-storage>.
- [4] U. Krengel. *Press Releases*. 2016. URL: https://www.goethe-university-frankfurt.de/74987561/Energy_storage_system_of_tomorrow_tested_for_the_first_time_in_Lake_Constance (visited on 07/25/2023).
- [5] Alexander Slocum et al. "Ocean Renewable Energy Storage (ORES) System: Analysis of an Undersea Energy Storage Concept". In: *Proceedings of the IEEE* 101 (Apr. 2013), pp. 906–924. DOI: 10.1109/JPROC.2013.2242411.
- [6] C. Marrewijk. "Form Finding for a Submerged Floating Tunnel". MA thesis. Delft University of Technology, 2020.
- [7] Christian Dick, Matthias Puchta, and Jochen Bard. "StEnSea – Results from the pilot test at Lake Constance". In: *Journal of Energy Storage* 42 (2021), p. 103083. ISSN: 2352-152X. DOI: <https://doi.org/10.1016/j.est.2021.103083>. URL: <https://www.sciencedirect.com/science/article/pii/S2352152X21007891>.
- [8] M. Puchta et al. "Development and testing of a novel offshore pumped storage concept for storing energy at sea – Stensea". In: *Journal of Energy Storage* 14 (2017). On The Waterfront: Offshore and Seaside Energy Storage for Rapidly Growing Coastal Populations, pp. 271–275. ISSN: 2352-152X. DOI: <https://doi.org/10.1016/j.est.2017.06.004>. URL: <https://www.sciencedirect.com/science/article/pii/S2352152X17302207>.
- [9] Henning Hahn et al. "Techno-economic assessment of a subsea energy storage technology for power balancing services". In: *Energy* 133 (2017), pp. 121–127. ISSN: 0360-5442. DOI: <https://doi.org/10.1016/j.energy.2017.05.116>. URL: <https://www.sciencedirect.com/science/article/pii/S0360544217308733>.
- [10] B. Speelman. *Design specification; conceptual design of a Full-Scale M-PHES System*. Tech. rep. Witteveen+Bos, 2022.
- [11] P. C. Nikolaos, F. Marios, and K. Dimitris. "A Review of Pumped Hydro Storage Systems". In: *Energies* 16.11 (2023). ISSN: 1996-1073. DOI: 10.3390/en16114516. URL: <https://www.mdpi.com/1996-1073/16/11/4516>.
- [12] power-technology. *Power plant profile*. 2023. URL: <https://www.power-technology.com/marketdata/> (visited on 07/21/2023).
- [13] Bernhard Ernst. *Interview with Dr. Bernhard Ernst, Deputy Head of Energy Storage at Fraunhofer Institute for Energy Economics and Energy System Technology*. Personal interview. Sept. 2023.
- [14] H. Díaz and C. Guedes Soares. "Review of the current status, technology and future trends of offshore wind farms". In: *Ocean Engineering* 209 (2020), p. 107381. ISSN: 0029-8018. DOI: <https://doi.org/10.1016/j.oceaneng.2020.107381>. URL: <https://www.sciencedirect.com/science/article/pii/S002980182030411X>.
- [15] Emanuel P.P. Soares-Ramos et al. "Current status and future trends of offshore wind power in Europe". In: *Energy* 202 (2020), p. 117787. ISSN: 0360-5442. DOI: <https://doi.org/10.1016/j.energy.2020.117787>. URL: <https://www.sciencedirect.com/science/article/pii/S036054422030894X>.
- [16] Jan Kroon. *Floating solar panels*. 2023. URL: <https://www.tno.nl/en/sustainable/renewable-electricity/sustainable-solar-land-water/floating-solar-panels/>. (accessed: 14.11.2023).

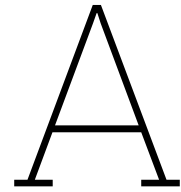
- [17] Chiyembekezo Kaunda, Cuthbert Kimambo, and Torbjørn Nielsen. "Potential of Small-Scale Hydropower for Electricity Generation in Sub-Saharan Africa". In: *ISRN Renewable Energy 2012* (Aug. 2012). DOI: 10.5402/2012/132606.
- [18] H. Abdi et al. "Chapter 7 - Energy Storage Systems". In: *Distributed Generation Systems*. Ed. by G.B. Gharehpetian and S. Mohammad Mousavi Agah. Butterworth-Heinemann, 2017, pp. 333–368. ISBN: 978-0-12-804208-3. DOI: <https://doi.org/10.1016/B978-0-12-804208-3.00007-8>. URL: <https://www.sciencedirect.com/science/article/pii/B9780128042083000078>.
- [19] G.L. Bullard et al. "Operating principles of the ultracapacitor". In: *IEEE Transactions on Magnetics* 25.1 (1989), pp. 102–106. DOI: 10.1109/20.22515.
- [20] Florian Klumpp. "Comparison of pumped hydro, hydrogen storage and compressed air energy storage for integrating high shares of renewable energies—Potential, cost-comparison and ranking". In: *Journal of Energy Storage* 8 (2016), pp. 119–128. ISSN: 2352-152X. DOI: <https://doi.org/10.1016/j.est.2016.09.012>. URL: <https://www.sciencedirect.com/science/article/pii/S2352152X16301712>.
- [21] D. Connolly et al. "Practical operation strategies for pumped hydroelectric energy storage (PHES) utilising electricity price arbitrage". In: *Energy Policy* 39.7 (2011). Special Section: Renewable energy policy and development, pp. 4189–4196. ISSN: 0301-4215. DOI: <https://doi.org/10.1016/j.enpol.2011.04.032>. URL: <https://www.sciencedirect.com/science/article/pii/S0301421511003156>.
- [22] Marcus King et al. "Overview of current compressed air energy storage projects and analysis of the potential underground storage capacity in India and the UK". In: *Renewable and Sustainable Energy Reviews* 139 (2021), p. 110705. ISSN: 1364-0321. DOI: <https://doi.org/10.1016/j.rser.2021.110705>. URL: <https://www.sciencedirect.com/science/article/pii/S1364032121000022>.
- [23] Behnam Zakeri and Sanna Syri. "Electrical energy storage systems: A comparative life cycle cost analysis". In: *Renewable and Sustainable Energy Reviews* 42 (2015), pp. 569–596. ISSN: 1364-0321. DOI: <https://doi.org/10.1016/j.rser.2014.10.011>. URL: <https://www.sciencedirect.com/science/article/pii/S1364032114008284>.
- [24] Maurice Moonitz and E. Cary Brown. "The Annuity Method of Estimating Depreciation". In: *The Accounting Review* 14.4 (1939), pp. 424–429. ISSN: 00014826. URL: <http://www.jstor.org/stable/239369> (visited on 08/01/2023).
- [25] R. Ansorena Ruiz et al. "Low-head pumped hydro storage: A review on civil structure designs, legal and environmental aspects to make its realization feasible in seawater". In: *Renewable and Sustainable Energy Reviews* 160 (2022), p. 112281. ISSN: 1364-0321. DOI: <https://doi.org/10.1016/j.rser.2022.112281>. URL: <https://www.sciencedirect.com/science/article/pii/S1364032122002003>.
- [26] Chuangxin Lyu, Junghee Park, and J. Carlos Santamarina. "Depth-Dependent Seabed Properties: Geoacoustic Assessment". In: *Journal of Geotechnical and Geoenvironmental Engineering* 147.1 (2021), p. 04020151. DOI: 10.1061/(ASCE)GT.1943-5606.0002426. eprint: <https://ascelibrary.org/doi/pdf/10.1061/%28ASCE%29GT.1943-5606.0002426>. URL: <https://ascelibrary.org/doi/abs/10.1061/%28ASCE%29GT.1943-5606.0002426>.
- [27] Gabriel Falzone. *Interview with Gabriel Falzone, PHD. Leading developer of MPHES at RCAM*. Personal interview. Sept. 2023.
- [28] René Mazur. *Interview with René Mazur, Structural Engineer at Hochtief Solutions*. Personal interview. Oct. 2023.
- [29] H. van de Vreede. "Design of concrete spheres for energy storage at the ocean bed". MA thesis. Delft University of Technology, 2023.
- [30] Hochtief Solutions AG. "Verfahren zur Herstellung eines Unterwasserspeichers". EP2700594A1. 2014. URL: <https://patents.google.com/patent/EP2700594B1/de>.
- [31] Technip FMC. *Demonstration of a Next Generation, Low Cost, Additively Manufactured Marine Pumped Hydroelectric Storage Technology. Deliverable 2E Method Statement for Installation*. Tech. rep. Submitted to the Department for Business, Energy and Industrial Strategy. *Confidential document*. Technip, Mar. 2022.
- [32] Fernando Núñez, David Canca, and Ángel Arcos-Vargas. "An assessment of European electricity arbitrage using storage systems". In: *Energy* 242 (2022), p. 122916. ISSN: 0360-5442. DOI:

- <https://doi.org/10.1016/j.energy.2021.122916>. URL: <https://www.sciencedirect.com/science/article/pii/S0360544221031650>.
- [33] [guinnessworldrecords.com](https://www.guinnessworldrecords.com/world-records/heaviest-weight-lifted-by-a-crane). *Guinness World Records*. 2008. URL: <https://www.guinnessworldrecords.com/world-records/heaviest-weight-lifted-by-a-crane> (visited on 08/12/2023).
- [34] Unknown. *Demonstration of a next generation, low cost, additively manufactured marine pumped hydroelectric storage technology*. Tech. rep. STORE Consortium, 2022.
- [35] Petra C. van Hennik and Rogier Houtman. "Pneumatic Formwork for Irregular Curved Thin Shells". In: *Textile Composites and Inflatable Structures II*. Dordrecht: Springer Netherlands, 2008, pp. 99–116. ISBN: 978-1-4020-6856-0. DOI: 10.1007/978-1-4020-6856-0_7. URL: https://doi.org/10.1007/978-1-4020-6856-0_7.
- [36] P.C.J. Hoogenboom. *Notes on shell structures*. Lecture book CT5143. 2007.
- [37] Ehud Kroll and Eldad Buchris. "Weight reduction of 3D-printed cylindrical and toroidal pressure vessels through shape modification". In: *Procedia Manufacturing 21* (2018). 15th Global Conference on Sustainable Manufacturing, pp. 133–140. ISSN: 2351-9789. DOI: <https://doi.org/10.1016/j.promfg.2018.02.103>. URL: <https://www.sciencedirect.com/science/article/pii/S2351978918301380>.
- [38] David Roylance. "Pressure Vessels". In: (Aug. 2001). Department of Materials Science and Engineering, Massachusetts Institute of Technology, Cambridge, MA 02139.
- [39] Paul Webb. *Introduction to Oceanography*. Last update: August, 2023. Pressbooks, 2023. Chap. 6. URL: [https://rwu.pressbooks.pub/webboceanography/chapter/6-2-temperature/#:~:text=There%20is%20little%20temperature%20change,the%20deep%20ocean%20\(Figure%206.2..](https://rwu.pressbooks.pub/webboceanography/chapter/6-2-temperature/#:~:text=There%20is%20little%20temperature%20change,the%20deep%20ocean%20(Figure%206.2..)
- [40] M. Lewis et al. "Characteristics of the velocity profile at tidal-stream energy sites". In: *Renewable Energy 114* (2017). Wave and Tidal Resource Characterization, pp. 258–272. ISSN: 0960-1481. DOI: <https://doi.org/10.1016/j.renene.2017.03.096>. URL: <https://www.sciencedirect.com/science/article/pii/S0960148117302884>.
- [41] Jian Gong, Weijiu Cui, and Yong Yuan. *Shanghai Tower. Monolithic Pouring of the Foundation Slab of the 632 m High Tower*. Published on 27 June 2017, Accessed on 29 November 2023. Cement. 2017. URL: <https://www.cementonline.nl/shanghai-tower>.
- [42] Andrei Jipa and Benjamin Dillenburger. "3D printed formwork for concrete: state-of-the-art, opportunities, challenges, and applications". In: *3D Printing and Additive Manufacturing 9.2* (2022), pp. 84–107.
- [43] Camille Boutemy et al. "Reusable Inflatable Formwork for Complex Shape Concrete Shells". In: *Towards Radical Regeneration*. Springer International Publishing, 2023, pp. 198–210. ISBN: 978-3-031-13249-0.
- [44] Jørgen Andersen, Claus Iversen, and Eelco van Putten. "Marine Works Operations and Environmental Considerations When Building the Fehmarnbelt Tunnel". In: *Terra et Aqua 127* (June 2012).
- [45] Guo Liang Tian. "Research on Application of New Concrete Silo Construction Technical System". In: *Advanced Materials Research 1065–1069* (Dec. 2014), pp. 1577–1585. ISSN: 1662-8985. DOI: 10.4028/www.scientific.net/amr.1065-1069.1577. URL: <http://dx.doi.org/10.4028/www.scientific.net/AMR.1065-1069.1577>.
- [46] M.K. Hurd. "Climbing Formwork System Goes Horizontal". In: *Concrete Construction* (2003). Publication#C03A061 Copyright© 2003 Hanley-Wood, LLC. All rights reserved.
- [47] Doka. *Tunnel Steinhaus*. Accessed on 2023-11-29. 2003. URL: https://www.doka.com/en/references/europe/Unterflurtrasse_Steinhaus.
- [48] Stefano Guanziroli et al. "A New Concept of Additive Manufacturing for the Regeneration of Existing Tunnels". In: Sept. 2023, pp. 116–124. ISBN: 978-3-031-43101-2. DOI: 10.1007/978-3-031-43102-9_10.
- [49] Antonio Maria D'Altri et al. "Stability analysis of leaning historic masonry structures". In: *Automation in Construction 92* (2018), pp. 199–213. ISSN: 0926-5805. DOI: <https://doi.org/10.1016/j.autcon.2018.04.003>. URL: <https://www.sciencedirect.com/science/article/pii/S0926580517310294>.
- [50] Jung-Han Lee et al. "Evaluation of Rocking and Toe Crushing Failure of Unreinforced Masonry Walls". In: *Advances in Structural Engineering - ADV STRUCT ENG 11* (Oct. 2008), pp. 475–489. DOI: 10.1260/136943308786411998.

- [51] Matthijs Langelaar. "An additive manufacturing filter for topology optimization of print-ready designs". In: *Structural and Multidisciplinary Optimization* 55 (Mar. 2017). DOI: 10.1007/s00158-016-1522-2.
- [52] Xinpeng Wang Shengxiang Huang Guanqing Li and Wen Zhang. "Geodetic network design and data processing for Hong Kong–Zhuhai–Macau link immersed tunnel". In: *Survey Review* 51.365 (2019), pp. 114–122. DOI: 10.1080/00396265.2017.1385200.
- [53] Paul Acker and Franz-Josef Ulm. "Creep and shrinkage of concrete: physical origins and practical measurements". In: *Nuclear Engineering and Design* 203.2 (2001), pp. 143–158. ISSN: 0029-5493. DOI: [https://doi.org/10.1016/S0029-5493\(00\)00304-6](https://doi.org/10.1016/S0029-5493(00)00304-6). URL: <https://www.sciencedirect.com/science/article/pii/S0029549300003046>.
- [54] G.G. van den Berg, J.H. Blonk, and A.P. Dost. *Stortnaden*. Tech. rep. STUBECO, Sept. 2001.
- [55] Nicas van den Brink. *High Pressure Cylinder*. Presentation at a meeting on January 16, 2024, online. Design Engineer at Trelleborg Group. Trelleborg Group. 2024.
- [56] A. Glerum. *Watertightness of Concrete Tunnel Structures*. Tech. rep. Paper presented at the meeting of the working group "Research" of the International Tunnelling Association in Brighton. Technische Hogeschool Delft, June 1982.
- [57] Nautical Channel. *The impressive process of launching a ship*. Feb. 2022. URL: <https://nauticalchannel.com/new/the-impressive-process-of-launching-a-ship#:~:text=Well%2C%20the%20process%20is%20named,machanical%20type%20and%20airbag%20launching..> (accessed: 13.3.2024).
- [58] Wei Lin et al. "Design of Immersed Tunnel and How We Research Submerged Floating Tunnel". In: July 2019. ISBN: 978-1-78985-465-7. DOI: 10.5772/intechopen.88169.
- [59] G.W. Nagel. "Dynamic behaviour of tunnel elements during the immersion process: A study to the influence of swell waves and wind waves on the immersion system". Masters thesis. Delft, Netherlands: Faculty of Civil Engineering and Geosciences, Department of Hydraulic Engineering, Feb. 2011.
- [60] Alireza Jahanpour and Maryam Jegarvand. "Elastic design of skid beams in offshore load-out systems". In: *Marine Structures* 84 (2022), p. 103228. ISSN: 0951-8339. DOI: <https://doi.org/10.1016/j.marstruc.2022.103228>. URL: <https://www.sciencedirect.com/science/article/pii/S0951833922000673>.
- [61] Hugo Corres Peireti Vicente Perez Perez Luis Peset Gonzalez and Felipe Tarquis Alfonso. "The Launching of the Pavilion Bridge, Zaragoza, Spain". In: *Structural Engineering International* 21.4 (2011), pp. 437–442. DOI: 10.2749/101686611X1313137725848. URL: <https://doi.org/10.2749/101686611X1313137725848>.
- [62] Johan Blaauwendraad and Jeroen Hoefakker. *Structural Shell Analysis. Understanding and Application*. Springer, 2014. Chap. 15, pp. 257–267.
- [63] M. Khaldi et al. "Analysis of thick-walled spherical shells subjected to external pressure: Elastoplastic and residual stress analysis". In: *Proceedings of the Institution of Mechanical Engineers, Part L: Journal of Materials: Design and Applications* 234.1 (2020), pp. 186–197. DOI: 10.1177/1464420719882958. URL: <https://doi.org/10.1177/1464420719882958>.
- [64] G.B. Sinclair and J.E. Helms. "A review of simple formulae for elastic hoop stresses in cylindrical and spherical pressure vessels: What can be used when". In: *International Journal of Pressure Vessels and Piping* 128 (2015), pp. 1–7. ISSN: 0308-0161. DOI: <https://doi.org/10.1016/j.ijpvp.2015.01.006>. URL: <https://www.sciencedirect.com/science/article/pii/S0308016115000071>.
- [65] P. C. J. Hoogenboom. "Ronde schijven en platen". Dutch. In: *Stichting Postacademisch Onderwijs (PAO) Delft* (Oct. 2005).
- [66] Cuemath. *Volume of a Section of a Sphere*. 2023. URL: <https://www.cuemath.com/measurement/volume-of-a-section-of-a-sphere/> (visited on 12/29/2023).
- [67] Wei Li et al. "A review of formwork systems for modern concrete construction". In: *Structures* 38 (2022), pp. 52–63. ISSN: 2352-0124. DOI: <https://doi.org/10.1016/j.istruc.2022.01.089>. URL: <https://www.sciencedirect.com/science/article/pii/S2352012422000911>.
- [68] Tarek Zayed et al. "Slip-Form Application to Concrete Structures". In: *Journal of Construction Engineering and Management-asce - J CONSTR ENG MANAGE-ASCE* 134 (Mar. 2008). DOI: 10.1061/(ASCE)0733-9364(2008)134:3(157).

- [69] A. Hasselqvist and E. Gegerfelt. "Concrete in vertical slipforms, A process for determining a suitable concrete composition". MA thesis. KTH Royal Institute of Technology, 2021.
- [70] M. Lachemi et al. "Application of maturity method to slipforming operations: Performance validation". In: *Cement and Concrete Composites* 29.4 (2007), pp. 290–299. ISSN: 0958-9465. DOI: <https://doi.org/10.1016/j.cemconcomp.2006.12.001>. URL: <https://www.sciencedirect.com/science/article/pii/S0958946506002150>.
- [71] B.M. Kahsai. "E39 and Slipforming of environmental-friendly concrete". MA thesis. University of Stavanger, 2020.
- [72] unknown. *What is the Difference Between Jumpform and Slipform Formwork?* 2023. URL: <https://www.eiffeltrading.com/blog/post/what-is-the-difference-between-jumpform-and-slipform-formwork>. (accessed: 20.11.2023).
- [73] Femern. *Building the tunnel*. Accessed on 2023-11-29. 2023. URL: <https://femern.com/the-construction/building-the-tunnel/>.
- [74] G. Bernardo, A. Guida, and I. Mecca. "Advancements in shotcrete technology". In: July 2015, pp. 591–602. DOI: 10.2495/STR150491.
- [75] L. Zhang. "Is Shotcrete Sustainable?" In: *Shotcrete* 12.4 (2010), pp. 20–26.
- [76] Bruno Mattle et al. "Multi-Layer Shotcrete Design for Tunnel Construction". In: *Shotcrete for Underground Support XIII: New Developments in Rock Engineering, Tunneling, Underground Space and Deep Excavation*. 2017.
- [77] L. Malmgren, E. Nordlund, and S. Rolund. "Adhesion strength and shrinkage of shotcrete". In: *Tunnelling and Underground Space Technology* 20.1 (2005), pp. 33–48. ISSN: 0886-7798. DOI: <https://doi.org/10.1016/j.tust.2004.05.002>. URL: <https://www.sciencedirect.com/science/article/pii/S0886779804002913>.
- [78] Zeeshan Ahmed Freek Bos Rob Wolfs and Theo Salet. "Additive manufacturing of concrete in construction: potentials and challenges of 3D concrete printing". In: *Virtual and Physical Prototyping* 11.3 (2016), pp. 209–225. DOI: 10.1080/17452759.2016.1209867.
- [79] Wenwei Yang et al. "An integrated method of topological optimization and path design for 3D concrete printing". In: *Engineering Structures* 291 (2023), p. 116435. ISSN: 0141-0296. DOI: <https://doi.org/10.1016/j.engstruct.2023.116435>. URL: <https://www.sciencedirect.com/science/article/pii/S0141029623008507>.
- [80] Chao Zhang et al. "Mix design concepts for 3D printable concrete: A review". In: *Cement and Concrete Composites* 122 (2021), p. 104155. ISSN: 0958-9465. DOI: <https://doi.org/10.1016/j.cemconcomp.2021.104155>. URL: <https://www.sciencedirect.com/science/article/pii/S0958946521002237>.
- [81] *What is the Capacity of Batching Plant*. Date Written: 31 May 2020, Accessed on 29 November 2023. Atlas Industries. 2020. URL: <https://www.atlasindustries.in/blog/what-is-batching-plant-capacity/>.
- [82] *Liste der trockenen Docks*. Accessed on 29 November 2023. URL: https://dreipage.de/List_of_dry_docks#gsc.tab=0.
- [83] *Bouwdok Barendrecht – Tunnelwerkplaats in een badkuip*. Uitgave: december 1997 | Geüpload op: 1 mei 2016, Accessed on 29 November 2023. Ministerie van Verkeer en Waterstaat. 1997. URL: <https://www.cob.nl/document/bouwdok-barendrecht-tunnelwerkplaats-in-een-badkuip/>.
- [84] *Daewoo Mangalia Heavy Industries - Facility*. Published on 6 September 2011, accessed on 29 November 2023. URL: <http://www.dmhi.ct.ro/facility.htm>.
- [85] *Soreni Dry dock*. Accessed on 29 November 2023. URL: <https://web.archive.org/web/20071012065106/http://www.soreni.fr/index.htm>.
- [86] Jae-gyeong Kwon. *Shipyards in Korea*. Tech. rep. Korean Register, Dec. 2015.
- [87] *Sasebo Heavy Industries - main facilities*. Accessed on 29 November 2023. URL: <http://www.ssk-sasebo.co.jp/ssk/us/corporate/factory/index.html>.
- [88] *All shipyards, shipbuilders and docks in Indonesia*. Accessed on 29 November 2023. URL: <https://www.trusteddocks.com/catalog/country/101-indonesia>.
- [89] *MHB's Newly Built Dry Dock No. 3 Welcomes First Vessel*. Accessed on 29 November 2023. URL: <https://mhb.com.my/mhbs-newly-built-dry-dock-no-3/#:~:text=The%20dry%20dock%20is%20an,wide%20and%2014%20metres%20deep..>

- [90] *PORT OF CAPE TOWN*. Accessed on 29 November 2023. URL: <https://africaports.co.za/cape-town/#:~:text=The%20main%20dry%20dock%2C%20known,with%20a%20depth%20of%2014m.>
- [91] Joseph R. Crosswell et al. "Geophysical controls on metabolic cycling in three Patagonian fjords". In: *Progress in Oceanography* 207 (2022), p. 102866. ISSN: 0079-6611. DOI: <https://doi.org/10.1016/j.pocean.2022.102866>. URL: <https://www.sciencedirect.com/science/article/pii/S0079661122001252>.
- [92] Heidi K. Meyer et al. "Drivers of Megabenthic Community Structure in One of the World's Deepest Silled-Fjords, Sognefjord (Western Norway)". In: *Frontiers in Marine Science* 7 (2020). ISSN: 2296-7745. DOI: 10.3389/fmars.2020.00393. URL: <https://www.frontiersin.org/articles/10.3389/fmars.2020.00393>.
- [93] Ivar Holand, Ove Gudmestad, and Erik Jersin. *Design of Offshore Concrete Structures*. Jan. 2003. ISBN: 9780429204296. DOI: 10.4324/9780203478257.
- [94] Thomas Bianchi et al. "Fjords as Aquatic Critical Zones (ACZs)". In: *Earth-Science Reviews* 203 (Apr. 2020), p. 103145. DOI: 10.1016/j.earscirev.2020.103145.
- [95] Robert Hallmark. "Prefabricated Composite Bridges - a Study of Dry Deck Joints". PhD thesis. Lulea University of Technology, Sept. 2012.
- [96] Trelleborg. *A safe crossing*. 2022. URL: <https://www.trelleborg.com/en/media/products-and-solutions-news/a-safe-crossing>.
- [97] Regbar Construction Technology Solutions. *BARCOUP L*. 2023. URL: <https://regbar.com/products/rebar-couplers/barcoup-l/>.
- [98] Max Frank Building Common Ground. *Continuity strip Stabox*. 2023. URL: <https://www.maxfrank.com/au-en/products/reinforcement-technologies/01-continuity-strip-stabox/>.
- [99] Hakron. *Waterstop W9U*. 2023. URL: <https://www.hakron.nl/producten/waterkerende-systemen/voegenbanden/binnenliggend/3440300099-dilatatievoegprofiel-type-w9u-lengte-vlg-opgave---inkoop>.



Draughts

A.1. Draught of sphere in state-of-the-art

This Section details the calculation of the draught of the spherical reservoir using parameters from Table 2.1. The relevant parameters are as follows:

- $r_{in} = 13,37 \text{ m}$
- $t = 2,72 \text{ m}$
- $\rho_{sw} = 1025 \text{ kg m}^{-3}$
- $\rho_{concrete} = 2400 \text{ kg m}^{-3}$

The volume of the sphere is calculated using the formula:

$$\begin{aligned} V_{\text{sphere}} &= \frac{4}{3}\pi (r_{in} + t)^3 \\ &= \frac{4}{3}\pi (13,37 + 2,72)^3 \\ &= 17.448,45 \text{ m}^3 \end{aligned}$$

The weight of the sphere is determined by:

$$\begin{aligned} W_{\text{sphere}} &= V_{\text{concrete}} \cdot \rho_{\text{concrete}} \cdot g \\ &= \frac{4}{3}\pi r^3 \left((r_{in} + t)^3 - r_{in}^3 \right) \rho_{\text{concrete}} \cdot g \\ &= \frac{4}{3}\pi r^3 \left((13,37 + 2,72)^3 - 13,37^3 \right) 2400 \cdot 9,81 \\ &= 175,10 \text{ MN} \end{aligned}$$

Where V_{concrete} is the volume of the concrete, and g is the acceleration due to gravity. The displaced volume of water is then calculated as:

$$\begin{aligned} V_{\text{water,displaced}} &= \frac{W_{\text{sphere}}}{\rho_{sw} \cdot g} \\ &= \frac{175,10 \cdot 10^6}{1025 \cdot 9,81} \\ &= 17.414,22 \text{ m}^3 \end{aligned}$$

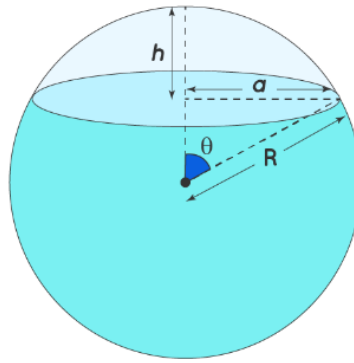


Figure A.1: Spherical cap volume [66]

The draught of the sphere is calculated by solving the spherical cap formula provided in Equation A.1, where h represents the height of the cap. A graphical representation of this cap is shown in Figure A.1. Here, the parameter R in Figure A.1 corresponds to r_{out} , and V_{sc} denotes the volume of the upper section of the sphere.

$$V_{\text{sc}} = \frac{1}{3}\pi h^2 (3r_{\text{out}} - h) \quad (\text{A.1})$$

The free height h follows a third-order polynomial, reduced with parameters $a = -3r_{\text{out}}$, $b = 0$, and $c = \frac{3V_{\text{sc}}}{\pi}$:

$$\begin{aligned} 0 &= h^3 - 3r_{\text{out}}h^2 + \frac{3V_{\text{sc}}}{\pi} \\ &= h^3 + ah^2 + bh + c \\ &= \left(h + \frac{a}{3}\right)^3 + \left(b - \frac{1}{3}a^2\right)\left(h + \frac{a}{3}\right) + \frac{2}{27}a^3 - \frac{1}{3}ab + c \\ &= x^3 + px + q \end{aligned}$$

In this reduced form, the following applies:

$$\begin{aligned} x &= h + \frac{a}{3} = h - r_{\text{out}} \\ p &= b - \frac{1}{3}a^2 = -3r_{\text{out}}^2 \\ q &= \frac{2}{27}a^3 - \frac{1}{3}ab + c = -2r_{\text{out}}^3 + \frac{3V_{\text{sc}}}{\pi} \end{aligned}$$

Applying Cardano's formula, as presented in Equation A.2, to find the solution of the reduced form:

$$x = \sqrt[3]{\frac{-q}{2} + \sqrt{\frac{q^2}{4} + \frac{p^3}{27}}} + \sqrt[3]{\frac{-q}{2} - \sqrt{\frac{q^2}{4} + \frac{p^3}{27}}} \quad (\text{A.2})$$

Substituting $V_{\text{sc}} = V_{\text{water,displaced}}$ results in $x = 15,26$ m. Consequently, the draught of the sphere can be determined:

$$\begin{aligned}
d_{\text{sphere}} &= h \\
&= x + r_{\text{out}} \\
&= 15,26 + 13,37 + 2,72 \\
&= 31,35 \text{ m}
\end{aligned}$$

This corresponds to 97.42% of its diameter, while the volume of displaced water is 99.80% of the total volume. Similarly, applying the internal radius and thickness of the proposed sphere in [10], a draught of 25.96 meters is obtained, accounting for 84.85% of the total diameter.

A.2. Draught of sphere in summary of results

The sphere, as detailed in Table 7.1, possesses parameters outlined in Table A.1. These parameters were obtained following the methodology outlined in Appendix D. For the geometry of the structure, please consult Section 3.2.1.

Parameter	Value	Unit
Internal volume	9.000	m ³
Total volume of concrete	7.003	m ³
Internal radius	12,9	m
Wall thickness	2,21	m
Pedestal thickness	0,86	m
Pedestal height	7,25	m
Foundation plate thickness	1,47	m

Table A.1: Parameters of sphere as described in Section 7.1

Draught of sphere during transport

The total weight of the structure is equal to 164,9 MN.

$$W_{\text{total}} = \rho_{\text{concrete}} g V_{\text{concrete}} = 2.400 \cdot 9,81 \cdot 7.003 = 164,9 \text{ MN}$$

The displaced water volume is calculated for different segments of the structure, including the foundation plate, pedestal, and the portions of the sphere below and above the pedestal. Specifically, the pedestal volume is computed under closed conditions, accounting for entrapped air between the pedestal, foundation plate, and sphere. The volume of the sphere segment is calculated following Equation A.1.

$$V_{\text{foundation}} = \pi (a + t)^2 t_{\text{plate}} = \pi (12,9 + 2,21)^2 \cdot 1,47 = 1.054 \text{ m}^3$$

$$V_{\text{pedestal}} = \pi \left(a + \frac{t_{\text{pedestal}}}{2} \right)^2 h_{\text{pedestal}} = \pi \left(12,9 + \frac{0,86}{2} \right) \cdot 7,25 = 4.047 \text{ m}^3$$

$$V_{\text{sphere below pedestal}} = \frac{1}{3} \pi h^2 (3r_{\text{out}} - h) = \frac{1}{3} \pi \cdot 7,25^2 (3 \cdot (12,9 + 2,21) - 7,25) = 2.095 \text{ m}^3$$

$$V_{\text{sphere above pedestal}} = \frac{4}{3} \pi r_{\text{out}}^3 - V_{\text{sphere below pedestal}} = \frac{4}{3} \pi \cdot (12,9 + 2,21)^3 - 2.095 = 12.340 \text{ m}^3$$

By summing the relevant volumes, the weight of the displaced water can be calculated.

$$\begin{aligned}
W_{\text{displaced,water}} &= \rho_{\text{sw}} g (V_{\text{foundation}} + V_{\text{pedestal}} + V_{\text{sphere above pedestal}}) \\
&= 1.025 \cdot 9,81 \cdot (1.054 + 4.047 + 12.340) \\
&= 175,4 \text{ MN}
\end{aligned}$$

Since the buoyancy of the structure exceeds its own weight, it will float. The height of the structure above the water is 4,97 meters, calculated as follows:

$$\begin{aligned} V_{\text{above surface}} &= \frac{W_{\text{displaced,water}} - W_{\text{total}}}{\rho_{\text{concrete}}g} = \frac{(175,4 - 164,9) \cdot 10^6}{1.025 \cdot 9,81} = 1.044 \text{ m}^3 \\ &= \frac{1}{3}\pi h^2 (3r_{\text{out}} - h) = \frac{1}{3}\pi \cdot 4,97^2 (3 \cdot (12,9 + 2,21) - 4,97) = 1.044 \text{ m}^3 \end{aligned}$$

Therefore, the draught of the structure is 26,71 meters.

$$\text{draught} = 2(a + t) + t_{\text{plate}} - h_{\text{above surface}} = 2(12,9 + 2,21) + 1,47 - 4,97 = 26,71 \text{ m}$$

Required extra buoyancy for 10 meter draught

To calculate the required additional buoyancy for a 10 meter draught of the sphere, as described in Table A.1, the volume of the displaced water is calculated first.

$$\begin{aligned} h_{\text{sphere below surface}} &= 10 - t_{\text{plate}} = 10 - 1,47 = 8,53 \\ V_{\text{sphere below surface}} &= \frac{1}{3}\pi h^2 (3r_{\text{out}} - h) = \frac{1}{3}\pi \cdot 8,53^2 (3 \cdot (12,9 + 2,21) - 8,53) = 2.803 \text{ m}^3 \\ V_{\text{total below surface}} &= V_{\text{foundation}} + V_{\text{pedestal}} + V_{\text{sphere below surface}} - V_{\text{sphere below pedestal}} \\ &= 1.054 + 4.047 + 2.095 - 2.095 \\ &= 5.808 \text{ m}^3 \end{aligned}$$

The additional required buoyancy for this draught is 106,5 MN.

$$F_{\text{buoyancy,required}} = W_{\text{total}} - V_{\text{sphere below surface}}\rho_{\text{sw}}g = 164,9 - 5.808 \cdot 1.025 \cdot 9,81 \cdot 10^{-6} = 106,5 \text{ MN}$$

This translates to 10.589 m³ or 123 standard shipping containers.

$$\begin{aligned} V_{\text{buoyancy,required}} &= \frac{106,5 \cdot 10^6}{\rho_{\text{sw}}g} = \frac{106,5 \cdot 10^6}{1.025 \cdot 9,81} = 10.589 \text{ m}^3 \\ n_{\text{containers}} &= \frac{V_{\text{buoyancy,required}}}{12,19 \cdot 2,44 \cdot 2,89} = 123,19 \end{aligned}$$

A.3. Draught of cylinder in summary of results

The cylinder described in Table 7.1 exhibits parameters specified in Table A.2. For detailed information regarding the structure's geometry, please refer to Section 3.2.2.

Parameter	Value	Value	Unit
Internal volume	9.000	9.000	m ³
Total volume of concrete	9.811	9.528	m ³
Internal radius	4,84	4,11	m
Wall thickness	2,06	1,74	m
External length	129,8	176,0	m

Table A.2: Parameters of cylinder as described in Section 7.1

The weight of the cylinder structure in water is 231,0 MN.

$$W_{\text{total}} = V_{\text{concrete}} \rho_{\text{concrete}} g = 9.811 \cdot 2.400 \cdot 9,81 = 231,0 \text{ MN}$$

The weight of the displaced water is 189,8 MN, indicating that the structure does not float. Therefore, its draught is equal to its height, which is 13,8 meters.

$$W_{\text{displaced water}} = (V_{\text{concrete}} + V_{\text{internal}}) \rho_{\text{sw}} g = (9.811 + 9.000) \cdot 1.025 \cdot 9,81 = 189,8 \text{ MN}$$

$$h_{\text{cylinder}} = 2 \cdot (a + t) = 2 \cdot (4,84 + 2,06) = 13,79 \text{ m}$$

Required extra buoyancy for 10 meter draught

The height of the cylinder above the water surface is 3,79 meters when a 10 meter draught is applied. The area of the circle segment that is above the water surface can be calculated as follows:

First, the angle α between the center of the cross-section and the points where the cylinder touches the surface is calculated:

$$\alpha = 2 \arccos \left(\frac{r_{\text{out}} - h_{\text{above water}}}{r_{\text{out}}} \right) = 2 \arccos \left(\frac{6,89 - 3,79}{6,89} \right) = 2,21 \text{ rad.}$$

Then, the area of the circle segment that is above the water surface can be calculated:

$$A_{\text{cylinder above water}} = \frac{1}{2} r_{\text{out}}^2 (\alpha - \sin \alpha) = \frac{1}{2} \cdot 6,89^2 (2,21 - \sin(2,21)) = 33,3 \text{ m}^2$$

The volume of the displaced water is 14.481 m³. In this calculation, the hemispheres are considered flat, which has little influence on the results since the majority of the volume comes from the mid-tube of the cylinder.

$$V_{\text{displaced water}} = V_{\text{concrete}} + V_{\text{internal}} - A_{\text{cylinder above water}} L_{\text{external}} = 9.811 + 9.000 - 33,3 \cdot 129,8 = 14.481 \text{ m}^3$$

The extra buoyancy required is 85,4 MN.

$$F_{\text{buoyancy,required}} = W_{\text{total}} - V_{\text{displaced water}} \rho_{\text{sw}} g = 189,1 - 14.481 \cdot 1.025 \cdot 9,81 \cdot 10^{-6} = 85,4 \text{ MN}$$

This translates to 8.490 m³ or 99 standard shipping containers.

$$V_{\text{buoyancy,required}} = \frac{85,4 \cdot 10^6}{\rho_{\text{sw}} g} = \frac{85,4 \cdot 10^6}{1.025 \cdot 9,81} = 8.490 \text{ m}^3$$

$$n_{\text{containers}} = \frac{V_{\text{buoyancy,required}}}{12,19 \cdot 2,44 \cdot 2,89} = 98,78$$

Similarly, a cylinder with a slenderness of $\frac{L}{2a} = 20$ and parameters as described in Table A.2, has a draught of 11,69 meters. For a draught of 10 meters, an additional buoyancy of 54,9 MN or 5.463 m³ is required.

B

Hochtief construction technique

This Appendix offers an elaborate description of the construction technique patented by HTS in [30]. An overview of the components in the drawings is presented by Table B.1.

Index	Component	Index	Component
1	Spherical storage tank	14	Central support mast
2	Wind turbines	15	Spherical inner formwork
3	Cable connection to wind turbine	17	Inner toroidal rings
4	Pump	17	Scaffolding tower
5	Interior of storage tank	18	Bracing elements
6	Turbine	19	Outer formwork
7	Cable connection to grid	20	Outer toroidal rings
8	Ring support	21	Concrete
9	Pontoon	22	Pedestal
10	Lower outer base formwork	23	Portal crane
11	Wire mesh net	24	Curved crane towers
12	Base formwork membrane	25	Concrete pump
13	Underside formwork floor		

Table B.1: Components in HTS construction technique

In the first phase a support ring in the form of a ring-shaped lattice girder is mounted on pontoons floating on the water surface. The lower outer base formwork is connected to the support ring. This outer base formwork comprises a wire mesh net and a base formwork membrane applied to its inside. Furthermore, an underside formwork floor is connected to or placed on the wire mesh net, and a central support mast is mounted on this formwork floor. See Figures B.1 and B.2.

In the second phase, the underside formwork floor with the connected wire mesh net and the base formwork membrane is lowered below the water surface by flooding and/or ballasting. The wire mesh net is tensioned and has taken its final shape. Construction of the spherical inner formwork has started on the support mast. For this purpose, inner toroidal rings with different ring diameters are stacked on top of each other. These rings are pressurized with compressed air and should provide lateral stability to the formwork, with gluing and hook-and-loop fasteners serving as the primary connection methods between the rings. The inner toroidal rings are attached to the inner formwork membrane using loop bands. Additionally, in this second phase the construction of a scaffold tower on the support mast has begun. See Figure B.3.

In the third phase, the construction of the inner formwork is continued with additional inner toroidal rings, and the scaffold tower is built up further. The scaffold tower is connected to the inner formwork via bracing elements. Additionally, the construction of the outer formwork has begun using outer toroidal rings. Similar to the inner formwork, outer toroidal rings with different ring diameters are stacked on top

of each other to achieve a spherical shape. Concrete has already been poured into the space between the lower outer base formwork and the inner formwork. In the area of the underside formwork floor, a pedestal is formed for the underwater storage tank, allowing it to securely stand on the seabed. See Figure B.4.

In figure B.5, the fourth phase is depicted. In this phase, the construction of the spherical inner formwork is almost completed, and the assembly of the outer formwork is continued by placing additional outer toroidal rings. The outer base formwork and the outer formwork complement each other to form a spherical outer formwork. Additionally, an inner formwork membrane is preferably applied to the outside of the inner formwork, which is not shown in the figures. Furthermore, in the construction example, an outer formwork membrane is applied segment by segment to the inside of the outer formwork as its construction progresses.

The construction of the underwater storage tank is carried out using a portal crane. This portal crane preferably has four curved crane towers in the embodiment shown, allowing it to be movable on the support ring and capable of rotating about a central axis. Each crane tower is equipped with a concrete supply device in the form of a concrete pump. As the construction of the outer formwork progresses, concrete can be introduced into the space between the outer formwork and the inner formwork layer by layer and preferably continuously through these concrete pumps. Due to the rotation of the portal crane, the concrete is effectively distributed, resulting in an even distribution of pressure on the formworks. The introduced concrete is compacted using internal vibrators or immersion vibrators (not shown). After the concrete has cured, the formworks can be removed.

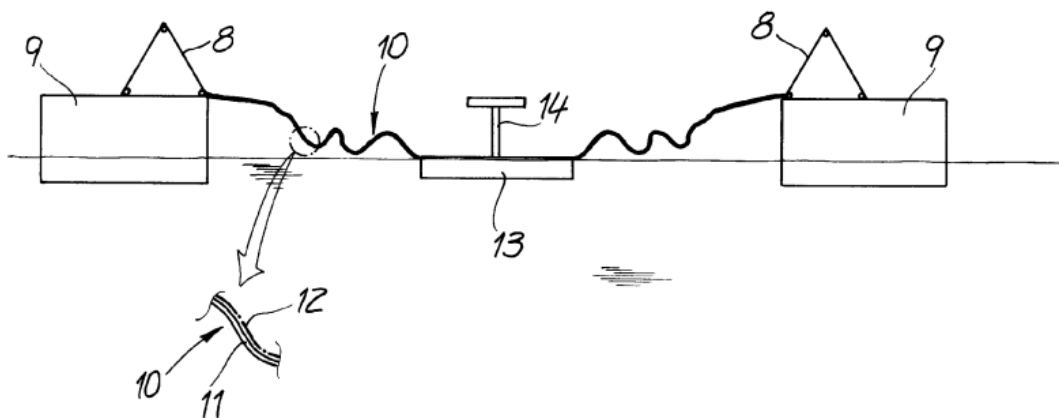


Figure B.1: HTS construction method: Phase 1, front view [30]

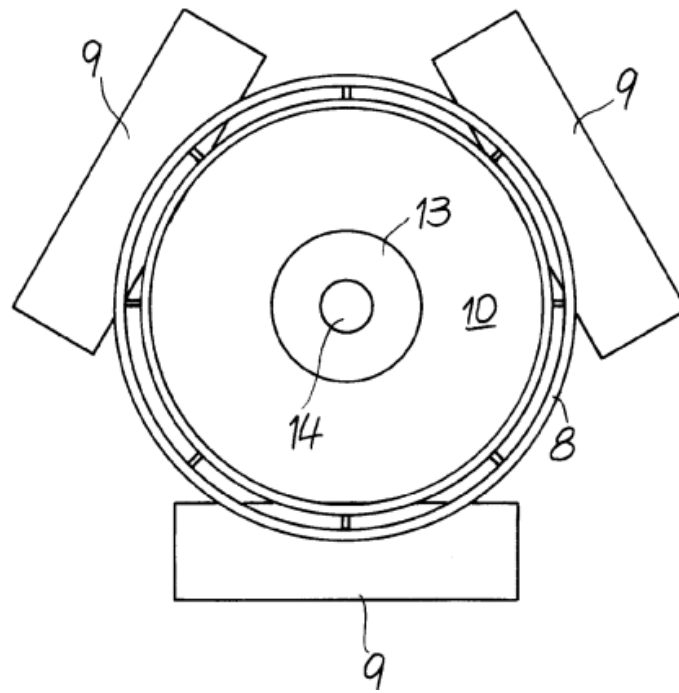


Figure B.2: HTS construction method: Phase 1, top view [30]

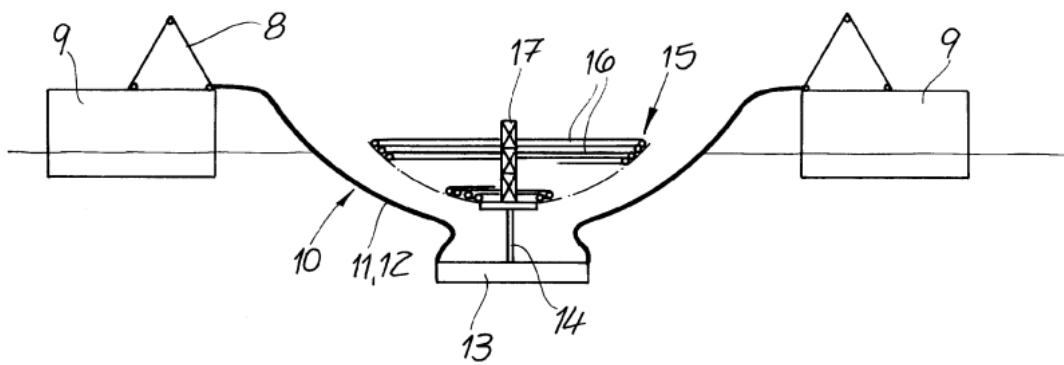


Figure B.3: HTS construction method: Phase 2, front view [30]

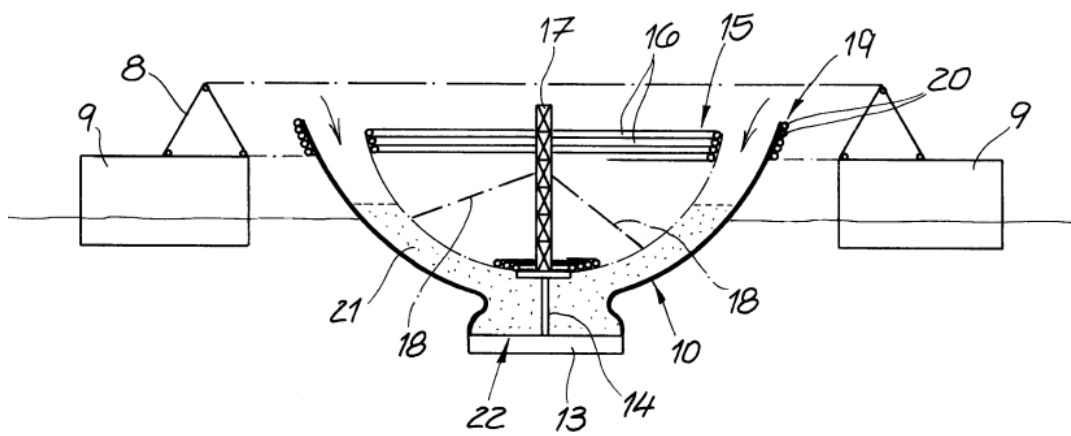


Figure B.4: HTS construction method: Phase 3, front view [30]

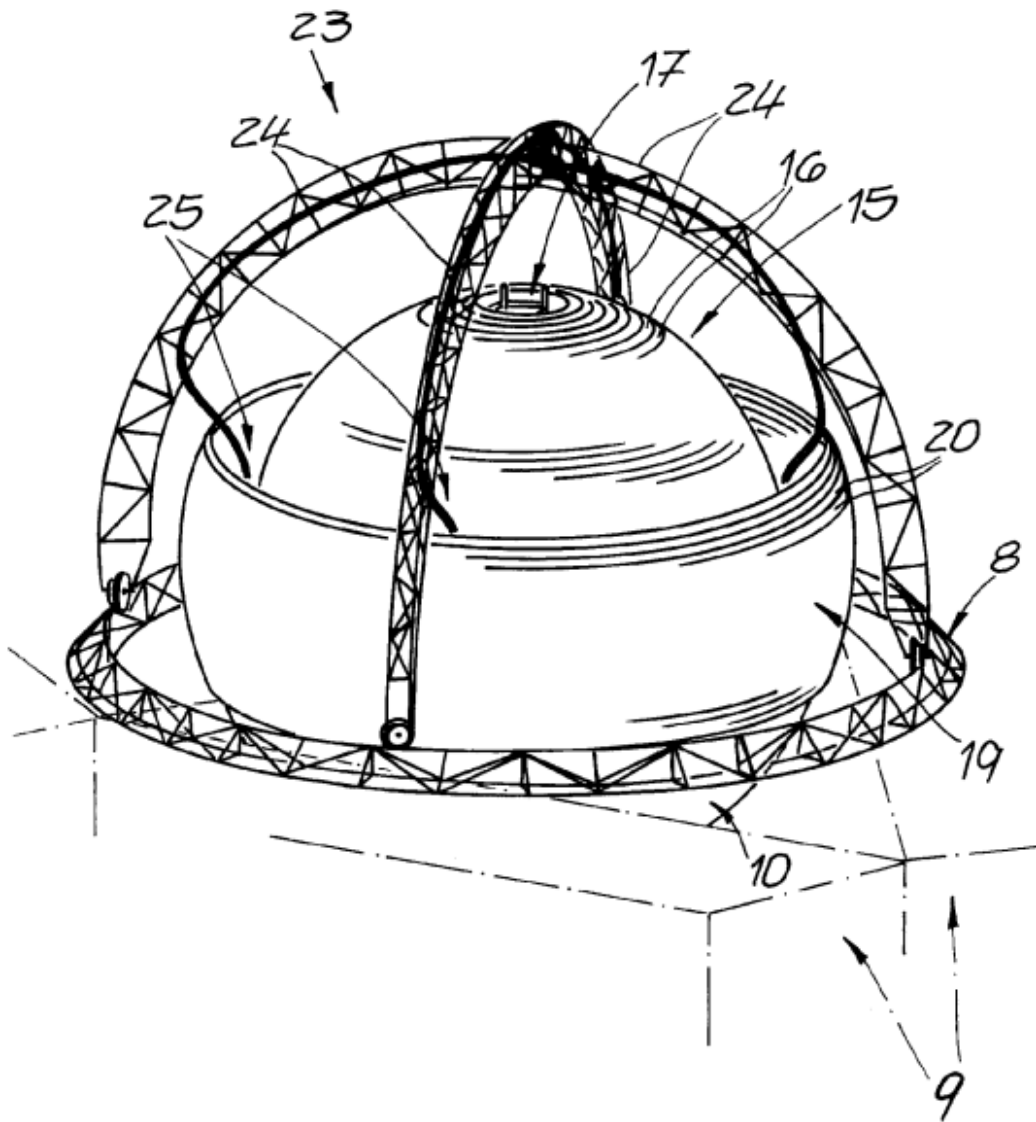
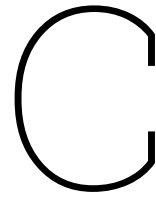


Figure B.5: HTS construction method: Phase 4, 3D view [30]



Membrane forces

In this appendix the membrane forces for a thin-walled sphere, cylinder and torus are presented. Table C.1 serves as an overview of the results derived.

Shape	Max. membrane force	Multiplication factor
Sphere	$-\frac{1}{2}pa$	1
Cylinder	$-pa$	2
Torus	$\frac{b}{a} = 2$ $-\frac{3}{2}pa$	3
	$\frac{b}{a} = 3$ $-\frac{5}{4}pa$	2.5
	$\frac{b}{a} = 4$ $-\frac{7}{6}pa$	2.33
	$\frac{b}{a} = 6$ $-\frac{11}{10}pa$	2.2

Table C.1: Membrane forces overview for several thin-walled shapes

C.1. Spherical and cylindrical membrane forces

When considering a two-dimensional circle with an internal pressure equal to p (as shown in Figure C.1), the circle can be extended into a three-dimensional structure, specifically as a cylinder or a sphere. Cutting the three-dimensional structure in half results in the following for the cylinder:

$$2n_{\text{cylinder}}l_{\text{cylinder}} = 2pal_{\text{cylinder}}$$

$$n_{\text{cylinder}} = pa \tag{C.1}$$

Equation C.1 is known as Barlow's formula. For the sphere, the following is obtained:

$$n_{\text{sphere}}2\pi a = p\pi a^2$$

$$n_{\text{sphere}} = \frac{pa}{2} \tag{C.2}$$

For a thin walled cylinder the normal force in the shell wall is twice as high as for a sphere.

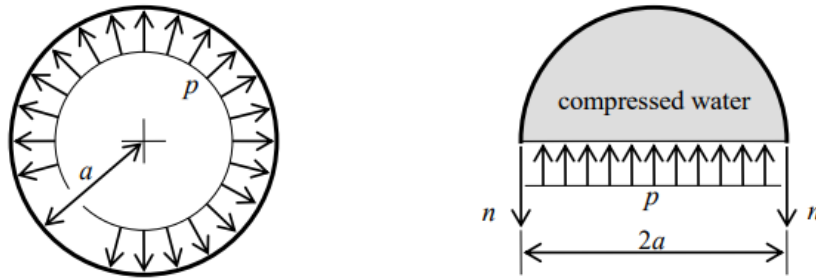


Figure C.1: Derivation of Barlow's formula [36]

C.2. Toroidal membrane forces

A torus is considered, depicted in Figure C.2. Its geometry is determined by the inner minor radius a and the major radius b . A curvilinear coordinate system is introduced with $0 < v < 2\pi a$ and $0 < u < 2\pi b$. The geometry of the torus has a non-uniform curvature over the cross-section. These parameters are listed in Table C.2. The curvatures are defined in the local coordinate system, where the local x - and y -axis follow the u - and v -axis. The right-hand rule then determines that the z -axis is always pointing outwards.

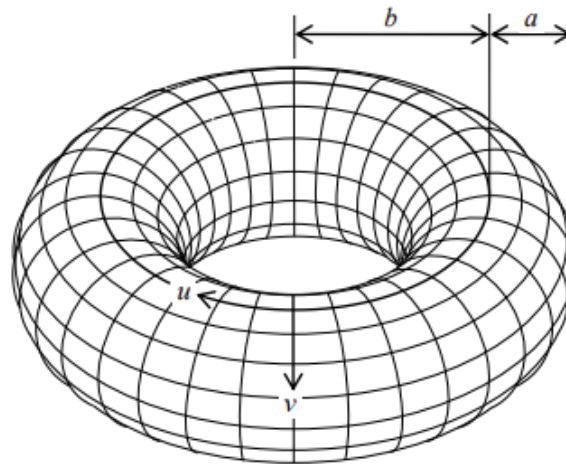


Figure C.2: The geometry of a torus [36]

Parameter	Symbol	Function
Curvature	k_{xx}	$\frac{-1}{a + \frac{b}{\sin(v/a)}}$
Curvature	k_{yy}	$\frac{-1}{a}$
Curvature	k_{xy}	0
Lamé	α_x	$1 + \frac{a}{b} \sin(v/a)$
Lamé	α_y	1

Table C.2: Geometrical torus parameters [36]

The Lamé parameters in Table C.2 are used to differentiate the orthogonal parameterisation of the torus:

$$\frac{\partial u}{\partial x} = \frac{1}{\alpha_x}, \frac{\partial v}{\partial y} = \frac{1}{\alpha_y}, \frac{\partial u}{\partial y} = \frac{\partial v}{\partial x} = 0$$

To obtain the normal forces in the shell wall of a torus under hydro static pressure, the membrane equilibrium equations are applied:

$$k_{xx}n_{xx} + 2k_{xy} + k_{yy}n_{yy} + p_z = 0$$

$$\frac{\partial n_{xx}}{\partial x} + \frac{\partial n_{xy}}{\partial y} + k_y (n_{xx} - n_{yy}) + 2k_x n_{xy} + p_x = 0$$

$$\frac{\partial n_{yy}}{\partial y} + \frac{\partial n_{xy}}{\partial x} + k_x (n_{yy} - n_{xx}) + 2k_y n_{xy} + p_y = 0$$

The external loads in these equations should reflect the hydro static pressure:

$$p_x = p_y = 0, p_z = -p$$

The goal is to find the membrane forces n_{xx} , n_{yy} and n_{xy} . From equilibrium it can already be found that $n_{xy} = 0$. Consider any cross-section that cuts the torus into two symmetrical shapes. Due to symmetry, the shear stress n_{xy} should have the same direction on both sides of the cut. Due to equilibrium, they should be in opposite direction. This can only be accomplished if $n_{xy} = 0$. Since there are infinitely many cuts that result in two symmetrical shapes, this applies everywhere in the torus.

Now solving the membrane equilibrium equations for n_{xx} and n_{yy} :

$$n_{xx} = -pa \frac{\frac{\sin(\frac{v}{a})^2}{2} + \frac{C_1}{a^2 p} + \frac{1}{4}}{\sin(\frac{v}{a})} \quad (C.3)$$

$$n_{yy} = -pa \frac{\sin(\frac{v}{a}) \left(\frac{\sin(\frac{v}{a})}{2} + \frac{b}{a} \right) - \frac{C_1}{a^2 p} - \frac{1}{4}}{\sin(\frac{v}{a}) \left(\sin(\frac{v}{a}) + \frac{b}{a} \right)} \quad (C.4)$$

When Expressions C.3 and C.4 are plotted for any value of C_1 , a singularity for both membrane forces is present at $v = k\pi a$ for $k = 0, 1, 2, \dots$. The singularity can be taken out of the expression by choosing $C_1 = -\frac{pa^2}{4}$. These results are plotted in Figure C.3. The attentive reader notices that b is not present in the plots axes. It appears that, for $C_1 = -\frac{pa^2}{4}$, b only influences the amplitude of n_{yy} . n_{xx} is constant and not dependent on b . Substituting the value for C_1 ¹:

$$n_{xx} = -\frac{pa}{2} \quad (C.5)$$

$$n_{yy} = -pa \frac{\frac{\sin(\frac{v}{a})}{2} + \frac{b}{a}}{\sin(\frac{v}{a}) + \frac{b}{a}} \quad (C.6)$$

As this result will be used to obtain the maximum normal stress in the cross-section, it is interesting to investigate n_{yy} further. It can be shown that n_{yy} is extreme for $v = \frac{\pi}{2}a, \frac{3\pi}{2}a$. The maximum compression in the cross-section is found at $v = \frac{3\pi}{2}a$. Its value is:

$$n_{yy,\max} = -pa \frac{-\frac{1}{2} + \frac{b}{a}}{-1 + \frac{b}{a}} \quad (C.7)$$

The maximum can be plotted, see Figure C.4. Now the influence of b on the normal stress in y-direction is found. This graph presents meaningful insights into the required parameters for normal stress minimization.

The parameters n_{xx} and n_{yy} in this example correspond to n_{ll} and $n_{\theta\theta}$ respectively, as defined in Section 3.3.

¹The value for C_1 was found by Pierre Hoogenboom

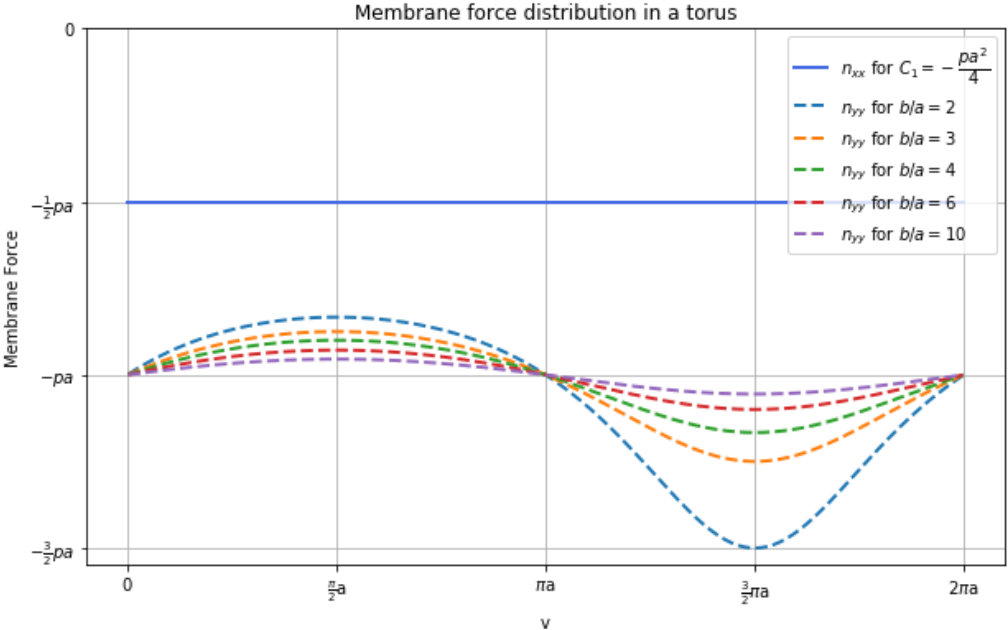


Figure C.3: Membrane forces in a torus under hydro static pressure p

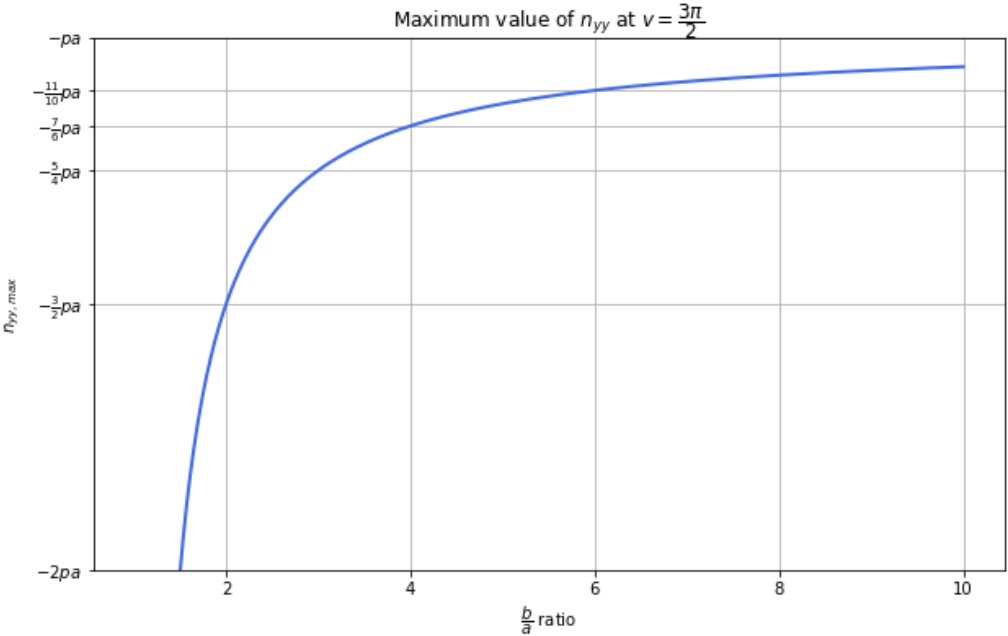


Figure C.4: Maximum value for membrane force n_{yy} in a torus under hydro static pressure p

D

Calculation of concrete volumes

This Appendix offers a systematic breakdown of the results discussed in Chapter 4. The primary objective of these calculations is to ascertain the ratio between the internal volume, which serves as the space for energy storage, and the volume of concrete employed. These calculations have been performed for various geometric shapes to ensure comparability of results.

The initial reference point for these calculations is the internal volume. When dealing with a sphere, the internal volume alone dictates the shape and dimensions of the reservoir, as it involves only one parameter, which is the radius (a). In contrast, for both cylinders and toroids, determining the shape and dimensions based on the internal volume requires an additional parameter, namely the slenderness. By starting with the prescribed internal volume and slenderness values for cylinders and toroids, the ensuing shape and dimensions can be deduced.

For reference, Table 4.1 is reproduced below:

Shape	Max. membrane force	Volume	Slenderness
Sphere	$-\frac{pa}{2}$	$\frac{4}{3}\pi a^3$	–
Cylinder	$-pa$	$\pi a^2 L$	$\frac{L}{2a}$
Torus	$-pa \frac{-\frac{1}{2} + \frac{b}{a}}{-1 + \frac{b}{a}}$	$2\pi^2 a^2 b$	$\frac{b}{a}$

To maintain clarity, the parameters mentioned in Chapter 4 are reproduced below:

- $g = 9,81 \text{ m/s}^2$
- $\rho_{\text{sw}} = 1025 \text{ kg/m}^3$
- $\rho_{\text{concrete}} = 2400 \text{ kg/m}^3$

D.1. Determination of reservoir dimensions

This Section elucidates the calculations used to determine the CIV-ratio for the different shapes. As mentioned earlier, the internal volume serves as the starting point.

For illustrative purposes, the following parameters were employed:

- $V_{\text{internal}} = 10.000 \text{ m}^3$
- $f_{cd} = 40 \text{ MPa}$

Subsequently, the hydrostatic pressure (p) at a depth of 1000 meters is calculated as follows:

$$\begin{aligned}
 p &= \rho_{sw}gd \\
 &= 1025 \cdot 9,81 \cdot 1000 \\
 &= 1,01 \cdot 10^7 \text{ N/m}^2
 \end{aligned}$$

For the sake of consistency, this hydrostatic pressure is employed in each of the subsequent examples. Initially, the thicknesses are estimated using the same methodology for each shape, after which an iterative algorithm is employed to enhance the precision of these thickness estimations.

D.1.1. Initial thickness estimation of spherical design

To initiate the estimation process for the required thickness of a spherical reservoir, the sphere's radius is derived from the specified internal volume. As presented in subsection 3.2.1, a refers to the internal radius of the sphere.

$$\begin{aligned}
 V_{\text{internal}} &= \frac{4}{3}\pi a^3 \\
 a &= \sqrt[3]{\frac{3V_{\text{internal}}}{4\pi}} \\
 &= \sqrt[3]{\frac{3 \cdot 10.000}{4\pi}} \\
 &= 13,36 \text{ m}
 \end{aligned}$$

With the internal radius (a) now determined, the maximum membrane force can be calculated:

$$\begin{aligned}
 n &= -\frac{pa}{2} \\
 &= -\frac{10^7 \cdot 13,36}{2} \\
 &= -6,719 \cdot 10^7 \text{ N/m}
 \end{aligned}$$

The membrane force is expressed in units of Newton per meter [N/m]. Given the assumption that the compressive stress remains constant throughout the thickness of the cross-section, an estimation of the initial thickness can be made. Since the thickness is determined based on the compressive design strength of concrete, the following expression is solely applicable to negative membrane forces.

$$\begin{aligned}
 t &= \frac{|n|}{f_{cd}} \\
 &= \frac{|-6,719 \cdot 10^7|}{40 \cdot 10^6} \\
 &= 1,68 \text{ m}
 \end{aligned}$$

Applying this thickness leads to an increase of $1,68/13,36 = 12,6\%$ of the external radius of the cross-section.

D.1.2. Initial thickness estimation of cylindrical design

To estimate the initial thickness for a cylinder, a similar approach is employed. In this case, slenderness also plays a significant role, with a chosen configuration of $\frac{L}{2a} = 10$. As detailed in subsection 3.2.2, both L and a refer to the internal surface of the cylinder.

The volume of the cylinder is calculated as:

$$\begin{aligned} V_{\text{internal}} &= \pi a^2 L \\ &= \pi a^2 \cdot 2a \cdot \frac{L}{2a} \end{aligned}$$

This calculation yields the internal radius:

$$\begin{aligned} a &= \sqrt[3]{\frac{V_{\text{internal}}}{2\pi \cdot \frac{L}{2a}}} \\ &= \sqrt[3]{\frac{10.000}{2\pi \cdot 10}} \\ &= 5,42 \text{ m} \end{aligned}$$

Subsequently, the internal length of the cylinder can be determined:

$$\begin{aligned} L &= \frac{L}{2a} \cdot 2a \\ &= 10 \cdot 2 \cdot 5,42 \\ &= 108,4 \text{ m} \end{aligned}$$

With these values established, the membrane force can be calculated:

$$\begin{aligned} n &= -pa \\ &= -1,01 \cdot 10^7 \cdot 5,42 \\ &= -5,45 \cdot 10^7 \text{ N/m} \end{aligned}$$

From this point, the thickness can be estimated, under the assumption that compressive stress remains consistent across the thickness of the cross-section:

$$\begin{aligned} t &= \frac{|n|}{f_{cd}} \\ &= \frac{|-5,45 \cdot 10^7|}{40 \cdot 10^6} \\ &= 1,36 \text{ m} \end{aligned}$$

Applying this thickness leads to an increase of $1,36/5,42 = 25,1\%$ of the external radius of the cross-section.

D.1.3. Initial thickness estimation of toroidal design

In this section, the calculations are performed for the torus, utilizing the same slenderness factor, with $\frac{b}{a} = 10$ as an example. It is important to note that the major radius b remains constant with varying thickness. Therefore, there is no distinction between b_{internal} and b_{external} , referring simply to b . Conversely, a refers to the internal surface of the torus, as defined in subsection 3.2.3

The volume of the torus is calculated as follows:

$$\begin{aligned} V_{\text{internal}} &= 2\pi^2 a^2 b \\ &= 2\pi^2 a^3 \cdot \frac{b}{a} \end{aligned}$$

This calculation yields the internal radius:

$$\begin{aligned} a_{\text{internal}} &= \sqrt[3]{\frac{V_{\text{internal}}}{2\pi^2 \cdot \frac{b}{a}}} \\ &= \sqrt[3]{\frac{10.000}{2\pi^2 \cdot 10}} \\ &= 3,70 \text{ m} \end{aligned}$$

For the major radius of the torus:

$$\begin{aligned} b &= \frac{b}{a} \cdot a \\ &= 10 \cdot 3,70 \\ &= 37,0 \text{ m} \end{aligned}$$

Consequently, the membrane force can be calculated.

$$\begin{aligned} n &= -pa \frac{-\frac{1}{2} + \frac{b}{a}}{-1 + \frac{b}{a}} \\ &= -1,01 \cdot 10^7 \cdot 3,70 \cdot \frac{-\frac{1}{2} + 10}{-1 + 10} \\ &= -3,93 \cdot 10^7 \text{ N/m} \end{aligned}$$

From this point, the thickness can be estimated, under the assumption that compressive stress remains consistent across the thickness of the cross-section:

$$\begin{aligned} t &= \frac{|n|}{f_{cd}} \\ &= \frac{|-3,93 \cdot 10^7|}{40 \cdot 10^6} \\ &= 0,98 \text{ m} \end{aligned}$$

Applying this thickness leads to an increase of $0,98/3,71 = 26,5\%$ of the external radius of the cross-section.

D.1.4. Iterative thickness determination

Through the application of the calculated thicknesses, a significant increase in the external radius is observed for each shape: 12,6% for the sphere, 25,1% for the cylinder and 26,5% for the torus. Consequently, the maximum membrane force, which is determined by the radius of each shape, increases too. The initial thickness estimation was based on the assumption that the compressive stress in the cross-section is constant over the thickness and is equal to the design compressive strength. An increase in the membrane force subsequently results in the maximum compressive stress exceeding the design compressive strength.

To illustrate this principle, the cylinder's membrane force is used as an example:

$$\begin{aligned} n_0 &= -p \cdot a \\ &= -5,45 \cdot 10^7 \text{ N/m} \end{aligned}$$

$$\begin{aligned} t_0 &= \frac{|n_0|}{f_{cd}} \\ &= 1,36 \text{ m} \end{aligned}$$

This establishes the foundation for the iterative scheme used to determine the thickness:

$$n_{i+1} = -p(a + t_i)$$

Check whether $\left| \frac{n_{i+1}}{t_i} \right| - f_{cd} > 0,001 \text{ MPa}$. If so:

$$t_{i+1} = \frac{|n_{i+1}|}{f_{cd}} \text{ for } i = 0, 1, 2..$$

For the cylinder this results in:

$$\begin{aligned} n_1 &= -p(a + t_0) \\ &= -1,01 \cdot 10^7 (5,42 + 1,36) \\ &= -6,82 \cdot 10^7 \text{ N/m} \end{aligned}$$

$$\begin{aligned} \left| \frac{n_1}{t_0} \right| - f_{cd} &= \frac{6,13 \cdot 10^7}{1,36} \cdot 10^{-6} - 40 \\ &= 10,055 \text{ MPa} > 0,001 \end{aligned}$$

$$\begin{aligned} t_1 &= \frac{|n_{i+1}|}{f_{cd}} \\ &= \frac{|-6,82 \cdot 10^7|}{40 \cdot 10^6} \\ &= 1,70 \text{ m} \end{aligned}$$

The first iteration results in a substantial increase in the required thickness. These iterations are continued until the tolerance is met, at which point the final thickness is determined:

$$\frac{|n_{i+1}|}{t_i} - f_{cd} < 0,001$$

The graph in Figure D.1 illustrates the required number of iterations for each shape. Interestingly, the number of iterations remains constant for the internal volume of each shape. Additionally, the slenderness of the cylinder does not impact the required number of iterations to meet the tolerance, whereas in the case of the torus, it does. This can be attributed to the parameters affecting the maximum membrane force.

The maximum membrane force of the torus increases not only with an increased minor radius but also with a decreased slenderness. An increase in thickness leads to a larger minor radius a . This aspect applies to both the sphere and cylinder as well. However, the maximum membrane force of the torus is also influenced by its slenderness, defined as $\frac{b}{a}$. For an increased minor radius a , the slenderness of the torus decreases. A lower slenderness results in a higher maximum membrane force, necessitating an even greater thickness. Consequently, more iterations are required to meet the tolerance, especially when the torus is less slender. This geometrical second-order effect does not apply to the cylinder, as its maximum membrane force is solely determined by the radius and is not dependent on its slenderness.

This observation aligns with the earlier comments made in Section 4.1.1, where it was noted that the nonlinearity in the CIV-ratio of the cylinder with varying slenderness was exclusively attributed to the inclusion of the caps.

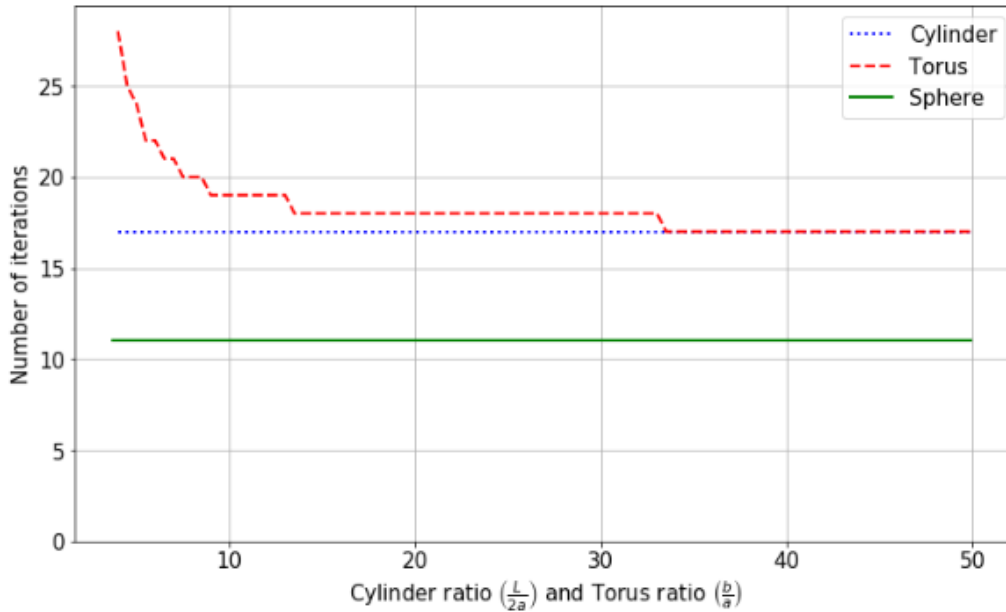


Figure D.1: Number of iterations required to determine thickness, for $V = 10.000 \text{ m}^3$, $depth = 1000 \text{ m}$

D.1.5. Calculation of volumes of concrete

Once the thickness of the shell is determined, the volumes of concrete required to construct the reservoir can be calculated. This is achieved by calculating the external volume and subtracting the internal volume:

For a sphere:

$$V_{\text{concrete,sphere}} = \frac{4}{3}\pi (a+t)^3 - V_{\text{internal}}$$

For a cylinder, where the caps are modeled as circular plates with a thickness of twice the shell thickness:

$$V_{\text{concrete,cylinder}} = \pi (a+t)^2 (2t + L + 2t) - V_{\text{internal}}$$

And for a torus:

$$V_{\text{concrete,torus}} = 2\pi^2 (a+t)^2 b - V_{\text{internal}}$$

The CIV-ratio that ensures neutral buoyancy was determined as follows, where subscript c represents concrete and i denotes internal:

$$\rho_c V_c = \rho_{sw} (V_c + V_i)$$

$$\begin{aligned} \frac{V_c}{V_i} &= \frac{\rho_{sw}}{\rho_c - \rho_{sw}} \\ &= \frac{1025}{2400 - 1025} \\ &= 0,75 [-] \end{aligned}$$

D.1.6. Iterations of calculations for graph production

The calculations described between Subsections D.1.1 and subsection D.1.4 were executed following the outlined procedures. These calculations were repeatedly performed using Python to generate the results presented in the graphs from Section 4.1.

In Figures 4.2 and 4.4 the required volume of concrete was simply calculated with a specific internal volume as input. The calculations were then executed for various cylinder and torus slenderness values.

In Figure 4.6 the internal volume was set at 10.000 m^3 , and the slenderness of the cylinder and torus reservoir was varied within the range $4 \leq \frac{L}{2a} = \frac{b}{a} \leq 50$. The required volume of concrete was then calculated and divided by the internal volume, to obtain the CIV-ratio.

In Figure 4.7 the internal volume was also set at 10.000 m^3 . For a concrete design compressive strength $f_{cd} = 40 \text{ MPa}$, the required volume of concrete was calculated for each shape, with various cylinder and torus configurations. In the context of this explanation, this is referred to as the base volume. It is important to note that each shape and configuration has its own base volume. Subsequently, the concrete strength was gradually varied, from -25% to $+25\%$ with respect to f_{cd} . At intervals, spaced $0,2 \text{ MPa}$ apart, the required volume of concrete was calculated. For each shape and configuration, the variation in required volume of concrete (in %) with respect to the base volume was determined. Ultimately, for each concrete strength variation, the concrete volume variation was calculated, as depicted in Figure 4.7.

D.2. Determination of foundation dimensions

This section presents the calculations performed to derive preliminary results for the contribution of foundations to the CIV-ratios for each shape. It begins by discussing the foundational design principles for spheres, followed by the determination of the required concrete volume. The section then moves on to the foundation design for cylinders, including the calculation of concrete volume requirements. The same methodology is subsequently applied to toroidal foundations.

D.2.1. Sphere

The foundation design for a spherical reservoir consists of a pedestal and a circular slab. The design, as outlined in [10], serves as the basis for scaling the foundation dimensions to accommodate various internal volumes. The following parameters apply, derived from Figure D.2:

- $a_{\text{sphere}} = 12,9 \text{ m}$
- $a_{\text{pedestal}} = 12,5 \text{ m}$
- $a_{\text{plate}} = 15 \text{ m}$
- $t_{\text{shell}} = 2,4 \text{ m}$
- $t_{\text{pedestal}} = 1 \text{ m}$
- $t_{\text{plate}} = 1,6 \text{ m}$
- $A_{\text{pedestal}} = \pi \left(\left(a_{\text{pedestal}} + \frac{t_{\text{pedestal}}}{2} \right)^2 - \left(a_{\text{pedestal}} - \frac{t_{\text{pedestal}}}{2} \right)^2 \right) = \pi (13^2 - 12^2) = 78,5 \text{ m}^2$

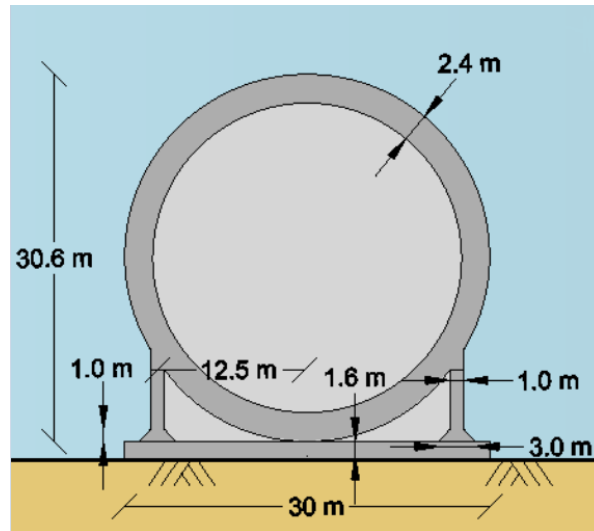


Figure D.2: Sphere foundation design in [10]

$$\bullet h_{\text{pedestal}} = \sqrt{(a_{\text{sphere}} + t_{\text{shell}})^2 - a_{\text{pedestal}}^2} = \sqrt{15,3^2 - 12,5^2} = 8,82 \text{ m}$$

With these parameters in place, the normal compressive stress in the bottom of the pedestal can be calculated. The thickness of the pedestal is determined based on this maximum normal stress at the pedestal's bottom. It is dependent on both the volume of concrete in the reservoir and the pedestal. The highest stress value is achieved at 100% reservoir filling, which is employed in the calculations.

The entire weight of the sphere is borne by the pedestal, and the design is such that the midpoint of the sphere does not make contact with the foundation slab, as indicated in [10]. The weight of the sphere can be calculated as follows:

$$\begin{aligned} F_v &= (V_{\text{concrete,reservoir}} + V_{\text{concrete,pedestal}}) (\rho_{\text{concrete}} - \rho_{\text{sw}}) g \\ &= \left(\frac{4}{3} \pi (15,3^3 - 12,9^3) + 78,5 \cdot 8,82 \right) (2400 - 1025) 9,81 \\ &= 90,42 \text{ MN} \end{aligned}$$

The pedestal's bottom's normal stress, denoted as $\sigma_{\text{pedestal,bottom}}$, is calculated as follows:

$$\begin{aligned} \sigma_{\text{pedestal,bottom}} &= \frac{F_v}{A_{\text{pedestal}}} \\ &= \frac{90,42}{78,5} \\ &= 1,15 \text{ MPa} \end{aligned}$$

It is important to note that these calculations do not account for the tapered foot in the pedestal. The value of 1,15 MPa representing the normal stress at the pedestal's bottom is later used to scale the foundation design for spherical reservoirs with different internal volumes.

Moving on to the analysis of the foundation plate, the line load of the pedestal on the foundation plate results in a negative bending moment in the plate, as shown in Figure D.3. The plate's thickness is determined based on the magnitude of this moment, as outlined in [10]. The model can be simplified as depicted in Figure D.4. The magnitude of the line-load under the center of the pedestal is calculated as follows:

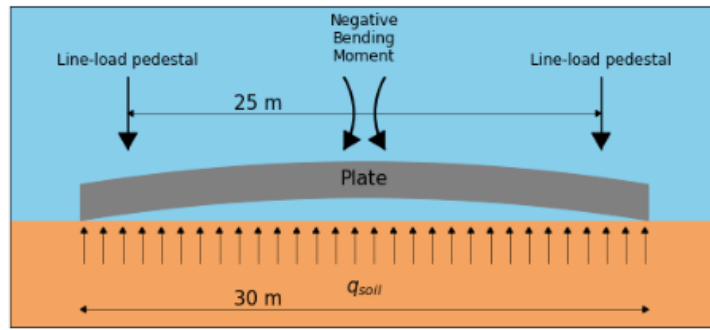


Figure D.3: Negative bending moment in circular foundation plate

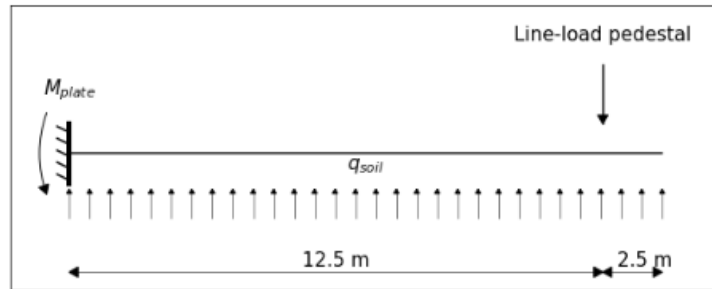


Figure D.4: Schematization of negative bending moment in circular foundation plate

$$\begin{aligned}
 F_{\text{line-load}} &= \frac{F_v}{L_{\text{pedestal}}} \\
 &= \frac{F_v}{2\pi a_{\text{pedestal}}} \\
 &= \frac{90,42}{2\pi \cdot 12,5} \\
 &= 1,15 \text{ MN/m}
 \end{aligned}$$

The resistant pressure in the soil under the plate foundation is calculated as follows:

$$\begin{aligned}
 q_{\text{soil}} &= \frac{F_{\text{line-load}}}{a_{\text{plate}}} \\
 &= \frac{1,15}{15} \\
 &= 76,75 \text{ kPa}
 \end{aligned}$$

The moment at the center of the plate, arising from the line load and soil stress (across a 1-meter wide strip), is calculated as:

$$\begin{aligned}
 M_{\text{plate}} &= F_{\text{line-load}} \cdot 12,5 - q_{\text{soil}} \cdot \frac{1}{2} \cdot 15^2 \\
 &= 1,15 \cdot 12,5 - 0,0768 \cdot \frac{1}{2} \cdot 15^2 \\
 &= 5,76 \text{ MNm}
 \end{aligned}$$

The foundation plate, as depicted in Figure D.2, has a thickness of 1,6 m. Thus, a negative bending moment of 5,76 MN necessitates a thickness of 1,6 m.

The bending moment resistance design value per meter, considering the calculated moment and plate thickness, is:

$$\begin{aligned} M_{\text{plate,design}} &= \frac{M_{\text{plate}}}{t_{\text{plate}}} \\ &= \frac{5,76}{1,6} \\ &= 3,60 \text{ MNm/m} \end{aligned}$$

These computed values of $\sigma_{\text{pedestal}} = 1,15 \text{ MPa}$ and $M_{\text{plate,design}} = 3,60 \text{ MNm/m}$ will be utilized to scale the foundation dimensions for a spherical reservoir with varying internal volumes.

Scaling foundation for varying internal volumes

This section outlines the process of adapting the foundation dimensions for a spherical reservoir with different internal volumes using the previously established parameters. For illustrative purposes, an internal volume of 10.000 m^3 is used.

- $V_{\text{internal}} = 10.000 \text{ m}^3$
- $a = 13,37 \text{ m}$
- $t = 1,92 \text{ m}$

The internal volume is utilized to determine the reservoir radius and the requisite shell thickness, following the methodology described in section 4.1 and section D.1. The weight of the sphere is then calculated as follows:

$$\begin{aligned} F_{\text{weight,reservoir}} &= V_{\text{concrete,reservoir}} (\rho_{\text{concrete}} - \rho_{\text{sw}}) g \\ &= \frac{4}{3} \pi \left((13,37 + 1,92)^3 - 13,37^3 \right) (2400 - 1025) 9,81 \\ &= 66,94 \text{ MN} \end{aligned}$$

The adapted foundation design can be observed in Figure D.5, which closely mirrors the design presented in [10]. Figure D.5a is a reproduction of Figure 3.1.

The height of the pedestal can be determined using Pythagoras:

$$\begin{aligned} h_{\text{pedestal}} &= a + t - \sqrt{(a + t)^2 - a^2} \\ &= 13,37 + 1,92 - \sqrt{(13,37 + 1,92)^2 - 13,37^2} \\ &= 7,87 \text{ m} \end{aligned}$$

The required value of A_{pedestal} is now calculated as:

$$\begin{aligned} A_{\text{pedestal}} \sigma_{\text{design}} &= F_{\text{weight,reservoir}} + F_{\text{weight,pedestal}} \\ &= F_{\text{weight,reservoir}} + A_{\text{pedestal}} h_{\text{pedestal}} (\rho_{\text{concrete}} - \rho_{\text{sw}}) g \end{aligned}$$

Solving for A_{pedestal} :

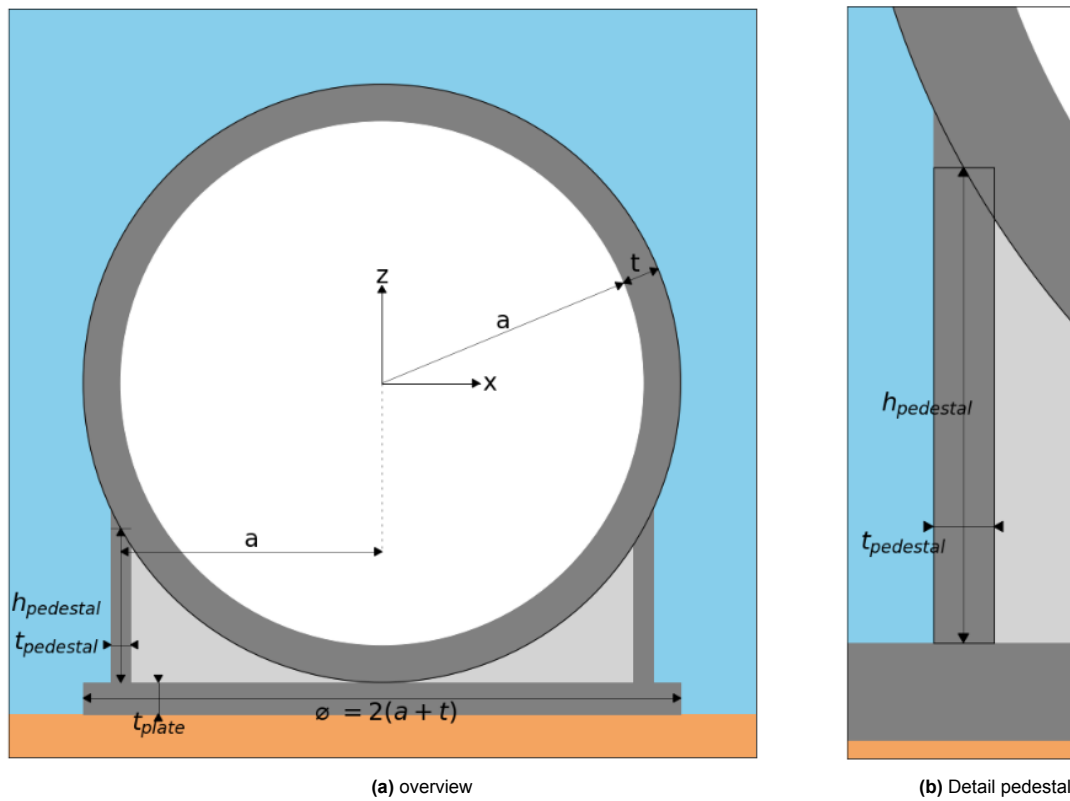


Figure D.5: Cross-section of sphere

$$\begin{aligned}
 A_{\text{pedestal}} &= \frac{F_{\text{weight,reservoir}}}{\sigma_{\text{design}} - h_{\text{pedestal}} (\rho_{\text{concrete}} - \rho_{\text{sw}}) g} \\
 &= \frac{66,94}{1,15 - 7,87 (2400 - 1025) 9,81 \cdot 10^{-6}} \\
 &= 64,05 \text{ m}^2
 \end{aligned}$$

The total weight of the reservoir and pedestal is now determined:

$$\begin{aligned}
 F_v &= F_{\text{weight,reservoir}} + F_{\text{weight,pedestal}} \\
 &= F_{\text{weight,reservoir}} + A_{\text{pedestal}} h_{\text{pedestal}} (\rho_{\text{concrete}} - \rho_{\text{sw}}) g \\
 &= 66,94 + 64,05 \cdot 7,87 (2400 - 1025) 9,81 \cdot 10^{-6} \\
 &= 73,73 \text{ MN}
 \end{aligned}$$

The volume of the pedestal is approximated as a ring with a flat top. While the top isn't entirely flat, the effect on the pedestal's volume is considered negligible and is therefore disregarded.

Now, the thickness of the pedestal can be calculated as:

$$\begin{aligned}
 A_{\text{pedestal}} &= \pi \left(\left(a + \frac{t}{2} \right)^2 - \left(a - \frac{t}{2} \right)^2 \right) \\
 &= 2\pi at
 \end{aligned}$$

$$\begin{aligned}
 t_{\text{pedestal}} &= \frac{A_{\text{pedestal}}}{2\pi a} \\
 &= \frac{64,05}{2\pi \cdot 13,37} \\
 &= 0,76 \text{ m}
 \end{aligned}$$

The foundation plate thickness must also be determined. For this, the magnitude of the line-load under the pedestal and the soil stress should be calculated.

$$\begin{aligned}
 F_{\text{line-load}} &= \frac{F_v}{L_{\text{pedestal}}} \\
 &= \frac{F_v}{2\pi a_{\text{pedestal}}} \\
 &= \frac{73,73}{2\pi \cdot 13,37} \\
 &= 0,878 \text{ MN/m}
 \end{aligned}$$

The resistant pressure in the soil under the plate foundation is calculated as:

$$\begin{aligned}
 q_{\text{soil}} &= \frac{F_{\text{line-load}}}{a_{\text{plate}}} \\
 &= \frac{1,15}{13,37 + 1,92} \\
 &= 57,44 \text{ kPa}
 \end{aligned}$$

The moment at the middle of the plate due to the line load and soil stress, across a 1-meter wide strip, is computed as:

$$\begin{aligned}
 M_{\text{plate}} &= F_{\text{line-load}} \cdot a - q_{\text{soil}} \cdot \frac{1}{2} \cdot (a + t)^2 \\
 &= 0,878 \cdot 13,37 - 0,05744 \cdot \frac{1}{2} \cdot (13,37 + 1,92)^2 \\
 &= 5,02 \text{ MNm}
 \end{aligned}$$

Since it was established that the plate should be 1 meter thick to resist a bending moment of 3,60 MNm/m, the required thickness of the plate becomes:

$$\begin{aligned}
 t_{\text{plate}} &= \frac{M_{\text{plate}}}{M_{\text{plate,design}}} \\
 &= \frac{5,02}{3,60} \\
 &= 1,40 \text{ m}
 \end{aligned}$$

The volume of concrete required for constructing the foundation can now be computed:

$$\begin{aligned}
 V_{\text{concrete, foundation}} &= V_{\text{pedestal}} + V_{\text{plate}} \\
 &= A_{\text{pedestal}} h_{\text{pedestal}} + \pi (a + t)^2 t_{\text{plate}} \\
 &= 64,05 \cdot 7,87 + \pi (13,37 + 1,92)^2 \cdot 1,40 \\
 &= 1.529 \text{ m}^3
 \end{aligned}$$

D.2.2. Cylinder foundation width

The design approach for a cylinder foundation initiates with an initial assessment of its width, which is expressed as a fraction of the overall width of the cross-section. This width serves as the basis for creating a foundational block, supporting the cylinder structure. The area of the base in the cross-section is calculated and multiplied with the length of the cylinder, to obtain the volume of the foundation. To assist in visualizing this process, a cross-sectional representation of the cylinder foundation is presented in Figure D.6, with particular areas highlighted to aid in comprehending the cross-sectional area calculations.

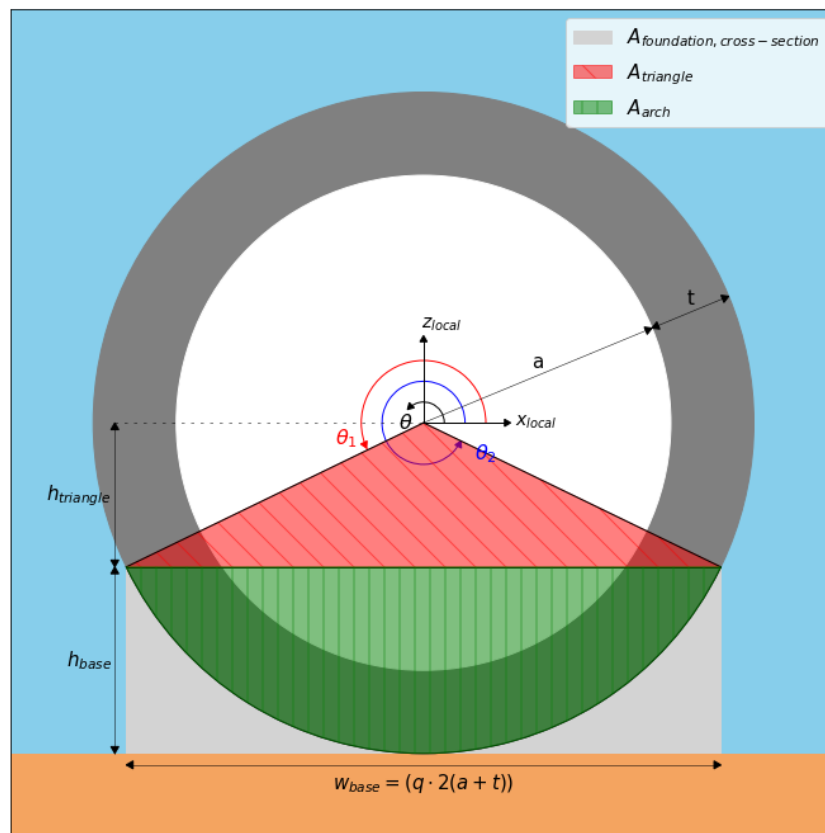


Figure D.6: Cylinder foundation side view

For illustrative purposes, an internal volume of 10.000 m³ is considered, with a slenderness value of 10. Following the methodology detailed in Section 4.1 and Appendix D.1, the following cross-sectional parameters are derived:

- $a = 5,42 \text{ m}$
- $L_{\text{external}} = 115,66 \text{ m}$
- $t = 1,82 \text{ m}$

The width of the foundation is selected as 90% of the total width of the cross-section, denoted as $q = 0.9$. It is worth noting that this exaggerated width was chosen for clarity in the plot.

Calculating the cross-sectional area of the foundation block, as shown in the light grey shading in Figure D.6, requires subtracting the green arch area from the rectangular foundation area. The green arch area can be found by subtracting the red triangular area from a segment of the total circular area.

The calculations begin by finding the values of θ_1 and θ_2 :

$$\begin{aligned}\theta_1 - \pi &= \arccos\left(\frac{\frac{1}{2} \cdot \text{width}_{\text{foundation}}}{\frac{1}{2} \cdot \text{width}_{\text{total}}}\right) \\ &= \arccos\left(\frac{\frac{1}{2}q \cdot 2(a+t)}{\frac{1}{2} \cdot 2(a+t)}\right) \\ &= \arccos(q) = \arccos(0,9) = 0,451 \text{ rad.}\end{aligned}$$

$$\theta_1 = 0,451 + \pi = 3,59 \text{ rad.}$$

$$\theta_2 = 2\pi - 0,451 = 5,83 \text{ rad.}$$

With these angles defined, the area of the circle-segment and the triangle can be computed:

$$\begin{aligned}A_{\text{circle-segment}} &= A_{\text{triangle}} + A_{\text{arch}} \\ &= \pi(a+t)^2 \frac{\theta_2 - \theta_1}{2\pi} \\ &= \pi(5,42 + 1,82)^2 \frac{5,83 - 3,59}{2\pi} \\ &= 58,68 \text{ m}^2\end{aligned}$$

$$\begin{aligned}A_{\text{triangle}} &= \frac{1}{2}w_{\text{triangle}}h_{\text{triangle}} \\ &= \frac{1}{2}(q \cdot 2(a+t)) \cdot -(a+t) \sin \theta_1 \\ &= \frac{1}{2}(0,9 \cdot 2(5,42 + 1,82)) \cdot -(5,42 + 1,82) \sin(3,59) \\ &= 20,56 \text{ m}^2\end{aligned}$$

As previously mentioned, the area of the green arch in Figure D.6 is calculated by subtracting the area of the triangle from the area of the circle segment:

$$\begin{aligned}A_{\text{arch}} &= A_{\text{triangle}} - A_{\text{circle-segment}} \\ &= 58,68 - 20,56 \\ &= 38,12 \text{ m}^2\end{aligned}$$

Now, the cross-sectional area of the foundation can be determined:

$$\begin{aligned}A_{\text{foundation,cross-section}} &= h_{\text{base}}w_{\text{base}} - A_{\text{triangle}} \\ &= (a+t(1 + \sin \theta_1)) \cdot (q \cdot 2(a+t)) - A_{\text{triangle}} \\ &= ((5,42 + 1,82)(1 + \sin(3,59))) \cdot (0,9 \cdot 2(5,42 + 1,82)) - 32,07 \\ &= 15,09 \text{ m}^2\end{aligned}$$

Following this, the volume of concrete in the foundation can be calculated:

$$\begin{aligned} V_{\text{foundation}} &= A_{\text{foundation, cross-section}} L_{\text{external}} \\ &= 15,09 \cdot 115,66 \\ &= 1745,20 \text{ m}^3 \end{aligned}$$

Additionally, the area of the footprint of the foundation is determined as follows:

$$\begin{aligned} A_{\text{foundation}} &= w_{\text{base}} L_{\text{external}} \\ &= q \cdot 2(a + t) L_{\text{external}} \\ &= 0,9 \cdot 2(5,42 + 1,82) \cdot 115,66 \\ &= 1507,13 \text{ m}^2 \end{aligned}$$

D.2.3. Torus foundation width

Similar to the cylinder foundation, the design process for the torus foundation commences with an initial estimation of its width, expressed as a percentage of the total width of the cross-section. The foundational base is conceived as a robust, solid block that provides essential support to the torus structure. A cross-sectional representation is presented in Figure D.7. The precise volume of this foundation base is a critical parameter, as it forms the basis for calculating the stress exerted by the structure on the underlying soil and it contributes to the CIV-ratio.

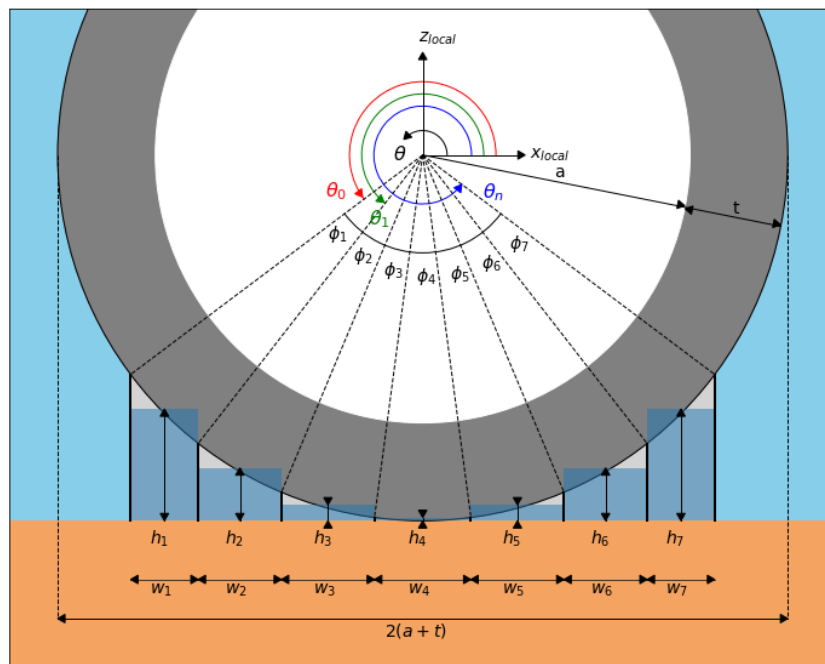


Figure D.7: Torus foundation side view, cross-section AA of Figure D.8

The volume of the torus foundation base is established through numerical methods. This base is discretized into n sections, each characterized by a certain height h and width w , as depicted in Figure D.7. Subsequently, these sections are rotated about the global center of the torus, as illustrated in Figure D.8. This rotational process transforms each section into a ring, whose volume can be readily computed. Although, in practical calculations, a value of $n = 100$ is employed for precision, the process is here illustrated with $n = 7$ for simplicity.

For the sake of a numerical example, an internal volume of 10.000 m^3 is assumed, with a slenderness value of 10. Based on the methodology described in Section 4.1 and Appendix D.1, this leads to the following cross-sectional parameters:

- $a = 3,70 \text{ m}$
- $b = 37,00 \text{ m}$
- $t = 1,38 \text{ m}$

The width of the foundation is chosen as 90% of the total width of the cross-section.

To proceed, the various angles involved need to be determined:

$$\begin{aligned}\theta_0 - \pi &= \arccos\left(\frac{\frac{1}{2} \cdot \text{width}_{\text{foundation}}}{\frac{1}{2} \cdot \text{width}_{\text{total}}}\right) \\ &= \arccos\left(\frac{\frac{1}{2}q \cdot 2(a+t)}{\frac{1}{2} \cdot 2(a+t)}\right) \\ &= \arccos(q) \\ &= \arccos(0,9) \\ &= 0,451 \text{ rad.}\end{aligned}$$

Where q is the width percentage of the foundation and $0 < q \leq 1$. Subsequently, θ_0 can be determined as $3,59 \text{ rad.}$, which is equal to $0,451 + \pi$. Once θ_0 is known, the remaining angles can be calculated:

$$\begin{aligned}\theta_n &= 2\pi - \arccos(q) \\ &= 5,83 \text{ rad.} \\ &= \theta_0 + \sum_{i=1}^n \phi_i\end{aligned}$$

$$\begin{aligned}\phi_i \text{ for } i = 1, 2 \dots n &= \frac{\theta_n - \theta_0}{n} \\ &= \frac{5,83 - 0,451}{7} \\ &= 0,320 \text{ rad.}\end{aligned}$$

By introducing $\phi_0 = 0$, θ_i is calculated as follows:

$$\begin{aligned}\theta_i \text{ for } i = 0, 1 \dots n &= \theta_0 + \sum_{i=0}^i \phi_i \\ &= [3,59 \quad 3,91 \quad 4,23 \quad 4,55 \quad 4,87 \quad 5,19 \quad 5,51 \quad 5,83] \text{ [rad.]}\end{aligned}$$

Subsequently, the local x-coordinates and the widths can be determined. The widths are not actually used in further calculations, since the volumes are determined based on the local x-coordinates. However, the calculation of the values of the widths are mentioned for clarity.

$$\begin{aligned}x_{\text{local},i} \text{ for } i = 0, 1 \dots n &= (a+t) \cos \theta_i \\ &= [-4,57 \quad -3,64 \quad -2,34 \quad -0,81 \quad 0,81 \quad 2,34 \quad 3,64 \quad 4,57] \text{ [m]}\end{aligned}$$

$$w_i = \frac{x_{i-1} + x_i}{2} \text{ for } i = 1, 2 \dots n$$

$$= [0,93 \ 1,30 \ 1,54 \ 1,62 \ 1,54 \ 1,30 \ 0,93] \text{ [m]}$$

The heights are calculated similarly:

$$z_{\text{local},i} = (a + t) \sin \theta_i \text{ for } i = 0, 1 \dots n$$

$$= [-2,21 \ -3,54 \ -4,50 \ -5,01 \ -5,01 \ -4,50 \ -3,54 \ -2,21] \text{ [m]}$$

$$h_i = a + t + \frac{z_{i-1} + z_i}{2} \text{ for } i = 1, 2 \dots n$$

$$= [2,20 \ 1,01 \ 0,32 \ 0,06 \ 0,32 \ 1,01 \ 2,20] \text{ [m]}$$

As previously mentioned, the rectangles in Figure D.7 are rotated around the global center of the torus to create rings, as depicted in Figure D.8. The volume of each ring is calculated as follows:

$$V_{\text{ring},i} = h_i \left(\pi (b + x_{\text{local},i})^2 - \pi (b + x_{\text{local},i-1})^2 \right)$$

$$= [422,44 \ 293,01 \ 109,12 \ 24,39 \ 118,84 \ 344,59 \ 527,91] \text{ [m}^3\text{]}$$

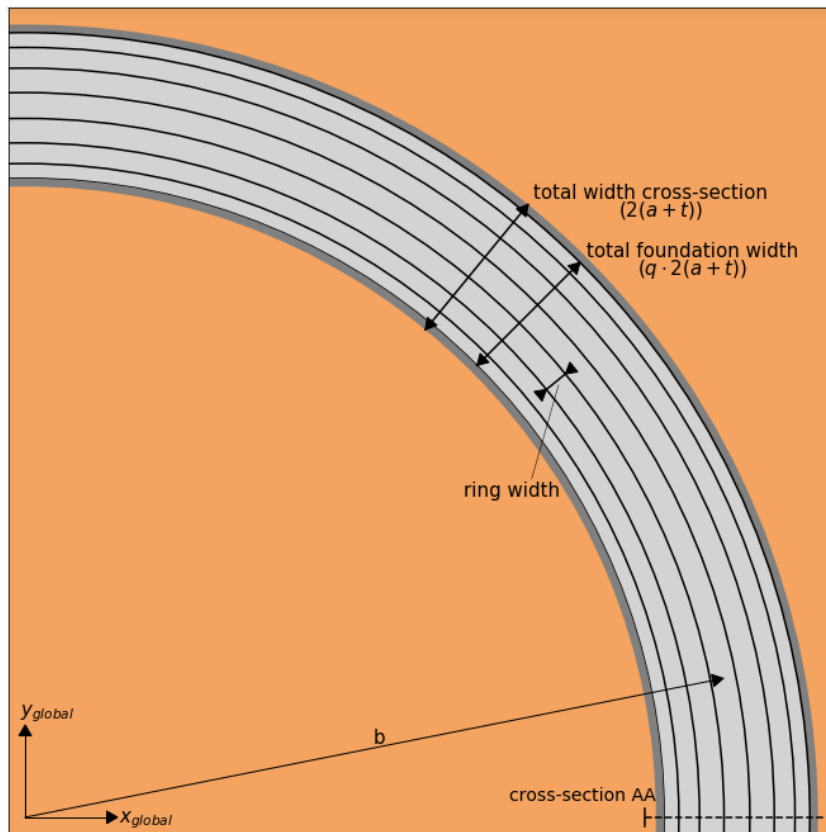


Figure D.8: Torus foundation top view; Quadrant plot

Subsequently, the total volume of the foundation is determined as the sum of the volumes of the rings:

$$V_{\text{foundation, total}} = \sum_{i=1}^n V_{\text{ring}, i} = 1840,3 \text{ [m}^3\text{]}$$

To determine the footprint of the foundation, the horizontal cross-sectional area is considered, which is defined as:

$$\begin{aligned} A_{\text{foundation}} &= \pi \left((b + q(a + t))^2 - (b - q(a + t))^2 \right) \\ &= \pi \left((37,0 + 0,9(3,70 + 1,37))^2 - (37,0 - 0,9(3,70 + 1,37))^2 \right) \\ &= 2125,18 \text{ [m}^2\text{]} \end{aligned}$$

Finally, the CIV-ratio of the foundation is calculated. This can later be added up to the CIV-ratio of the reservoir and be compared to the other shapes.

$$\frac{V_{\text{concrete, foundation}}}{V_{\text{internal}}} = \frac{1840,3}{10.000} = 0,184 \text{ [-]}$$

D.2.4. Iterative foundation width determination for cylinder and torus

Sections D.2.2 and D.2.3 provide the methodology for computing the dimensions of foundations for a torus and a cylinder. These parameters play a pivotal role in assessing the pressure exerted by these structures on the underlying soil. As detailed in Subsection 4.2.2, the maximum allowable bearing capacity of the soil is 200 kPa. In this Section, the optimal foundation width that adheres to this threshold is determined, using an illustrative example.

The initial stress imposed on the soil is contingent upon the key parameters presented in Table D.1. These parameters are derived following the method described in Section 4.1, utilizing a slenderness value of $\frac{L}{2a} = \frac{b}{a} = 10$ and a concrete strength of $f_{cd} = 40$ MPa. The computations for the foundation's volume and the area are based on the methodologies presented in Appendices D.2.2 and D.2.3. It is worth noting that the values for the torus slightly deviate from those presented in Section D.2.3. This discrepancy arises due to the utilization of $n = 100$ in the calculations, as opposed to the example employing $n = 7$.

Description	Symbol	Cylinder	Torus	Unit
Internal volume	V_{internal}	10.000	10.000	m ³
Volume of concrete in reservoir	$V_{\text{concrete, reservoir}}$	9.042	8.836	m ³
Initial foundation width	q	0,9	0,9	-
Volume of concrete in foundation	$V_{\text{concrete, foundation}}$	1.745	1.727	m ³
Area footprint of foundation	$A_{\text{foundation}}$	1.507	2.125	m ²

Table D.1: Relevant parameters for soil stress assessment in cylinder and torus foundation

To assess the stress imposed by the foundation on the underlying soil, it is imperative to compute the weight of the structure. Given that a 100% filling level of the reservoir is normative, this value will be used in the calculations. For the sake of clarity, the calculation focuses on the cylinder example alone, as the methodology for determining soil stress in the case of the torus is analogous.

The resultant vertical force acting on the soil is determined as follows:

$$\begin{aligned}
 F_v &= V_{\text{concrete, total}} (\rho_{\text{concrete}} - \rho_{\text{sw}}) g \\
 &= (V_{\text{concrete, reservoir}} + V_{\text{concrete, foundation}}) (\rho_{\text{concrete}} - \rho_{\text{sw}}) g \\
 &= (9.042 + 1.745) (2400 - 1025) 9,81 \\
 &= 145,5 \text{ MN}
 \end{aligned}$$

Subsequently, the stress exerted on the soil is calculated as follows:

$$\begin{aligned}
 \sigma_{\text{soil}} &= \frac{F_v}{A_{\text{foundation}}} \\
 &= \frac{145,5}{1.507} \\
 &= 96,5 \text{ kPa}
 \end{aligned}$$

Since this stress value is significantly lower than the designated maximum allowable bearing capacity, the foundation width can be reduced to optimize material usage. To achieve this, an iterative process is employed, in which the foundation width is decreased by 0,05% when the effective stress in the soil is lower than the design stress. Conversely, the width is increased by 0,05% when the effective stress exceeds the design stress. This iterative process continues until the effective stress is within a 0,5 kPa margin of the design stress.

For further clarity, Figure 4.10 is reproduced.

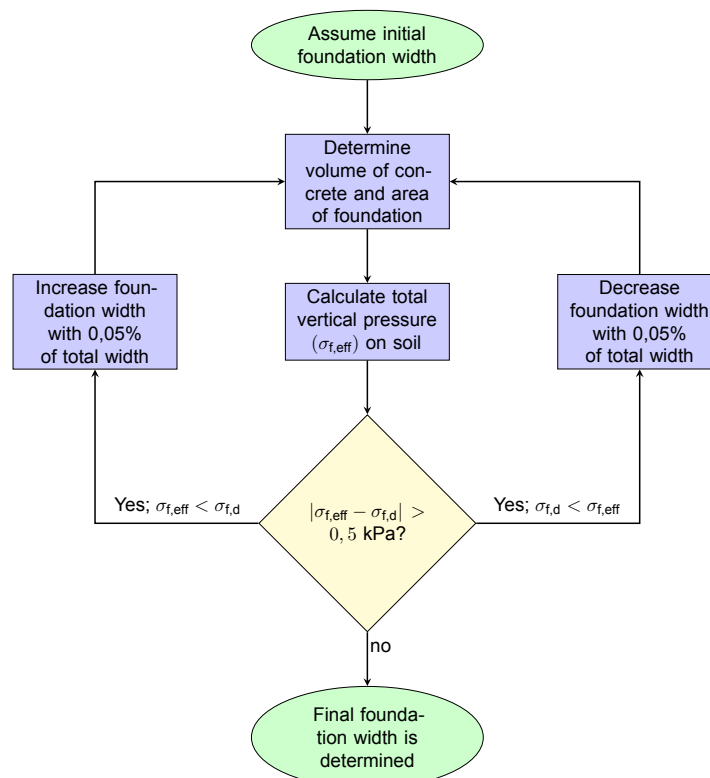


Figure D.9: Algorithm for determining foundation width for cylinder and torus

It is acknowledged that a more sophisticated algorithm could have been employed for increasing or decreasing the foundation width. Nevertheless, this 'brute-force' method yielded sufficiently rapid results, with the speed of calculations contingent on the initial foundation width estimate. It is worth noting that

a more substantial increment in width adjustment percentage could compromise the precision of the results.

The number of iterations necessary to arrive at the foundation width that guarantees a soil stress within the tolerance of the design stress is presented in Figure D.10. The V-shaped patterns observed in some of the lines are a consequence of the initial foundation width estimate being positioned at a critical threshold, where the effective stress fluctuates between being too low and too high due to variations in the internal volume.

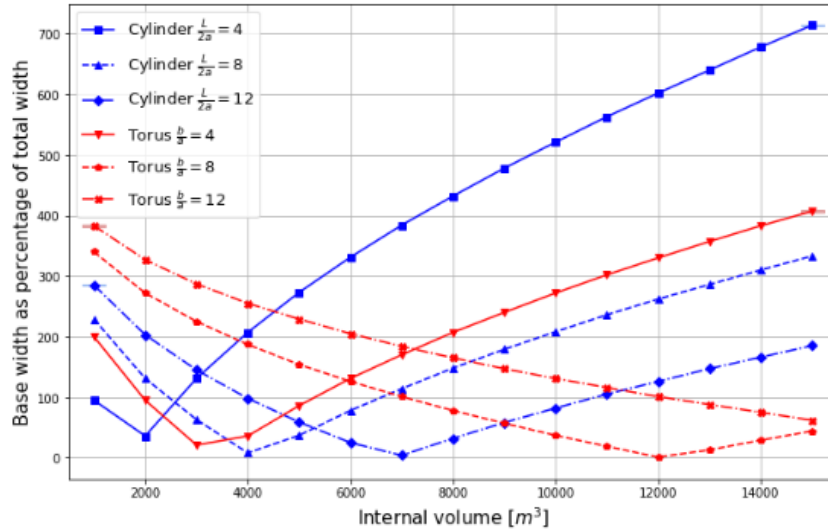


Figure D.10: Number of iterations in cylinder and torus foundation design

D.3. CIV-ratio for cylinder with hemisphere cap

This section details the determination of the cylinder's CIV-ratio with a hemisphere cap, contrasting the flat cap design presented in Section 3.2.2. In these calculations, the hemisphere has a thickness equal to the determined wall thickness of the cylinder tube, resulting in a slight overestimation of the required concrete volumes. The actual required wall thickness of the hemisphere is slightly lower than assumed in these calculations, as explained in Section 6.1.

Similar to the procedure in Appendix D.1, the required internal diameter is determined as a function of the internal volume V and the slenderness $\frac{L}{2a}$:

$$\begin{aligned} V &= \frac{4}{3}\pi a^3 + \pi a^2 L \\ &= \frac{4}{3}\pi a^3 + \pi a^2 2a \frac{L}{2a} \\ &= \left(\frac{4}{3} + 2 \frac{L}{2a} \right) \pi a^3 \end{aligned}$$

Rewriting gives:

$$a = \sqrt[3]{\frac{V}{\left(\frac{4}{3} + 2 \frac{L}{2a}\right) \pi}}$$

The required wall thickness is then determined using the same approach outlined in Appendices D.1.2 and D.1.4. Once the required wall thickness is determined, the calculation of the required volume of concrete is as follows:

$$V_{concrete} = \pi(a+t)^2 \cdot \frac{L}{2a} \cdot 2a + \frac{4}{3}\pi(a+t)^3 - V$$

Subsequently, these values are employed to estimate the required size of the foundation, following the procedure outlined in Appendix D.2.

D.4. Python code

This Section contains the Python code that executes the calculations described in Appendices D.1 and D.2 and with which the plots in Chapter 4 were generated.

```

1
2 # coding: utf-8
3
4 # In[1]:
5
6
7 import numpy as np
8 import matplotlib.pyplot as plt
9 get_ipython().run_line_magic('matplotlib', 'inline')
10 import matplotlib.ticker as mtick
11 from matplotlib.ticker import FuncFormatter
12 from matplotlib.patches import Arc, RegularPolygon, Rectangle, Circle
13 import math
14 from matplotlib.path import Path
15 import pandas as pd
16
17 # Define constants
18 g = 9.81 # gravitational constant in m/s^2
19 d = 1000 # depth in m
20 rho_seawater = 1025 # weight of seawater in kg/m^3
21 rho_concrete = 2400 # weight of concrete in kN/m^3
22 p = rho_seawater * g * d # hydrostatic pressure in N/m^2
23 fcd = 60 / 1.5 # max compressive strength in N/mm^2
24 buoyancy_ratio = rho_seawater / (rho_concrete - rho_seawater) # Ratio of concrete-to-internal
    -volume to overcome buoyant force
25 sigma_max_foundation = 200 # max bearing capacity of soil under foundation [kN/m^2]
26 initial_width_percentage = 30 # Percentage of total width used as initial guess for width of
    cylinder and torus foundation
27
28 # Define a list of linestyles and markers for better readability
29 linestyles = ['-', '--', '-.', '-', ':', (0, (3, 1, 1, 1)), (0, (5, 2))]
30 markers = ['o', 's', '^', 'D', 'v', 'p', 'X']
31
32
33 # In[2]:
34
35
36 # Function to find membrane force for each shape
37 def get_thickness(shape,d,a,b,sigma_max):
38     p = rho_seawater * g * d
39     tolerance = 10**-3
40     count = 0
41     if shape == 'sphere':
42         n_initial = a * p / 2
43         t_initial = n_initial / (sigma_max * 10**6)
44         t = t_initial
45         n_new = (a + t_initial) * p / 2
46         while n_new / t - sigma_max * 10**6 > tolerance:
47             t = n_new / (sigma_max * 10**6)
48             n_new = (a + t) * p / 2
49             count +=1
50     if shape == 'cylinder':
51         n_initial = a * p
52         t_initial = n_initial / (sigma_max * 10**6)
53         t = t_initial
54         n_new = (a + t_initial) * p
55         while n_new / t - sigma_max * 10**6 > tolerance:
56             t = n_new / (sigma_max * 10**6)

```

```

57         n_new = (a + t) * p
58         count +=1
59     if shape == 'torus':
60         n_initial = p * a * (-0.5 + b / a) / (-1 + b / a)
61         t_initial = n_initial / (sigma_max * 10**6)
62         t = t_initial
63         ba_new = b / (a + t_initial)
64         n_new = p * (a + t) * (-0.5 + ba_new) / (-1 + ba_new)
65         while n_new / t - sigma_max * 10**6 > tolerance:
66             t = n_new / (sigma_max * 10**6)
67             ba_new = b / (a + t)
68             n_new = p * (a + t) * (-0.5 + ba_new) / (-1 + ba_new)
69         count += 1
70     return t, count, t_initial
71
72 def get_thickness_non_uniform(shape,d,a,sigma_max):
73     p = rho_seawater * g * d
74     tolerance = 10**-20
75     count = 0
76     t = 0.5
77     if shape == 'sphere':
78         n = 3 * p * (a + t) ** 3 / (2 * ((a + t)**3 - a**3))
79         while n - sigma_max * 10**6 > tolerance:
80             t = t * 1.0001
81             n = 3 * p * (a + t) ** 3 / (2 * ((a + t)**3 - a**3))
82             count +=1
83     if shape == 'cylinder':
84         n = 2 * p * (a + t) ** 2 / ((a + t)**2 - a**2)
85         while n - sigma_max * 10**6 > tolerance:
86             t = t * 1.0001
87             n = 2 * p * (a + t) ** 2 / ((a + t)**2 - a**2)
88             count +=1
89     return t, count
90
91 # Function to calculate the volume of concrete for a sphere
92 def sphere(V, sigma_max, d=1000, method_t = 'uniform'):
93     a = ((3 * V) / (4 * np.pi)) ** (1/3)
94     if method_t == 'uniform':
95         t, count, t_initial = get_thickness('sphere',d,a,0,sigma_max)
96         V_initial = 4 / 3 * np.pi * (a + t_initial) ** 3 - V
97         volume_of_concrete = 4 / 3 * np.pi * (a + t) ** 3 - V
98     elif method_t == 'non-uniform':
99         t, count = get_thickness_non_uniform('sphere',d,a,sigma_max)
100         V_initial = 'No initial value is known'
101         volume_of_concrete = 4 / 3 * np.pi * (a + t) ** 3 - V
102     geometry = [a, t]
103     return volume_of_concrete, count, V_initial, geometry
104
105 # Function to calculate the volume of concrete for a cylinder
106 def cylinder(V, slenderness, sigma_max, d=1000, method_s = 'flat', method_t = 'uniform'):
107     a = (V / (2 * np.pi * slenderness)) ** (1 / 3)
108     if method_t == 'uniform':
109         t, count, t_initial = get_thickness('cylinder',d,a,0,sigma_max)
110         if method_s == 'flat':
111             Length_ext = slenderness * 2 * a + 4 * t
112             Length_ext_initial = slenderness * 2 * a + 4 * t_initial
113             V_initial = np.pi * (a + t_initial) ** 2 * Length_ext_initial - V
114             volume_of_concrete = np.pi * (a + t) ** 2 * Length_ext - V
115         elif method_s == 'hemisphere':
116             a = (V / ((4 / 3 + 2 * slenderness) * np.pi)) ** (1/3)
117             Length_int = slenderness * 2 * a
118             Length_ext = Length_int + 2 * (a + t)
119             V_initial = np.pi * (a + t_initial) ** 2 * Length_int + 4 / 3 * np.pi * (a +
120                 t_initial) ** 3 - V
121             volume_of_concrete = np.pi * (a + t) ** 2 * Length_int + 4 / 3 * np.pi * (a + t)
122                 ** 3 - V
123     elif method_t == 'non-uniform':
124         t, count = get_thickness_non_uniform('cylinder',d,a,sigma_max)
125         V_initial = 'No initial value is known'
126         if method_s == 'flat':
127             Length_ext = slenderness * 2 * a + 4 * t

```

```

126     volume_of_concrete = np.pi * (a + t) ** 2 * Length_ext - V
127     elif method_s == 'hemisphere':
128         a = (V / ((4 / 3 + 2 * slenderness) * np.pi)) ** (1/3)
129         Length_int = slenderness * 2 * a
130         Length_ext = Length_int + 2 * (a + t)
131         volume_of_concrete = np.pi * (a + t) ** 2 * Length_int + 4 / 3 * np.pi * (a + t)
132         ** 3 - V
133     geometry = [a, Length_ext, t]
134     return volume_of_concrete, count, V_initial, geometry
135
136 # Function to calculate the volume of concrete for a torus
137 def torus(V, slenderness, sigma_max, d=1000):
138     b_int = (V * slenderness ** 2 / (2 * np.pi ** 2)) ** (1 / 3)
139     a_int = b_int / slenderness
140     t, count, t_initial = get_thickness('torus', d, a_int, b_int, sigma_max)
141     V_initial = 2 * np.pi ** 2 * (a_int + t_initial) ** 2 * b_int - V
142     volume_of_concrete = 2 * np.pi ** 2 * (a_int + t) ** 2 * b_int - V
143     geometry = [a_int, b_int, t]
144     return volume_of_concrete, count, V_initial, geometry
145
146 # In[3]:
147
148 # Defining foundation functions
149
150 def sphere_foundation(a,t):
151     sigma_design_pedestal = 1.15126559484811 #[MPa]
152     M_design_plate = 3.59770498390034 * 10**6 #[MNM/m]
153
154     h_pedestal = a + t - np.sqrt((a + t)**2 - a**2)
155     F_reservoir = 4 / 3 * np.pi * ((a + t)**3 - a**3) * (rho_concrete - rho_seawater) * g
156     A_pedestal = F_reservoir * 10**(-6) / (sigma_design_pedestal - h_pedestal * (rho_concrete
157         - rho_seawater) * g * 10**(-6))
158     t_pedestal = A_pedestal / (2*np.pi*a)
159     V_pedestal = A_pedestal * h_pedestal
160     A_foundation = np.pi * (a + t)**2
161
162     F_reservoir_plus_pedestal = F_reservoir + V_pedestal * (rho_concrete - rho_seawater) * g
163     F_lineload = F_reservoir_plus_pedestal / (2 * np.pi * a)
164     q_soil = F_lineload / (a + t)
165     M_plate = F_lineload * a - q_soil * 0.5 * (a + t) ** 2
166     t_plate = M_plate / M_design_plate
167
168     V_foundation = A_pedestal * h_pedestal + np.pi * (a+t)**2 * t_plate
169     sigma_soil = (F_reservoir + V_foundation * (rho_concrete - rho_seawater) * g) / (
170         A_foundation * 10**6) #[MPa]
171
172     return V_foundation, sigma_soil, [t_pedestal, t_plate], h_pedestal
173
174 def cylinder_foundation_VA(a,t,Length,width):
175     q = width / (2 * (a + t))
176
177     theta_1 = np.arccos(q) + np.pi
178     theta_2 = 2 * np.pi - np.arccos(q)
179
180     w_base = q * 2 * (a + t)
181     h_triangle = - (a + t) * np.sin(theta_1)
182     h_base = a + t - h_triangle
183
184     A_circle_segment = np.pi * (a + t) ** 2 * (theta_2 - theta_1) / (2 * np.pi)
185     A_triangle = 0.5 * w_base * h_triangle
186     A_arch = A_circle_segment - A_triangle
187     A_foundation_rectangle = w_base * h_base
188     A_foundation_cross_section = A_foundation_rectangle - A_arch
189
190     V_foundation = A_foundation_cross_section * Length
191     A_foundation_footprint = Length * width
192     return V_foundation, A_foundation_footprint
193
194 def torus_foundation_VA(a,b,t,width,steps=100):

```

```

194     q = width / (2 * (a + t))
195     theta_0 = np.arccos(q) + np.pi
196     theta_n = 2 * np.pi - np.arccos(q)
197     phis = np.linspace(theta_0, theta_n, steps)
198
199     inner_diameters = b + (a + t) * np.cos(phis[:-1])
200     outer_diameters = b + (a + t) * np.cos(phis[1:])
201     mid_heights = ((a + t) * np.sin(phis[:-1]) + (a + t) + (a + t) * np.sin(phis[1:]) + (a +
202         t)) / 2
203
204     V_rings = np.pi * (outer_diameters**2 - inner_diameters**2) * mid_heights
205     A_foundation_footprint = np.pi * ((b + width / 2) ** 2 - (b - width / 2) ** 2)
206     return np.sum(V_rings), A_foundation_footprint
207
208 # In[4]:
209
210
211 # Setting up functions to determine desired width for torus and cylinder
212
213 def get_cylinder_foundation(V, slenderness, sigma_max_foundation, width_percentage,
214     stepsize_percentage = 0.05, method_s = 'flat', method_t = '
215     uniform'):
216     reservoir_results = cylinder(V, slenderness, fcd, method_s = method_s, method_t =
217         method_t)
218
219     weight_reservoir = reservoir_results[0] * g * (rho_concrete - rho_seawater) * 10 ** -3 #
220         Weight of the reservoir in kN
221     a_cylinder, h_cylinder, t_cylinder = reservoir_results[3][:3]
222
223     count = 0
224     initial_width = width_percentage / 100 * 2 * (a_cylinder + t_cylinder)
225     foundation_results = cylinder_foundation_VA(a_cylinder, t_cylinder, h_cylinder,
226         initial_width)
227     total_weight = weight_reservoir + foundation_results[0] * g * (rho_concrete -
228         rho_seawater) * 10 ** -3
229
230     while np.abs(total_weight / foundation_results[1] - sigma_max_foundation) > 0.5:
231         count += 1
232         if total_weight / foundation_results[1] - sigma_max_foundation > 0:
233             width_percentage = width_percentage + stepsize_percentage
234         if total_weight / foundation_results[1] - sigma_max_foundation < 0:
235             width_percentage = width_percentage - stepsize_percentage
236         width = width_percentage / 100 * 2 * (a_cylinder + t_cylinder)
237         foundation_results = cylinder_foundation_VA(a_cylinder, t_cylinder, h_cylinder, width
238             )
239         total_weight = weight_reservoir + foundation_results[0] * g * (rho_concrete -
240             rho_seawater) * 10** -3
241
242     return foundation_results[0], width_percentage, count
243
244 def get_torus_foundation(V, slenderness, sigma_max_foundation, width_percentage,
245     stepsize_percentage = 0.05):
246     reservoir_results = torus(V, slenderness, fcd)
247     weight_reservoir = reservoir_results[0] * g * (rho_concrete - rho_seawater) * 10 ** -3 #
248         Weight of the reservoir in kN
249     minor_radius, major_radius, t_torus = reservoir_results[3][:3]
250
251     count = 0
252     initial_width = width_percentage / 100 * 2 * (minor_radius + t_torus)
253     foundation_results = torus_foundation_VA(minor_radius, major_radius, t_torus,
254         initial_width)
255     total_weight = weight_reservoir + foundation_results[0] * g * (rho_concrete -
256         rho_seawater) * 10 ** -3
257
258     while np.abs(total_weight / foundation_results[1] - sigma_max_foundation) > 0.5:
259         count += 1
260         if total_weight / foundation_results[1] - sigma_max_foundation > 0:
261             width_percentage = width_percentage + stepsize_percentage
262         if total_weight / foundation_results[1] - sigma_max_foundation < 0:
263             width_percentage = width_percentage - stepsize_percentage

```

```

252     width = width_percentage / 100 * 2 * (minor_radius + t_torus)
253     foundation_results = torus_foundation_VA(minor_radius, major_radius, t_torus, width)
254     total_weight = weight_reservoir + foundation_results[0] * g * (rho_concrete -
        rho_seawater) * 10**-3
255
256     return foundation_results[0], width_percentage, count
257
258
259 # In[5]:
260
261
262 def bandwidth_indication(patches, start, end, distance, bar_length, text, fig_width,
        fig_height, xrange, yrange, color='black', linewidth = 0.5,
        x_offset=0, y_offset=0, fontsize=13):
263     # Calculate the slope of the line
264     slope = (end[1] - start[1]) / (end[0] - start[0])
265
266     # Calculate the angle of the line
267     angle = np.arctan(slope)
268
269     # Calculate the offset in x and y for the parallel lines
270     dx = distance * np.sin(angle) * (xrange / yrange)**2 * (fig_height / fig_width) ** 2
271     dy = distance * np.cos(angle)
272
273     # Calculate the offset in x and y for the bars
274     dx_bar_start = (distance + bar_length / 2) * np.sin(angle) * (xrange / yrange)**2 * (
        fig_height / fig_width) ** 2
275     dx_bar_end = (distance - bar_length / 2) * np.sin(angle) * (xrange / yrange)**2 * (
        fig_height / fig_width) ** 2
276     dy_bar_start = (distance + bar_length / 2) * np.cos(angle)
277     dy_bar_end = (distance - bar_length / 2) * np.cos(angle)
278
279     # Plot parallel line
280     ax.plot([start[0] + dx, end[0] + dx], [start[1] - dy, end[1] - dy], color=color,
        linewidth=linewidth)
281
282     # Plot bars on end of parallel line
283     ax.plot([start[0] + dx_bar_start, start[0] + dx_bar_end], [start[1] -
        dy_bar_start, start[1] - dy_bar_end], color=color, linewidth=linewidth)
284     ax.plot([end[0] + dx_bar_start, end[0] + dx_bar_end], [end[1] - dy_bar_start,
        end[1] - dy_bar_end], color=color, linewidth=linewidth)
285
286     # Plot text
287     ax.text((start[0] + end[0])/2 + dx + x_offset, (start[1] + end[1])/2 - dy + y_offset,
        text, ha='center', va='center', rotation = np.degrees(angle) * (xrange /
        yrange)**2 * (fig_width / fig_height)**2 + 180, fontsize=fontsize, color=color)
288
289
290 # In[6]:
291
292
293 # Generate data for initial and iterative CIV-ratios reservoir
294 slenderness = [4, 8, 12]
295 volumes = np.arange(1, 16) * 10**3
296 buoyancy = [V * buoyancy_ratio for V in volumes]
297
298 sphere_results_iterative = [sphere(v, fcd)[0] for v in volumes]
299 sphere_results_initial = [sphere(v, fcd)[2] for v in volumes]
300 cylinder_results_iterative = [[cylinder(v, s, fcd)[0] for s in slenderness] for v in volumes]
301 cylinder_results_initial = [[cylinder(v, s, fcd)[2] for s in slenderness] for v in volumes]
302 torus_results_iterative = [[torus(v, s, fcd)[0] for s in slenderness] for v in volumes]
303 torus_results_initial = [[torus(v, s, fcd)[2] for s in slenderness] for v in volumes]
304
305
306 # In[7]:
307
308
309 # Plot data for initial CIV-ratios reservoir
310
311 fig, ax = plt.subplots(figsize=(12, 7))
312

```

```

313 # Plot 1: Left subplot
314 ax.plot(volumes, sphere_results_initial, label="Sphere", color='green', marker=markers[0],
          linestyle=linestyles[0], linewidth=1)
315
316 for i, s in enumerate(slenderness):
317     linestyle = linestyles[i % len(linestyles)]
318     marker = markers[(i + 1) % len(markers)] # Use a different marker
319     ax.plot(volumes, [res[i] for res in cylinder_results_initial], label=rf'Cylinder $\frac{{L}}
          {{{2a}}}={s}$',
          linestyle=linestyle, marker=marker, color='blue', linewidth=1)
320
321
322 for i, s in enumerate(slenderness):
323     linestyle = linestyles[i % len(linestyles)]
324     marker = markers[(i + 1+len(slenderness)) % len(markers)] # Use a different marker
325     ax.plot(volumes, [res[i] for res in torus_results_initial], label=rf'Torus $\frac{{b}}
          {{{a}}}={s}$',
          linestyle=linestyle, marker=marker, color='red', linewidth=1)
326
327
328 ax.plot(volumes, buoyancy, color='black', label='Neutral buoyancy', linewidth=2)
329
330 # Setting colors of axes
331 ax.tick_params(axis='x', labelsz=14)
332 ax.tick_params(axis='y', labelsz=14)
333
334 ax.set_xlabel('Internal volume $[m^3]$', fontsize=15)
335 ax.set_ylabel(r'Volume of Concrete $[m^3]$', fontsize=15)
336 ax.legend(fontsize=15)
337 ax.grid(True)
338
339 # Show the subplots
340 plt.show()
341
342
343 # In[8]:
344
345
346 # Plot data for iterative CIV-ratios reservoir
347
348 fig, ax = plt.subplots(figsize=(12, 7))
349
350 # Plot the sphere data
351 ax.plot(volumes, sphere_results_iterative, label="Sphere", color='green', marker=markers[0],
          linestyle=linestyles[0], linewidth=1)
352
353 # Plot the cylinder data
354 for i, s in enumerate(slenderness):
355     linestyle = linestyles[i % len(linestyles)]
356     marker = markers[(i + 1) % len(markers)] # Use a different marker
357     ax.plot(volumes, [res[i] for res in cylinder_results_iterative], label=rf'Cylinder $\frac
          {{{L}}}{2a}={s}$',
          linestyle=linestyle, marker=marker, color='blue', linewidth=1)
358
359
360 # Plot the torus data
361 for i, s in enumerate(slenderness):
362     linestyle = linestyles[i % len(linestyles)]
363     marker = markers[(i + 1+len(slenderness)) % len(markers)] # Use a different marker
364     ax.plot(volumes, [res[i] for res in torus_results_iterative], label=rf'Torus $\frac{{b}}
          {{{a}}}={s}$',
          linestyle=linestyle, marker=marker, color='red', linewidth=1)
365
366
367 # Plot the buoyancy
368 ax.plot(volumes, buoyancy, color='black', label='Neutral buoyancy', linewidth=2)
369
370 # Setting colors of axes
371 ax.tick_params(axis='x', labelsz=14)
372 ax.tick_params(axis='y', labelsz=14)
373
374 ax.set_xlabel('Internal volume $[m^3]$', fontsize=15)
375 ax.set_ylabel(r'Volume of Concrete $[m^3]$', fontsize=15)
376 ax.legend(fontsize=15)
377 ax.grid(True)

```

```

378
379 # Show the subplots
380 plt.show()
381
382
383 # In[9]:
384
385
386 # Generate data for wall thickness and internal diameter plot
387
388 volumes = np.arange(1000,16001,5000)
389 slenderness = np.arange(4, 20.5, 2)
390
391 columns_sphere = ['V', 'fcd', 'a', 't']
392 columns_CT = ['V', 'fcd', 'slenderness', 'a', 't']
393 sphere_df = pd.DataFrame(columns=columns_sphere)
394 cylinder_df = pd.DataFrame(columns=columns_CT)
395 torus_df = pd.DataFrame(columns=columns_CT)
396
397 for V in volumes:
398     geometry_sphere = sphere(V, fcd)[3]
399     sphere_df = sphere_df.append({'V': V, 'fcd': fcd, 'a': geometry_sphere[0], 't':
400         geometry_sphere[1]}, ignore_index=True)
401     for s in slenderness:
402         geometry_cylinder = cylinder(V,s,fcd)[3]
403         cylinder_df = cylinder_df.append({'V': V, 'fcd': fcd, 'slenderness':s,
404             'a': geometry_cylinder[0], 't': geometry_cylinder
405                 [2]}, ignore_index=True)
406
407         geometry_torus = torus(V,s,fcd)[3]
408         torus_df = torus_df.append({'V': V, 'fcd': fcd, 'slenderness':s,
409             'a': geometry_torus[0], 't': geometry_torus[2]},
410             ignore_index=True)
411
412
413 # In[10]:
414
415 # Plotting wall thickness and internal diameter
416 fig_width, fig_height = 14, 7
417 xrange, yrange = 17, 3
418
419 fig, ax = plt.subplots(figsize=(fig_width, fig_height))
420 distances = [0.05, 0.05, 0.15, .25]
421
422 patches = []
423
424 # Plot 'Sphere' first
425 scatter_sphere = ax.scatter(sphere_df['a'], sphere_df['t'], label=rf'Sphere', color='green',
426     marker='o', s=100)
427
428 lines, labels = [], []
429
430 for i, V in enumerate(volumes):
431     ax.text(sphere_df['a'].iloc[i], sphere_df['t'].iloc[i]-0.15, 'V=' + str(V), fontsize=13,
432         ha='center', color='green')
433
434     subset_cylinder = cylinder_df[cylinder_df['V'] == V]
435     line_cylinder, = ax.plot(subset_cylinder['a'], subset_cylinder['t'], color='blue', label=
436         '', linestyle='dotted')
437
438     end_cylinder = [subset_cylinder['a'].iloc[0], subset_cylinder['t'].iloc[0]]
439     start_cylinder = [subset_cylinder['a'].iloc[-1], subset_cylinder['t'].iloc[-1]]
440     bandwidth_indication(patches, start_cylinder, end_cylinder, distances[i], 0.05, 'V=' +
441         str(V),
442             fig_width, fig_height, xrange, yrange, y_offset = -0.02, x_offset =
443                 0.2, color='blue')
444
445     subset_torus = torus_df[torus_df['V'] == V]
446     line_torus, = ax.plot(subset_torus['a'], subset_torus['t'], color='red', label='',
447         linestyle = '--')

```

```

440     ax.text(subset_torus['a'].iloc[0] - 0.3, subset_torus['t'].iloc[0] - 0.1, 'V=' + str(V),
441             ha='right', va='top', color='red',fontsize=13)
442
443     lines.extend([line_cylinder, line_torus])
444     labels.extend(['', ''])
445
446     for patch in patches:
447         ax.add_patch(patch)
448
449     ax.plot([], [], color='blue', label=r'Cylinder $4 \leq \frac{L}{2a} \leq 20$')
450     ax.plot([], [], color='red', label=r'Torus $4 \leq \frac{b}{a} \leq 20$')
451
452     ax.set_xlabel('Internal radius $a$ [m]', fontsize=15)
453     ax.set_ylabel('Wall thickness $t$ [m]', fontsize=15)
454     ax.tick_params(axis='both', which='major', labels=15)
455
456     ax.set_xlim(0, 0 + xrange)
457     ax.set_ylim(0, 0 + yrange)
458     ax.grid(True)
459
460     # Create a custom legend with the desired order, excluding the second blue line
461     legend = ax.legend([scatter_sphere, lines[0], lines[1], lines[3]],
462                       ['Sphere', r'Cylinder $4 \leq \frac{L}{2a} \leq 20$', r'Torus $4 \leq \frac{b}{a} \leq 20$'],
463                       loc='lower right', fontsize=15)
464
465     # Set the legend labels to be displayed correctly
466     for text in legend.get_texts():
467         if text.get_text() == ' ':
468             text.set_text('')
469
470     plt.show()
471
472     # In[11]:
473
474
475     # Generate data for optimalization cylinder and torus slenderness
476     def ratio_iterations(shape, v, ratio_values):
477         results = []
478         if shape == 'cylinder':
479             results.append([cylinder(v, i, fcd)[0] / v for i in ratio_values])
480             results.append([cylinder(v, i, fcd)[1] for i in ratio_values])
481         if shape == 'torus':
482             results.append([torus(v, i, fcd)[0] / v for i in ratio_values])
483             results.append([torus(v, i, fcd)[1] for i in ratio_values])
484         return results
485
486     ratios = np.arange(4, 50.5, 0.5)
487     volume = 10 * 10 ** 3
488
489     # Generating results
490     cylinder_results = ratio_iterations('cylinder', volume, ratios)
491     torus_results = ratio_iterations('torus', volume, ratios)
492     sphere_result = sphere(volume, fcd)
493
494     # In[12]:
495
496
497     # Plotting CIV-data for optimalization cylinder and torus slenderness
498     fig, ax = plt.subplots(figsize=(12, 7))
499
500     ax.plot(ratios, cylinder_results[0], label=f"Cylinder", color='blue', linestyle=':',
501            linewidth=2)
502     ax.plot(ratios, torus_results[0], label=f"Torus", color='red', linestyle='--', linewidth=2)
503     ax.axhline(sphere_result[0]/volume, xmin=0.04, xmax=0.953, label='Sphere', color='green',
504               linestyle='-', linewidth=2)
505     ax.axhline(buoyancy_ratio, xmin=0.04, xmax=0.953, label='Neutral buoyancy', color='black',
506               linewidth=2)
507
508     ax.set_ylim(0, torus_results[0][0]*1.035)

```

```

506 ax.legend(loc='upper right', fontsize=15)
507 ax.grid(True)
508
509 ax.tick_params(axis='both', which='major', labelsize=15)
510 ax.set_yticks(np.arange(0, torus_results[0][0]*1.05, 0.1))
511 ax.set_ylabel(r'CIV-ratio  $\left(\frac{V_{\text{concrete}}}{V_{\text{internal}}}\right)$ ', fontsize=15)
512 ax.set_xlabel(r'Cylinder ratio  $\left(\frac{L}{2a}\right)$  and Torus ratio  $\left(\frac{b}{a}\right)$ ', fontsize=15)
513
514 plt.show()
515
516
517 # In[13]:
518
519
520 # Plotting number_of_iterations-data for optimalization cylinder and torus slenderness
521 fig, ax = plt.subplots(figsize=(12, 7))
522
523 ax.plot(ratios, cylinder_results[1], label=f"Cylinder", color='blue', linestyle=':',
524        linewidth=2)
525 ax.plot(ratios, torus_results[1], label=f"Torus", color='red', linestyle='--', linewidth=2)
526 ax.axhline(sphere_result[1], xmin=0.04, xmax=0.953, label='Sphere',
527           color='green', linestyle='-', linewidth=2)
528
529 ax.legend(loc='upper right', fontsize = 15)
530 ax.grid(True)
531 ax.tick_params(axis='both', which='major', labelsize=15)
532
533 ax.set_ylim(0,torus_results[1][0]*1.05)
534 ax.set_ylabel(r'Number of iterations', fontsize=15)
535 ax.set_xlabel(r'Cylinder ratio  $\left(\frac{L}{2a}\right)$  and Torus ratio  $\left(\frac{b}{a}\right)$ ', fontsize=15)
536
537 plt.show()
538
539
540 # In[14]:
541
542
543 # Generate data for concrete strength sensitivity analysis
544 slenderness = [4, 8, 12]
545 p_min = 25
546 p_plus = 25
547
548 stepsize = 0.2
549 sigma_max = np.arange(fcd * (1-p_min/100), fcd * (1+ p_plus/100) + stepsize / 2 , stepsize)
550 V = 10000
551
552 sphere_CV_ratios = [] # Initialize an empty list for sphere ratios
553 cylinder_CV_ratios = [[] for _ in range(len(slenderness))] # Initialize empty lists for
554 cylinder ratios
555 torus_CV_ratios = [[] for _ in range(len(slenderness))] # Initialize empty lists for torus
556 ratios
557
558 for sigma in sigma_max:
559     sphere_ratio = sphere(V, sigma)[0] / V
560     sphere_CV_ratios.append(sphere_ratio) # Append sphere_ratio to sphere_CV_ratios
561     for i, s in enumerate(slenderness):
562         cylinder_ratio = cylinder(V, s, sigma)[0] / V
563         torus_ratio = torus(V, s, sigma)[0] / V
564         cylinder_CV_ratios[i].append(cylinder_ratio) # Append cylinder_ratio to the
565         corresponding list in cylinder_CV_ratios
566         torus_CV_ratios[i].append(torus_ratio) # Append torus_ratio to the corresponding
567         list in torus_CV_ratios
568
569 # Calculate percentage values for the x-axis
570 percentage_sigma_max = ((sigma_max - fcd) / fcd) * 100
571
572 # Calculate mid-values
573 mid_value_sphere = sphere_CV_ratios[int(p_min*2)]
574 mid_values_cylinder = [cylinder_CV_ratios[i][int(p_min*2)] for i in range(len(slenderness))]
575 mid_values_torus = [torus_CV_ratios[i][int(p_min*2)] for i in range(len(slenderness))]

```

```

570
571 # Normalize sphere values
572 sphere_percentages = [(x - mid_value_sphere) / mid_value_sphere for x in sphere_CV_ratios]
573
574 # Normalize cylinder values
575 cylinder_percentages = []
576 for i, line_data in enumerate(cylinder_CV_ratios):
577     mid_value_cylinder = mid_values_cylinder[i]
578     normalized_data = [(x - mid_value_cylinder) / mid_value_cylinder for x in line_data]
579     cylinder_percentages.append(normalized_data)
580
581 # Normalize torus values
582 torus_percentages = []
583 for i, line_data in enumerate(torus_CV_ratios):
584     mid_value_torus = mid_values_torus[i]
585     normalized_data = [(x - mid_value_torus) / mid_value_torus for x in line_data]
586     torus_percentages.append(normalized_data)
587
588
589 # In[15]:
590
591
592 # Plot the sensitivity analysis for concrete strength
593 fig, ax = plt.subplots(figsize=(12, 7))
594
595 # Create a function to format y-axis as percentages
596 def percent_formatter(x, pos):
597     return f'{x * 100:.0f}%'
598
599 # Plot sphere data with a unique marker
600 plt.plot(percentage_sigma_max, sphere_percentages, label="Sphere", color='green',
601         marker=markers[0], linestyle=linestyles[0], linewidth=1, markevery=15)
602
603 # Plot cylinder data with distinct linestyles and markers
604 for i, s in enumerate(slenderness):
605     linestyle = linestyles[i % len(linestyles)]
606     marker = markers[(i + 1) % len(markers)]
607     color = 'blue'
608     plt.plot(percentage_sigma_max, cylinder_percentages[i], label=rf'Cylinder $\frac{{L}}{{{2a}}}$
609             }={s}$',
610             linestyle=linestyle, marker=marker, color=color, linewidth=1, markevery=15)
611
612 # Plot torus data with distinct linestyles and markers
613 for i, s in enumerate(slenderness):
614     linestyle = linestyles[i % len(linestyles)]
615     marker = markers[(i + 1 + len(slenderness)) % len(markers)]
616     color = 'red'
617     plt.plot(percentage_sigma_max, torus_percentages[i], label=rf'Torus $\frac{{b}}{{{a}}}$={s}$
618             ',
619             linestyle=linestyle, marker=marker, color=color, linewidth=1, markevery=15)
620
621 ax.set_xlabel(r'Concrete strength variation [%] at base $f_{cd} = 40$ ; MPa$', fontsize=15)
622 ax.set_ylabel('Variation in volume of concrete [%]', fontsize=15)
623 #plt.title('Normalized CV-ratios vs. Percentage Change in Sigma Max')
624 ax.legend(fontsize=15)
625 ax.tick_params(axis='both', which='major', labelsize=15)
626
627 # Set custom x-ticks with '+' signs for positive values, leaving out '+' at 0%
628 xticks = [f'{tick:+}%' if tick != 0 else '0%' for tick in np.arange(-p_min, p_plus + 10, 10)]
629
630 # Plot the graph
631 plt.gca().yaxis.set_major_formatter(mtick.FuncFormatter(percent_formatter))
632 plt.xticks(np.arange(-p_min, p_plus + 10, 10), xticks)
633 plt.grid(True)
634 plt.show()
635
636 # In[16]:
637
638 # Plot for CIV-ratio sphere foundation

```

```

639 volumes = np.arange(1, 16) * 10**3
640
641 geos = [sphere(v, fcd)[3][:2] for v in volumes]
642 sphere_foundation_volume = [sphere_foundation(geos[i][0], geos[i][1])[0] for i in range(len(
    geos))]
643 sphere_foundation_CIV = [sphere_foundation_volume[i] / volumes[i] for i in range(len(volumes)
    )]
644
645 fig, ax = plt.subplots(figsize=(10,6))
646 ax.plot(volumes, sphere_foundation_CIV, color='green', marker='o')
647 ax.grid(True)
648 ax.tick_params(axis='both', which='major', labelsize=15)
649
650 ax.set_xlabel(r'Internal volume $\left[m^3\right]$', fontsize=15)
651 ax.set_ylabel(r'CIV-ratio $\left(\frac{V_{\text{concrete}}}{V_{\text{internal}}}\right)$', fontsize=15);
652
653
654 # In[17]:
655
656
657 # Plot for CIV-ratios and widths cylinder and torus foundation
658
659 # Create a 1x2 subplot with two rows
660 fig, axs = plt.subplots(2, 1, figsize=(10, 12), sharex=True)
661
662 # First subplot (top)
663 axs[0].set_ylabel(r'CIV-ratio $\left(\frac{V_{\text{concrete}}}{V_{\text{internal}}}\right)$', fontsize=15)
664 axs[0].grid(True)
665
666 # Second subplot (bottom)
667 axs[1].set_xlabel('Internal volume $[m^3]$', fontsize=15)
668 axs[1].set_ylabel('Base width as percentage of total width', fontsize=15)
669 axs[1].grid(True)
670 axs[1].yaxis.set_major_formatter(FuncFormatter(lambda x, pos: f'{x:.0f}%'))
671
672 w, h = 450, 3 # Some trial and error parameters for square indication blocks
673 patches = []
674
675 for i, s in enumerate(slenderness):
676     results_cylinder = [get_cylinder_foundation(V, s, sigma_max_foundation,
        initial_width_percentage) for V in volumes]
677     CIV_cylinder = [results_cylinder[i][0] / volumes[i] for i in range(len(volumes))]
678     width_cylinder = [w[i] for w in results_cylinder]
679
680     linestyle = linestyles[i % len(linestyles)]
681     marker = markers[(i + 1) % len(markers)]
682     color = 'blue'
683     axs[0].plot(volumes, CIV_cylinder, label=rf'Cylinder $\frac{{L}}{{2a}}={s}$', linestyle=
        linestyle, marker=marker, color=color)
684     axs[1].plot(volumes, width_cylinder, label=rf'Cylinder $\frac{{L}}{{2a}}={s}$', linestyle
        =linestyle, marker=marker, color=color)
685     if s == 12:
686         block = Rectangle((volumes[0]-w/2,width_cylinder[0]-h/2), w, h, color='cornflowerblue
        ', alpha=0.5)
687         patches.append(block)
688     if s == 4:
689         block = Rectangle((volumes[-1]-w/2,width_cylinder[-1]-h/2), w, h, color='
        cornflowerblue', alpha=0.5)
690         patches.append(block)
691
692 for i, s in enumerate(slenderness):
693     results_torus = [get_torus_foundation(V, s, sigma_max_foundation,
        initial_width_percentage) for V in volumes]
694     CIV_torus = [results_torus[i][0] / volumes[i] for i in range(len(volumes))]
695     width_torus = [w[i] for w in results_torus]
696
697     linestyle = linestyles[i % len(linestyles)]
698     marker = markers[(i + 1 + len(slenderness)) % len(markers)]
699     color = 'red'
700     axs[0].plot(volumes, CIV_torus, label=rf'Torus $\frac{{b}}{{a}}={s}$', linestyle=
        linestyle, marker=marker, color=color)

```

```

701     axs[1].plot(volumes, width_torus, label=rf'Torus $\frac{{b}}{{a}}={s}$', linestyle=
702         linestyle, marker=marker, color=color)
703     if s == 12:
704         block = Rectangle((volumes[0]-w/2,width_torus[0]-h/2), w, h, color='indianred', alpha
705             =0.5)
706         patches.append(block)
707     if s == 4:
708         block = Rectangle((volumes[-1]-w/2,width_torus[-1]-h/2), w, h, color='indianred',
709             alpha=0.5)
710         patches.append(block)
711
712 for patch in patches:
713     axs[1].add_patch(patch)
714
715 # Add legends to both subplots
716 axs[0].legend(fontsize=15)
717 axs[1].legend(fontsize=15)
718
719 axs[1].set_ylim(10,69)
720 axs[1].set_xlim(500,15500)
721
722 axs[1].tick_params(axis='both', which='major', labelsize=15)
723 axs[0].tick_params(axis='both', which='major', labelsize=15)
724
725 plt.tight_layout()
726 plt.show()
727
728 # In[18]:
729
730 # Plot for CIV-ratios of reservoir and foundation combined
731
732 sphere_CIV = []
733 cylinder_CIV = []
734 torus_CIV = []
735 cylinder_CIV_hemisphere = []
736
737 for i in range(len(volumes)):
738     sphere_reservoir_results = sphere(volumes[i], fcd)
739     sphere_foundation_volume = sphere_foundation(sphere_reservoir_results[3][0] ,
740         sphere_reservoir_results[3][1])[0]
741     sphere_CIV.append((sphere_reservoir_results[0] + sphere_foundation_volume) / volumes[i])
742
743 slenderness = np.arange(4, 50.5, 0.5)
744 volume = 10 * 10 ** 3
745
746 for s in slenderness:
747     cylinder_reservoir_volume = cylinder(volume, s, fcd)[0]
748     cylinder_foundation_volume = get_cylinder_foundation(volume, s, sigma_max_foundation,
749         initial_width_percentage)[0]
750     cylinder_CIV.append((cylinder_reservoir_volume + cylinder_foundation_volume) / volume)
751
752     torus_reservoir_volume = torus(volume, s, fcd)[0]
753     torus_foundation_volume = get_torus_foundation(volume, s, sigma_max_foundation,
754         initial_width_percentage)[0]
755     torus_CIV.append((torus_reservoir_volume + torus_foundation_volume) / volume)
756
757     cylinder_reservoir_volume_hemisphere = cylinder(volume, s, fcd, method_s = 'hemisphere')
758     [0]
759     cylinder_foundation_volume_hemisphere = get_cylinder_foundation(volume, s,
760         sigma_max_foundation, initial_width_percentage,
761
762         hemisphere')[0]
763     cylinder_CIV_hemisphere.append((cylinder_reservoir_volume_hemisphere +
764         cylinder_foundation_volume_hemisphere) / volume)
765
766 # Plotting CIV-ratios vs. internal volume/configuration
767 fig, ax1 = plt.subplots(figsize=(12, 7))
768 ax1.grid(True)
769 ax2 = ax1.twinx()

```

```

761
762 # Plot the data
763 ax1.plot(volumes, sphere_CIV, label="Sphere", color='green', marker=markers[0], linestyle='-.
    ', linewidth=1)
764 ax2.plot(slenderness, cylinder_CIV, label='Cylinder', color='blue', linestyle=':', linewidth
    =2)
765 ax2.plot(slenderness, torus_CIV, label='Torus', color='blue', linestyle='--', linewidth=2)
766 plt.axhline(buoyancy_ratio, xmin=0.04, xmax=0.953, label='Neutral buoyancy', color='black',
    linewidth=2)
767
768 # Combine the legends
769 lines, labels = ax1.get_legend_handles_labels()
770 lines2, labels2 = ax2.get_legend_handles_labels()
771 lines.extend(lines2)
772 labels.extend(labels2)
773 ax1.legend(lines, labels, loc='upper right', fontsize=15)
774
775 # Setting ticks
776 ax1.tick_params(axis='x', colors='green', labelsize=15)
777 ax2.tick_params(axis='x', colors='blue', labelsize=15)
778
779
780 # Setting labels
781 ax1.set_ylabel(r'CIV-ratio  $\left(\frac{V_{\text{concrete}}}{V_{\text{internal}}}\right)$ ', fontsize=15);
782 ax1.set_xlabel(r'Internal volume  $\left[m^3\right]$ ', fontsize=15, color='green')
783 ax2.set_xlabel(r'Cylinder ratio  $\left(\frac{L}{2a}\right)$  and Torus ratio  $\left(\frac{b}{a}\right)$ ',
    fontsize=15, color='blue')
784 ax1.set_ylim(0,1.25);
785
786
787 # In[19]:
788
789
790 # Plotting CIV-ratios vs. internal volume/configuration
791 fig, ax1 = plt.subplots(figsize=(12, 7))
792 ax1.grid(True)
793 ax2 = ax1.twinx()
794
795 # Plot the data
796 ax1.plot(volumes, sphere_CIV, label="Sphere", color='green', marker=markers[0], linestyle='-.
    ', linewidth=1)
797 ax2.plot(slenderness, cylinder_CIV, label='Cylinder flat', color='blue', linestyle=':',
    linewidth=2)
798 ax2.plot(slenderness, cylinder_CIV_hemisphere, label='Cylinder hemisphere', color='blue',
    linestyle='--', linewidth=2)
799 plt.axhline(buoyancy_ratio, xmin=0.04, xmax=0.953, label='Neutral buoyancy', color='black',
    linewidth=2)
800
801 # Combine the legends
802 lines, labels = ax1.get_legend_handles_labels()
803 lines2, labels2 = ax2.get_legend_handles_labels()
804 lines.extend(lines2)
805 labels.extend(labels2)
806 ax1.legend(lines, labels, loc='upper right', fontsize=15)
807
808 # Setting ticks
809 ax1.tick_params(axis='x', colors='green', labelsize=15)
810 ax2.tick_params(axis='x', colors='blue', labelsize=15)
811
812 # Setting labels
813 ax1.set_ylabel(r'CIV-ratio  $\left(\frac{V_{\text{concrete}}}{V_{\text{internal}}}\right)$ ', fontsize=15,
    color='black');
814 ax1.set_xlabel(r'Internal volume  $\left[m^3\right]$ ', fontsize=15, color='green')
815 ax2.set_xlabel(r'Cylinder ratio  $\left(\frac{L}{2a}\right)$ ', fontsize=15, color='blue')
816 ax1.set_ylim(0,1.25);
817
818
819 # In[20]:
820
821
822 # Cylinder dimensions

```

```

823 slenderness = [12, 16, 20]
824 fig, ax = plt.subplots(figsize=(12,7))
825 volumes = np.arange(1, 17) * 10**3
826
827 for i, s in enumerate (slenderness):
828     external_diameters = []
829     Ls_cylinder = []
830     for V in volumes:
831         a_cylinder, L_cylinder, t_cylinder = cylinder(V, s, fcd)[3][:3]
832         external_diameters.append(2 * (a_cylinder + t_cylinder))
833         Ls_cylinder.append(L_cylinder)
834     ax.plot(Ls_cylinder,external_diameters, label=rf'$\frac{{L}}{{2a}}={s}$',
835           color='black', marker='o', markevery=3, linestyle=linestyles[i])
836     for j in range(int((len(volumes)+2)/3)):
837         ax.text(Ls_cylinder[3*j] + 7, external_diameters[3*j], volumes[3*j], ha='center', va=
838             'center', fontsize=12)
839
840 ax.set_xlabel('External length [m]', fontsize=15)
841 ax.set_ylabel('External diameter [m]', fontsize=15)
842 ax.grid(True)
843
844 # Adding the internal volume in the legend of the plot
845 ax.plot([], [], label=r'$V_{\text{internal}} \backslash; \backslash; [m^3]$', color='black', marker='', linestyle='',
846         markersize=5)
847 ax.text(53,13.2,'1000', fontsize=14, zorder=10)
848 ax.legend(fontsize=16, loc='upper left')
849
850 ax.tick_params(axis='both', which='major', labelsize=15)
851
852 ax.set_xlim(50,220)
853 ax.set_ylim(4,18)
854 plt.show()
855
856 # In[21]:
857
858 # Torus dimensions
859 fig, ax = plt.subplots(figsize=(12,7))
860
861 for i, s in enumerate (slenderness):
862     minor_diameters = []
863     major_diameters = []
864     for V in volumes:
865         a_torus, b_torus, t_torus = torus(V, s, fcd)[3][:3]
866         minor_diameters.append(2 * (a_torus + t_torus))
867         major_diameters.append(2 * (a_torus + b_torus + t_torus))
868     ax.plot(major_diameters, minor_diameters, label=rf'$\frac{{b}}{{a}}={s}$',
869           color='black', marker='o', markevery=3, linestyle=linestyles[i])
870     for j in range(int((len(volumes)+2)/3)):
871         ax.text(major_diameters[3*j] + 5,minor_diameters[3*j], volumes[3*j], ha='center', va=
872             'center', fontsize=12)
873
874 ax.set_xlabel('Major external diameter [m]', fontsize=15)
875 ax.set_ylabel('Minor external diameter [m]', fontsize=15)
876 ax.grid(True)
877
878 # Adding the internal volume in the legend of the plot
879 ax.plot([], [], label=r'$V_{\text{internal}} \backslash; \backslash; [m^3]$', color='black', marker='', linestyle='',
880         markersize=5)
881 ax.text(43,9.05,'1000', fontsize=14, zorder=10)
882
883 ax.legend(fontsize=16, loc= 'upper left')
884 ax.set_ylim(3,12)
885 ax.set_xlim(40,155)
886
887 ax.tick_params(axis='both', which='major', labelsize=15)
888
889 plt.show()
890
891
892

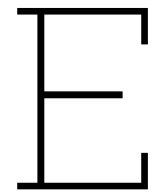
```

```

888 # In[22]:
889
890
891 volumes = list(np.linspace(1,15,15) * 10**3)
892 slenderness = list(np.arange(4, 50.5, 0.5))
893
894 sphere_CIV_NU = []
895 cylinder_CIV_NU = []
896
897 for V in volumes:
898     sphere_reservoir_results = sphere(V, fcd, method_t = 'non-uniform')
899     a_sphere = sphere_reservoir_results[3][0]
900     t_sphere = sphere_reservoir_results[3][1]
901     V_sphere_reservoir = sphere_reservoir_results[0]
902     V_sphere_foundation = sphere_foundation(a_sphere, t_sphere)[0]
903     sphere_CIV_total = (V_sphere_reservoir + V_sphere_foundation) / V
904     sphere_CIV_NU.append(sphere_CIV_total)
905
906 for s in slenderness:
907     cylinder_reservoir_results = cylinder(9000, s, fcd, method_s = 'hemisphere', method_t = '
908         non-uniform')
909     a_cylinder = cylinder_reservoir_results[3][0]
910     t_cylinder = cylinder_reservoir_results[3][1]
911     V_cylinder_reservoir = cylinder_reservoir_results[0]
912     V_cylinder_foundation = get_cylinder_foundation(9000, s, sigma_max_foundation, 30)[0]
913     cylinder_CIV_total = (V_cylinder_reservoir + V_cylinder_foundation) / 9000
914     cylinder_CIV_NU.append(cylinder_CIV_total)
915
916 sphere_CIV_high = [CIV * 1.06 for CIV in sphere_CIV_NU]
917 cylinder_CIV_high = [CIV * 1.05 for CIV in cylinder_CIV_NU]
918
919 sphere_average = [(sphere_CIV_NU[i] + sphere_CIV_high[i])/2 for i in range(len(sphere_CIV_NU)
920 )]
921
922 sphere_CIVs_uncertain = sphere_CIV_NU + sphere_CIV_high[::-1]
923 sphere_Vs = volumes + volumes[::-1]
924
925 cylinder_CIVs_uncertain = cylinder_CIV_low + cylinder_CIV_high[::-1]
926 cylinders_ss = slenderness + slenderness[::-1]
927
928 # In[23]:
929
930 figure, ax1 = plt.subplots(figsize=(12,7))
931 ax1.grid(True)
932 ax2 = ax1.twinx()
933
934 ax1.axhline(buoyancy_ratio, xmin=0.04, xmax=0.953, label='Neutral buoyancy', color='black',
935     linewidth=2)
936 ax1.plot(volumes, sphere_CIV, linestyle=linestyles[1], label='Sphere uniform', color='green',
937     linewidth=2)
938 ax1.plot(volumes, sphere_CIV_NU, linestyle=linestyles[2], label='Sphere non-uniform', color='
939     green', linewidth=2)
940 ax2.plot(slenderness, cylinder_CIV, label='Cylinder uniform', color='blue', linestyle=
941     linestyles[4], linewidth=2)
942 ax2.plot(slenderness, cylinder_CIV_NU, label='Cylinder non-uniform', color='blue', linestyle=
943     linestyles[5], linewidth=2)
944
945 # Setting colors of axes
946 ax1.tick_params(axis='x', colors='green', labels=15)
947 ax2.tick_params(axis='x', colors='blue', labels=15)
948 ax1.tick_params(axis='y', labels=15)
949
950 # Combine the legends
951 lines, labels = ax1.get_legend_handles_labels()
952 lines2, labels2 = ax2.get_legend_handles_labels()
953 lines.extend(lines2)
954 labels.extend(labels2)
955 ax1.legend(lines, labels, loc='upper right', fontsize=15)

```

```
952 # Setting labels
953 ax1.set_ylabel(r'CIV-ratio  $\left(\frac{V_{\text{concrete}}}{V_{\text{internal}}}\right)$ ', fontsize=15);
954 ax1.set_xlabel(r'Internal volume  $\left[m^3\right]$ ', fontsize=15, color='green')
955 ax2.set_xlabel(r'Cylinder ratio  $\left(\frac{L}{2a}\right)$ ', fontsize=15, color='blue')
956 ax1.set_ylim(0,1.6);
957
958
959 # In[24]:
960
961
962 # Plotting uncertainty CIV-ratios vs. internal volume/configuration
963 fig, ax1 = plt.subplots(figsize=(12, 8))
964 ax1.grid(True)
965 ax2 = ax1.twinx()
966
967 # Plot the data
968 ax1.axhline(buoyancy_ratio, xmin=0.04, xmax=0.953, label='Neutral buoyancy', color='black',
969            linewidth=2)
970 ax1.fill(sphere_Vs, sphere_CIVs_uncertain, color='green', alpha=0.3)
971 ax1.plot(volumes, sphere_average, label='Sphere', linestyle='--', color='green')
972 ax2.fill(cylinders_ss, cylinder_CIVs_uncertain, color='blue', alpha=0.3)
973 ax2.plot(slenderness, cylinder_CIV_NU, label='Cylinder', linestyle='-.', color='blue')
974
975 # Setting colors of axes
976 ax1.tick_params(axis='x', colors='green', labelsz=15)
977 ax2.tick_params(axis='x', colors='blue', labelsz=15)
978 ax1.tick_params(axis='y', labelsz=15)
979
980 # Combine the legends
981 lines, labels = ax1.get_legend_handles_labels()
982 lines2, labels2 = ax2.get_legend_handles_labels()
983 lines.extend(lines2)
984 labels.extend(labels2)
985 ax1.legend(lines, labels, loc='upper right', fontsize=15)
986
987 # Setting labels
988 ax1.set_ylabel(r'CIV-ratio  $\left(\frac{V_{\text{concrete}}}{V_{\text{internal}}}\right)$ ', fontsize=15);
989 ax1.set_xlabel(r'Internal volume  $\left[m^3\right]$ ', fontsize=15, color='green')
990 ax2.set_xlabel(r'Cylinder ratio  $\left(\frac{L}{2a}\right)$ ', fontsize=15, color='blue')
991 ax1.set_ylim(0,1.6);
```



Interview Bernhard Ernst, Deputy Head of Energy Storage at Fraunhofer IEE

This Section presents the valuable insights gathered in an interview with the Deputy Head of Energy Storage at Fraunhofer Institute for Energy Economics and Energy System Technology, Bernhard Ernst. Mr. Ernst is currently overseeing the StEnSea project, an abbreviation for Storing Energy at Sea. The Fraunhofer Institute is a prominent developer of the MPHES concept.

The interview was conducted online via a video connection on the 27th of September, 2023. The content is presented in a question-and-answer format, summarizing Mr. Ernst's responses.

Why is your pump integrated in the system in the current design?

The integration of the pump into the system serves the purpose of simplifying installation and maintenance procedures. This design choice allows for the pump to be easily accessed by lifting it out vertically, ensuring convenient maintenance. Importantly, this integration minimally impacts the system's volume due to the pump's compact dimensions. The design specifications require the pump to be slender with a small diameter, and the envisioned pump for this design measures only 0.5 meters in diameter. Additionally, a small pump opening is essential to prevent excessive structural interference and the potential for increased local stresses.

What distances do you consider for grid connection?

For grid connection, we consider any location where an offshore wind or solar farm is already established, making it suitable for MPHES. In these locations, existing cables connect the farms to the grid. We can utilize these same cables for the transfer of both stored energy and energy generated by the farm. Importantly, the capacity of the cable is not a limiting factor, and it might even be used with lower capacity since it serves the dual purpose of transferring stored energy and harvested energy from the farm.

What are the main concerns in constructing multiple smaller reservoirs with respect to one big reservoir, provided that the total internal volume is equal?

One major challenge arises from the need to interconnect all smaller reservoirs, resulting in heightened demands for cables and installation efforts. Although the overall energy storage capacity remains consistent, the requirement for intricate networks of pipes or tubes to connect a single pump to multiple reservoirs, particularly in high hydrostatic pressure conditions, presents a substantial engineering challenge. Alternatively, using a single pump for each reservoir is an option, but this approach may escalate capital expenditures, and the efficiency of larger pumps typically surpasses that of smaller ones.

It is worth noting that pumps can be installed adjacent to the sphere without strict location requirements. Nevertheless, as previously mentioned, the design and implementation of the associated pipes or tubes

could present difficulties. Additionally, ensuring that the pump's inflow is located at the bottom of each reservoir is a crucial consideration for optimal functionality.

Considering these factors collectively, a larger reservoir holds advantages over multiple smaller reservoirs with equivalent internal volumes.

One could argue that in the construction of an MPHES system that much CO₂ is emitted, that the storage in its lifetime never compensates this. Was any such calculation performed?

The amount of energy that travels through a sphere in one year, if generated by a coal plant, generates the same amount of CO₂ as constructing the spheres does, only considering CO₂ emitted by concrete construction. This is no conclusive reasoning, since MPHES does not generate any electricity and one might as well compare it to other forms of energy generation. On the other hand, at the intended moment for MPHES to become commercially available, which is not earlier than eight years from now, the amount of CO₂ emitted by concrete construction might be significantly lower than it is now. It is necessary to have someone investigate this. I would like to make this into a graduation project.

Why is Hochtief not considering their patented technique from 2014 anymore?

HTS probably stepped off their patented construction method since the introduction of 3DCP around 2018.

What do you think of other storage technologies with respect to MPHES? At this stage, we do not believe it is appropriate to make direct comparisons between MPHES and other storage technologies. Our first priority is to establish a proof of concept and ensure that we can effectively manage the logistics associated with MPHES. Once we have achieved this and gathered sufficient data, we can then assess MPHES in relation to the feasibility and performance of other existing storage technologies.

Separate comments on pump efficiency *This last section contains some separate comments on pump efficiency, that were not directly the answer to a specific question.* Another field test is planned off the coast of California at a 1:3 scale, set to take place in 2025. During this upcoming test in the Pacific Ocean, an efficiency of 60% is anticipated. It is important to clarify that, at this stage, the primary focus is not on optimizing the efficiency of the pumps. Instead, the key priorities lie in constructing the sphere and managing the logistical aspects of the project, including immersion and installation.

An essential point to consider is that a pump optimized for water pumping might not necessarily be optimized for electricity generation through the associated turbine, and vice versa. Therefore, a pump/turbine system can typically be optimized for one specific function. To achieve maximum efficiency, it may be beneficial to utilize separate devices – one for pumping water out of the reservoir and another for generating electricity as water flows into the reservoir.

It is also important to acknowledge that lower efficiencies observed in earlier tests were often a result of using off-the-shelf pumps, which were not specifically designed to be as efficient as possible for the unique requirements of MPHES.

Pump efficiency tends to increase with a higher discharge of water. Hydropower plants, with turbines boasting significant power ratings, can achieve roundtrip efficiencies of up to 85%. In contrast, MPHES aims for a 5 MW power rating, which may result in efficiencies ranging between 75-80%.

F

General concrete construction techniques

This appendix provides a comprehensive overview of diverse concrete construction techniques, serving as a foundational framework for the proposed methodologies outlined in Chapter 5. The selection of these techniques is intentionally inclusive, spanning a broad range of approaches rather than being restricted solely to their immediate relevance to the specified structures. The intention is to facilitate a thoughtful selection of construction methods, enabling the presentation of potential techniques in Chapter 5.

Each section is organized to explicate the principles of a technique, outline its variations, and elucidate common applications. Subsequently, a brief assessment is carried out to evaluate its relevance in the specific context of constructing a cylinder or torus.

F.1. Conventional casting using formwork

The utilization of formwork in the construction of concrete structures has a rich history, involving the creation of a casing where concrete is poured to attain the desired shape.

In the following Section, drawing insights from [67], formwork techniques are categorized into three main types: traditional formwork, flexible formwork, and recyclable formwork. A comparative analysis of these techniques is detailed in Table F.1.

Traditional formwork systems utilize wooden or metal framing into which concrete is poured. These time-tested techniques are well-established due to their historical prevalence. Traditional formwork is particularly effective for producing thick concrete elements, as the formwork contains the concrete during setting.

Flexible formwork encompasses fabric or digitally fabricated structures designed to facilitate convenient adjustments during concrete pouring. Examples include pneumatically supported formwork and stay-in-place knitted formwork. These methods are well-suited for constructing relatively thin concrete shells. Digitally fabricated formwork involves CNC milling of materials like expanded polystyrene (styrofoam) or 3D-printing plastic to create intricate molds, enabling the construction of complex concrete shapes.

Recyclable formwork involves the use of sand or ice formwork placed on a horizontal surface. Concrete is then poured onto the shaped sand or ice, offering a cost-effective solution with limitless geometric possibilities.

This array of formwork techniques offers a range of options tailored to specific project requirements. In the context of construction of the cylindrical or toroidal reservoir, traditional formwork emerges as the most practical choice. While flexible and recyclable formwork excel in projects with highly intricate geometries, the motivation for this thesis revolves around determining if the torus and cylinder can be

more easily constructed than the sphere. Consequently, opting for formwork that allows for complex geometries would run contradict that motivation. Furthermore, the advantage of traditional formwork lies in its ability to accommodate the construction of larger volumes of concrete, a crucial factor in this project.

Formwork type	Labour cost	Material cost	Speed of construction	Geometry	Surface quality	Recycling and reuse of formwork
Wooden formwork	High	Medium	Low	Mostly for regular shapes (specific setting is required for complex shape)	Medium	Yes (limited to shape)
Metal formwork	Medium (reduced by reuses)	High	Low	Mostly for orthogonal shapes	High	Yes (limited to similar shapes)
Fabric formwork	Medium (reduced by knitting)	Low	High	Flexible (defined by support)	High	Limited (polluted after casting)
CNC-milled Styro-foam	Low	Medium	Medium	Unlimited	High (with coating)	Yes (limited to same shape)
3D printed plastic	Low	High	Medium (confined by scale)	Non-standard shapes are possible (limited to scale)	Low (surface may be damaged during de-moulding)	No
Mesh mould	Medium	Medium	High	Regular shapes	Medium	No
Sand formwork	Low (with 3D printing)	Very low	Dependent on fabrication method	Unlimited	High (with release agents)	Yes
Ice formwork	Low (with CNC milling)	Very low	Dependent on fabrication method	Unlimited	High	Yes

Table F.1: Comparison of various formwork systems [67]

F.2. Slip-forming

Slip-forming is a construction technique employed in the creation of continuous concrete structures, where the material is continuously poured onto a moving formwork. This method proves particularly valuable in crafting monolithic structures that are too extensive for traditional formwork. The application of slip-forming varies based on the direction of slippage.

Vertically, slip-forming is commonly used for constructing the cores of high-rise structures or silos [68]. In this process, a formwork is lifted by hydraulic jacks, and as each layer of concrete is poured, the formwork is incrementally raised along the climbing rod protruding from the concrete [69]. This vertical slip-forming is suitable for the construction of relatively long, vertical structures, as illustrated in Figure F.1.

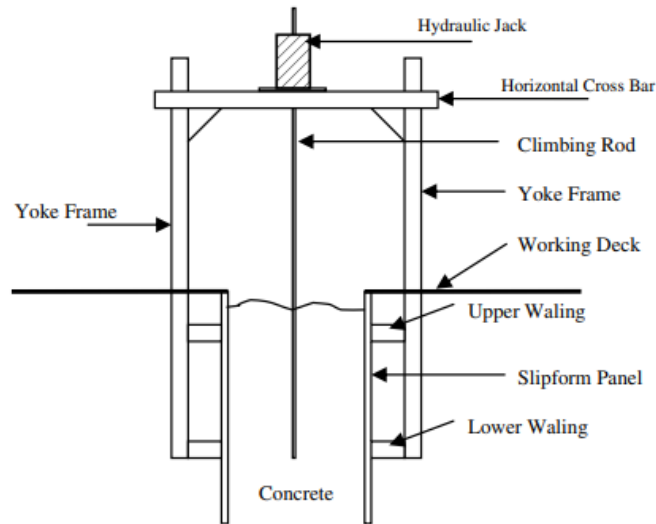


Figure F.1: Schematic diagram of a typical slip-form system [70]

Horizontal slip-forming, on the other hand, finds applications in structures without a span, such as canal linings, concrete pipes, highway pavements, and tunnel inverts [71]. An innovative application of horizontal slip-forming has been explored in the context of tunnel regeneration [48]. The technique combines horizontal slip-forming with 3DCP to achieve precise shaping. In a full-scale test (shown in Figure F.2), a tunnel lining with an inner radius of 2,25 meters and a thickness of 0,4 meters was produced. The material possesses self-sustaining properties immediately after casting, enabling immediate slip-forming. However, this necessitates the use of self-compacting, fast-setting concrete, requiring careful planning to prevent premature setting in the mixer or pump.

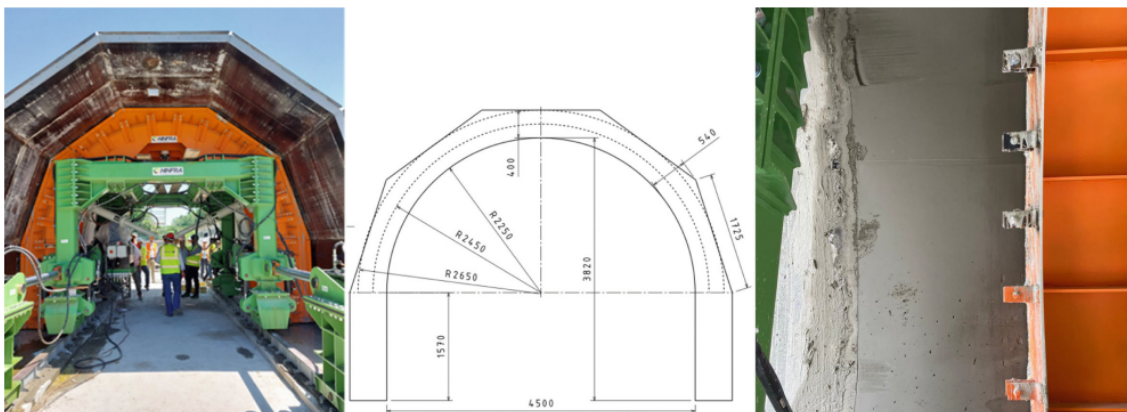


Figure F.2: Novel horizontal slip-form technique for regenerating existing tunnel [48]

While vertical slip-forming holds potential for the construction of cylindrical reservoir components, its application to toroidal elements is more intricate due to the eccentricity of the cross-section with respect to the base. Overcoming this challenge might involve rotating the base, introducing complexities to the process.

The creation of spans in horizontal slip-forming is an unexplored area. Although it has been demonstrated as possible, uncertainties remain regarding the achievable wall thickness and length of spans. Additionally, the curvature at the bottom of the cylinder or torus presents challenges. The absence of a solid base raises questions about the suitability of horizontally slip-forming these structures.

F.3. Jump-forming

Similar to slip-forming, jump-forming employs movable formwork for continuous construction. However, the key distinction lies in the level of continuity. While slip-forming is a semi-continuous process, jump-forming introduces a discontinuous element. Concrete is poured in distinct levels, and as it partially strengthens, the jump-form ascends for the next level, introducing a joint between two jumps [72].

This construction technique offers a significant advantage over slip-forming, particularly for the construction of extensive horizontal structures. A noteworthy example is the 2.4 km tunnel built by the Austrian construction company DOKA in 2003 using horizontal jump-forming. The tunnel comprised 100 sections, each 24 meters in length, with a construction rate of approximately one section per week [46, 47].

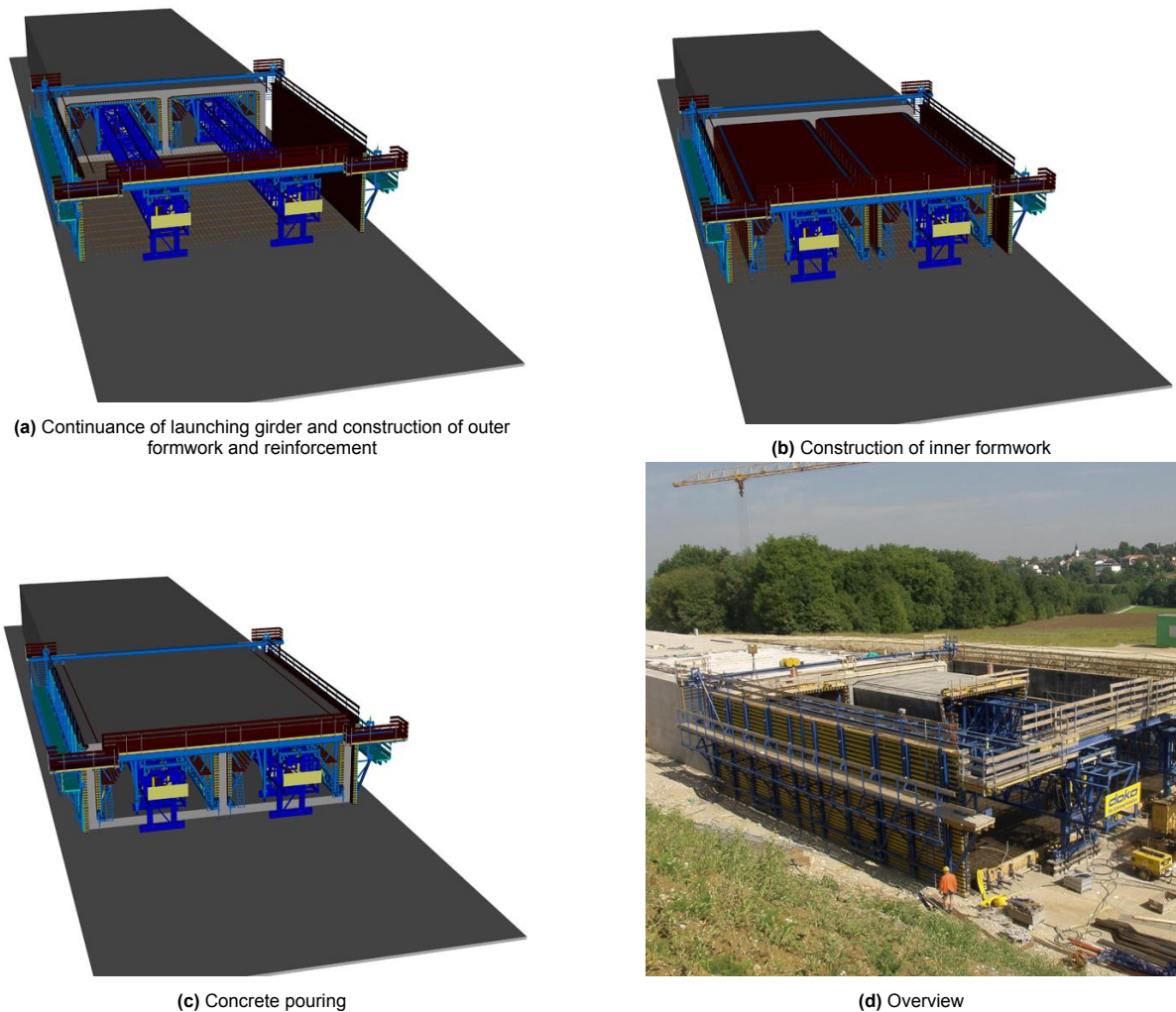


Figure F.3: Construction of Steinhaus tunnel [47]

The technique finds application in the ongoing construction of the Femern Belt tunnel, where tunnel elements, each 217 meters long, consist of 9 segments, each approximately 24 meters in length [73].

This horizontal jump-forming approach appears particularly suitable for the construction of a cylinder, given its similarity to tunnel structures. However, its applicability to the construction of a torus is more

nuanced. The curvature of the launching girder may pose challenges, and the rotational capacity might limit the ability to achieve a small radius of curvature for the cross-section. Consequently, this method may be better suited for torus designs with a significant major radius.

F.4. Shotcrete

Shotcrete is a cement-based mixture pneumatically projected at high velocity onto a receiving surface. The process involves pumping the mixture through a hose to a nozzle, from where it is sprayed onto the target surface. This technique is commonly employed in concrete repair, especially in areas where access to the working space is challenging, and the use of formwork for traditional casting is impractical [74], as illustrated in Figure F.4.

Two main shotcrete techniques exist: dry-mix and wet-mix. In the dry-mix method, cement and aggregate are mixed in a hopper, pressurized, and introduced into a high-velocity air stream, conveyed through hoses to the spraying nozzle. Water is added at the nozzle to hydrate the cement. In the wet-mix shotcrete, water is added to the mixture before reaching the nozzle, and compressed air propels the concrete onto the receiving surface. Generally, the wet-mix process produces less dust, waste, and rebound [74].

Shotcrete application reduces the need for formwork construction, as only a receiving surface in the desired shape needs to be prepared. This stands in contrast to conventional casting, which requires double-sided formwork to create an enclosing space. Additionally, shotcrete is self-compacting, eliminating the need for vibration at the construction site, leading to cost savings and reduced construction disturbance [75].



Figure F.4: Shotcrete application in the repair of a concrete face [75]

Shotcrete is typically applied in layers with a thickness of up to 150 mm [74]. Achieving greater thickness involves adding multiple layers, but the time lag between applying two layers must be short to prevent issues such as preloading due to shrinkage in the present layer while the newly added layer is stress-free [76]. Moreover, shotcrete layer thickness can vary significantly, with deviations of more than 50% being common, influenced by the skill level of the shotcrete operator [77].

In the context of this project, shotcrete may not be a cost-effective solution. Despite the time saved by using single-sided formwork, concerns arise due to the required wall thickness. The necessity of applying multiple layers increases the likelihood of achieving low uniformity in the final wall thickness. Additionally, the time-sensitive nature of adding layers for proper bonding may pose challenges.

F.5. 3D Concrete Printing

Three-dimensional concrete printing (3DCP) involves the layer-by-layer deposition of continuous concrete filament. Cement, mixed with water, is pumped into a hose by a mixer-pump. The hose is connected to the printer head at the end of a motion-controlled robot's vertical arm. Under pump pressure, the concrete is directed toward the printer head, allowing precise printing at the desired location, speed, and angle [78]. Typical 3DCP production parameters include a layer thickness of 20 mm, layer width of 100 mm, and a print rate ranging from 5-8 L/min [29].

The primary advantage of 3DCP lies in its ability to achieve complex geometries, thanks to the maneuverability of the printer head, enabling the creation of intricate curvatures and shapes. However, the stacking of layers is constrained by an overhang angle (see Figure F.5), typically limited to 45°[51].

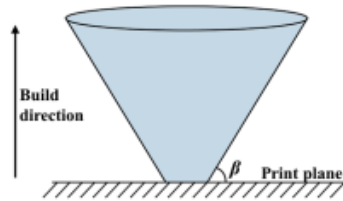


Figure F.5: Maximum overhang angle (β) [79]

The nozzle-based application limits the use of coarse aggregates in the concrete mixture. While some research groups and companies make progress in developing printable concrete with coarse aggregates, 3DCP mixtures generally remain in the scale of mortar [80]. Consequently, 3DCP mixtures often contain more cement, leading to increased CO₂ emissions when compared to conventional casted mixtures.

In the envisioned construction of the cylinder or torus, two approaches are possible with 3DCP. One involves constructing the entire structure using 3DCP, while the other entails printing the formwork followed by pouring concrete. The former is impractical due to the substantial volume of concrete required, leading to extended construction times. The latter approach, printing the formwork, is more feasible as it involves printing lower volumes of concrete. However, the necessity of complex formwork construction raises questions, as the primary goal of choosing the cylinder and torus shapes for the reservoir was to simplify construction methods.



Relevant construction locations

This appendix provides essential background information on potential construction locations, offering valuable insights for the design process. It explores various features and characteristics of construction locations to aid in the decision-making process.

G.1. Land-based factory

In the context of this research, with a factory is meant a land-based concrete production facility, where concrete structures or elements are produced. Such a place includes a concrete batching plant, where the concrete itself is produced. The construction of concrete structures can be performed inside a factory hall or in a tent, which ensures a controlled environment.

Considering the ambitious scale of the MPHES project, the construction of a dedicated concrete factory tailored for MPHES system assembly is a viable option. Concrete batching plants, integral to such facilities, can be established worldwide, leveraging the widespread availability of concrete ingredients—sand, aggregate, cement, and water.

Even if construction is not executed on land, a concrete batching plant remains essential to supply concrete. These plants often boast production capacities of up to 200 m³ per hour [81]. For projects requiring higher production rates, multiple plants can be combined, as exemplified by the construction of the Shanghai Tower, which achieved a total capacity of 1250 m³ per hour [41].

G.2. Dry dock

A dry dock is a basin or vessel engineered to facilitate the floating, emptying, and subsequent flooding of a ship or load for maintenance or transportation purposes. Dry docks exist in two forms: land-based dry docks (graving docks) and floating dry docks. In land-based docks, ships navigate to the dry dock, while in floating dry docks, the reverse is true. Notably, floating dry docks generally incur higher rental costs than their land-based counterparts. They often allow for a greater draught of ships [82].

Traditionally crafted for ship construction and maintenance, certain instances showcase the intentional construction of dry docks for concrete structure production. For example, bouwdok Barendrecht, established in 1966, was purpose-built for the production of tunnel elements. The dock boasts a depth of 10 meters and spans an area of 10 hectares [83].

Dry dock depths are typically customized to suit the draught requirements of the ships they serve. Since vessels usually enter dry docks without cargo, excessive depth is often considered unnecessary. The depth of dry docks is a critical factor, as highlighted in Table G.1, which compiles some of the world's significant dry docks organized by depth. While this table does not encompass all the world's deepest dry docks, it does provide a country-wise list of the deepest docks. The intention is to underscore that dry docks with substantial depth are found in numerous countries. Notably, Southeast Asia hosts the majority of the world's deepest dry docks, but those with a depth of at least 12 meters are distributed across all continents [82]. Dry docks with depths below 12 meters are more widely available

worldwide.

Name of shipyard	Country	City	Dimensions [m] (L x W x D)	Reference
Daewoo-Mangalia Heavy Industries	Romania	Mangalia	320 x 48 x 18	[84]
Soreni	France	Le Havre	319 x 38 x 17,5	[85]
Sungdong Shipbuilding & Marine Engineering	South Korea	Tongyeong	545 x 126 x 16	[86]
Sasebo Heavy Industries	Japan	Sasebo	400 x 57 x 15,6	[87]
Cosco Shipyard Group	China	Zhoushan	410 x 68 x 14,3	[82]
PT Pal Indonesia	Indonesia	Soerabaja	250 x 26 x 14	[88]
Malaysia Marine & Heavy Engineering	Malaysia	Johor	385 x 80 x 14	[89]
CSBC Corporation	Taiwan	Kaohsiung	950 x 92 x 14	[82]
National Ports Authority of South Africa	South Africa	Cape Town	370 x 45,1 x 13,7	[90]
Thales Australia	Australia	Sydney	346 x 41,6 x 13	[82]
Aker Philadelphia Shipyards	USA	Philadelphia	333 x 45,7 x 12,2	[82]

Table G.1: List of the worlds largest land-based dry docks

G.3. Fjord

A fjord is a distinctive geographical feature—a long, narrow, and deep inlet of the sea, typically bordered by steep cliffs or mountains. Fjords exhibit considerable water depth, ranging from 100 to 500 meters [91], with some exceeding 1000 meters [92]. This substantial depth facilitates the construction of structures with significant draughts. Additionally, fjords often offer calm water conditions, providing a reasonable environment for smooth construction processes [93].

Fjords are commonly found along the coasts of Norway, Iceland, and Canada. While the majority is situated in the northern hemisphere, fjords are also present in the southern hemisphere, particularly near the poles, as they are formed by glacial erosion [94]. Figure G.1 presents a global map showcasing the distribution of fjords.

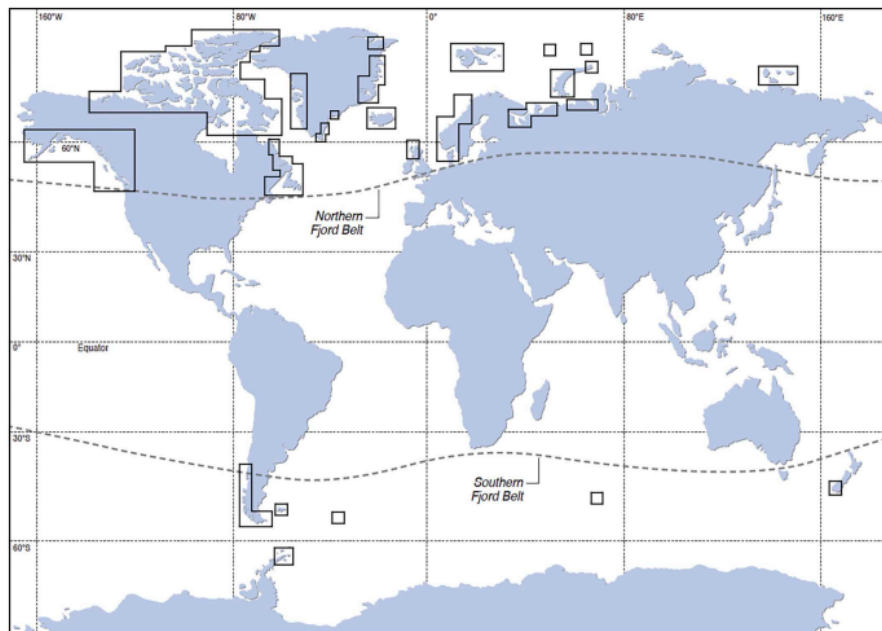


Figure G.1: Map of fjords [94]

A notable example of an extraordinary construction project in a fjord is the Troll A platform. This 369-meter-tall concrete structure, with a draught of 303 meters, was constructed in a Norwegian fjord [93]. Subsequently, the platform was towed to its final location, as illustrated in Figure G.2. Upon reaching the destination, the legs were gradually flooded, allowing the structure to descend to the seabed.



Figure G.2: Towing of Troll A platform to its final location [93]

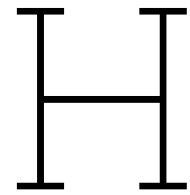
G.4. Open sea

In this context, open sea construction refers to the assembly of structural elements directly in the open sea, where the entire process takes place afloat. This involves utilizing offshore construction vessels to carry out various construction operations, including stabilization and making the element connections.

Complete construction directly in the open sea is considered impractical due to the challenges associated with concrete pouring, which would either have to be done in the water, leading to difficulties in maintaining the desired shape, or in a dry environment at open sea. Construction in a dry environment at open sea is essentially akin to construction in a floating dry dock, which incurs higher rental costs without offering significant advantages over land-based dry docks.

Similar to construction in a fjord, open sea construction allows for a significantly deep draught of the structure. However, unlike operations in the calm waters of a fjord, construction and installation in the open sea pose greater challenges. At the intended installation depth of the MPHES system, adverse weather conditions are anticipated. The presence of waves can considerably disrupt the smooth execution of any operation in open sea conditions.

Connecting structural elements in open sea requires stable conditions to prevent excessive movement during execution. This intricate task involves the use of specialized vessels that come with high rental costs. While open sea construction allows for a significantly deeper draught, the additional costs and complexities associated with element connection make it an impractical and less favorable construction method. As a result, the challenges outweigh the benefits, leading to the exclusion of open sea construction as a suitable approach for the MPHES system.



Concrete connection methods

In this Appendix an overview is presented of various concrete connection methods.

Dry joints

Dry joints, utilized in different types of superstructures such as pretensioned segmental concrete bridges and composite bridges without prestressing tendons, involve no additional material. In this joint, two concrete elements are slid into each other, capable of transferring shear forces but lacking watertightness [95].

Rubber joints

Specializing in watertight seals between concrete elements, Trelleborg, a Swedish company, has developed rubber products for this purpose. Notably, their products, like Gina gaskets and omega seals, were used in the construction of the Hong Kong-Macau tunnel, a project with a depth of 44 meters [52, 96].

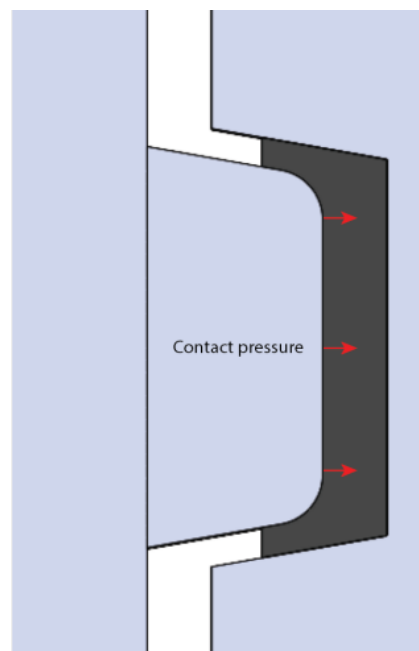


Figure H.1: Compression seal [55]

The compression seal, depicted in Figure H.1, comprises a concrete protrusion running along the entire cross-section and a corresponding recessed groove on the connecting cross-section. Positioned be-

tween them is a rubber band, serving to establish a watertight connection. To achieve watertightness, the contact pressure must exceed 250

$$\sigma_{\text{contact}} > 2.5p_{\text{hydraulic}}$$

Considering a water depth of 1000 meters, resulting in a hydraulic pressure of 10 MPa, a contact pressure of 25 MPa is required. Rubber can accommodate such contact pressures, but to meet these requirements, a high shore compound rubber becomes imperative. Notably, it is important to recognize that contact pressure decreases over time due to relaxation, underscoring the necessity for an initially higher contact pressure [55].

Given the intended installation depth of MPHES, a compression seal emerges as the sole viable rubber connection ensuring watertightness. At such depths, the hydraulic load cannot be adequately resisted by alternatives like an omega seal [55].

Wet joints

Wet joints involve pouring concrete at the interface between two elements, usually with reinforcement protruding from both elements. Fresh concrete seals off the exposed reinforcement, creating two cold joints—one on each side of the poured concrete. A visual representation of a wet joint is shown in Figure H.2 [95].

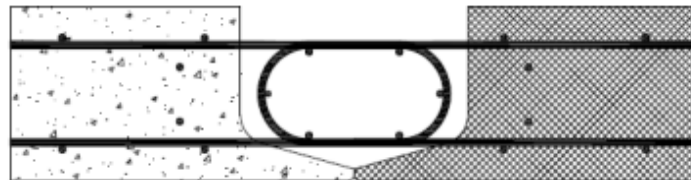


Figure H.2: Wet joint [95]

Cold joints

A cold joint is a planned and necessary temporary cessation of a concrete pour in a concrete structure. A cold joint occurs when a concrete pour is interrupted, both horizontally and vertically, and fresh concrete mix is poured against the hardened concrete. It is no longer possible for the freshly compacted concrete mix to blend with the previously poured mix [54]. Unlike other joint types, cold joints create a new element directly adjacent to the existing one.

Methods like reinforcement couplers and continuity strips are employed to continue reinforcement through a cold joint, as displayed in Figure H.3. For better bonding, rough surfaces on concrete elements are achieved through methods such as pressure washing.

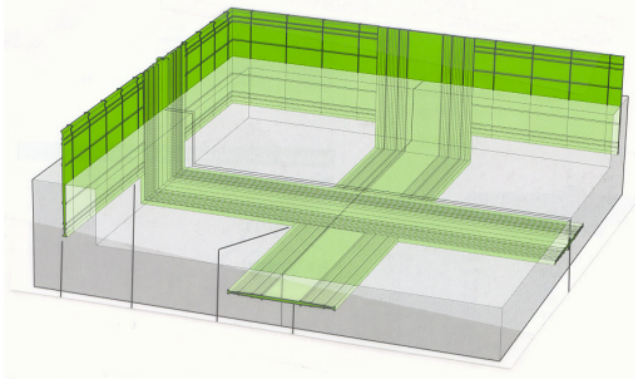


(a) Reinforcement coupler [97]

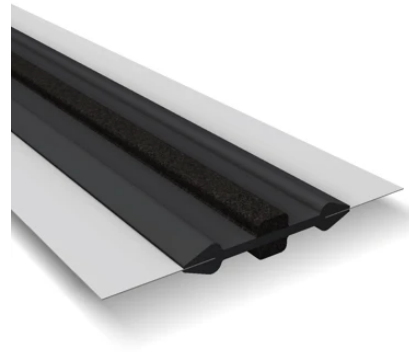
(b) Continuity strip

Figure H.3: Reinforcement continuities for cold joints [98]

In instances where watertightness is a prerequisite, additional measures, such as the incorporation of joint bands illustrated in Figure H.4a, can be implemented. Within tunnel construction, the application of waterstops, allowing for deformation, is common practice at the junction of two connecting elements. These products effectively extend the leakage path of water along the connection. For instance, the W9U profile showcased in Figure H.4b has proven successful at depths of up to 50 meters. However, the suitability of these profiles in deeper depths remains uncertain. It's noteworthy that the most susceptible point in the watertight connection is the bond between concrete and the profile, which comprises steel and rubber components [55].



(a) Water band [54]



(b) Trelleborg waterstop W9U [99]

Figure H.4: Water leakage prevention measures



Diana models

This Appendix offers in-depth insights into the numerical models developed in Diana FEA. In the main report, the focus is often on presenting results to maintain clarity, while a more detailed model description is provided here.

I.1. Verification of uniform stress assumption

This Section presents the details of the models as presented in Section 6.2.3. A reproduction of Table 6.4 is provided below:

Model parameter	Sphere	Cylinder
Internal volume V [m ³]	9000	9000
Internal radius a [m]	12,9	4,92
Wall thickness t [m]	1,86	1,65
Distributed normal force [MPa]	10,06	10,06
Young's Modulus [MPa]	39100	39100
Model dimension	3D	2D
Number of symmetry axes	3	2
Model fraction	$\frac{1}{8}$	$\frac{1}{4}$
Element type	Structural solids CHX60 & CPY39 CTE30 & CTP45	Plane stress CQ16M & CT12M
Element size [mm]	155	50
Number of elements	30.169	1.452
Number of nodes	108.358	4.547
Number of dofs	325.074	9.094
Number of elements over wall thickness	6	17
Element thickness [mm]	n.a.	1000
Type of analysis	Linear Elastic	Linear Elastic

Table I.1: Diana FEA model parameters for verification of uniform stress assumption

I.1.1. Sphere model

The model is illustrated in Figure I.1. It is symmetric in the global X-, Y- and Z-axis. The elements of which the output is used in Figure 6.29, are highlighted in Figure I.2. The choice for these elements was arbitrary, as all elements that form a line through the wall thickness give the same results.

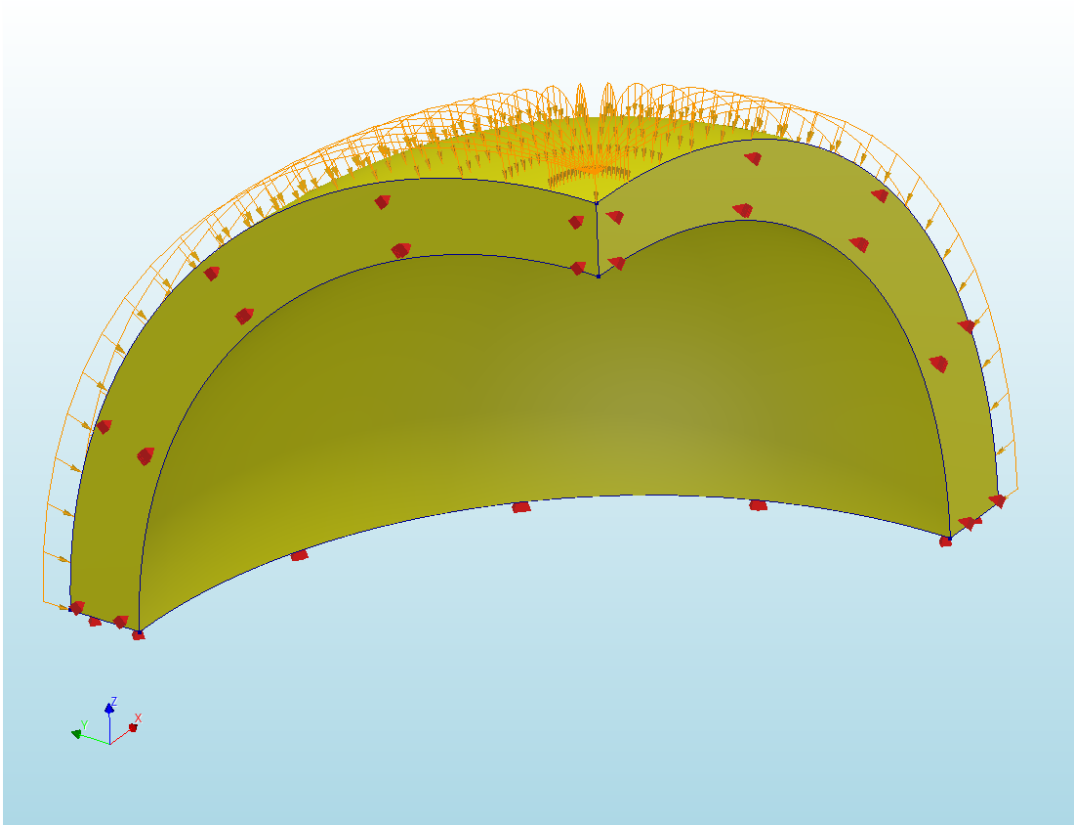


Figure I.1: Octant sphere 3D model

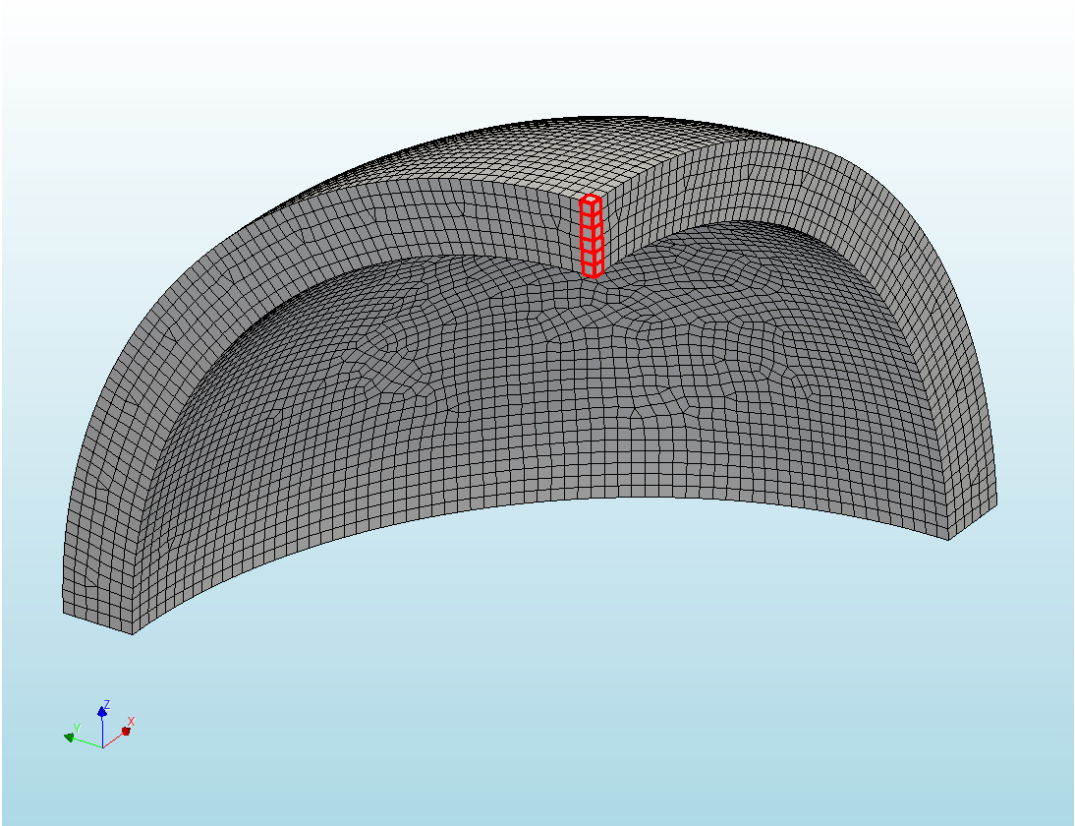


Figure I.2: Octant sphere mesh

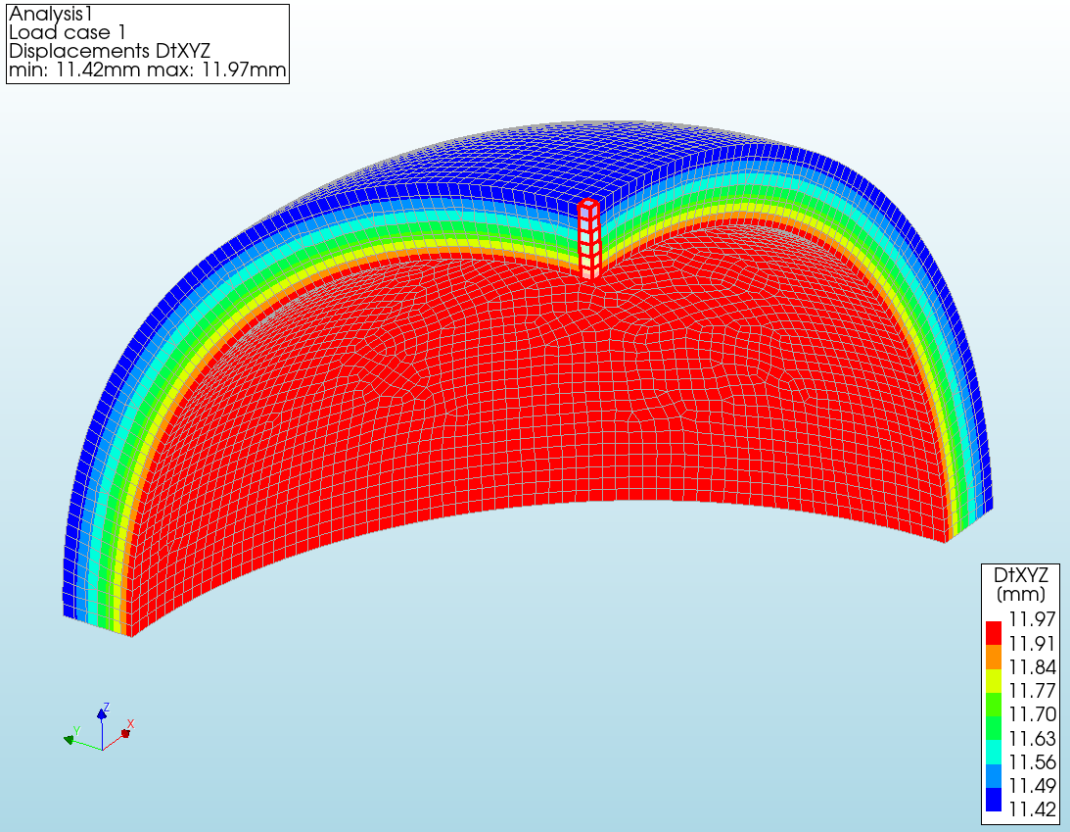


Figure I.3: Octant sphere global deformation

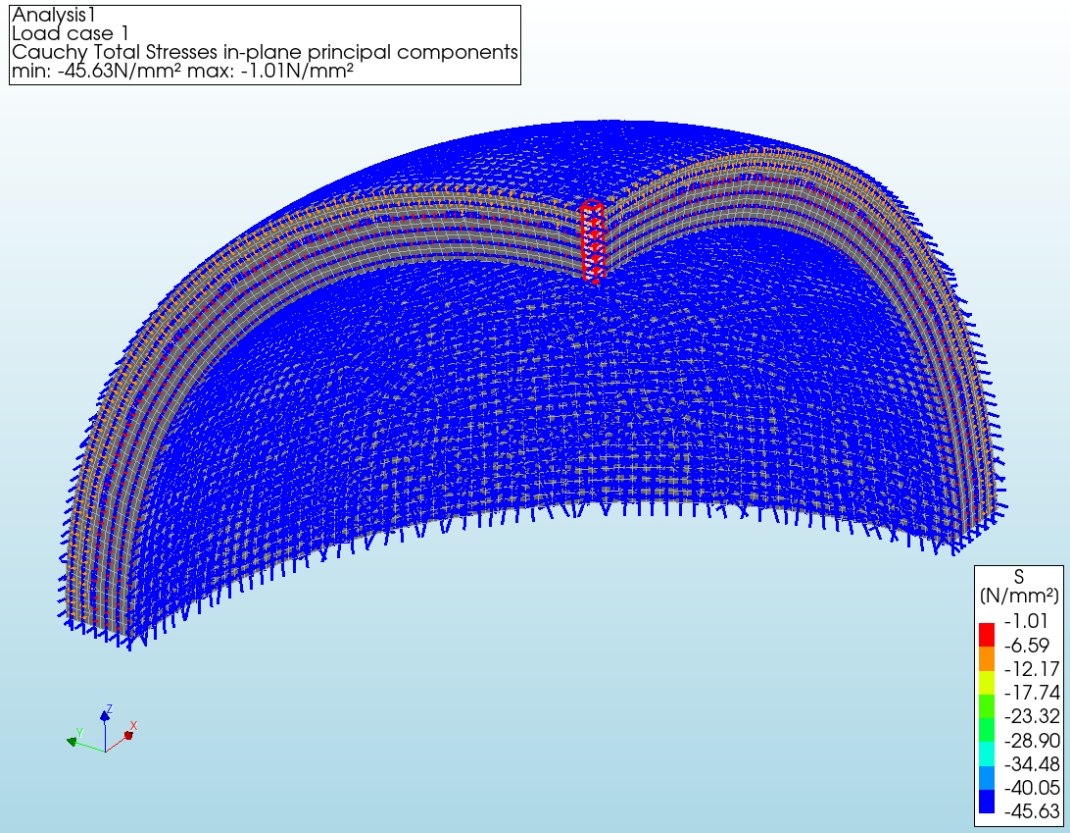


Figure I.4: Octant sphere principal stresses

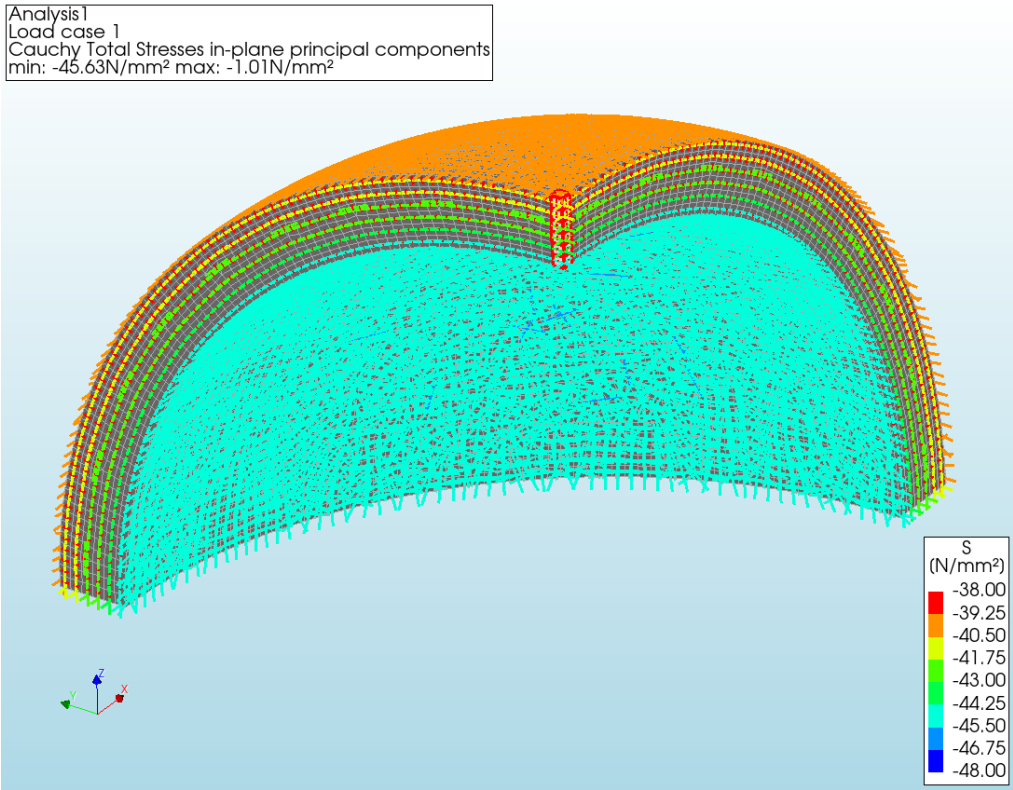


Figure I.5: Octant sphere principal stresses; range -38 to -48 MPa

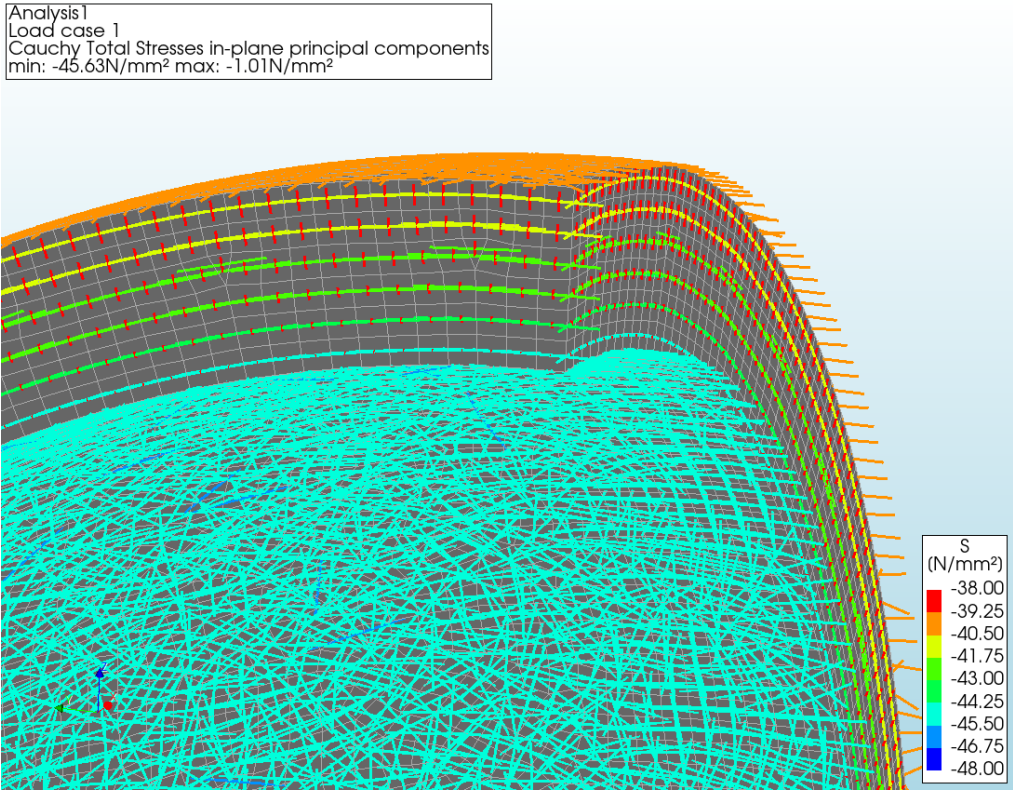


Figure I.6: Octant sphere principal stresses; zoomed in

I.1.2. Cylinder model

The model is illustrated in Figure I.7. It is symmetric in the global X- and Y-axis. The elements of which the output is used in Figure 6.29, are highlighted in Figure I.8. The choice for these elements was arbitrary, as all elements that form a line through the wall thickness give the same results.

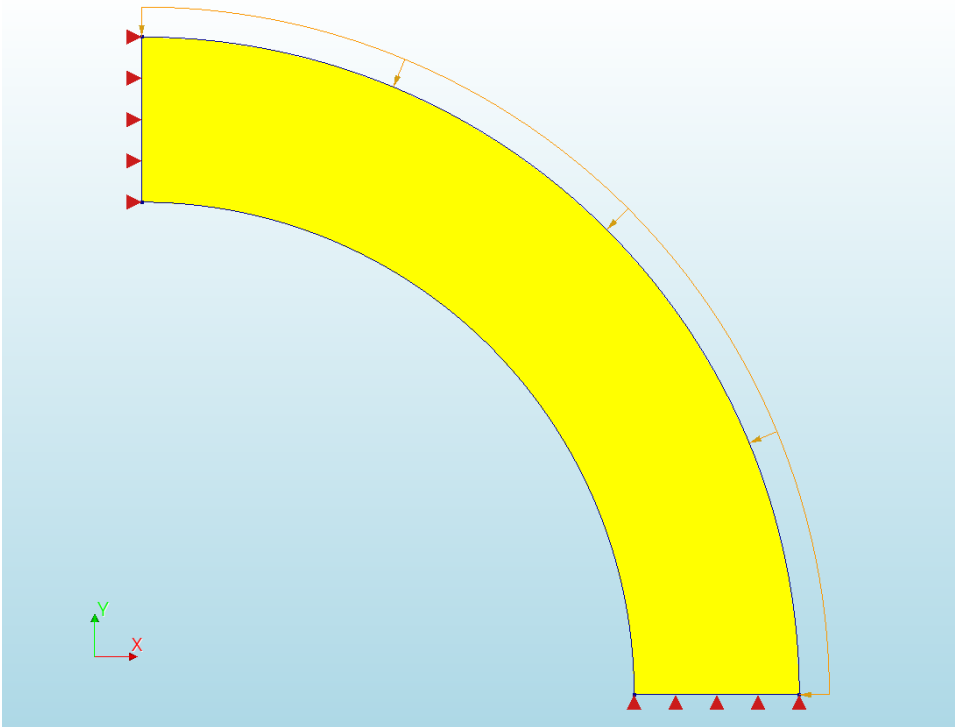


Figure I.7: Quarter cylinder 2D model

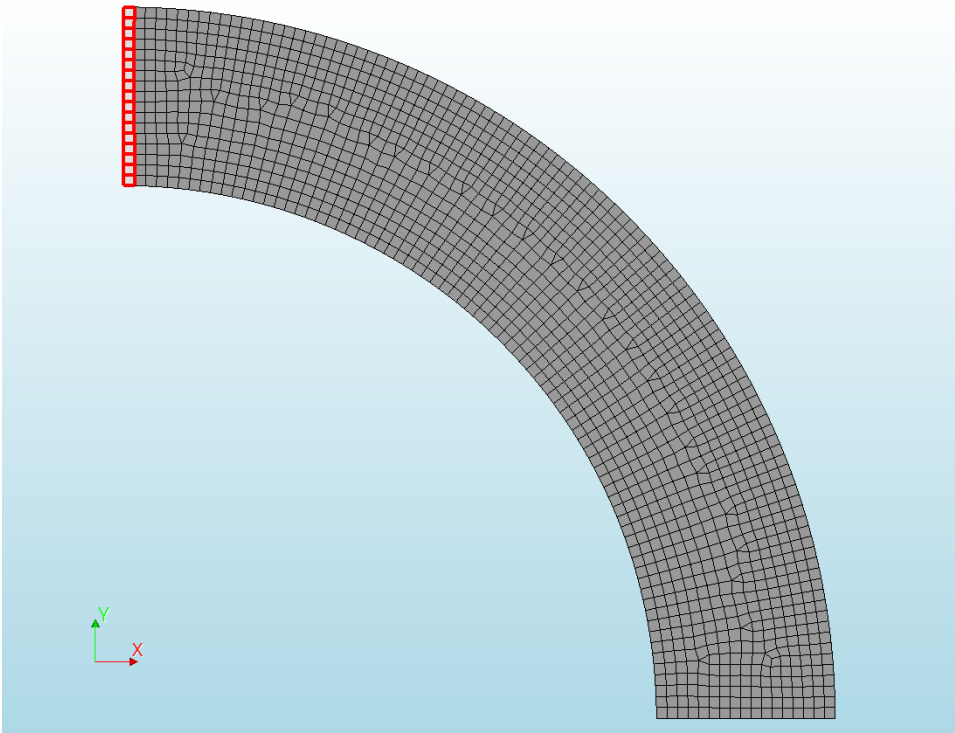


Figure I.8: Quarter cylinder mesh

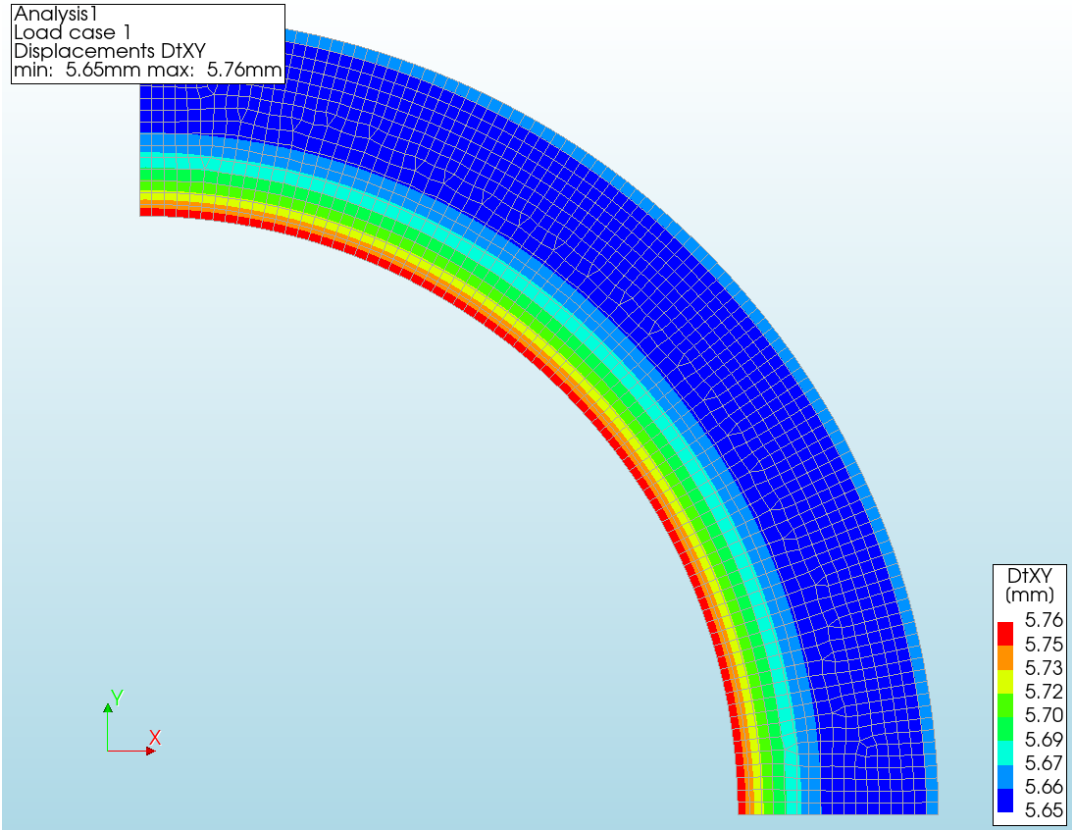


Figure I.9: Quarter cylinder global deformation

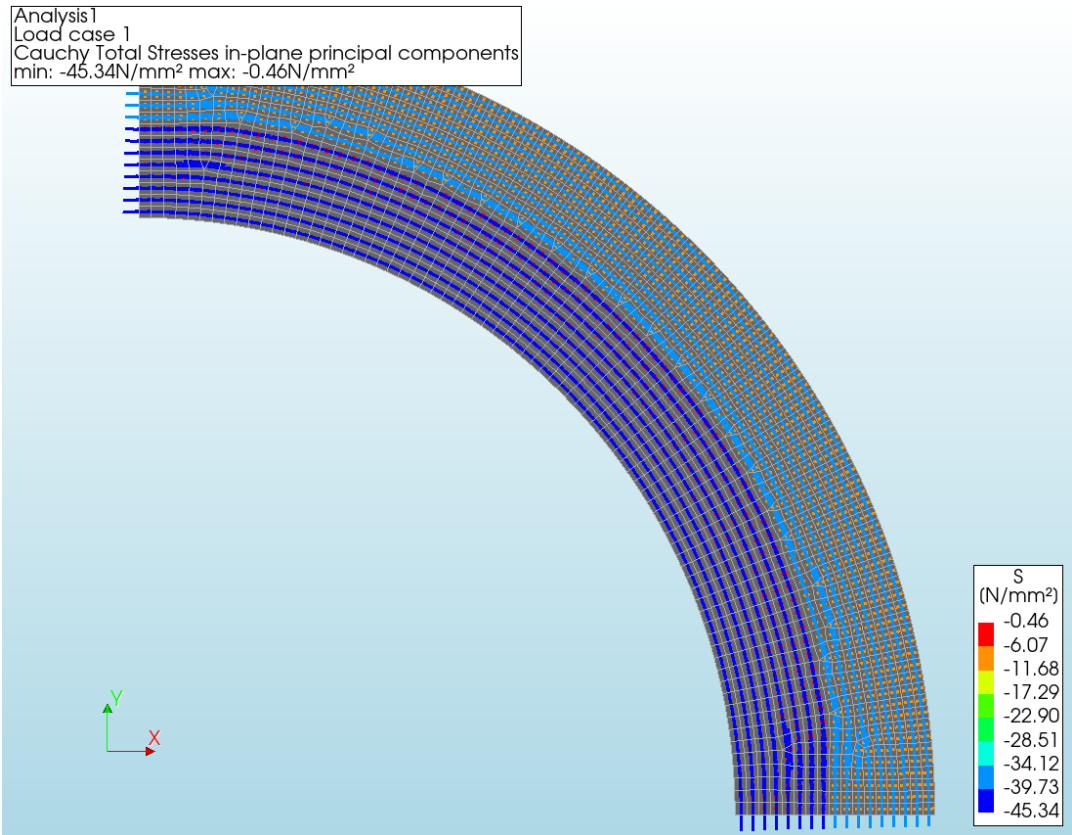


Figure I.10: Quarter cylinder principal stresses

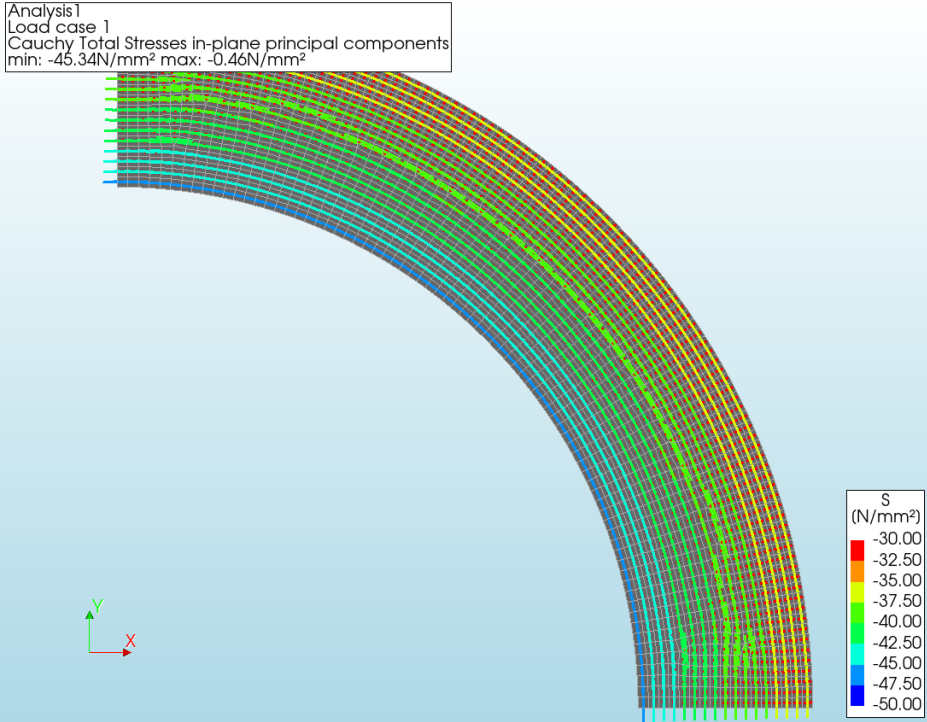


Figure I.11: Quarter cylinder principal stresses; range -30 to -50 MPa

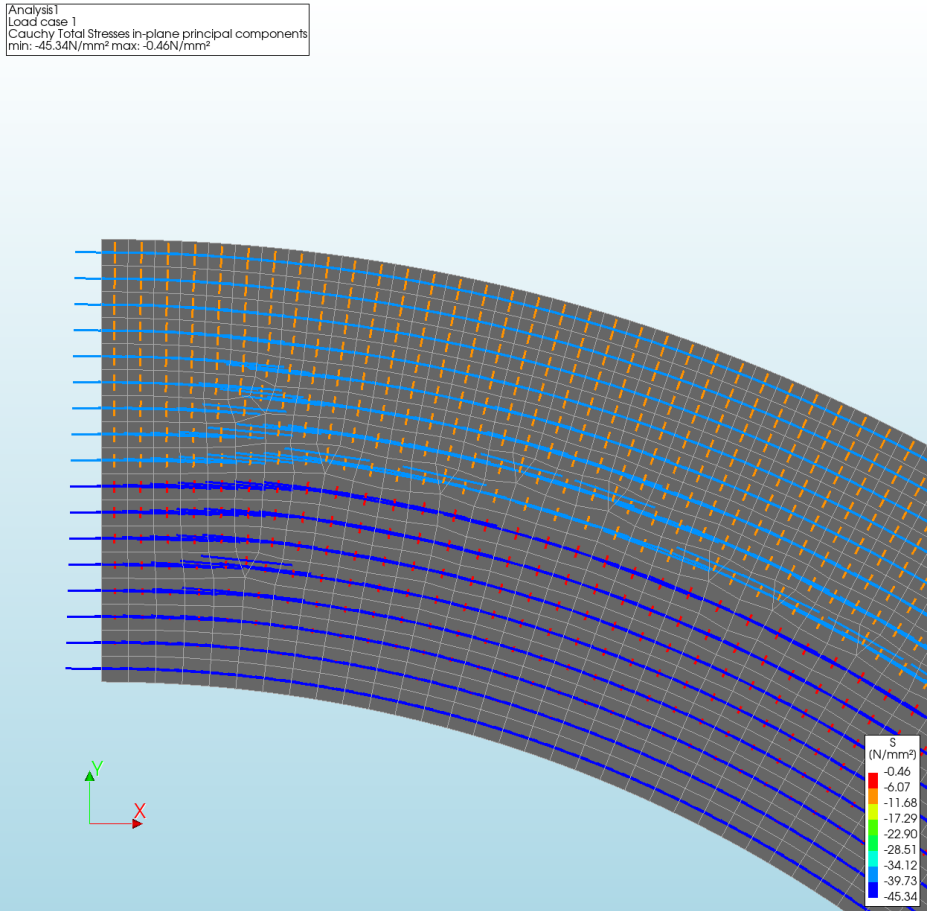


Figure I.12: Quarter cylinder principal stresses; zoomed in

I.2. Reduced models of cylindrical design

In this Section, the rationale behind the reduction of the models used in Section 6.1 is elucidated. It is crucial to note that the primary goal of these models is to capture the impact of the cap design on the internal stresses in the structure. Modeling only a portion of the actual structure leads to a reduction in the number of elements, allowing for a finer mesh and, consequently, more accurate results. The reduction of the cylinder model occurs in two steps: first, the length of the cylinder tube is decreased, and then an axisymmetric slice is modeled to represent the full cross-section.

I.2.1. Validation of reduction of cylinder tube length

Consider a cylindrical tube subjected to a constant distributed normal force. As explained in Section 6.2, such a tube has tangential and radial stresses that can be determined analytically. Now, envision the same tube, equipped with a flat cap on both ends, and still subjected to the same constant distributed normal force. The presence of the cap induces a disturbance in the internal stresses in the tube, referred to as an edge disturbance. The distance over which this edge disturbance has an effect is termed the influence length. For a cylinder, this length can be estimated using the formula provided in Equation I.1 [36]. In this equation, a represents the internal radius of the cylinder, and t is its thickness.

$$l_{i,\text{cylinder}} \approx 2, 4\sqrt{at} \quad (\text{I.1})$$

To assess the impact of the edge disturbance on the stresses in the cross-section, three models are examined. All models represent an octant of the cylinder, demonstrating symmetry along three axes. The foundation is disregarded, rendering this model a free-floating cylinder situated at a depth of 1000 meters. To mimic the hydrostatic load, a constant distributed normal force is applied, neglecting the gradient of the hydrostatic pressure. The first model features a modeled tube length equal to half of the internal length of the cylinder. The second model has a modeled tube length twice its influence length, and the third model has a modeled tube length of a single influence length. This analysis is conducted for both the flat cap design and the base hemispherical cap design. The graphical representations of the models are shown in Figures I.13 and I.14. Further details regarding the models are provided in Table I.2.

By definition, the influence of the edge disturbance on the internal stresses in the cylinder tube should become negligible after a single influence length. Conversely, a tube truncated at the influence length, with a constrained displacement perpendicular to the face of the cross-section of the truncation, should have no significant impact on the behavior in the edge disturbance. Therefore, such a reduced-length model can be employed to accurately capture the behavior of the structure in the edge disturbance.

To validate this hypothesis, the longitudinal, tangential, and radial stresses in the truncated cross-section are examined. These correspond to σ_{xx} , σ_{yy} , and σ_{zz} in the highlighted nodes, as indicated in Figures I.15 and I.16. The results of the linear elastic analyses in the edge nodes were plotted and compared with analytical solutions. The analytical solutions for $\sigma_{\theta\theta}$ and σ_{rr} were derived using Equations 6.10 and 6.11 presented in Section 6.2. The analytical solution for the longitudinal stress is defined as follows, assuming uniform stress over the wall thickness. It is essential to note that this is an approximation and not an exact solution.

$$\sigma_{LL} = \frac{(a+t)^2 p}{(a+t)^2 - a^2} \quad (\text{I.2})$$

As the $\frac{1}{8}$ th models exhibit complete identity with the full models, no loss of accuracy occurs through this reduction. Consequently, the longitudinal, tangential, and radial stresses in these models, indicated by blue triangular markers in Figure I.17, are considered true representations. A valid truncation of the tube can be confirmed when the values of σ_{LL} , $\sigma_{\theta\theta}$, and σ_{rr} in the reduced-length models are approximately equal to those in the $\frac{1}{8}$ th models. In such instances, the tube truncation is deemed valid, implying no impact on the structure's behavior in the edge disturbance.

The results of both analytical and numerical analyses are presented in Figure I.17. The analytical values are added as an extra verification.

For the model with a flat cap, the numerically determined stresses in the cross-section closely align with the analytical description and the $\frac{1}{8}$ th model, when the modeled tube length is equal to twice the influence length. However, when the modeled tube length is reduced to a single influence length, the longitudinal and tangential stresses become inaccurate, as depicted in Subfigures I.17a and I.17c. Therefore, the flat cap model can only be accurately reduced in length to twice the influence length to capture the behavior of the structure at the edge disturbance.

The hemispherical cap model closely follows the analytical stress description and the $\frac{1}{8}$ th model in all directions across both modeled reduced tube lengths. Consequently, accurately capturing the structure's behavior at the edge disturbance for the hemispherical cap model is feasible with a modelled tube length reduced to a single influence length.

Cap design	Flat	Hemisphere
Internal volume V [m ³]	9000	9000
Internal radius a [m]	4,92	4,84
Wall thickness t [m]	1,65	1,62
Cap thickness t_{cap} [m]	3,30	0,81
Tube length [m]	118,1	116,2
External length [m]	124,68	127,46
Influence length [m]	6,84	6,72
Distributed force [MPa]	10,06	10,06
Young's Modulus [MPa]	39100	39100
Poissons ratio	0,2	0,2
Element type	Structural solids CHX60 & CPY39 CTE30 & CTP45	Structural solids CHX60 & CPY39 CTE30 & CTP45
Element size [mm]	800 & 200	800 & 200
Number of elements over wall thickness	2 & 8	2 & 8
Model fraction	$\frac{1}{8}$	$\frac{1}{8}$
Model dimension	3D	3D
Type of analysis	Linear Elastic	Linear Elastic
Modelled length [m]	59,04	58,08
Number of elements	7.565	7.981
Number of nodes	32.333	31.151
Number of dofs	96.999	96.453
Modelled length [m]	13,68	13,44
Number of elements	11.948	11.035
Number of nodes	48.541	42.624
Number of dofs	145.623	127.872
Modelled length [m]	6,84	6,72
Number of elements	7.576	8.419
Number of nodes	30.518	35.212
Number of dofs	91.554	105.636

Table I.2: Cylinder flat cap and hemisphere model parameters

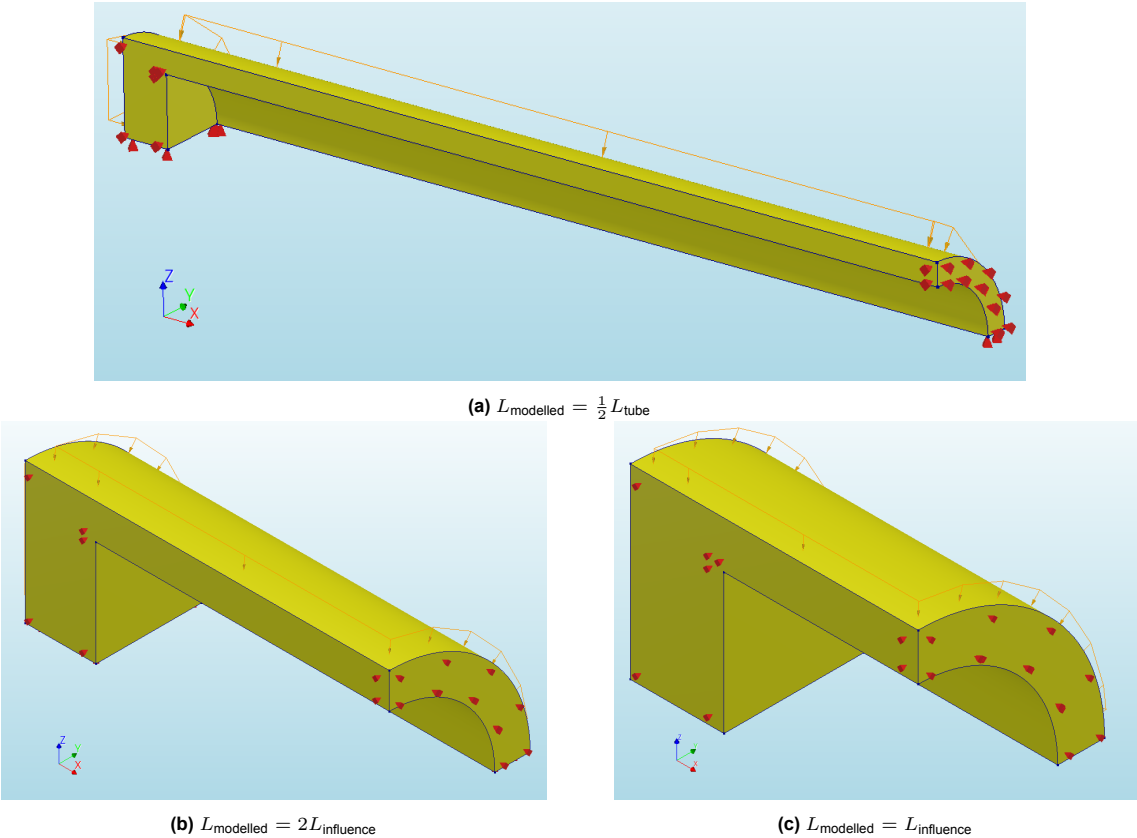


Figure I.13: Length-reduced flat cap models for analyzing influence length

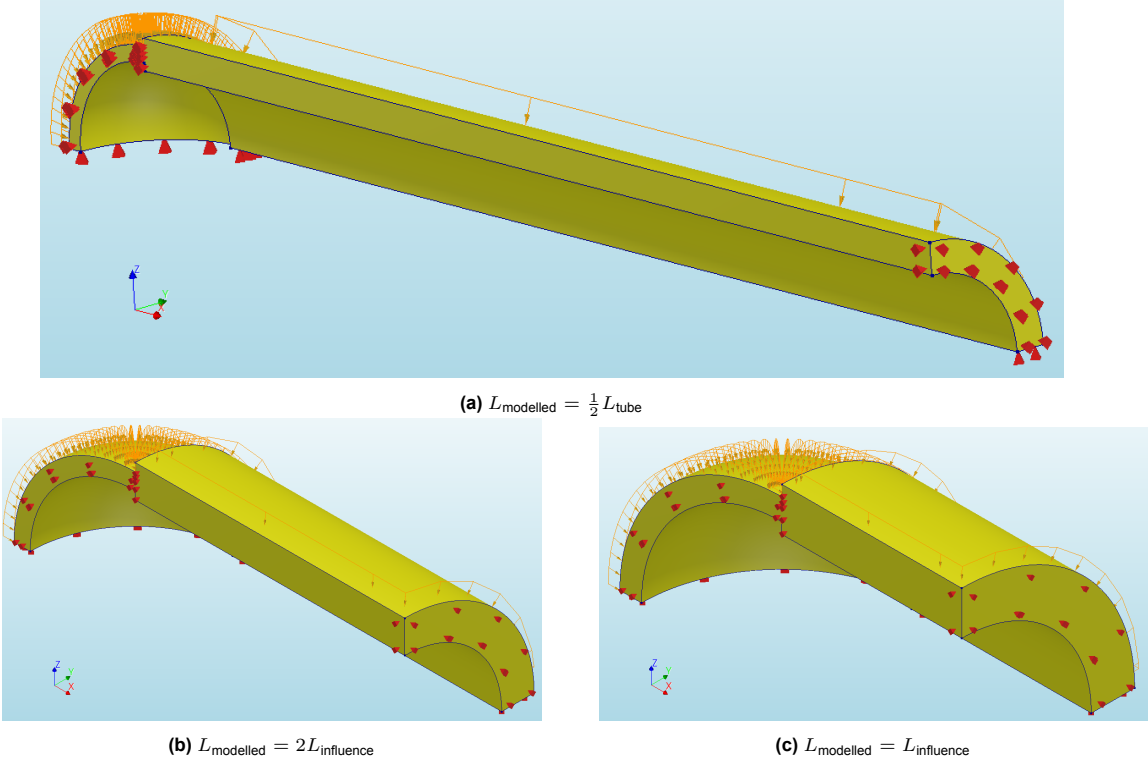


Figure I.14: Length-reduced hemisphere cap models for analyzing influence length

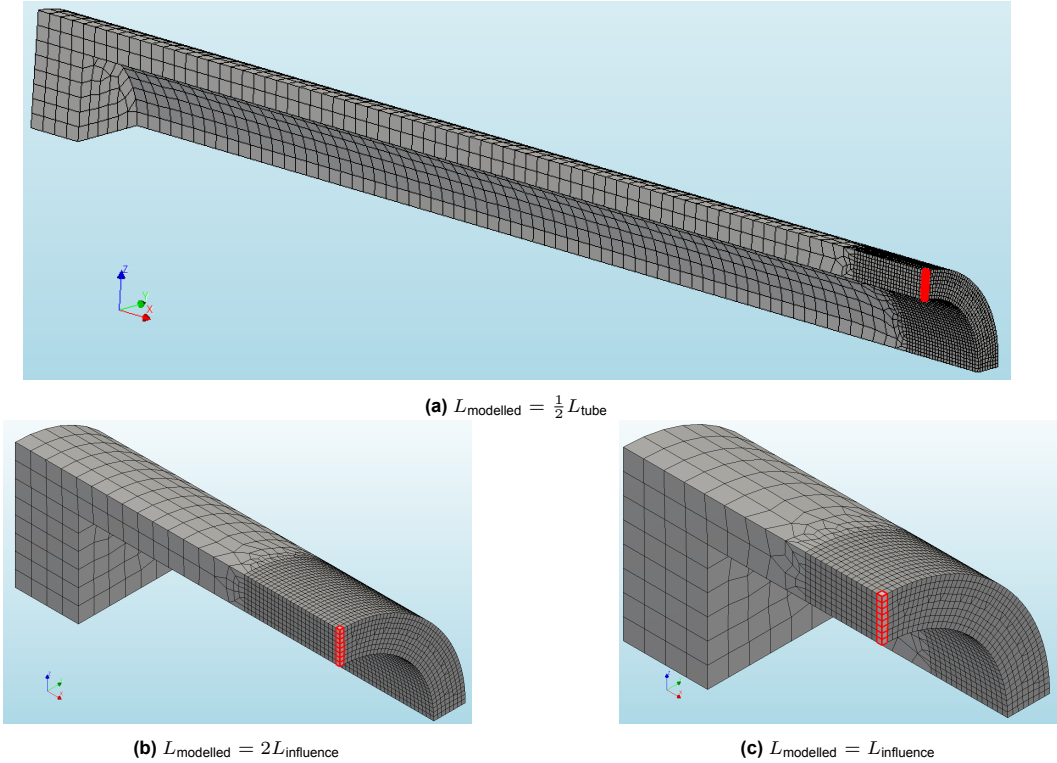


Figure I.15: Meshes of length-reduced flat cap models with nodes used for data collection highlighted

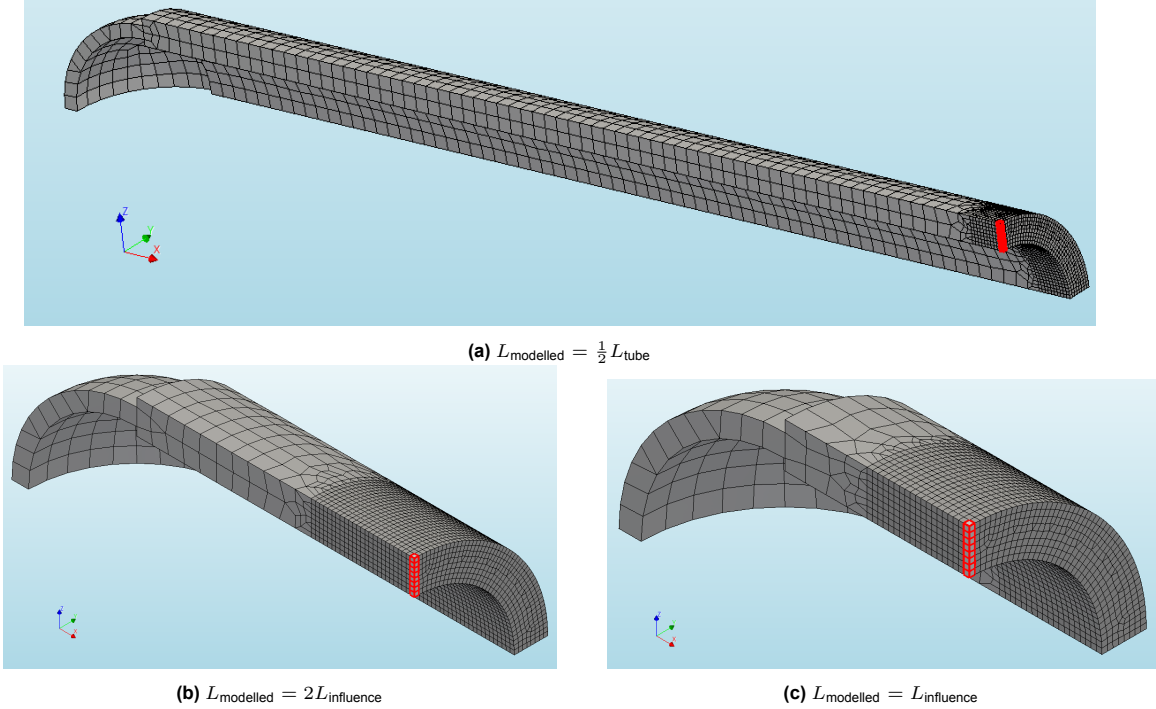


Figure I.16: Meshes of length-reduced hemisphere cap models with nodes used for data collection highlighted

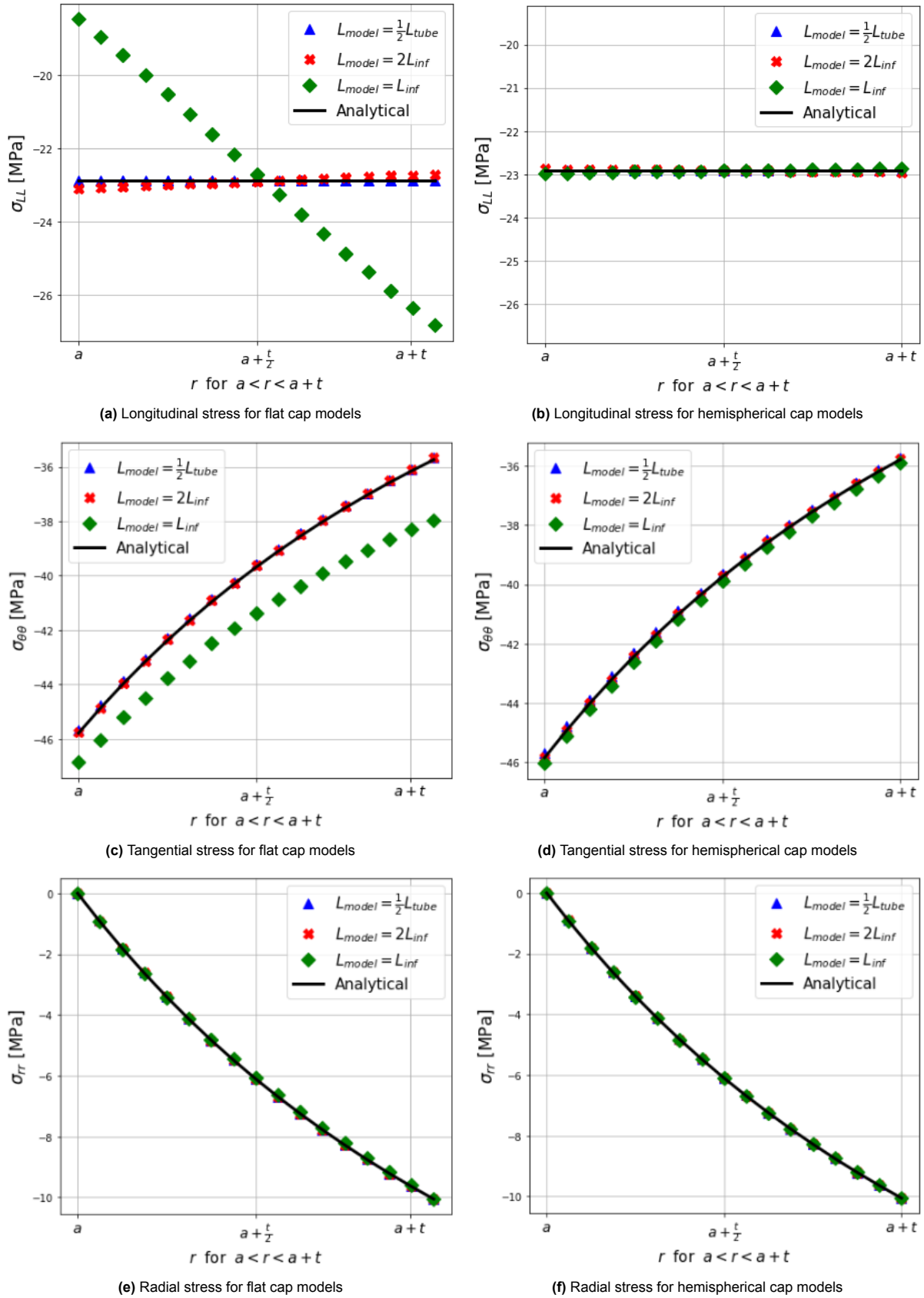


Figure I.17: Stresses in the cross-section of length-reduced flat and hemispherical cap models

I.2.2. Validation of axisymmetrical reduction

Given the complete axisymmetry of the cylinder, its structural behavior can be effectively represented by a slice of the cross-section. To further minimize the model's size, a slice of the cross-section is implemented in a 3D solid model. The slice is defined as the fraction of the structure that is in between the ZX-axis and a 5.71° rotated plane of which the tangent is equal to $\frac{1}{10}$. This results in a slice which is approximately $\frac{1}{64}$ th of the original cross-section.¹ Alongside the imposed symmetry in the YZ-plane and the reduced length, this model is more than 128 times smaller than the full model. A visual depiction of the cross-section is presented in Figure I.18.

To validate whether the sliced model accurately represents the full model, similar checks to those described in Appendix I.2.1 are performed. The models outlined in Table I.3 and Figures I.19 and I.20 are established for this purpose. Comparable to the verification of the length reductions, the stresses in the cylinder's tube are assessed and compared to the $\frac{1}{8}$ th model. This verification is exclusively conducted for the hemispherical cap model, as the flat cap model has not undergone an equally intensive examination.

Modelled length of tube Value [m]	$2L_{inf}$ 13,44	L_{inf} 6,72
Element type	Structural solids CHX60 & CPY39 CTE30 & CTP45	Structural solids CHX60 & CPY39 CTE30 & CTP45
Element size [mm]	200 & 80	200 & 80
Number of elements over wall thickness	4, 8, 10 & 20	4, 8, 10 & 20
Model fraction	$< \frac{1}{128}$	$< \frac{1}{128}$
Model dimension	3D	3D
Type of analysis	Linear Elastic	Linear Elastic
Number of elements	12.616	11.912
Number of nodes	52.856	48.867
Number of dofs	158.568	146.601

Table I.3: Cylinder hemisphere cap $\frac{1}{64}$ th slice model parameters

The slice model is subjected to constrained deformations perpendicular to the ZX-plane and the slightly tilted ZX-plane, as illustrated in Figure I.18 and Subfigures I.19a and I.20a. A challenge arises at the edge with the lowest Z-coordinate of the slice, where the planes intersect. In this location, the nodes, when subject to constraints from both planes, possess degrees of freedom that are not orthogonal. Diana FEA lacks a solution for this fundamental problem. To address this issue, a section with a height of 10 mm is introduced. This section is solely constrained on the face on the negative side of the XZ-plane. The unconstrained face on the positive side of the XZ-plane may induce a singularity in the solution. It is essential to investigate whether this singularity has any impact on the results.

The slice model permits a highly refined mesh, incorporating up to 20 elements across the wall thickness, as shown in Figure I.21. The highlighted elements are utilized for data collection on the stresses in the cylinder tube. In this region, σ_{xx} , σ_{yy} , and σ_{zz} correspond to σ_{LL} , $\sigma_{\theta\theta}$, and σ_{rr} , respectively. This data was utilized to generate the plots in Figure I.22. The slice models closely replicate the $\frac{1}{8}$ th model, with the model featuring double the influence length exhibiting slightly better performance. Consequently, this model is employed to verify the behavior in the transition zone of various hemispherical cap design variations.

As depicted in Figure I.23, the principal stresses in the singularity of the cylinder slice, as explained in Figure I.18, rapidly revert to non-extreme values. The impact of the singularity on the rest of the model is negligible.

¹While an axisymmetric model would have been more elegant, this realization occurred late in the process, leaving insufficient time for its implementation.

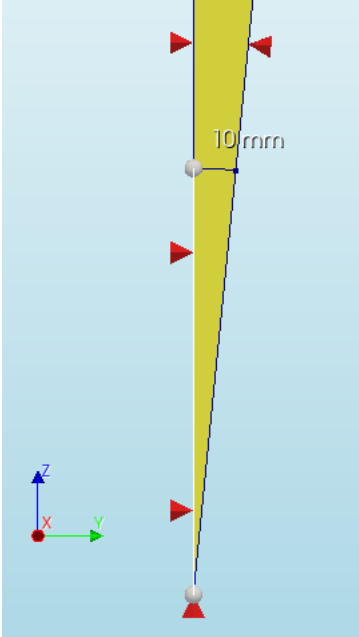


Figure I.18: Incompatible support conditions in edge of sliced model

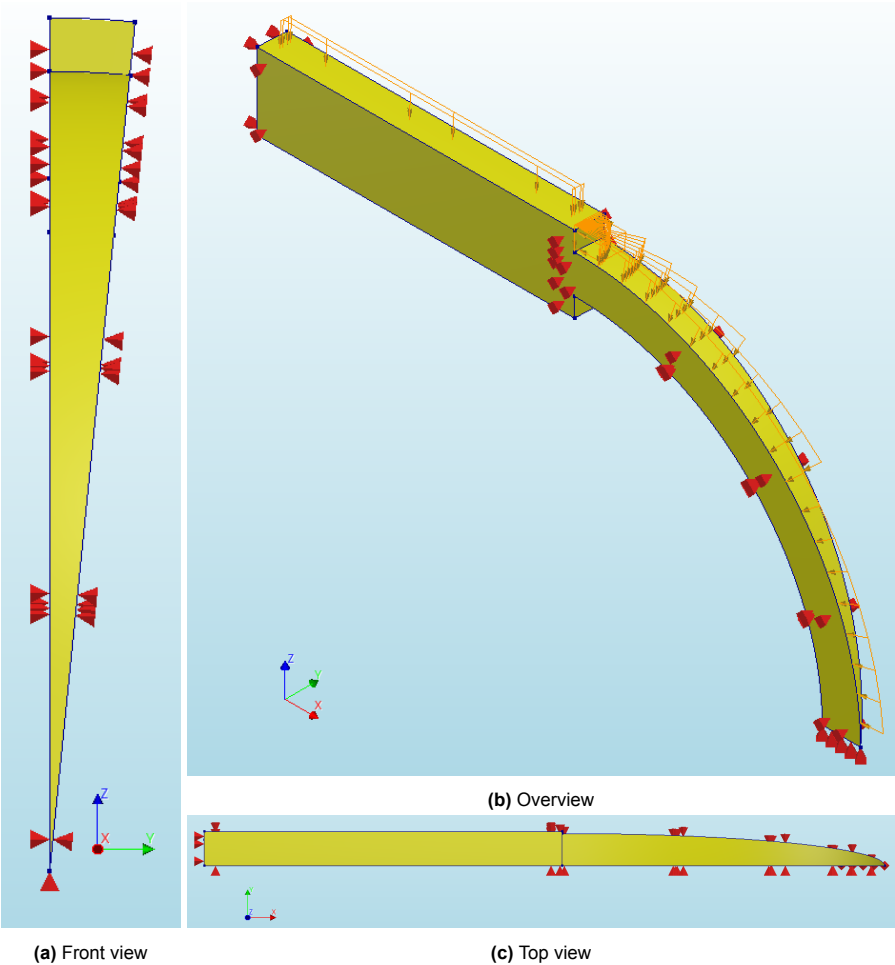


Figure I.19: $\frac{1}{64}$ th slice of hemisphere model with $L_{\text{tube}} = L_{\text{influence}}$

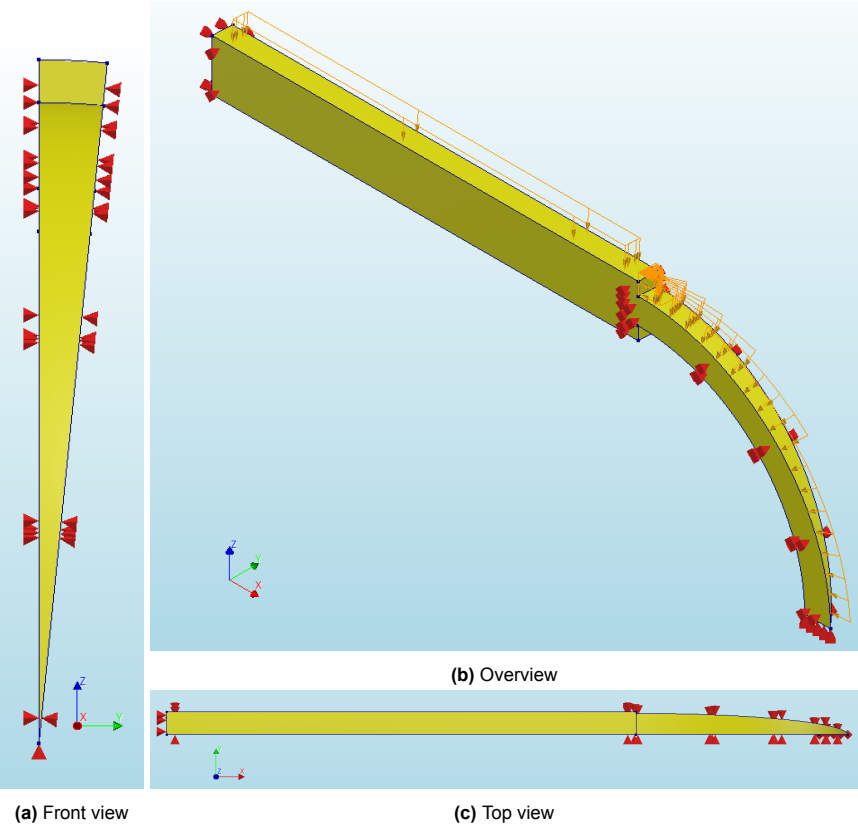


Figure I.20: $\frac{1}{64}$ th slice of hemisphere model with $L_{\text{tube}} = 2L_{\text{influence}}$

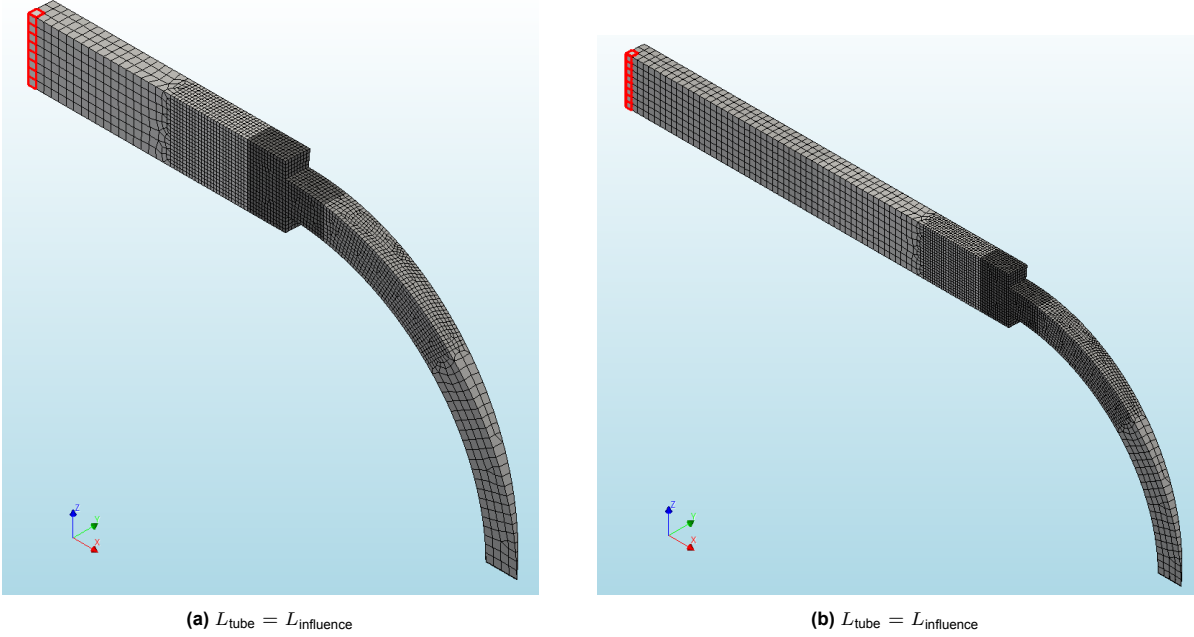
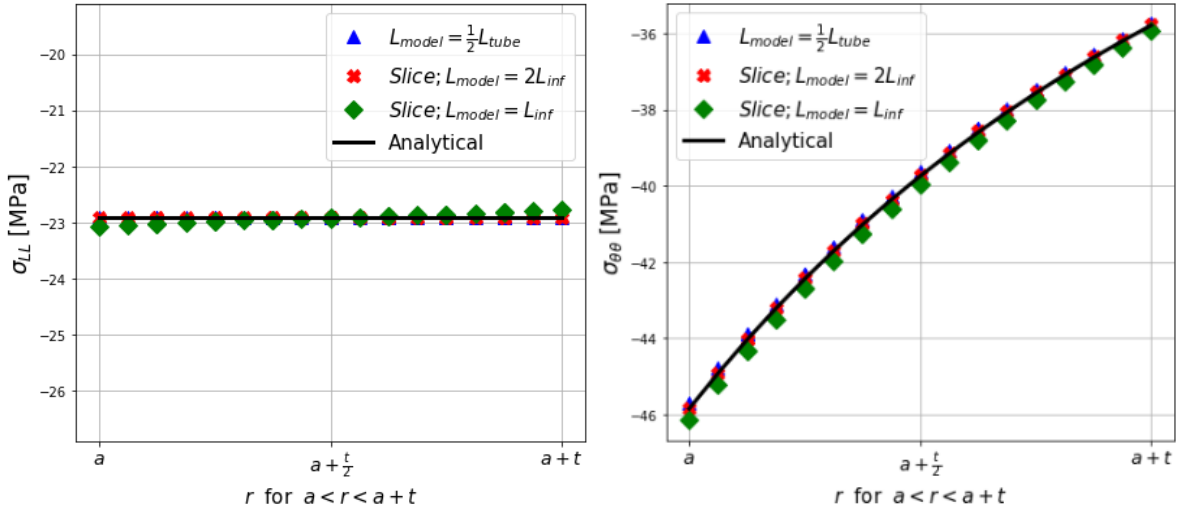
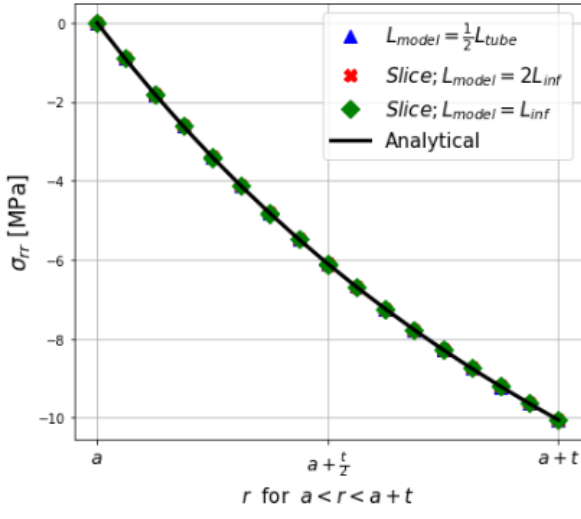


Figure I.21: Slice model mesh



(a) Longitudinal stress for flat cap models

(b) Tangential stress for slice models



(c) Radial stress for slice models

Figure I.22: Stresses in the cross-section of slice models

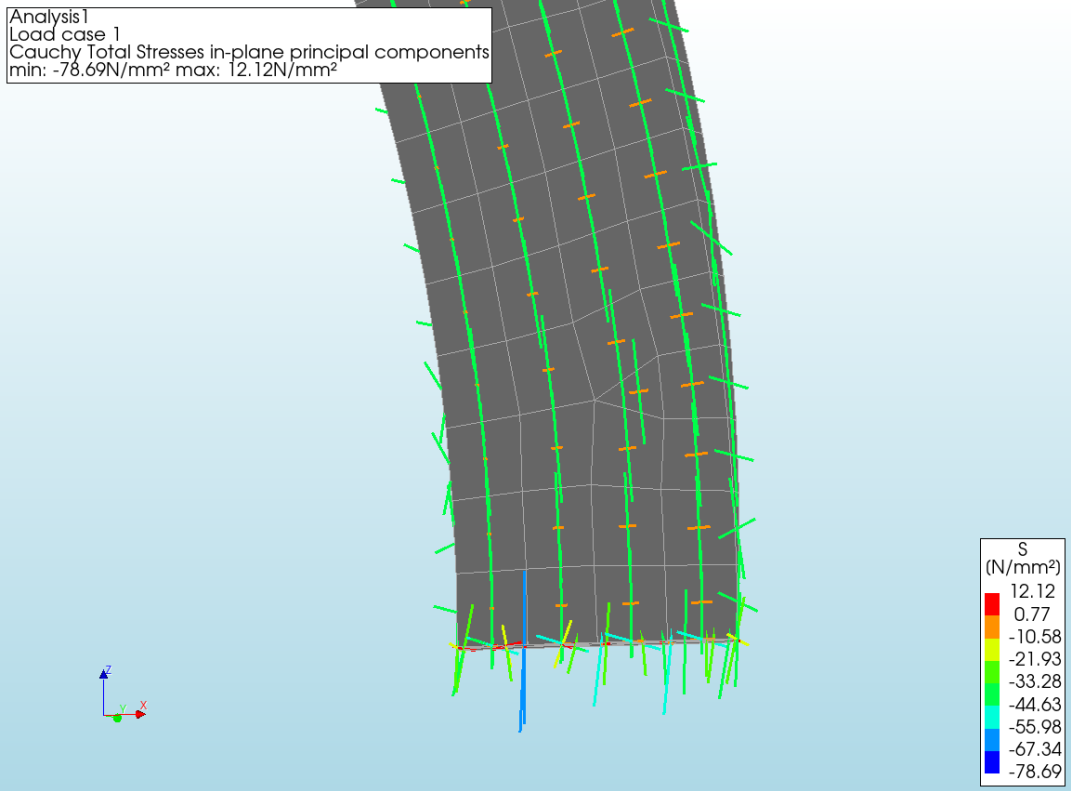


Figure I.23: Principal stresses at the singularity of the slice

I.3. Edge disturbance models

The model, as detailed and validated in Appendix I.2.2, is reoriented back to the XZ-plane. This adjustment aligns the centerline of the slice with the XZ-plane, resulting in a cross-section for the cylinder slice identical to that depicted in Figure I.24. Due to the inherent axisymmetry, this rotation does not impact the model's behavior, although this aspect is not further discussed.

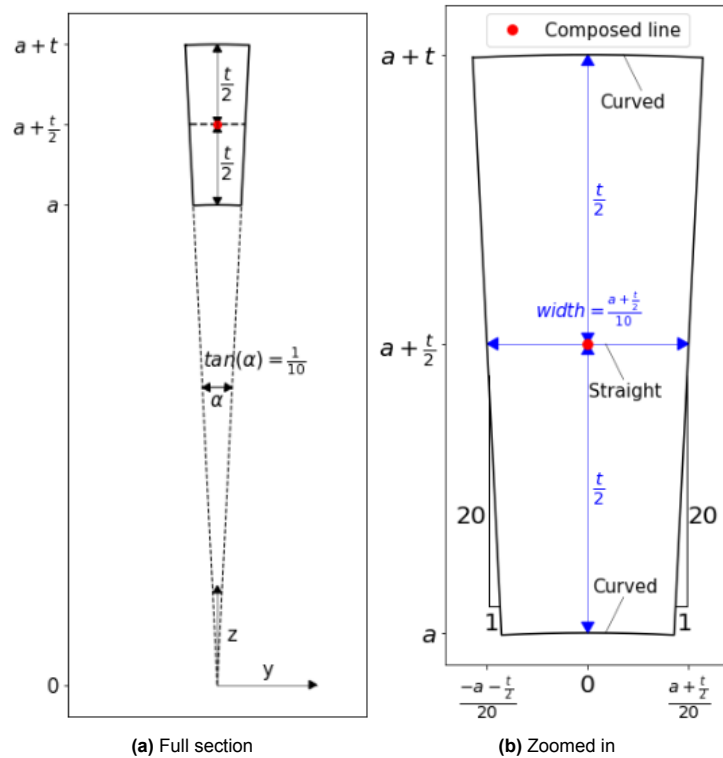


Figure I.24: Schematic representation of cross-section used for edge-disturbance

I.3.1. Validation of edge disturbance with thin shell

The bending moment induced by the edge disturbance can be calculated analytically using Equations 6.1 and 6.2. For clarity, these equations are reproduced below. However, it is important to note that these equations are specifically designed for thin shells. Given that the cylinder and hemispherical cap in this context are characterized as thick to very thick shells, as explained in Section 6.1, the results obtained from numerical analysis concerning edge disturbance cannot be validated. Consequently, the validation is conducted using a thin shell, while the rest of the model remains consistent.

$$m_{xx} = \frac{pl_i^2}{8\pi^2} \sin \frac{\pi x_c}{l_i} \exp \frac{-\pi x_c}{l_i}$$

$$m_{\phi\phi} = \frac{pl_i^2}{8\pi^2} \sin \frac{\pi x_s}{l_i} \exp \frac{-\pi x_s}{l_i}$$

The validation process involves two models, each with parameters listed in Table I.4. A composed line is introduced, positioned in the mid-surface. Given that the composed line is 1D, it considers all nodes concerning a straight surface, although the actual surface is curved. This concept is illustrated in Figure I.24b. An assessment is conducted to determine the significance of this simplification.

To ensure accurate results with the composed line, it is crucial that the mesh elements around it share the same x-coordinate. Any deviation in the x-coordinate can disrupt the summation process of node contributions to the bending moment. Consequently, considerable effort is invested in creating a mesh where all elements around the composed line are solid cubes, consistently distributed over the x-axis.

The mesh is finer at the transition zone between the cylinder and the hemisphere. Visual representations of the models are presented in Figure I.25, while the mesh details are observed in Figure I.26. These figures represent screenshots of the 1:20 model, and since the 1:40 model is identical in appearance with a narrower cross-section, its screenshots are omitted.

The composed line consists of two sections: a straight section in the cylinder edge and a curved section in the hemisphere. In the model's coordinate system, the moments around the Y-axis represent m_{xx} and $m_{\phi\phi}$ in the equations for edge-disturbance-induced moments. The output of the composed line is in Nm, while analytically, a moment per unit length [Nm/m] is calculated. To compare the two, the model outputs are divided by the width of the slice at the location of the node on the composed line.

In the cylinder tube, this width is equal to $\frac{a+t/2}{10}$, as indicated in Figure I.24b. In the hemisphere, the width gradually decreases towards the singularity of the arc. As the z-coordinate of the mid-surface decreases from a to 0 over the cylinder edge to the end of the hemisphere, the width of the slice in the hemisphere is calculated as follows:

$$width_{\text{slice, mid-surface}} = \frac{a + \frac{t}{2}}{10} \frac{z}{a} \text{ for } 0 < z < a$$

In the 1:40 model, the denominator for calculating the width of the slice at the mid-surface is 20 instead of 10.

The results of the models are shown in Figure I.27. Two notable observations are made. Firstly, the models appear to align with the shape of the analytical solution, as depicted in Figure 6.3. However, there is considerable noise, resulting in local peaks. Additionally, the unexpected negative bending moment in the hemisphere in the 1:40 model is noteworthy. Secondly, the moments in the 1:20 model are generally higher than in the 1:40 model, which aligns with expectations given the narrower width of the 1:40 model. It is important to note that the results in Figure I.27 are not adjusted for the width of the slice at the mid-surface.

The modified values have been visualized using Python, as depicted in Figure I.28. In the upper figure, inconsistent data, such as spikes, has been cleaned up, while in the lower figure, it is still included. Despite the noise, the model closely corresponds to the analytically determined moments, particularly within a distance of two influence lengths from the edge. Hence, it is deemed an accurate representation of the full model.

Inclination angel	1:20	1:40
Internal radius a [m]	5	5
Wall thickness t [m]	0,05	0,05
Tube length [m]	20	20
Influence length [m]	1,21	1,21
Distributed force [MPa]	10,06	10,06
Young's Modulus [MPa]	39.100	39.100
Poissons ratio	0,2	0,2
Element type	Structural solids CHX60 & CPY39 CTE30 &CTP45	Structural solids CHX60 & CPY39 CTE30 &CTP45
Edge divisions	100 & 200	100 & 200
Number of elements over wall thickness	4	4
Model dimension	3D	3D
Type of analysis	Linear Elastic	Linear Elastic
Composed line		
Element type	CL3CM	CL3CM
Element length [mm]	40	40
Number of elements	8.443	5.287
Number of nodes	40.214	25.384
Number of dofs	120.642	76.152

Table I.4: Thin shell model parameters

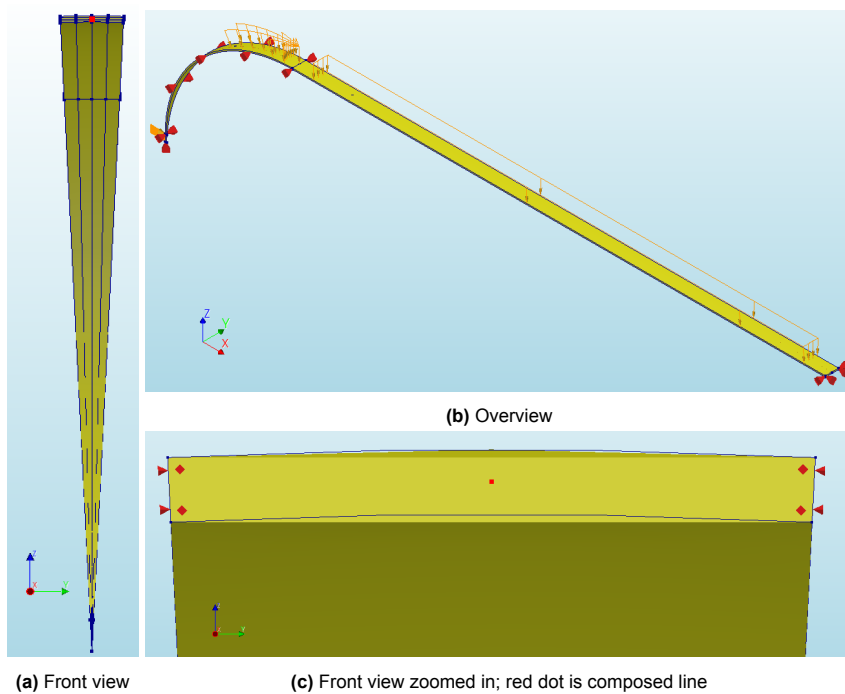


Figure I.25: Thin shell model for validation

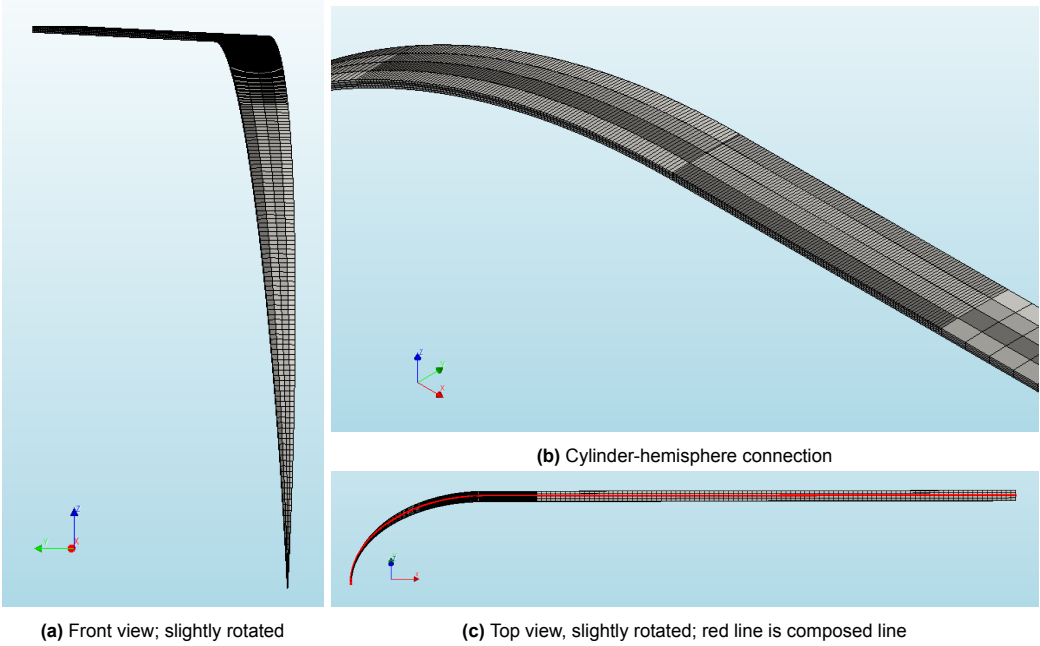


Figure I.26: Mesh of thin shell model for validation

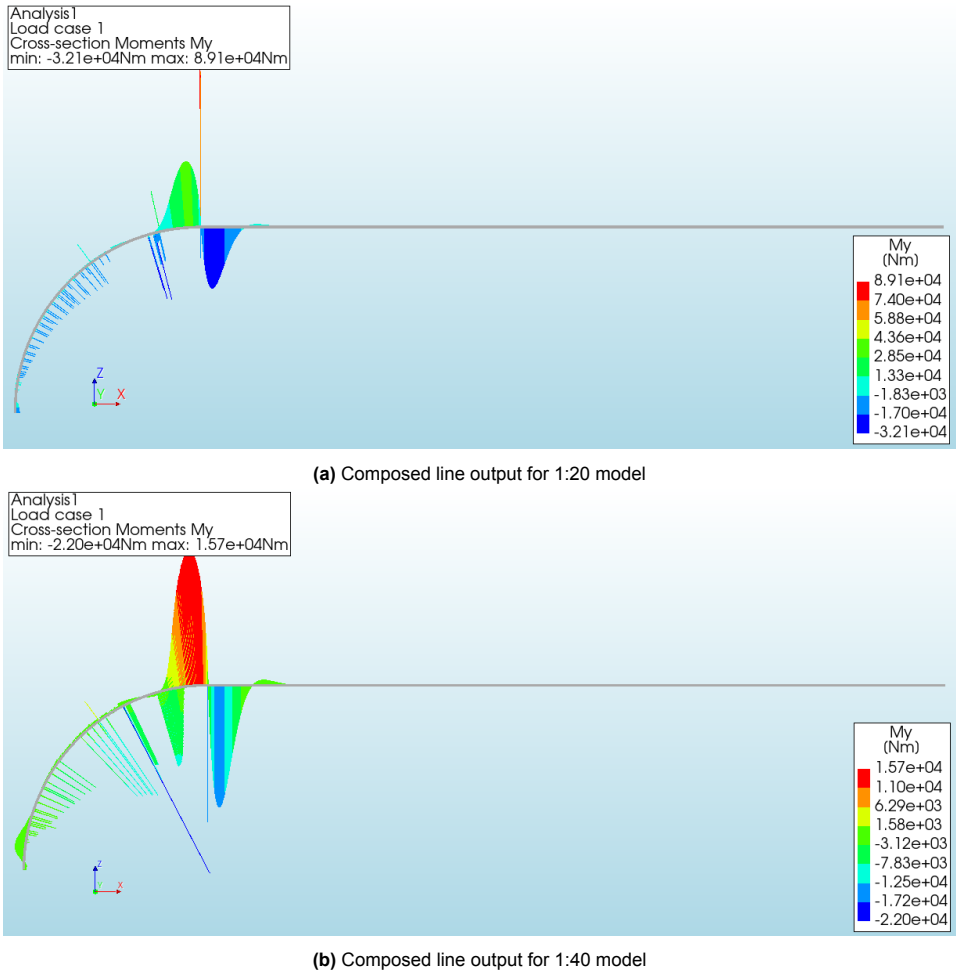
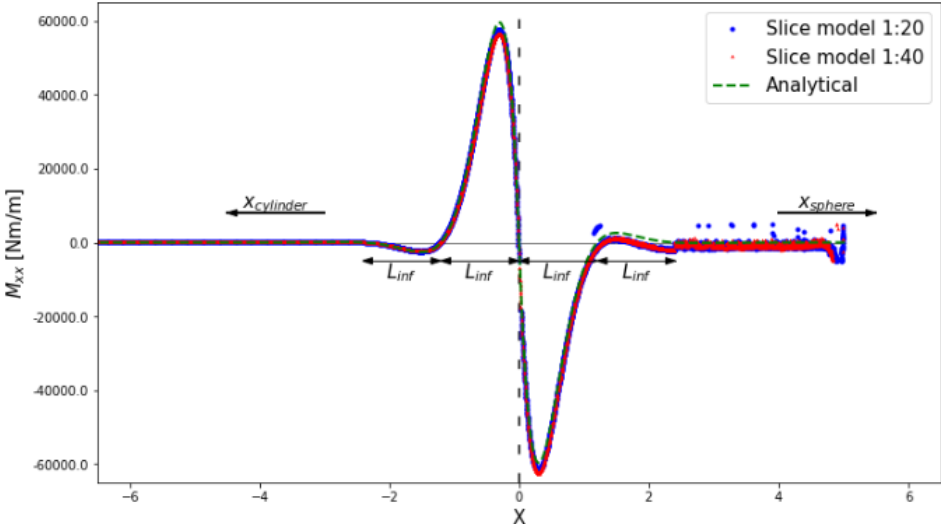
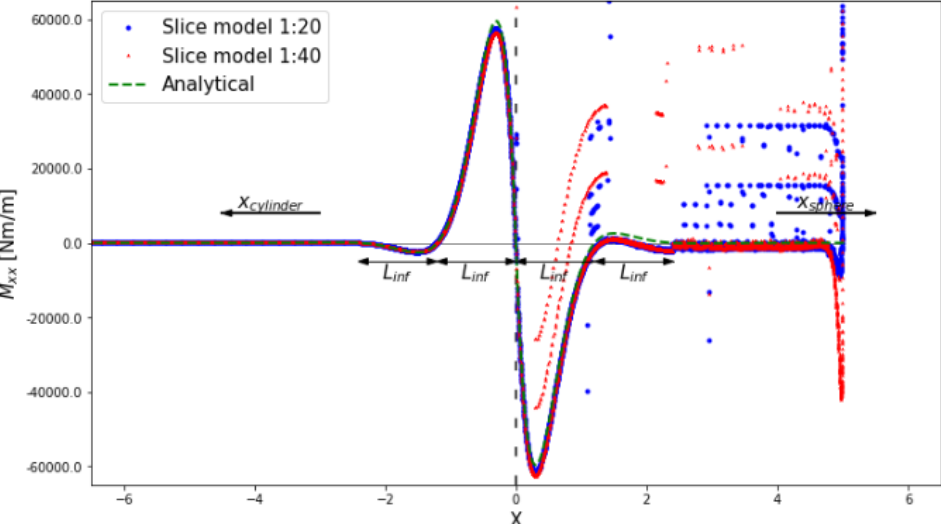


Figure I.27: Output of thin shell model for validation



(a) Composed line output, adjusted for slice width; cleaned data



(b) Composed line output, adjusted for slice width; including noise data

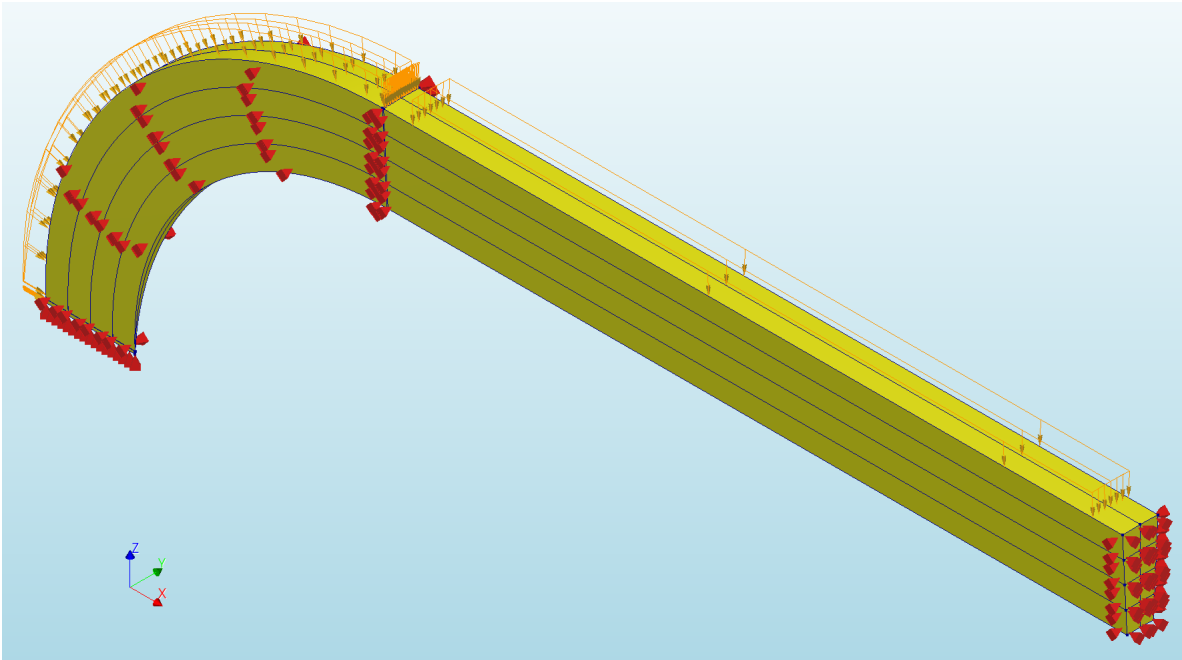
Figure I.28: Output of thin shell model for validation, adjusted for slice width

I.3.2. Models with various hemisphere thicknesses

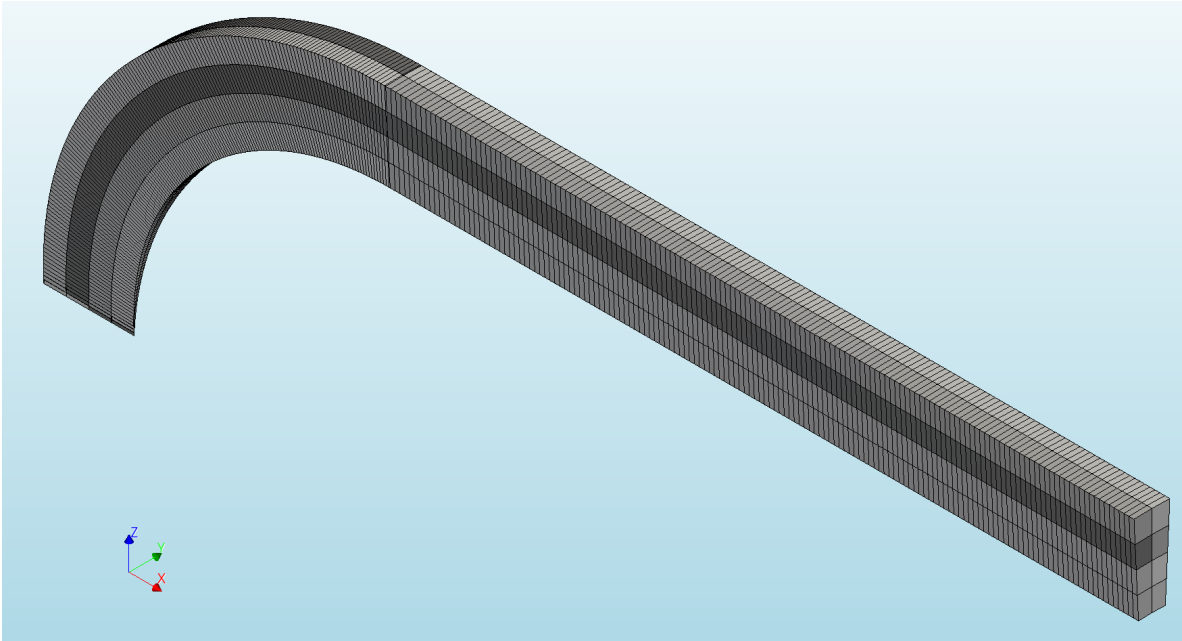
This Section outlines the specifications of the models employed to investigate the impact of hemisphere thickness on the moment induced by the edge disturbance, as discussed in Section 6.1.3. The properties of the models are listed in Table I.5.

Hemisphere thickness fraction	1	0,6	0,5	0,4
Internal radius a [m]	4,84	4,84	4,84	4,84
Wall thickness t [m]	1,62	1,62	1,62	1,62
Tube length [m]	13,44	13,44	13,44	13,44
Wall thickness t [m]	1,62	0,972	0,81	0,648
Distributed force [MPa]	10,06	10,06	10,06	10,06
Young's Modulus [MPa]	39.100	39.100	39.100	39.100
Poisson's ratio	0,2	0,2	0,2	0,2
Element type	Structural solids CHX60 & CPY39 CTE30 & CTP45			
Edge divisions	100	100	100	100
Number of elements over wall thickness	4	4 & 6	2 & 4	2 & 4
Model dimension	3D	3D	3D	3D
Type of analysis	Linear Elastic	Linear Elastic	Linear Elastic	Linear Elastic
Composed line				
Element type	CL3CM	CL3CM	CL3CM	CL3CM
Element length [mm]	27	27	27	27
Number of elements	3.819	3.013	4.624	5.287
Number of nodes	18.410	14.728	20.785	25.384
Number of dofs	55.230	44.184	62.355	76.152

Table 1.5: Moments caused by edge disturbance model parameters

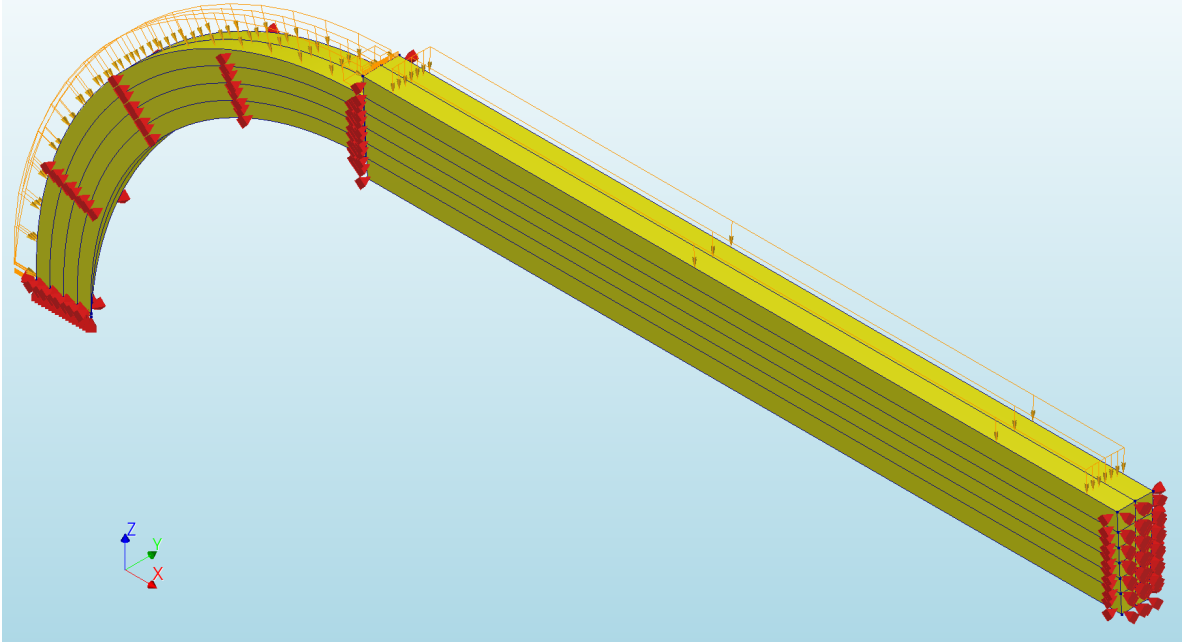


(a) Overview

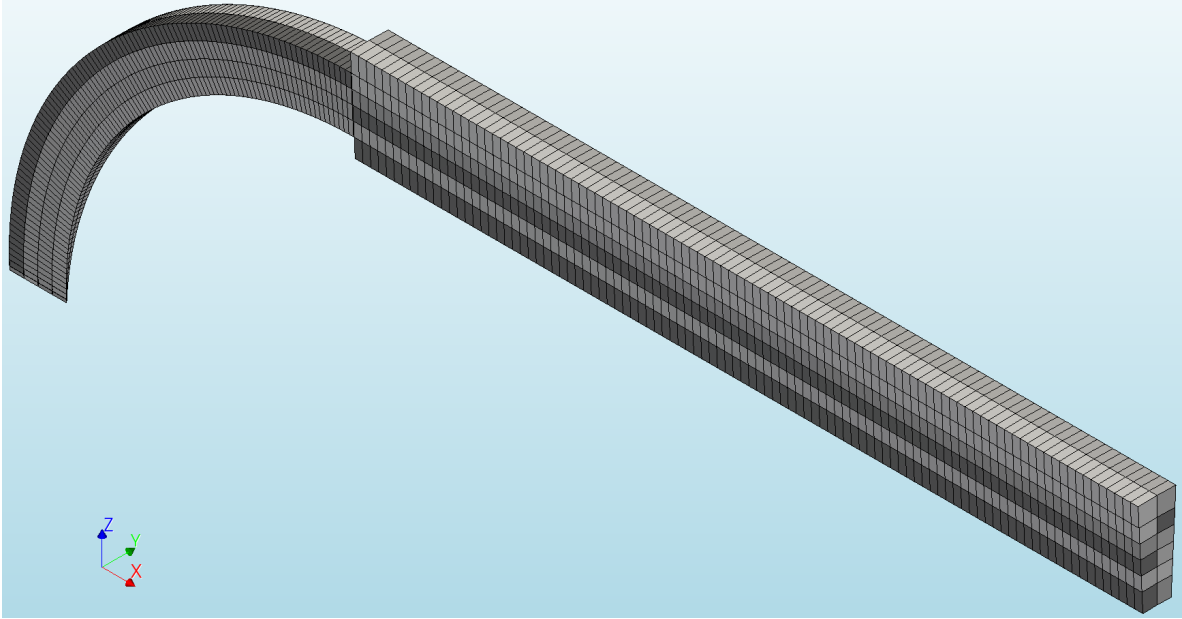


(b) Mesh

Figure I.29: Hemisphere thickness model; $t_h = t_c$

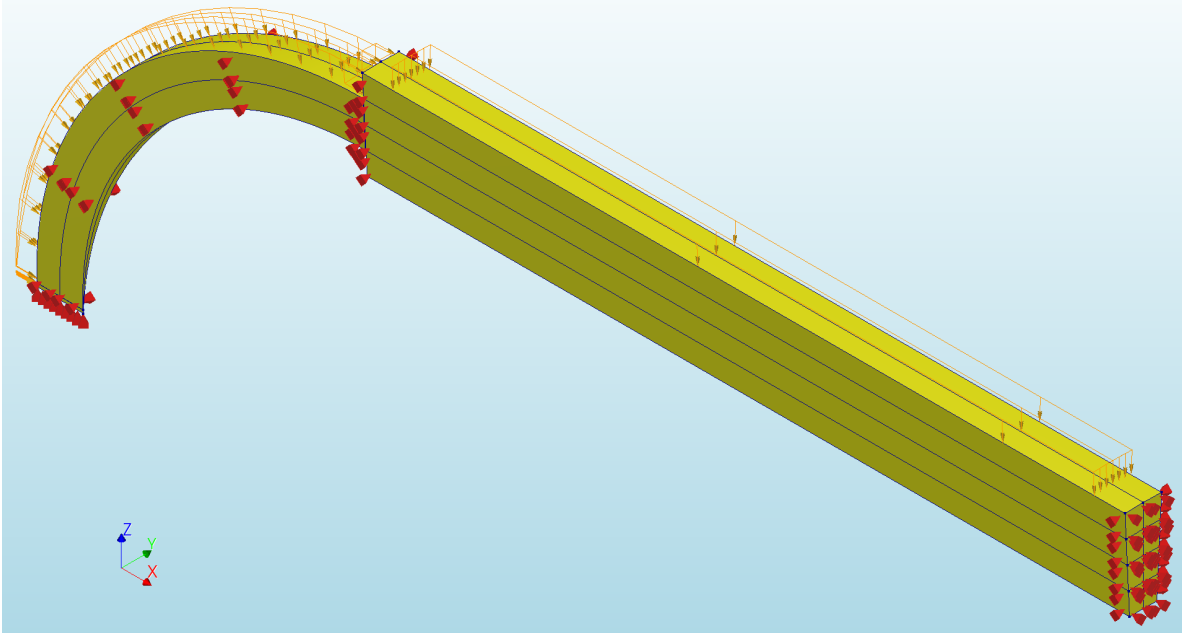


(a) Overview

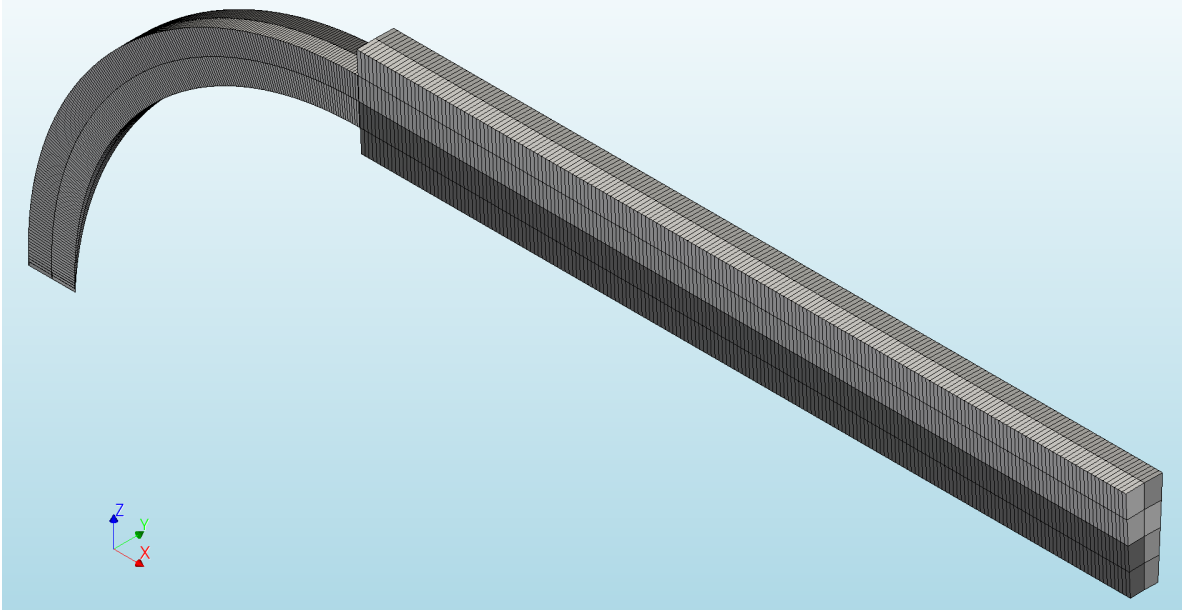


(b) Mesh

Figure I.30: Hemisphere thickness model; $t_h = 0,6t_c$

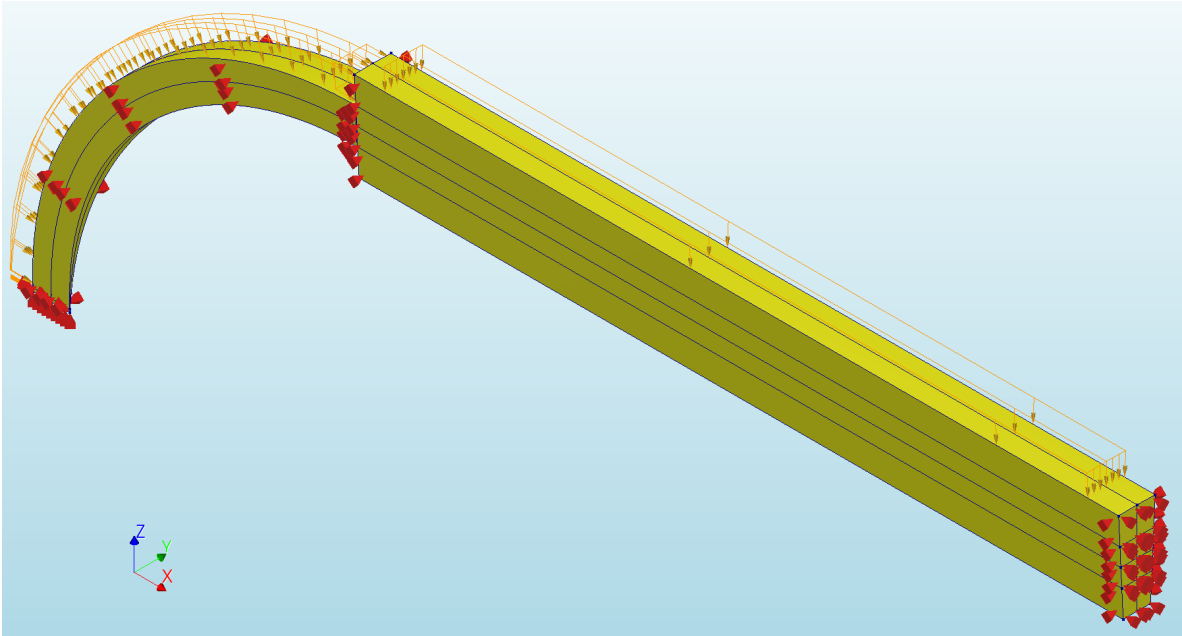


(a) Overview

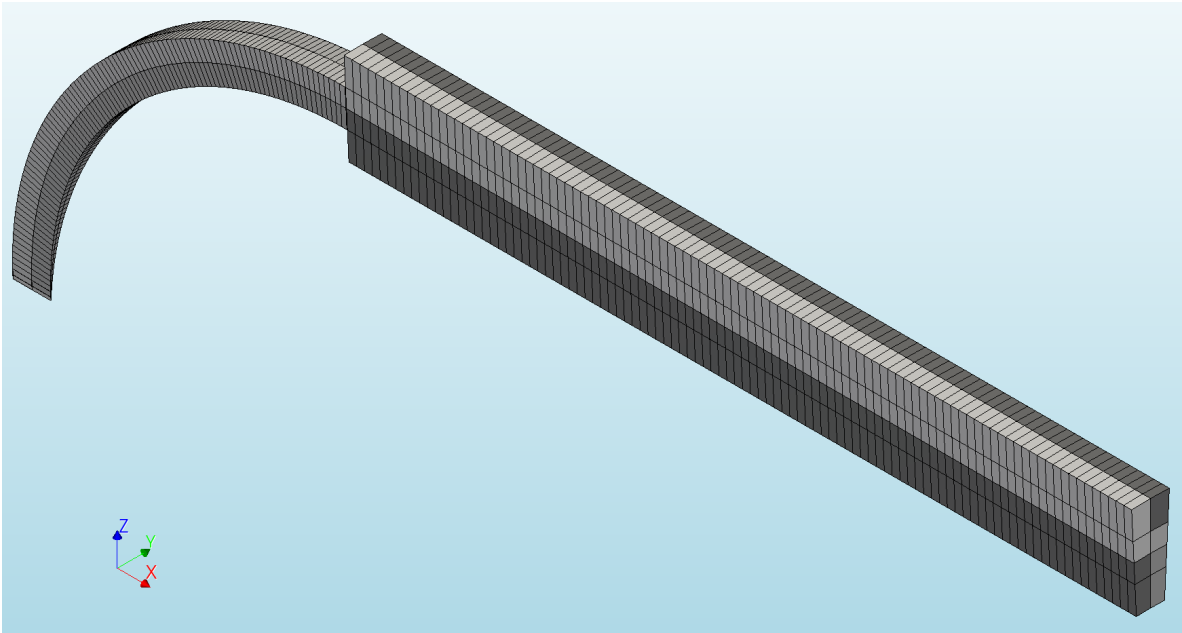


(b) Mesh

Figure I.31: Hemisphere thickness model; $t_h = 0,5t_c$



(a) Overview



(b) Mesh

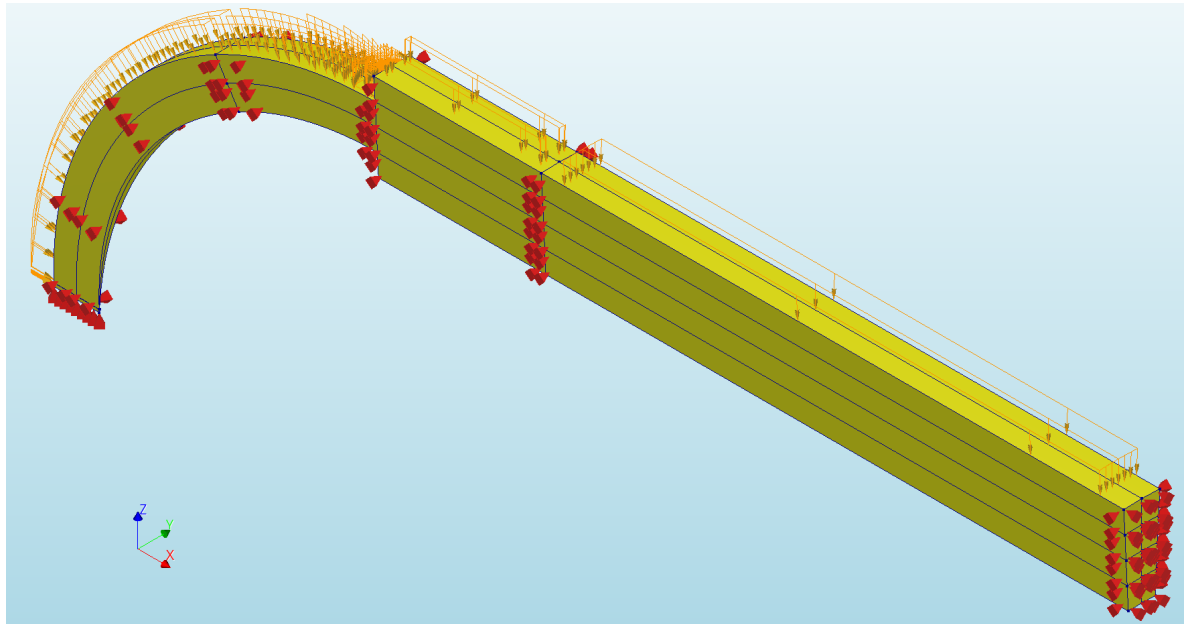
Figure I.32: Hemisphere thickness model; $t_h = 0, 4t_c$

I.3.3. Models for redistribution of stress concentration at cylinder-hemisphere transition

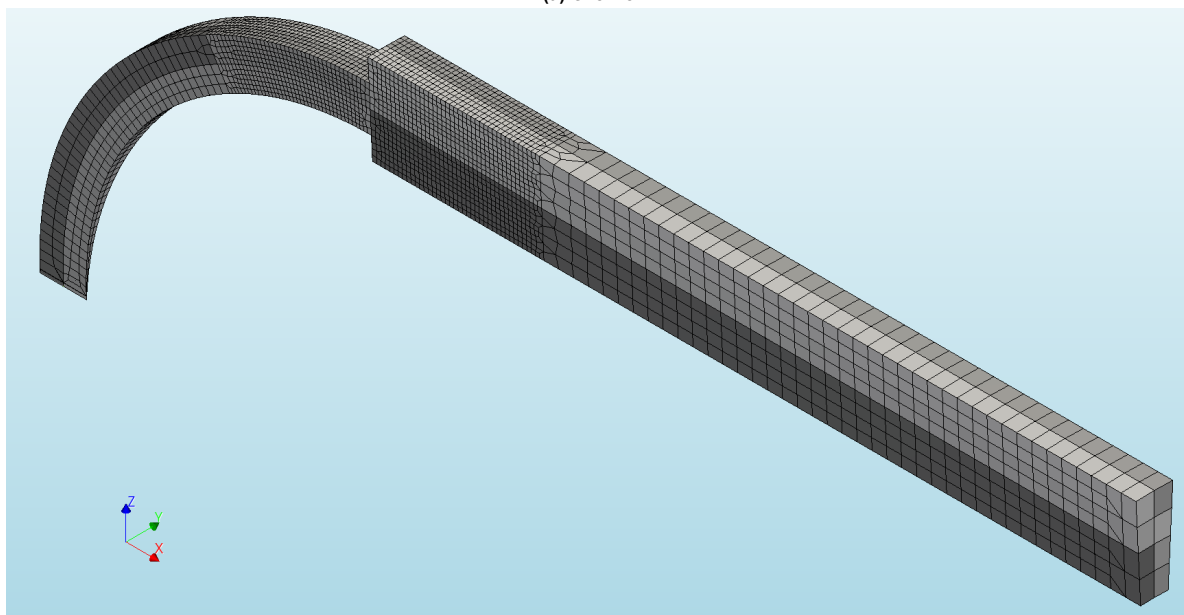
This section delineates the specifications of the models utilized in Section 6.1.4 to explore the impact of the transition design between the cylinder and hemisphere on stress concentrations within the transition zone. The parameters of the models are detailed in Table I.6, while an overview of the models and their meshes is presented in Figures I.33, I.34 and I.35 below.

Transition	Abrupt	Triangular	Circular
Internal radius a [m]	4,84	4,84	4,84
Wall thickness t [m]	1,62	1,62	1,62
Tube length [m]	13,44	13,44	13,44
Hemisphere thickness [m]	0,81	0,81	0,81
Distributed force [MPa]	10,06	10,06	10,06
Young's Modulus [MPa]	39.100	39.100	39.100
Poissons ratio	0,2	0,2	0,2
Element type	Structural solids CHX60 & CPY39 CTE30 & CTP45	Structural solids CHX60 & CPY39 CTE30 & CTP45	Structural solids CHX60 & CPY39 CTE30 & CTP45
Element size [mm]	50 & 200 & 400	20 & 80 & 400	400 & 200 & 80
Number of elements over wall thickness	4 & 12 & 16	2 & 4 & 20	4 & 20
Model dimension	3D	3D	3D
Type of analysis	Linear Elastic	Linear Elastic	Linear Elastic
Number of elements	12.072	15.955	6.378
Number of nodes	53.186	52.421	25.081
Number of dofs	159.558	157.263	75.243

Table I.6: Cylinder-hemisphere transition model parameters

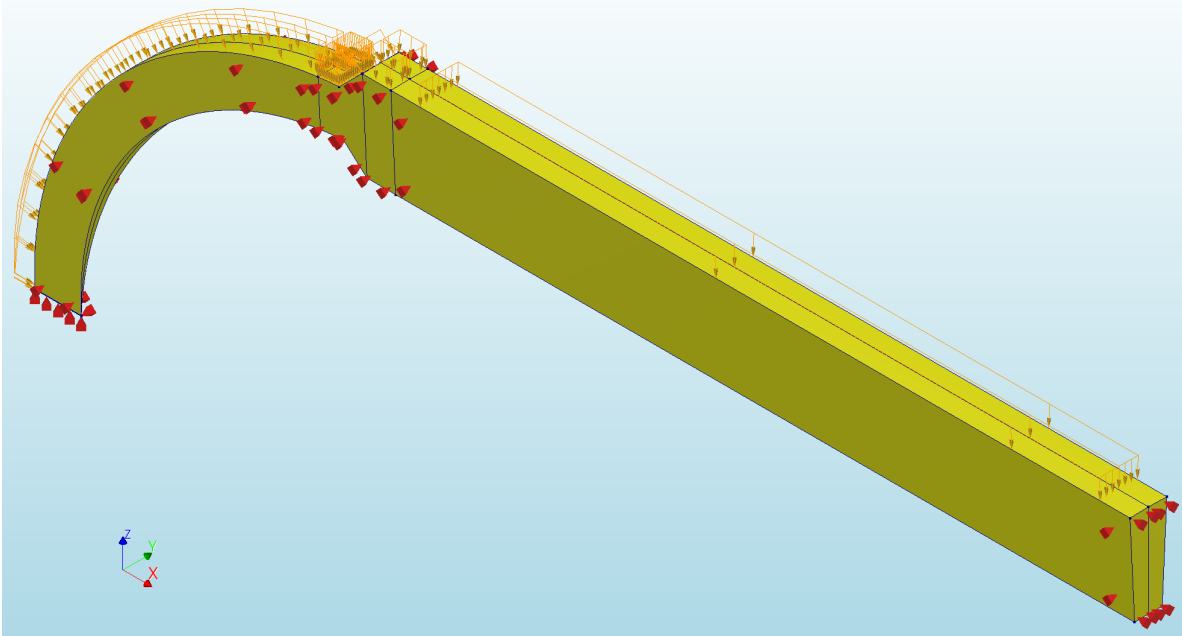


(a) Overview

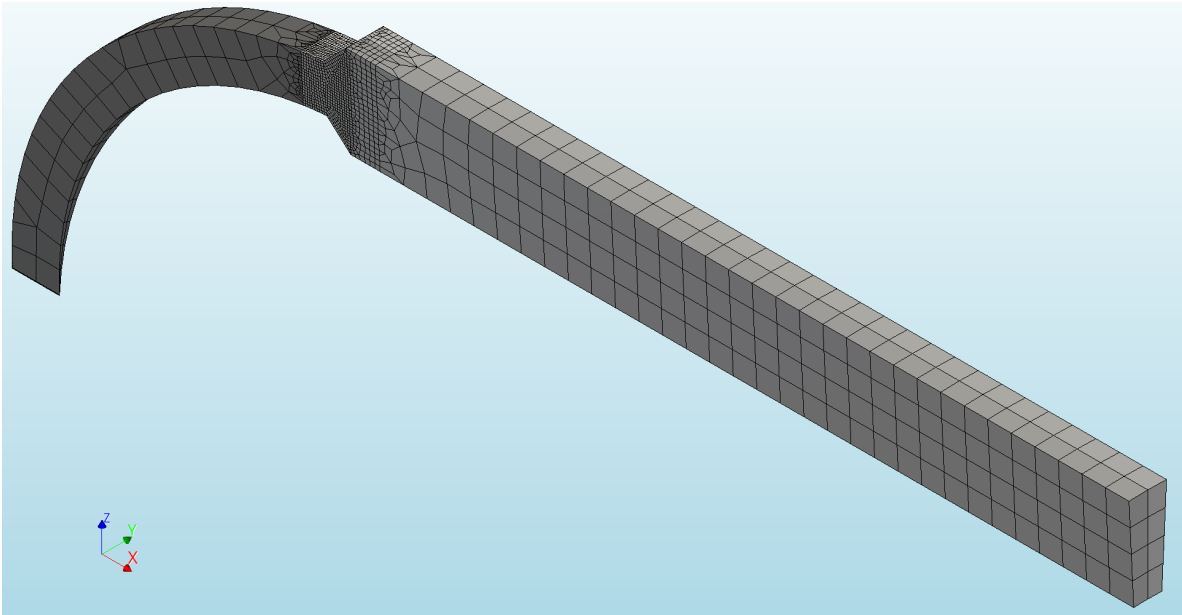


(b) Mesh

Figure I.33: Abrupt transition model; $t_h = 0, 5t_c$

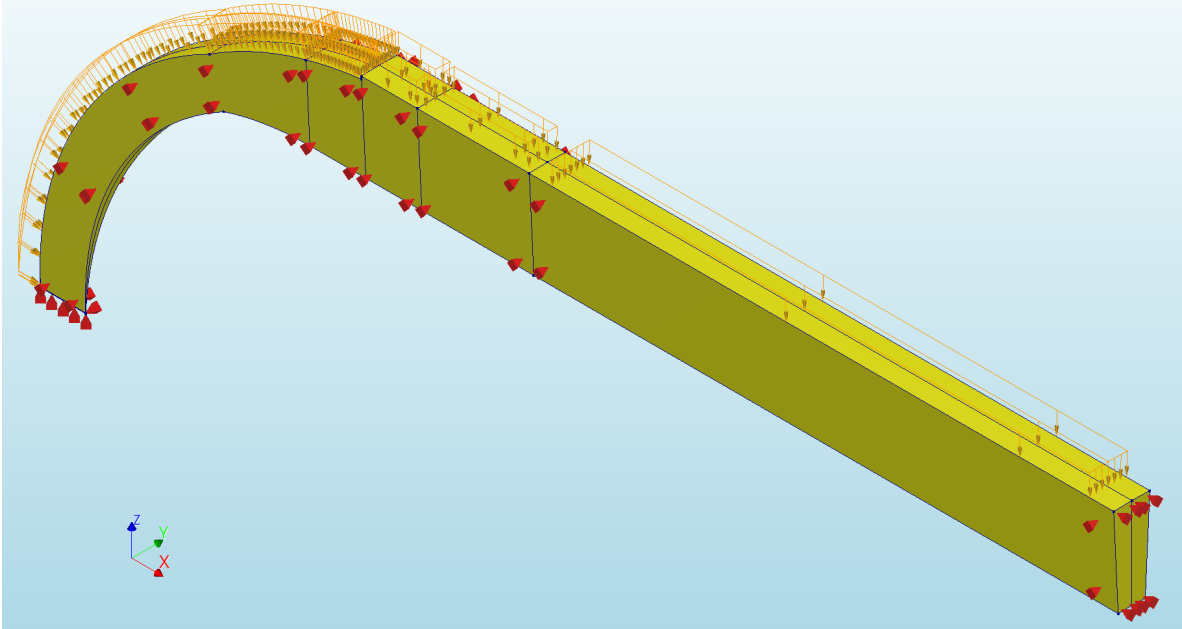


(a) Overview

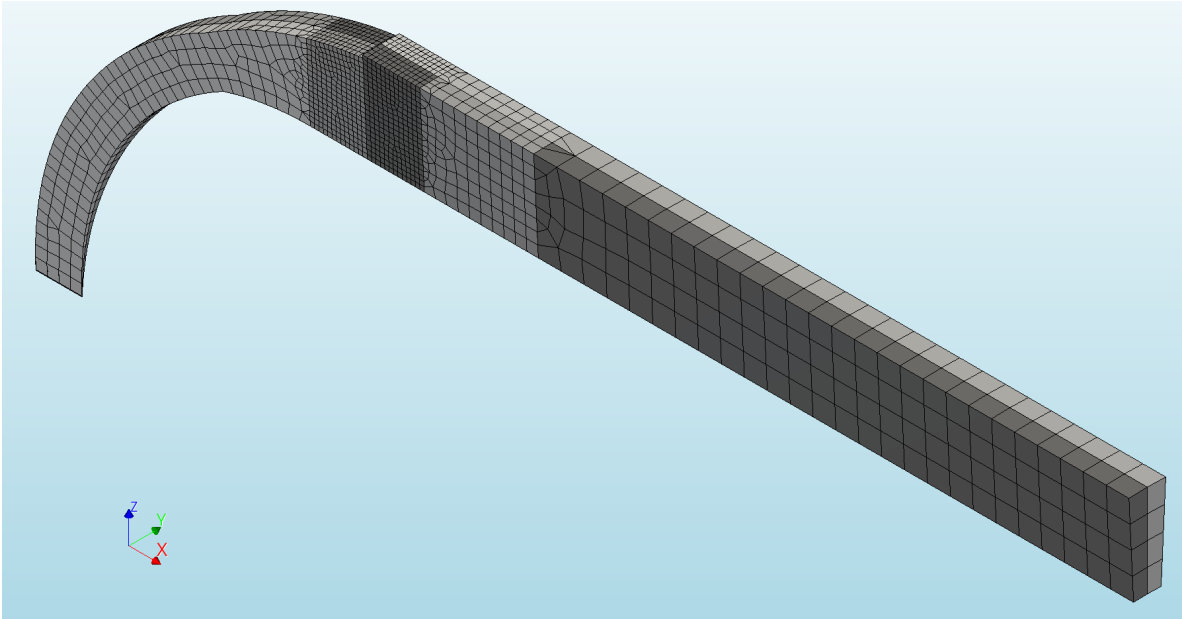


(b) Mesh

Figure I.34: Triangular transition model; $t_h = 0,5t_c$



(a) Overview



(b) Mesh

Figure I.35: Circular transition model; $t_h = 0,5t_c$